

SCUOLA DOTTORALE IN GEOLOGIA DELL'AMBIENTE E DELLE RISORSE
DOTTORATO IN GEOLOGIA DELL'AMBIENTE E GEODINAMICA

CICLO DEL CORSO DI DOTTORATO XXVII

SPATIO-TEMPORAL EVOLUTION OF INTRAPLATE STRIKE-SLIP
FAULTING: THE KUH-E-FAGHAN FAULT, CENTRAL IRAN

GABRIELE CALZOLARI
Nome e Cognome del dottorando



firma



firma


FEDERICO ROSSETTI
Docente Guida/Tutor: Prof.

MARTA DELLA SETA
Co-Tutor: Prof.



firma

CLAUDIO FACCENNA
Coordinatore: Prof.



firma

Collaborations

Alexis Ault	<i>Department of Geology, Utah State University</i>
Maria Laura Balestrieri	<i>CNR-Istituto di Geoscienze e Georisorse</i>
Domenico Cosentino	<i>Dipartimento di Scienze, Università Roma Tre</i>
Claudio Faccenna	<i>Dipartimento di Scienze, Università Roma Tre</i>
Reza Nozaem	<i>Department of Science, Imam Khomeini International University</i>
Valerio Olivetti	<i>Centre de Recherche et d'Enseignement de Géosciences de l'Environnement</i>
Gianluca Vignaroli	<i>Dipartimento di Scienze, Università Roma Tre</i>



Contacts:

*gabriele.calzolari@uniroma3.it
gabrielecalzolari@yahoo.it*

Acknowledgements

I would like to express my special appreciation and thanks to my supervisor professor Federico Rossetti, for the extensive guidance and mentoring provided during the research project. I would like to thank you for supporting my research and for allowing me to grow as a researcher. Your advice during both the field campaigns and during the writing stages have been priceless. I would also like to thank you for being always available to talk to me and for your patience and the time you dedicated to me during our very long discussions, which have been so fundamental to my doctoral training. I would also like to extend my gratitude and thanks to my co-supervisor doctor Marta Della Seta, for all the new skills she has taught me and for the time she has dedicated to my training and project. I will never forget the enjoyable, joyful and productive field trips that we had together in Central Iran.

A special thanks goes to all the people with whom I collaborated in this project: Alexis Ault, Maria Laura Balestrieri, Domenico Cosentino, Claudio Faccenna, Reza Nozaem, Valerio Olivetti and Gianluca Vignaroli. Your different expertise, advice and contributions have been fundamental to the successful outcome of this multidisciplinary research project. Professor Federico Salvini is thanked for his advice during fault population analysis.

A super special thanks goes to my friend and fellow colleague Mohammad Reza Mazinani for the great company and help during the twenty days long fieldtrip we endured together in the “hot Kavir”. I would have not made it without you. I am also grateful to the guest-house manager and staff of Khaney-e-Moallem of Kashmar for their kind hospitality. I also thank Ali Rastpour and Hassan Faraji for driving to the field and logistic support.

I would also like to thank my committee members, professor Maria Rita Palombo, professor Orlando Vaselli and, doctor Marco Bonini for serving as my committee. Furthermore, I am also grateful to doctor Paolo Ballato and professor Olivier Bellier for the comprehensive review of my thesis manuscript.

Many thanks go to my ex master supervisor, lecturer and long-time hero professor Peter Kokelaar, for encouraging and supporting me to continue my academic career. I probably would not be here without his guidance.

Special thanks goes also to all the people that made the TOPOMOD Marie Curie ITN project (Grant agreement 264517) possible, and in particular to Professor Claudio Faccenna and doctor Francesca Funicello who have invested so much time and energy of their own to make it happen.

Last but not least I would like to thank my family. Words cannot express how grateful I am to my mother and father for all of the sacrifices that you’ve made on my behalf. I would like to express appreciation to my beloved wife Maria Laura who spent sleepless nights with and was always my support in the moments when there was no one to answer my queries. At last, I would like to thank my eight month old boy Vincenzo, for giving me so much motivation in these last final months.

Spatio-temporal evolution of intraplate strike-slip faulting: the Kuh-e-Faghan Fault, Central Iran

Abstract

L'Iran Centrale fornisce un sito ideale per lo studio della risposta morfogenetica all'enucleazione e propagazione della fagliazione intraplacca. In questo studio viene adottato un approccio multidisciplinare, che integra il rilevamento geologico-strutturale e morfostratigrafico, con analisi termocronologiche (apatite fission track (AFT), (U-Th)/He su apatite (AHe) e ematite (HeHe)), geocronologiche (Luminescenza Otticamente Stimolata, OSL), e morfometriche al fine di ricostruire l'evoluzione spatio-temporale del sistema di faglie Kuh-e-Faghan Fault (KFF), in Iran Centrale.

Il rilevamento geologico-strutturale rivela che la KFF definisce una zona di deformazione lunga circa 80 km, la quale consiste di tre principali segmenti di faglia con orientamento E-W a *step* sinistro e cinematica trascorrente destra, i quali tagliano il substrato paleozoico-mesozoico e le coperture sedimentarie neogenico-quadernarie. Complessivamente i dati termocronologici provenienti dalle analisi AHe e AFT indicano che i sedimenti neogenici hanno avuto temperature di seppellimento superiori ai 60°C e inferiori al 110°C. In particolare, risultati delle analisi termocronologiche AHe indicano che i blocchi intra-faglia lungo la KFF hanno vissuto due eventi di esumazione legati alla fagliazione a ~18 Ma and ~4 Ma. Il primo episodio di fagliazione/esumazione a ~18 Ma, è principalmente registrato dall'architettura deposizionale delle successioni neogeniche. In particolare, uno scenario "*source-to-sink*" può essere ricostruito durante il Miocene inferiore, durante il quale la crescita topografica della KFF è stata accompagnata da erosione/esumazione delle unità pre-neogeniche e deposizione del materiale precedentemente eroso nei bacini strutturalmente controllati. Successivamente, la KFF gradualmente è entrata in un periodo di quiescenza tettonica, accompagnata probabilmente da subsidenza a scala regionale, durante la quale spesse sequenze di siltiti hanno ricoperto l'intera area della KFF, causando il *resetting* del sistema (U-Th)/He nelle apatiti contenute all'interno delle unità pre-neogeniche e alla base di quelle neogeniche. Il secondo episodio di fagliazione a ~4 Ma ha causato l'ultimo evento di esumazione ed ha originato l'attuale architettura strutturale della zona di faglia e la configurazione topografica della KFF. Le analisi termocronologiche HeHe eseguite su specchi di faglia decorati ad ematite registrano sia età correlabili al primo evento di (>6-4Ma), sia al secondo evento (<6-4 Ma) di fagliazione/esumazione; di fatto confermando la storia d'esumazione polifasica del sistema di faglie KFF.

L'integrazione del *dataset* strutturale, stratigrafico e termocronologico indica che la KFF si è nucleata ad ovest e si è propagata verso est in maniera polifasica.

L'analisi topografica del sistema KFF rivela che i due eventi di propagazione ed esumazione, i quali hanno formato l'architettura strutturale e stratigrafica del sistema di faglie, possono essere riconosciuta nella configurazione topografica della KFF. In particolare, il primo rilievo (and ovest) con una lunghezza d'onda di 10 km, corrispondente al *western topographic domain* lungo ~42 km e il secondo rilievo (ad est) corrispondente all'*eastern topographic domain* lungo ~23 km sono identificati rispettivamente come segnali topografici residui del primo (~ 18 Ma) e secondo (4 ~ Ma) evento d'esumazione. L'analisi geomorfologica e geocronologica (OSL) dei depositi di conoide alluvionale e di piana alluvionale che circondano la KFF mostrano che la genesi e lo sviluppo di tali depositi è stata primariamente controllata da fasi climatiche di aggradazione tardo-quadernarie e oloceniche già riconosciute da altri autori in tutto l'Iran. Ciononostante, la documentata configurazione e lo stile di deposizione di tali depositi indica che sono stati fortemente influenzati dall'attività tettonica del sistema di faglie e dalla conseguente riorganizzazione del reticolo idrografico. In particolare, le datazioni OSL su quarzo dei depositi quadernari fagliati indica che la KFF debba essere considerata una faglia attiva. L'analisi morfometrica dell'inclinazione delle superfici sommitali dei conoidi alluvionali quadernari rivela che la crescita topografica della KFF è ancora attiva.

I principali risultati di questo studio portano importanti implicazioni circa: (i) la comprensione dell'evoluzione spazio-temporale del e propagazione dei sistemi di faglie trascorrenti intraplacca, (ii) la risposta intraplacca alle riorganizzazioni tettoniche lungo i margini collisionali, e (iii) l'evoluzione cinematica e tettonica neogenico-quadernaria in Iran Centrale.

(i) In questo lavoro viene proposto un modello concettuale sull'enucleazione e la propagazione della fagliazione trascorrente intraplacca. Il modello prevede che la deformazione sia inizialmente delocalizzata ed distribuita lungo set di faglie *en-echelon* le quali controllano la crescita topografica iniziale e la localizzazione dell'erosione/sedimentazione. Le proprietà meccaniche di *strain hardening* e *velocity-strengthening* dei depositi sin-tettonici causano la progressiva inibizione della fagliazione all'interno dei depositi, causando la progressiva migrazione verso l'interno delle principali zone di faglia. Questo processo risulta in una localizzazione della deformazione lungo segmenti di faglia ben definiti e maturi. La dissipazione del rigetto trascorrente lungo le terminazioni dei principali segmenti di faglia viene ottenuta attraverso lo sviluppo di *trailing extensional imbricate fan* i quali inibiscono ulteriormente la propagazione delle zone di faglia. Tali terminazioni estensionali/trastensive sono associate a depocetri in subsidenza tettonica i quali controllano fortemente la distribuzione e gli spessori dei depositi associati. Conseguentemente il sistema di faglia si propaga attraverso la creazione di nuovi segmenti, con deformazione a carattere diffuso, in zone indeformante, lungo il *tip* del sistema di faglia.

(ii) I due eventi di esumazione legati alla fagliazione, documentati a ~18 and ~4 Ma lungo la KFF, coincidono con gli eventi regionali di accelerazione dell'esumazione legata alla collisione

continentale durante il Miocene inferiore, e di riorganizzazione tettonica della zona di collisione Turco-Iraniana durante il Miocene superiore-Pliocene inferiore. Pertanto questo studio mostra che l'evoluzione a lungo termine della KFF, situata nell'intraplacca iraniana, è caratterizzata da una storia polifasica d'esumazione legati alla fagliazione, quasi coincidenti con i due eventi tettonici registrati lungo il margine di placca. Questo suggerisce che i sistemi di faglia intraplacca siano particolarmente sensibili alle variazioni dei regimi di stress (*far-field*) che operano lungo i margini di placca e, di conseguenza, il loro studio può fornire importanti vincoli alle variazioni dei regimi tettonici ai margini di placca.

(iii) I risultati di questo studio, assieme a quelli recentemente pubblicati da altri autori, impongono una rivalutazione dell'evoluzione spazio-temporale e cinematica dell'Iran Centrale nel quadro della storia di collisione e convergenza di Arabia e Eurasia. In questo studio viene proposto che la deformazione neogenico-quadernaria dell'Iran sia stata principalmente controllata dal grado di accoppiamento lungo l'interfaccia collisionale Arabia-Eurasia. La variazione nello spazio e nel tempo di tale accoppiamento, insieme alla capacità di accomodare la convergenza lungo la zona di collisione, hanno controllato la quantità di convergenza trasferita ai domini intraplacca e pertanto hanno controllato la distribuzione, la cinematica e la configurazione della deformazione nello spazio e nel tempo.

Abstract

Central Iran provides an ideal test site to study the morphotectonic response to enucleation and propagation of intraplate faulting. In this study, a multidisciplinary approach that integrates structural and stratigraphic field investigations with geochronological (optically stimulated luminescence, OSL) and thermochronological (apatite fission track (AFT), (U-Th)/He su apatite (AHe) e ematite (HeHe)) analyses, is used to reconstruct the spatio-temporal evolution of the Kuh-e-Faghan Fault (KFF), in northeaster Central Iran.

Structural mapping reveals that KFF defines a narrow, ca. 80 km long, deformation zone consisting of three main broadly left stepping, E-W trending, right-lateral fault strands which cut through the Mesozoic-Paleozoic substratum and the Neogene-Quaternary sedimentary covers. The AHe thermochronology results indicate that the intra-fault blocks along the KFF experienced two major episodes of fault-related exhumation at ~18 Ma and ~4 Ma. The first faulting/exhumation episode at ~18 Ma is chiefly recorded by the Neogene deposits architecture along the KFF. In particular, a source-to-sink scenario can be reconstructed for this time frame, when topographic growth caused the synchronous erosion/exhumation of the pre-Neogene units and deposition of the eroded material in the surrounding fault-bounded continental depocenters. Successively, the KFF gradually

entered a period of relative tectonic quiescence and, probably, regional subsidence during which a thick pile of fine-grained onlapping sediments were deposited, caused the resetting of the (U-Th)/He system of the detritic apatite grains hosted both within the pre-Neogene and the basal Neogene successions. AFT dating indicates that the basement units, that are now exposed to the surface, where most probably below the closure temperature (100-120 °C) of the AFT system during the first exhumation event (at ~18 Ma) and, similarly, the AFT system of the pre-Neogene and Neogene deposits have not been reset by Miocene burial (>4 Ma). Together, the AHe and AFT data from the Neogene basin sediments imply burial temperatures in excess of ~60 °C and less than 100 °C. The second faulting episode at ~4 Ma caused the final fault exhumation event, resulting in the current fault zone and topographic architecture. The HeHe ages of hematite coated fault surfaces register both formation ages during the first exhumation event (>6-4Ma) and exhumation ages during the second exhumation event (<6-4 Ma), thus confirming the polyphase history of the KFF system. Collectively the stratigraphic, structural and thermochronological datasets shows that the KFF enucleated in the west and propagated eastward in two punctuated events.

Topographic analysis of the KFF reveals that the two fault propagation and exhumation events that shaped the structural and stratigraphic architecture of the fault system can be recognized in the current topographic configuration of the KFF. In particular 10-km wavelength relief corresponding to the ~42 km long western topographic domain and the overall eastward narrowing and decreasing in elevation and relief, ~23 km long eastern topographic domain, are identified as the remnant topographic signals of the first (~18 Ma) and second (~4 Ma) exhumation event, respectively.

Geomorphological analysis and OSL dating of the KFF Quaternary alluvial deposits show that the generation and development of the deposits were primarily controlled by late Quaternary and Holocene, climate-driven aggradation phases recognized throughout the Iranian plateau by other studies. Nevertheless, their geometric configuration and style of deposition documented along the KFF indicated that they have been strongly influenced by the fault system tectonic activity and the consequent drainage network rearrangement. In particular OSL of quartz grains from faulted alluvial deposits indicates that the KFF is interested by active E-W oriented, Late Pleistocene to Holocene right-lateral tectonics. The morphometric slope analysis of the quaternary alluvial deposits indicates that the KFF is still producing fault related topographic growth.

The major outcomes of this study have important implications on (i) understanding the propagation and spatio-temporal evolution of intraplate strike-slip fault systems; (ii) the intraplate response to tectonic reorganization at the collisional boundaries; and (iii) the Neogene-Quaternary kinematic and tectonic evolution of Central Iran.

(i) A conceptual model of fault initiation and propagation is proposed. Deformation starts from diffuse deformation accomplished by distributed en-echelon shears, which control initial topographic

growth and focused erosion/sedimentation. The strain hardening and velocity-strengthening properties of the syn-tectonic sedimentary deposits progressively inhibits the fault propagation and causes the overall inward migration of the fault zone. This results in an overall localization of the shear deformation along thoroughgoing fault strands and creation of mature fault zones. Strike-slip shear dissipation at eastern fault zone terminations is achieved through the development of trailing extensional imbricate fan, inhibiting further length-ward fault propagation. The extensional/transensional faulting and the associated tectonically-controlled subsiding depocenter, strongly control the deposits distribution and thicknesses. As a result, the fault systems may then propagate by renewed diffuse shear deformation in undeformed regions at the fault tip, creating new fault strands.

(ii) The two fault-related exhumation episodes, at ~18 and ~4 Ma, well fit with the regional early Miocene collision-enhanced uplift/exhumation and the late Miocene–early Pliocene widespread tectonic reorganization of the Turkish-Iranian collision zone, respectively. As such the study shows that the long term evolution history of the KFF system in intraplate Iran is characterized by punctuated events nearly coincident with major tectonic events at the plate boundaries. This strongly suggests that the intraplate response along strike-slip fault systems is particularly sensitive to major (far-field) tectonic changes occurring at the plate boundaries, and, as such, intraplate deformation zones can be regarded as a gage for plate-tectonics induced state of stress changes at the plate boundaries.

(iii) Results from this study, together with the outcomes from recently published studies, impose a reappraisal of the spatio-temporal kinematic evolution of Central Iran in the aftermath of the Arabia-Eurasia collision history. It is proposed that the Neogene-Quaternary deformation in Iran has been primarily controlled by the spatial and temporal variations in the degree of coupling along the Arabia-Eurasia collision interface. The spatio-temporal changes in the degree of coupling, together with the capacity of accommodating convergence along the collision zone, controlled the amount of northward convergence that was transferred to the intraplate domain and therefore controlled the deformation distribution kinematic configuration in space and time. The revised tectonic/kinematic model needs to be improved and validated by further studies to be carried out along the major fault systems of south-central Iran, in order to verify their persistence, distribution, kinematics and overall space-time evolution.

CONTENT

Acknowledgements	1
Abstract	2
CONTENT	7
1 INTRODUCTION.....	10
1.1 Hints from modelling	13
1.2 Hints from natural strike-slip fault systems	18
1.3 Topographic growth and exhumation	20
1.4 Investigating continental deformation.....	21
1.5 Open Questions	23
2 AIMS OF THE RESEARCH AND RATIONALE	25
3 GEOLOGICAL BACKGROUND	27
3.1 Regional tectonic setting	27
3.2 Central Iran.....	28
3.3 The study area	29
4 METHODOLOGY	32
4.1 Field work	32
4.1.2 Structural survey	32
4.1.3 Stratigraphic survey	32
4.1.4 Geomorphological survey	32
4.2 Digital Elevation Model and topographic analysis	33
4.3 Sampling and analytical work	34
4.3.1 Apatite (U-Th)/He (AHe) and Apatite Fission Tracks (AFT) dating	34
4.3.2 Hematite (U-Th)/He (HeHe) dating	35
4.3.3 OSL dating	36
5 TOPOGRAPHIC SIGNATURE OF THE KFF	38
6 NEOGENE STRATIGRAPHY	42
6.1 Stratigraphic cycles and units.....	42
Cycle-1	42
Cycle-2	47
Cycle-3	47
7 QUATERNARY LANDFORMS AND DEPOSITS	50
7.1 Sedimentological characters.....	55
7.2 Morphological characters.....	55

8 STRUCTURAL DATA AND FAULT KINEMATICS	59
8.1 Western fault strand	61
8.2 Central fault strand	64
8.3 Eastern fault strand.....	66
8.4 Minor Faults	70
8.5 Fault zone architecture	72
8.6 Quaternary faulting	72
9 MORPHOMETRIC ANALYSIS	74
9.1 Alluvial fan slope analysis	77
9.1 Results	77
10 THERMOCHRONOLOGY AND GEOCHRONOLOGY	80
10.1 Apatite (U-Th)/He (AHe) and Apatite Fission Tracks (AFT) dating	80
10.2 Hematite (U-Th)/He (HeHe) dating	83
10.3 Optically Stimulated Luminescence (OSL) dating	85
10.3.1 Results	86
11 DISCUSSION	89
11.1 Structural synthesis	89
11.2 Stratigraphic architecture: linking faulting to sedimentation.....	92
11.3 A two stage exhumation history.....	94
11.3.1 AHe and AFT dating	94
11.3.2 HeHe dating	96
10.4 Quantifying and comparing exhumation and slip rates.....	97
11.5 The long-term evolution of the Kuh-e-Faghan Fault: enucleation, propagation, and topographic growth	98
11.5.1 Fault system nucleation.....	99
11.5.2 Fault localization and propagation	99
11.5.3 Fault termination and tectonic quiescence	100
11.5.4 Renewed faulting	100
11.6 Topographic signal of KFF and geomorphic response to active tectonics	107
11.6.1 Linking exhumation history, style of deformation and topographic signal of KFF	107
11.6.2 Constraints on Quaternary morpho-evolution.....	108
11.6.3 Constraints on fault-related Quaternary uplift	109
11.7 Implications.....	110
11.7.1 Regional tectonics	110

11.7.2 Implications for topographic growth along intraplate strike-slip faults.....	114
12 SUMMARY AND CONCLUSIONS	115
References	119
Appendix	136
Appendix-A Figure location map.....	136
Appendix-B Structural data.....	137
Appendix C: Manuscript submitted to GSA Bulletin the 2 nd of January 2015	152
Appendix D: Manuscript to be submitted to Tectonics	203

1 INTRODUCTION

Strike-slip tectonics is a fundamental process affecting many parts of the Earth's lithosphere and resulting in prominent tectonic, geophysical and topographic expressions (for general review Biddle, 1985; Christie-Blick, 1985; Harding, 1985, 1990; Holdsworth et al., 1998; Lowell, 1985; Storti et al., 2003; Sylvester, 1984; Sylvester, 1988; Till, 2007; Woodcock and Schubert, 1994; Woodcock and Fischer, 1986).

Since the recognition of strike-slip dominated plate boundaries, also known as transform faults (Wilson, 1965), several studies have identified their geometric linkage and kinematic interaction with constructive and destructive plate margins (e.g. McKenzie and Parker, 1967; Morgan, 1968). Such studies were instrumental to the emergence of the plate tectonics theory, which assumes that lithosphere within the plate interior is to be considered rigid and plate motion-related deformation and interactions are concentrated along narrow belts outlining the plate boundaries. Despite this scenario well fits with oceanic plate settings, as attested by the seismic activity located along their active plate boundaries, deformation distribution in continental regions is complicated by the non-rigid behavior of the continental lithosphere (Molnar, 1988). This has been attributed to a weak quartzo-feldspatic dominated rheology of the continental lithosphere and to the occurrence of mechanical anisotropies (such as shear zones), which may be promptly reactivated during episodes of regional deformation (Di Vincenzo et al., 2013; Holdsworth et al., 2001a; Holdsworth et al., 2001b; Kocyigit and Beyhan, 1998; Marshak et al., 2003; Morley, 2007; Rutter et al., 2001; Storti et al., 2003; Vauchez and Tommasi, 2003). This behavior is well illustrated in regions affected by continental collision, where seismicity extends deep into the continental plate interiors defining broad diffuse zones of deformations (e.g. Central Iran, Turkey and Tibetan plateau Hatzfeld and Molnar, 2010; Fig. 1.1). It may be useful to view such regions of non-rigid behavior as broad, diffuse plate boundaries (e.g. Gordon, 1998 and references therein) but in the present work we shall refer to all regions located away from the major plate boundaries as 'intraplate' (as defined in: Storti et al., 2003).

In such settings the stresses and forces that produce intraplate deformation are thought to be governed by plate margin dynamics (England and McKenzie, 1982; Molnar, 1988; Tapponnier and Molnar, 1976). In particular it has been shown that the most important factor controlling the transmission of stresses from the plate boundaries to the intraplate domains is the degree of tectonic coupling at the collisional interface (Ellis, 1996; Ziegler et al., 1998). Figure 1.2 summarizes Ellis's (1996) theoretical work on continental deformation. As demonstrated by regional and global stress field maps (e.g. Heidbach et al., 2001; Heidbach et al., 2008; Zoback, 1992), compressional horizontal stresses can be transmitted from the plate boundaries across very large distances, through continental and oceanic lithosphere. In fact, compressive intraplate deformation can be found at distances up to

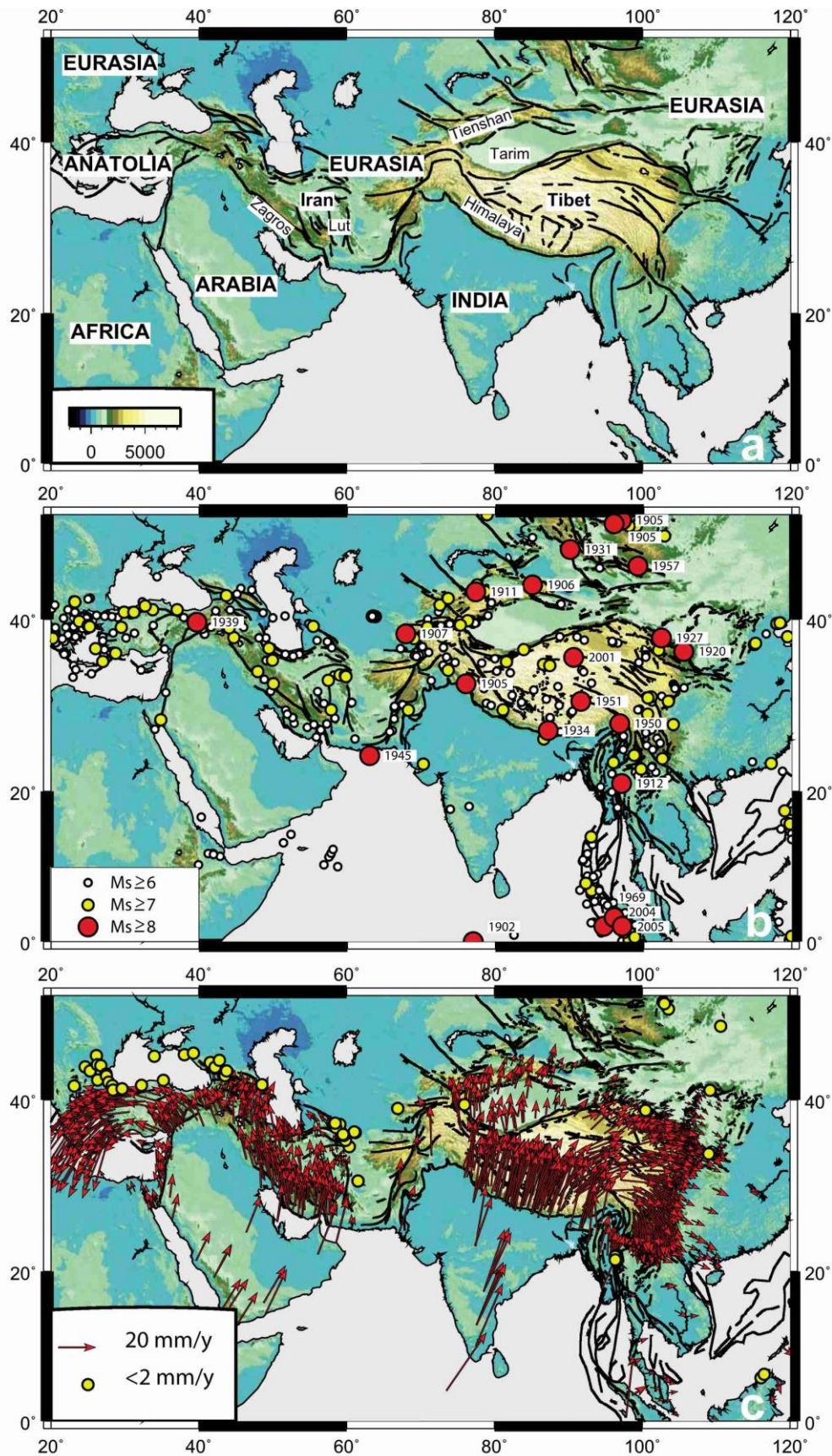


Figure 1.1 Topographic maps of Asia showing the (a) major fault system associated with orogenic belts and intraplate deformation terrains, (b) the historic and instrumental seismicity and (c) the GPS velocity vectors in a frame of stable Eurasia. After Hatzfeld and Molnar (2010)

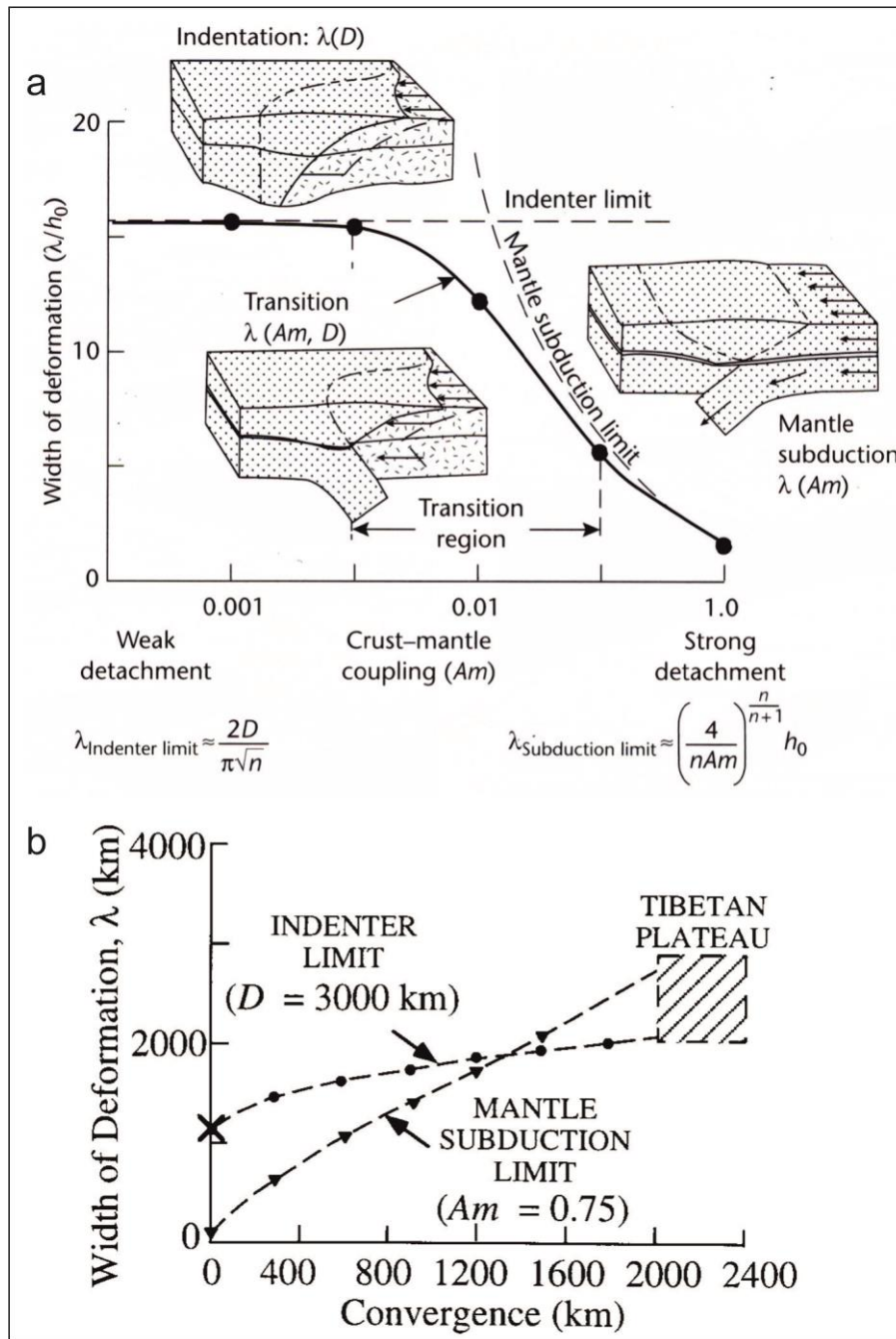


Figure 1.2 Ellis (1996) work on continental deformation theory. Figure after Ellis (1996). Terms: λ = deformation over an across strike width; D = along strike indentation length scale; n = power law exponent of viscous sheet; Am = Ampferer number; h_0 = original thickness of the crust. (a) The figure shows how with a small amount of continental convergence the continental deformation zone width is controlled by the degree of crust-mantel coupling at the collision interface. With a highly coupled system intraplate deformation is dominated by indentation processes (England and McKenzie, 1982; Tapponnier and Molnar, 1976) while if the system is weakly coupled intraplate deformation is dominated by mantle subduction processes (Ellis, 1995). (b) shows how the deformation width changes with increasing convergence for mantle subduction and indenter.

± 1600 km from the collision front (Ziegler et al., 1995). As attested by seismological and geodetic studies on intraplate neotectonics (e.g. Allen et al., 2011; Molnar and Tapponnier, 1975; Nilforoushan et al., 2003; Vernant et al., 2004; Walpersdorf et al., 2014), strike-slip faulting is the primary process

by which such horizontal movements are accommodated and stresses are transferred further away from the collision front (Fig.1.1).

Strike-slip dominated continental deformation zones typically consists of interlinked systems of fault- and shear zone-bounded blocks that partition strains to form complex regions of displacement, internal distortion and rigid block rotations on various scales (e.g. Dewey et al., 1986; Foster and Gleadow, 1992; Marshak et al., 2000; Storti et al., 2003; Walker and Khatib, 2006). This is mostly due to the intrinsic structural inheritance of continental crust and lithosphere, acquired through the continuous incorporation of plate margin structures by continental collision and accretion processes, that operate for geologically long periods of time. Such structures, constitute major zones of mechanical anisotropy and vertical planar fabric, which, once incorporated into the plate interiors, influence the location, orientation and style of deformation during successive phases of reactivation at various spatial and temporal scale (Holdsworth et al., 2001a; Salvini et al., 1997; Sutton and Watson, 1986). These weak zones are preferentially reactivated by strike-slip faulting because, energetically speaking, it requires the least “effort”, but also because of their vertical geometry. In fact, intraplate strike-slip system often display polyphase reactivation histories, which may record tens to hundreds million years of deformation history (Pineiro and Holdsworth, 1997; Rossetti et al., 2002; Walker and Khatib, 2006). The longevity of intraplate strike-slip fault system and there intimate linkage to plate boundary dynamics makes them excellent “recorder” of the intraplate deformation response to continental collision. Furthermore they represent zones of economic interest and important areas of elevated geological hazard (Storti et al., 2003). In particular, they are capable of producing extremely destructive earthquakes (e.g. north Anatolia, Turkey, Sengor et al. (2005) and Tan et al. (2008); Dasht-e-Bayaz, Central Iran, Tchalenko and Ambraseys (1970); Walker et al. (2004); Berberian (2014) hundreds of kilometers away from the plate boundaries. Moreover, intraplate strike-slip faults often influence location, geometry, subsidence history and evolution of associated hydrocarbon rich sedimentary basins (for review Morley, 2002) and additionally may control magma emplacement and distribution and the associated hydrothermal circulations, producing economically valuable ore deposits and geothermal reservoirs (Araujo et al., 2005; Cox, 1999; Cox and Ruming, 2004; Wannamaker et al., 2009).

1.1 Hints from modelling

The recognized importance of intraplate strike-slip fault systems and their long-lasting developmental history has driven the creation of an enormous amount of studies in the last decades. Knowledge about fault nucleation and propagation mechanics, fault zone geometries and architectures and style of deformation has progressed enormously. Nevertheless, the understanding

on how intraplate strike-slip fault systems propagate and evolve in space and time at the fault system scale, principally come from analogue modeling studies. Although experimental studies have inherent simplifications, such as, a simplified mechanical stratigraphy, the neglect of thermal flexural and isostatic effects, they allow us to observe the 3-D geometry of the developing structure.

Dooley and Schreurs (2012) extensively and exhaustively reviewed the huge literature on analogue modelling of intraplate strike-slip tectonics. Such review study shows that the models can be divided into two main categories: (i) Riedel experiment (Fig. 1.3), with structures forming in an overburden above a single planar and vertical basement fault reactivated in pure strike slip (Atmaoui et al., 2006; Burbidge and Braun, 1998; Cloos, 1928; Lazarte and Bray, 1996; Le Guerroué and Cobbold, 2006; Richard and Cobbold, 1990; Richard and Krantz, 1991; Richard et al., 1991; Richard et al., 1995; Riedel, 1929; Tchalenko, 1970); and (ii) Distributed strike-slip shear experiments (Fig. 1.4), with structure forming above a broad shearing plane (Davis et al., 2000; Gapais et al., 1991; Schreurs, 2003; Schreurs and Colletta, 1998; Schreurs and Colletta, 2002).

Variations in the modeling material (sand, dry/wet clay), mechanical stratigraphy of the model and model thickness produce marked differences. Nonetheless, some important distinctions for the two different groups of experiments are recognized and outlined by Dooley and Schreurs (2012).

Riedel experiments performed with granular materials such as sand show a lower variability in structural style than clay models. In clay experiments, faults, tension fractures, pull-apart structures, and folds have all been described in the published literature, although not all of these structures necessarily formed in one and the same model (Fig. 1.3a; Dooley and Schreurs, 2012). In sand experiments, only faults develop, except for the region in between closely overlapping *en-echelon* Riedel shears (R), where local uplift is accommodated by antiformal structures trending parallel to the strike of the shears (Fig. 1.3b and c; Dooley and Schreurs, 2012).

Generally, the first structures to appear at the surface are, partly overlapping, *en-echelon* R synthetic shears, striking at an angle of about $\phi/2$ ($\sim 15^\circ$ to 20°) clockwise to the trace of the basement fault (Fig. 1.3a and b). Such shear tend to extend lengthward, creating a slightly sigmoidal surface trace above the basement fault trace. In 3D, R-shears show a helicoidal shape that connects the sigmoidal surface fault trace with the basement fault at depth (Fig. 1.3c). With increasing displacement, short-lived splay faults formed at or near the tips of the R shears. Subsequently, synthetic P-shears develop at a low counterclockwise angle from the trace of the basement fault. Linkage of portions of all these shears result in the formation of a through-going, anastomosing fault zone called Principal Displacement Zone, PDZ, whose overall strike was parallel to the basement

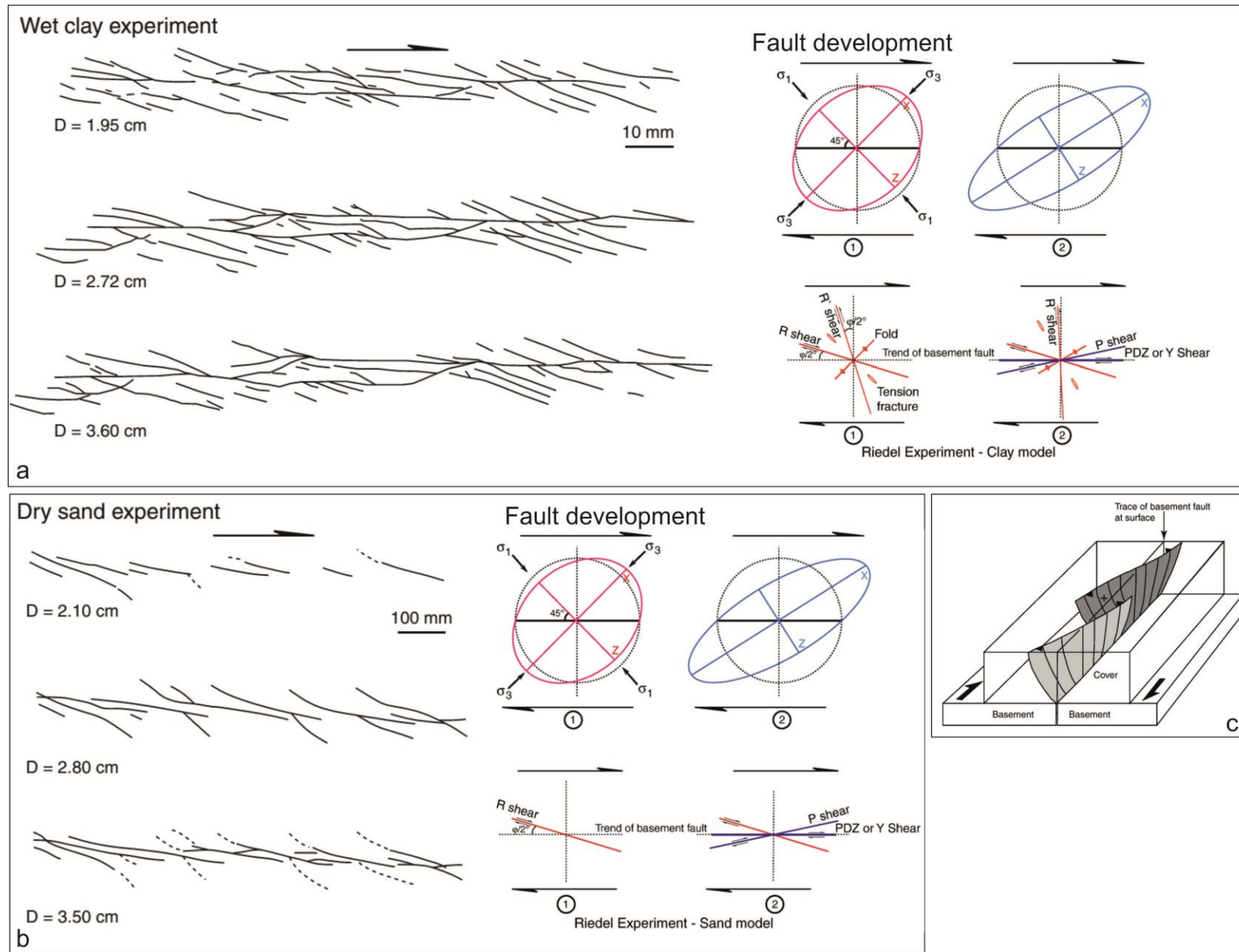


Figure 1.3: Typical fracture and fault parent development in wet clay (experiment from Tchalenko, 1970) (a) and dry sand (experiment from Taylor et al., 1986). (b) Riedel shear experiment for increasing displacement (D) values and associated structure developments for two stages of progressive dextral shear deformation. (c) 3D, geometry of a R-shears fault showing an helicoidal shape which connects to the sigmoidal surface

fault (Fig. 1.3b). In clay experiments after the later deformation stages, antithetic R'-shear develop at high angle ($90-\phi/2$, $\sim 75^\circ$) clockwise from and segmenting the PDZ.

In models undergoing distributed strike-slip shear, shearing is initially accommodated by a network of distributed en-echelon R-shear fault sets (Fig. 1.4a). Push-up zones form in the interaction areas between adjacent stepping R-shears. Adjacent R-shears merge by sideways propagation or link by short synthetic shears that strike sub-parallel to the bulk shear direction. Coalescence of en-echelon R-shears results in major, through-going master faults (Fig. 1.4a and b). Several parallel master faults develop due to the distributed nature of deformation. These major, through-going fault zones produce secondary faults, such as lower-angle synthetic and antithetic shears, which reflect local (kinematic) stress-field modifications (Fig. 1.4).

The same experiments were also performed applying a degree of shortening or extension perpendicular to the bulk shear direction to simulate transpressional and transtensional strike-slip regimes. Although the pattern of faulting changed depending on the degree of obliquity and the experimental setup some generalization can be made (Dooley and Schreurs, 2012).

Generally in experiment with transtension (e.g. Naylor et al., 1986; Richard and Cobbold, 1990) deformation zones are narrow and simple, with steeply dipping (dip $> 70^\circ$) synthetic shears striking at a lower angle to the basement fault than in the simple-shear experiments. In transpression experiments, the strike-slip deformation zones are instead wider and more complex, with the synthetic shears striking at higher angles with respect to the basement fault. In distributed strike-slip experiments with transtension (Schreurs and Colletta, 1998), initial faults form with a lower angle to the imposed shear direction accommodate horizontal displacements together with parallel dominated by extensional throws. In distributed transpression experiments (Schreurs and Colletta, 1998; Schreurs and Colletta, 2002) with low angles of obliquity ($\leq 15^\circ$) generate initial strike-slip faults, whose surface strike is at higher angles than those of R shears in distributed strike-slip shear experiments.

Furthermore, a vast amount analogue and numerical modelling studies have been produced on single structural elements and geometric configurations of strike-slip systems. Those include releasing bend (e.g. Atmaoui et al., 2006; Dooley and McClay, 1997; Dooley et al., 1999; Hempton and Neher, 1986; Petrunin and Sobolev, 2008; Wu et al., 2009), stopover geometries (e.g. Dooley et al., 1999; McClay and Bonora, 2001; Mitra and Paul, 2011; Richard et al., 1995) and termination structures (e.g. d'Alessio and Martel, 2004).

Le Guerroué and Cobbold (2006) investigated the effect of erosion and sedimentation along a developing single strike-slip fault. They designed a set of Riedel experiment in dry sand with structures forming in an overburden above a single planar and vertical basement fault. In some

Distributed strike-slip shear experiments

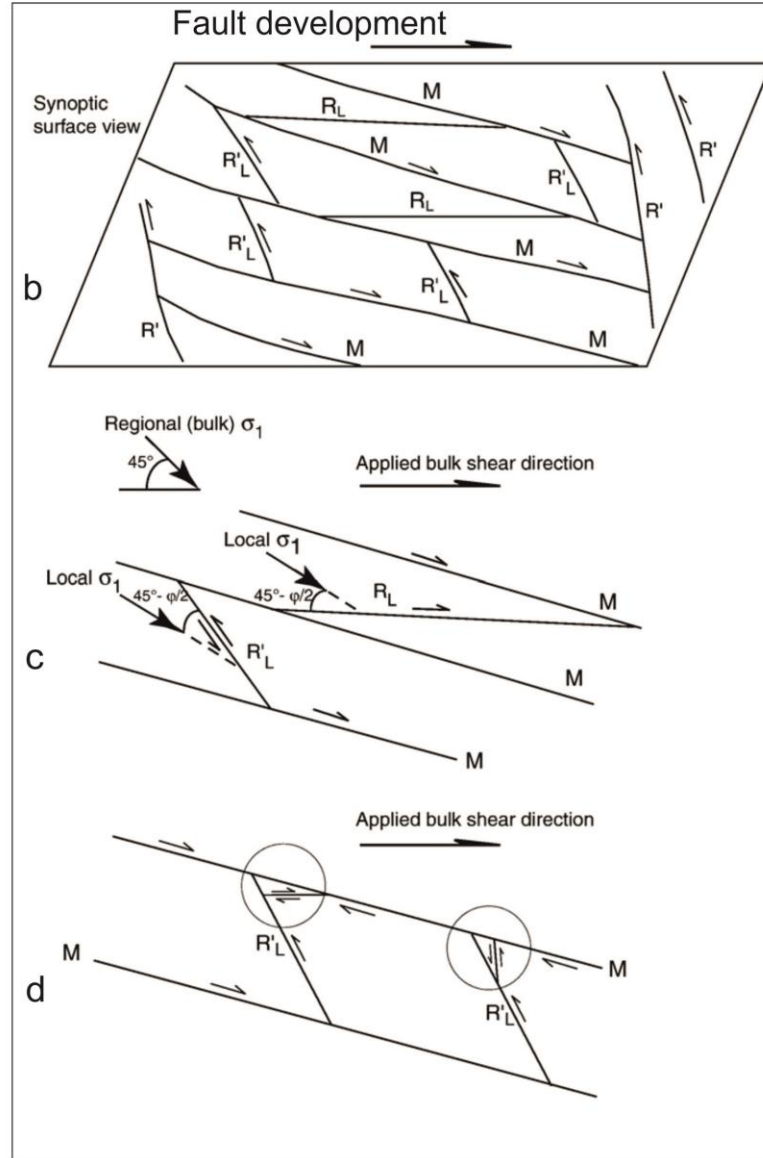
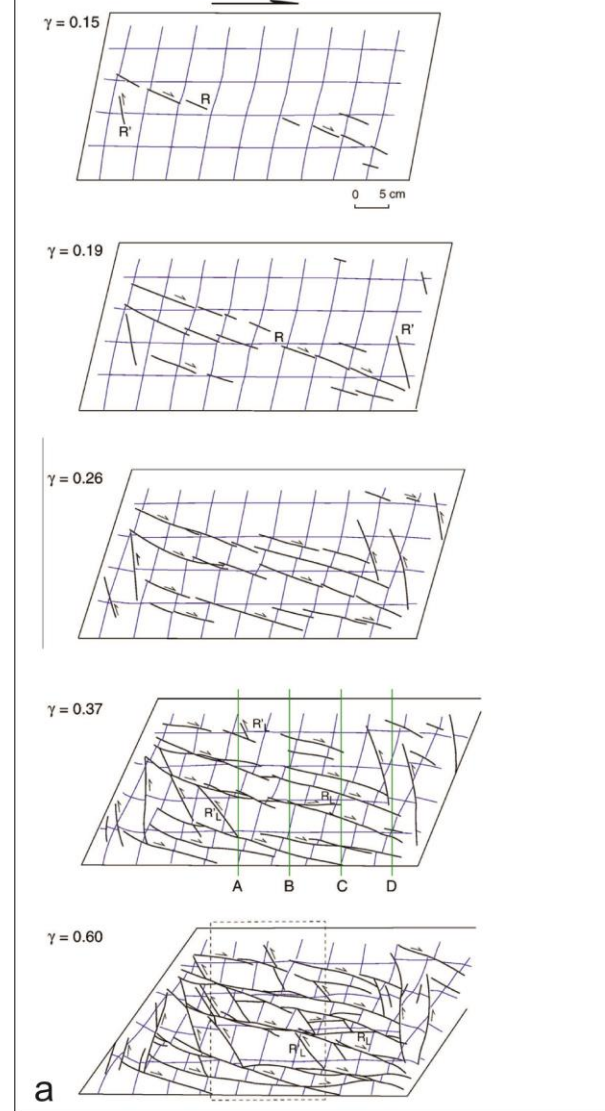


Figure 1.4: Typical fracture and fault pattern development in dry sand distributed strike-slip shear experiment, for increasing displacement values (γ). (b) Conceptual mechanical and temporal development of fault and fracture population with increasing shear displacement (R , R' than M ; than R_L and R'_L). Figures after Schreurs (2003).

experiments, uplifted areas where subjected erosion. In other experiments, all surface areas were subject to sedimentation. Successively the two processes were combined. From their study, it emerges that positive flower geometries, which normally form along restraining bends (Mann, 2007) or in overall transpressive regimes (Woodcock and Rickards, 2003), commonly form after substantial pure-strike displacement along the entire fault system, developing substantial linear relief. In experiments with erosion and sedimentation, some faults propagated through their syn-kinematic cover, others became buried and inactive, whilst yet others were exposed by erosion. This caused the average fault dip to progressively increase and the fault zone to narrow, focusing and localizing the uplift along the central portion of the fault (Le Guerroué and Cobbold, 2006).

Another important aspect of strike-slip faulting, extensively studied by modelers, is fault propagation in brittle rocks. Two main fault propagation processes have been identified: (1) propagation by shear fracture within the host rock where faults grow by the development of a 'process zone' where microfractures forming near the fault tip eventually coalesce into a through-going fault (Cowie and Scholz, 1992; Scholz et al., 1993; Tuckwell et al., 1999; Vermilye and Scholz, 1998) and (2) linkage of fault segments that originate as planes of preexisting weaknesses (Martel and Pollard, 1989; Segall and Pollard, 1983). The two processes produce distinct pattern of fracture damage. In the first instance the stress concentration at the fault tip, which allows the length ward propagation of the fault migrates with the fault tip, progressively creating fracture damage along the entire fault. Conversely, when fault propagate by linking to neighboring structures the stress concentration operates only at the tip of the linking structure, resulting in a fracture damage to be principally distributed along the linking segments. Preexisting facture damage however can inhibit fault propagation by a process known by "crack-tip shielding" (d'Alessio and Martel, 2004). In this instance a pervasive fracture network at the tip of the fault can diffuse and therefore reduce the stress concentration at the fault tip effectively stopping further lengthward propagation. Depending on the kinematic and stress field of the fault in question and on the orientation of the fracture network the fault may splay out at an angle to the main fault and create transpressive or transtensive terminations.

1.2 Hints from natural strike-slip fault systems

Riedel experiments are thought to represent good analogues for fault systems that form above a reactivated basement fault, while distributed strike-slip shear are thought to better represent deformation in intraplate setting where deformation is distributed over broad areas (Dooley and Schreurs, 2012). It is clear from all analogue-modelling studies that the development of strike-slip fault systems are dominated by Riedel shear structures. This makes the modelling studies particularly useful and relevant when looking at natural examples of strike-slip fault. In fact Riedel shear structures have been reported in nature at the macro-scale in coseismal surface rupture (e.g.

Tchalenko and Ambraseys, 1970), within the basement faults (e.g. Moore, 1979), in intraplate settings (e.g. Cunningham, 1993) and also at the meso- and micro-scale (e.g. Ahlgren, 2001; Antonellini and Aydin, 1995; Arboleya and Engelder, 1995; Jamison and Stearns, 1982).

The results from these analogue modelling studies have been therefore instrumental in identifying the structural geometry and the theoretical temporal progression of fault population generation during the nucleation and propagation of strike-slip faults system. This partially explains the wide collection of faults orientations observed along regional strike-slip systems (e.g. Rossetti et al., 2002; Storti et al., 2006). However, in natural examples of strike-slip systems, the fault development is complicated by a combination of: (i) regional or far field stress, (ii) transient kinematically induced stress field, (iii) local rotation of regional stress in the fracture damage zones and (iv) coexisting transpressional and transtensional fault segments, results in very complex fault patterns at different spatial and temporal scales (Davis, 1984; Faulkner et al., 2006; Mandl, 2000; Storti et al., 2006; Sylvester, 1988; Tchalenko and Berberian, 1975; Woodcock and Schubert, 1994; Woodcock and Fischer, 1986). This is particularly important in intraplate settings where dynamically and kinematically induced stress fields interact with mechanical anisotropies of the continental lithosphere and ultimately control the distribution of deformation. Overall, this commonly produces intraplate strike slip-system with complex patterns of fault population reflecting spatial and temporal variations in structural style along a fault zone (Fig. 1.5). Those include:

- (1) **Termination structures** forming at the tip of intraplate strike-slip systems which include: (i) normal faults, forming a wing cracks type geometry (e.g. the La Tet strike-slip fault, Cerdanya Basin, eastern Pyrenees Cabrera et al. (1988)), (ii) Horsetail splay faults also referred to as trailing imbricate fan (Woodcock and Fischer, 1986), which may be extensional (e.g. Ales's Basin at the tip of the Villefort's Fault, France Granier (1985)) or contractional (e.g. Lucanian Apennines, Southern Italy, Catalano et al. (1993)), (iii) synthetic branch fault (e.g. along a segment of the North Anatolian Fault, Turkey Barka and Kadinsky-Cade (1988)), (iv) synthetic fault sets in front of the fault tip (e.g. Malta Fault in the Rio do Peixe Basin, Brazil (Françolin et al., 1994)). Furthermore regional strike-slip systems may terminate into rift systems (e.g. Priestley Fault which terminates into the Terror rift, north Victoria Land, Antarctica, Storti et al. (2001)) and orogenic systems (e.g. western Mongolia, Bayasgalan et al. (1999) and Altyn Tagh fault system of central Asia, Cobbold and Davy (1988)).
- (2) **Releasing bends and stepover** forming within fault system, constitute a rhomboidal generally transtensive segment of the fault system. They typically create depression that, become depocenter called pull-apart basins which sedimentary history and facies distribution is intimately linked to the tectonic evolution of the bounding fault system (for general review

Aydin and Nur, 1982; Blair and Bilodeau, 1988; Cunningham and Mann, 2007; Ioganson, 2005; Mann, 2007).

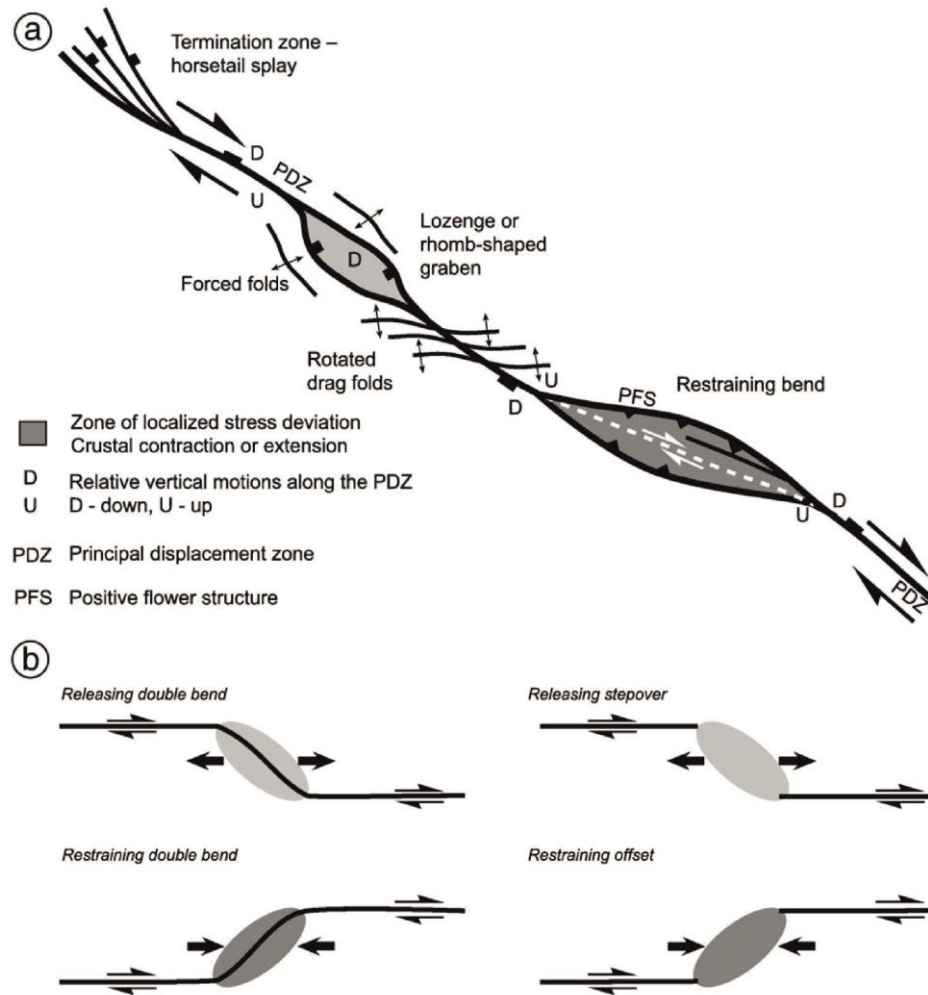


Figure 1.5. (a) It shows the possible range of coexisting structural styles along a strike-slip system. (b) Releasing and restraining bends and step over structural geometries. Figure after Dooley and Schreurs (2012), original diagram from Christie-Blick (1985).

- (3) **Restraining bends and stepover** forming within fault system they constitute a generally rhomboidal transpressive segment of the fault system. Typically they are associated with prominent topography, they form anticlinal uplifts, commonly with doubly plunging arrangements of folds, and are of limited strike (for general review Christie-Blick, 1985; Cunningham and Mann, 2007; Mann, 2007; Zolnai, 1991).

1.3 Topographic growth and exhumation

Strike-slip fault system have always been known for their capacity to produce prominent topography (Storti et al., 2003; Sylvester, 1988; Woodcock and Schubert, 1994). Outcrops of middle to deep crustal material are commonly found in association with strike-slip fault systems (Fitzgerald et al., 1995; Redfield and Fitzgerald, 1993) and studies of metamorphic rocks within strike-slip fault systems document that at least part of their exhumation pathways is synchronous with strike-slip

movement (Foster et al., 2007; Gordon et al., 2010; Roeske et al., 2007). Additionally, strike-slip fault systems are often associated with regions of focused rapid exhumation > 0.5 mm/y (e.g. the Alpine Fault in New Zealand, Little et al. (2005); the Denali fault in Alaska, Benowitz et al. (2011); Fitzgerald et al. (1995); Redfield and Fitzgerald (1993); and the San Andrea fault in California Niemi et al. (2013); Spotila et al. (2007b)).

The cause of focused exhumation along these faults is often complex, with near-field (< 20 km) boundary conditions and far-field plate tectonic driving mechanisms contributing to the observed exhumation patterns (Buscher and Spotila, 2007). Nevertheless, several process and conditions have been invoked to explain topographic growth and focused exhumation along strike-slip systems and may play an important role in observed regional exhumation and topographic patterns: (1) the degree of obliquity of the plate motion vector with respect to the fault trace (e.g. Cunningham, 2013; Fossen and Tikoff, 1993; Robin and Cruden, 1994; Sanderson and Marchini, 1984), (2) structural irregularities such as stepovers (Aydin, 1985; Carne and Little, 2012; Finzi et al., 2009; Hilley and Arrowsmith, 2008), (3) variations in master fault dip (Dair and Cooke, 2009), (4) enhanced erosion due to the highly fractured rocks (Cox et al., 2012; Molnar et al., 2007), (5) pervasive tectonically induced fracturation and associated volume increase (between 5 to 10% volume increase; Braun, 1994; Le Guerroué and Cobbold, 2006; Schopfer and Steyrer, 2001; Schrank and Cruden, 2010) and (6) changes in plate motion (Fitzgerald et al., 1995; Fitzgerald et al., 1993). This results in very complex spatial and temporal patterns of exhumations and exhumation rates. Normally the exhumed terrains show greater exhumation patterns closer to the main faults which rapidly decrease away from it (in kilometers to tens of kilometers from the fault), with typical exhumation rate values ranging from 0.4 mm/yr (Buscher and Spotila, 2007) to 7 mm/y (Spotila et al., 2001). Unexpectedly, the amount of exhumation along a strike-slip fault is not always a simple correlation with the degree of transpression nor the composition of the juxtaposed rocks (Roeske et al., 2007; Spotila et al., 2007a; Spotila et al., 2007b). In addition it is important to emphasize that topography itself, located in correspondence or alongside fault systems, can affect fault orientation (Fialko et al., 2005), fault-slip direction (Cowgill et al., 2004) and fault strength (Koons et al., 2002).

1.4 Investigating continental deformation

Crustal deformation in tectonically active regions produces topographic perturbations on the Earth's surface at multiple spatial scale, through isostatic/dynamic-, fold- or fault-related uplift/subsidence. Geomorphic processes tend to counterbalance the growth of topographic perturbations, over time scales that depend on the wavelength of the morpho-structures as well as on climate changing over space and time (Burbank et al., 1996; Burbank, 1992; Mitchell and Montgomery, 2006; Montgomery et al., 2001; Whipple, 2001; Whipple and Tucker, 1999). Roe et al.

(2006) defined climate, erosion and tectonics as a “triumvirate” that control rock and surface uplift in mountainous terrains. Furthermore, the scientific literature on this topic outlined clearly that they also interact through mutual feedback relationships (England and Molnar, 1990; Morisawa and Hack, 1985; Wegmann and Pazzaglia, 2009; Whipple and Tucker, 1999; Willett et al., 2006).

Over decadal time scales the rate of crustal deformation can be directly monitored through geodetic techniques, both satellite-based such as D-InSAR (e.g. Massonnet et al., 1993) and GPS (e.g. Serpelloni et al., 2013) and ground-based such as TLS (e.g. Wilkinson et al., 2010). The record of longer-timescale deformation is instead encoded in geological and/or geomorphic signatures that, however, encompass the time/space superimposition of climatic and tectonic inputs (Bull, 2007; Merritts and Ellis, 1994). Geological signature can be decoded through fission-track and (U-Th)/He dating of zircon and apatite (Farley, 2000; Reiners and Brandon, 2006) along with $^{40}\text{Ar}/^{39}\text{Ar}$ dating of micas and feldspars (Harrison and Zeitler, 2005). These thermochronological methods let rock cooling histories now be resolved from 350 °C to 70 °C, thus tracking the relatively long-term (Myr time scale) exhumation processes from mid-crustal depth to few kilometers below the Earth’s surface.

The geomorphic signature of crustal deformation can be best decrypted over the kyr time scale, at which erosion/deposition rates, drainage network geometry, longitudinal river elevation profiles, and topography all reflect the interaction between surface uplift rate and the dynamics of Earth surface processes. Drainage network provides the most rapid response to topographic perturbations (Castelltort et al., 2012; Royden and Taylor Perron, 2013; Whipple, 2004; Willett et al., 2014) and their deposits record information about climate (Bull, 1977; Frostick and Reid, 1989; Harvey, 2004; Ritter et al., 1995). Feedback in river dynamics occur since changes in base level can be driven not only by tectonics (rock uplift) and climate (eustasy) but also by drainage re-organization (e.g. Castelltort et al., 2012; Harvey, 2004). Moreover, fault-offset rivers have been widely used to quantify localized deformation (e.g. Walker and Jackson, 2002).

Due to the increasing availability of remotely sensed data, considerable focus is set on the processing of high-resolution DEMs to extract topographic and morphometric information about landforms (Tarboton et al., 1991; Whittaker et al., 2008). For the estimation of morpho-evolution rates in response to tectonic and climate geomorphic markers are widely used (Della Seta, 2003; Di Bucci and Mazzoli, 2003; Pérez-Peña et al., 2009; Rockwell et al., 1984; Schiattarella et al., 2006). They are represented by areal and/or linear landforms that display: i) a known initial, unreformed geometry; ii) a known age; iii) high preservation potential with respect to the time scale of the tectonic processes being studied (Burbank and Anderson, 2011). By examining the plano-altimetric configuration of geomorphic markers, qualitative and/or quantitative tools for isolating the topographic effects ascribable to active tectonics have been developed (Keller and Pinter, 1996;

Pedrerera et al., 2009; Troiani and Della Seta, 2008) also through the geostatistical analysis (Johansson et al., 1999; Troiani and Della Seta, 2011).

For a correct use of geomorphic markers, it is very important the contribution of both detailed geomorphological surveys and advanced geochronological methods (i.e. cosmogenic and OSL dating) able to provide even more significant constraints for the analysis of the morpho-evolution rates and their variability over different paleoclimatic frames. In addition to methods based on the estimation of erosion/deformation rates from geomorphic markers (Gioia et al., 2014; Pérez-Peña et al., 2009), the geomorphic response to tectonic perturbations can be quantified through river incision rates (Brocard et al., 2003; Burbank et al., 1996; Finnegan et al., 2014; Lavé and Avouac, 2001; Pederson et al., 2006; Stock and Montgomery, 1999; Whipple and Tucker, 1999; Whittaker et al., 2007), or through near-surface erosion rates obtained by cosmogenic nuclides techniques (Brown et al., 1995; Cyr et al., 2010).

1.5 Open Questions

Analogue and numerical modelling studies have contributed to the understanding, how strike-slip fault systems propagate and evolve structurally and mechanically. Numerous studies however, have shown that several processes, chiefly topographic growth, erosion/exhumation and syn-tectonic sedimentation operate during the propagation and evolution of strike-slip systems. It may be expected therefore that such processes interact and influence each other with several feedback mechanisms, which may ultimately modulate and or respond and therefore register the structural development of a fault system.

It is therefore clear that strike-slip fault systems are complex structures, geometrically linked and kinematically influenced by the plate margins dynamics but locally influenced by numerous near-field effects which remain to be fully understood. This is particularly relevant in intraplate settings where near and far field effects together control the location, orientation and kinematics of fault systems. Even though to a first approximation, intraplate deformation is necessarily driven by plate margins dynamics, the spatio-temporal distribution of deformation in the intraplate domains is the result of dynamically and kinematically induced stress fields interacting with preexisting mechanical anisotropies.

From the above description it emerges that several key issues are still unclear:

How the spatio-temporal propagation and long-term evolution of natural intraplate strike-slip systems influence topographic growth, erosion/exhumation and syn-tectonic sedimentation (source-to-sink history) and vice versa, how those processes influence the propagation of intraplate strike-slip faults?

How such evolution reflects the intraplate response to the far field plate boundaries evolution: how temporally and spatially connected are intraplate and plate boundaries (punctuated vs. continuous response)?

In order address such questions, detailed studies constraining the kinematic, structural architecture, stratigraphic evolution, fault related exhumation/subsidence processes associated with faulting and the overall history of fault nucleation and propagation in the intraplate domains are therefore needed.

2 AIMS OF THE RESEARCH AND RATIONALE

The main goal of this research is to contribute, through a field- and laboratory-based study, to the understanding of how intraplate strike-slip faulting propagates and evolves in space and time (long-term evolution).

The study focuses on a major, previously unstudied, strike-slip fault system cutting through the intraplate domain of north Central Iran, the Kuh-e-Faghan Fault (Fig. 2.1). Central Iran is an ideal study area, due to (i) its active and relatively young history of continental collision

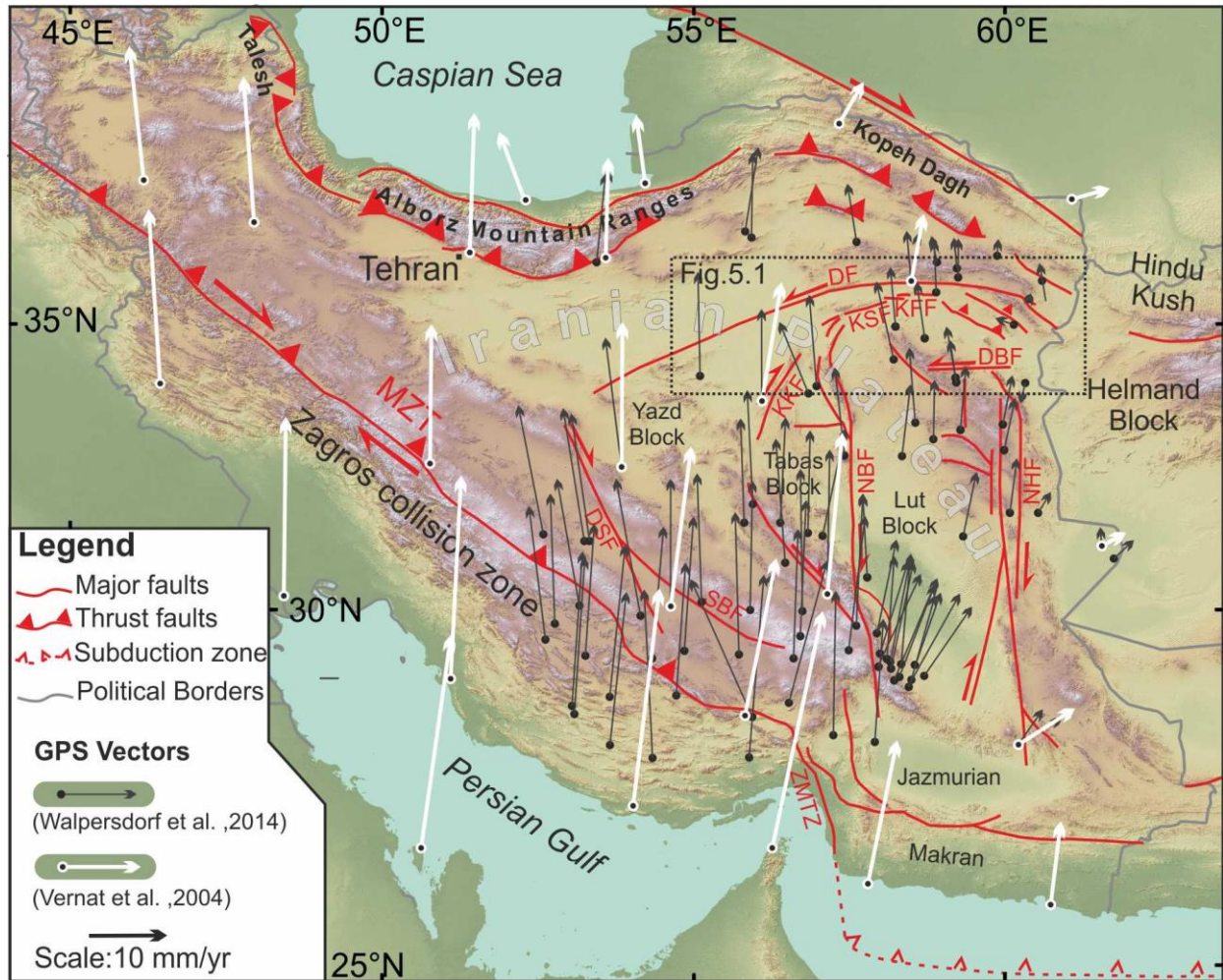


Figure 2.1 Simplified tectonic map of Iran, showing the main collisional and intraplate strike-slip fault domains accommodating the Arabia-Eurasia convergence (modified after Berberian and King, 1981). The dashed rectangle indicates the study area. DSF: Dehshir fault; KKF Kalmard-Kuhbanan Fault, KSF: Kuh-e-Sarhangi Fault; KFF Kuh-e-Faghan Fault MZT: Main Zagros Thrust; NBF: Nayband Fault; NHF: Nehbandan fault; SBF: Shahr-e-Babak Fault; ZMTZ: Zagros-Makran Transfer Zone. . GPS velocities vectors in Iran relative to stable Eurasia are shown with different colors according to Vernat et al. (2004) and Walpersdorf et al. (2014);

accommodated in its intraplate domain by array of distributed strike-slip fault systems, and (ii) its arid climatic conditions, which guarantee good outcrop preservation and rock exposures. The tens to hundreds of kilometer long seismically active fault systems of intraplate Central Iran are associated

with linear mountainous ridges along which basement rocks and mid to deep crustal blocks are often exposed attesting for the capacity to exhume. Furthermore, Central Iran has a relatively well-preserved Neogene-Quaternary continental sedimentary record. Such continental sedimentary successions have been strongly influenced by structural development of the region, related to the Arabia-Eurasia collision. In particular the structurally controlled architecture and syn-depositional deformation structures of Neogene sedimentary record can be used to reconstruct its source-to-sink evolution in order to investigate the relative timing and development of intraplate deformation. Moreover, the Quaternary deposits distributions and their geomorphological characters can be used to constrain the tectonic evolution in recent geological times. The study describes the Neogene-Quaternary structural architecture, kinematics and exhumation history of the KFF system, together with its associated Neogene and Quaternary continental deposits.

Using a multidisciplinary approach that integrates, structural, stratigraphic and geomorphological field investigation, with thermochronological and geochronological analysis the study aims to investigate how the KFF systems propagate and evolve in space and time. Successively the study aims to assess how KFF system evolution relates/responded to the deformation history documented along the Iran collisional plate boundary.

Based on the new evidence this study presents a morpho-structural evolutionary model of the KFF. Such model explains 1) the structural growth evolution and spatio-temporal propagation of the KFF system, 2) the stratigraphic succession, sediment distribution and thicknesses variations of the Neogene continental deposits 3) the geomorphic signal of active tectonics in a very preservative (arid) landscape. Finally, the new findings are contextualized into their regional tectonic framework, proposing an innovative spatio-temporal evolutionary tectonic model, which explains the complex evolution and distribution of deformation in Central Iran since ~20 Ma.

These new results have important implications on understanding how natural intraplate strike-slip fault systems propagate and evolve in space and time. Furthermore it presents, for the first time, much needed direct age constraints on the deformation history of Central Iran and brings new important considerations on the Neogene-Quaternary kinematic and tectonic evolution of Central Iran and on collisional intraplate domains in general.

3 GEOLOGICAL BACKGROUND

3.1 Regional tectonic setting

The Arabia-Eurasia collision zone is one of the largest and most spectacular examples of continental convergent deformation on Earth (Hatzfeld and Molnar, 2010). Convergence may have initiated in the mid-Jurassic (Agard et al., 2005; Agard et al., 2011) and culminated with the Arabia–Eurasia continental collision through a polyphase tectonic history: (i) onset of collision, estimated to have started at the Eocene–Oligocene boundary (e.g. Allen and Armstrong, 2008; Boulton and Robertson, 2007; Ershov et al., 2003; Hafkenscheid et al., 2006; Hessami et al., 2001; Homke et al., 2009; Homke et al., 2010; Jolivet and Faccenna, 2000; McQuarrie et al., 2003; Morley et al., 2009; Mouthereau et al., 2012; Robertson et al., 2006; Vincent et al., 2005; Vincent et al., 2007); (ii) a regional increase in collision-related uplift, exhumation, and subsidence in adjacent basins, beginning in the early Miocene, as documented by thermochronological (Axen et al., 2001; Ballato et al., 2013; Gavillot et al., 2010; Guest et al., 2006; Madanipour et al., 2013; Okay et al., 2010; Verdel et al., 2007), stratigraphic (e.g. Ballato et al., 2008; Ballato et al., 2011; Guest et al., 2006; Hessami et al., 2001; Khadivi et al., 2009; Morley et al., 2009; Mouthereau et al., 2007) and structural (e.g. Allen et al., 2004; Mouthereau et al., 2007) evidence; and (iii) a widespread tectonic reorganization during late Miocene–early Pliocene, as attested by enhanced exhumation in the Alborz and Talesh mountains (Axen et al., 2001; Madanipour et al., 2013; Rezaeian et al., 2012), fault kinematic changes in the Kopeh Dagh (Shabanian et al., 2010; Shabanian et al., 2009a; Shabanian et al., 2009b) and in the Zagros–Makran transfer zone (Regard et al., 2004; Regard et al., 2005a), which is thought to have resulted in the current regional kinematic configuration (Allen et al., 2004).

The lag-time (15–20 Ma) between phase (i) and phase (ii), has been interpreted by Ballato et al. (2011) as two-phase collisional process. During the initial, “soft” stage of continental collision, plate convergence was absorbed along the subduction zone, while a minor fraction was accommodated by the upper-plate by contractional deformation. During the second stage is inferred that, the decrease in convergence rate by 20 Ma was associated with the “hard” collision of unstretched Arabian lithosphere, which ultimately caused widespread upper-plate deformation (Ballato et al., 2011, p. 128). The evidences gathered in those studies principally come from the orogenic belts situated at the edges of the Iranian plateau (Fig. 2.1); Zagros Alborz, Kopeh Dagh and Talesh). By contrast, little is known about the deformation history of the intraplate domain of Central Iran.

3.2 Central Iran

The Central Iran Micro Continent (CIMC) consists of an amalgamation of continental blocks bordered by topographically prominent mountain ranges, comprising the Kopeh Dagh, Alborz and Talesh orogenic belts to the north, and the Zagros orogenic belt and Makran active subduction related complex to the north-west and south (Fig 2.1). In particular, the CIMC includes the Lut, Tabas, and Yazd microblocks (Aghanabati, 2004), which are bounded by linear mountain-belts developed along major strike-slip fault zones that have peculiar stratigraphy, deformation style and pattern of recent seismicity (Berberian, 2014; Berberian and King, 1981).

The GPS displacement vectors indicate a NNE motion of the Arabian plate relative to Eurasia of $\sim 25 \text{ mm yr}^{-1}$ at the longitude of eastern Iran (McClusky et al., 2003; Reilinger et al., 2006; e.g. Sella et al., 2002; Vernant et al., 2004; Walpersdorf et al., 2014). Such convergence is mostly absorbed in the orogenic terrains through contractional deformation (Zagros, Alborz, Kopeh Dagh and Talesh in the north) (Fig 2.1). The CIMC is moving northward at 6–13 mm/yr with respect to the stable Afghan crust at the eastern edge of the collision zone (Walpersdorf et al., 2014). Such differential motion is accommodated by distributed N-S oriented right-lateral strike-slip faults and E-W oriented left-lateral and right-lateral strike-slip faults. GPS studies determined their current slip rates (Fig. 2.1, from east to west, data Walpersdorf et al. (2014)): the Nehbandan fault (NHF) $5.6 \pm 0.6 \text{ mm yr}^{-1}$, Nayband Fault (NBF) $4.4 \pm 0.4 \text{ mm yr}^{-1}$, Kalmard-Kuhbanan Fault (KKF) $3.6 \pm 1.3 \text{ mm yr}^{-1}$, Dehshir fault (DS) $1.4 \pm 0.9 \text{ mm yr}^{-1}$ and Doruneh faults (DF), $1.3 \pm 0.8 \text{ mm yr}^{-1}$ (Walpersdorf et al., 2014).

A large number of studies have detailed kinematics and total cumulative shear along the active strike-slip faults systems of Central Iran, organized into N-S dextral (from west to east: the Deshir, Anar, Nayband–Gowk, and Nehbandan faults) and E–W sinistral (from north to south: Doruneh and Dasht-e Bayaz faults) shears (Fig. 2.1). Several studies estimated the total cumulative shear along the active strike-slip faults systems of Central Iran, using geologic and geomorphic displaced markers from satellite imagery (Allen et al., 2004; Allen et al., 2011; Farbod et al., 2011; Walker and Jackson, 2004). Taking into account the present-day slip rates ($\sim 2\text{--}10 \text{ mm/yr}$) along the major fault systems, the onset of strike-slip tectonics is inferred to date back to $\sim 5 \text{ Ma}$ (Allen et al., 2004). This shear pattern is inferred to be accompanied by diffuse rigid block rotation and strain partitioning during ongoing Arabia-Eurasia convergence (Allen et al., 2011; Farbod et al., 2011; Fattahi et al., 2007; Jackson and McKenzie, 1984; Walker and Jackson, 2004; Walker et al., 2004; Walker and Khatib, 2006). The analogue modelling results presented in Bonini et al. (2003) show that the deformation pattern within the Iranian Plateau is compatible with partitioning of the N-directed Arabia indentation into a composite system of: (i) collision-oblique seismogenic belts, with two main conjugate

transpressive belts (the dextral NW–SE-trending Zagros belt and the NE–SW-trending sinistral Alborz-Aran-Torud belt) and (ii) collision-parallel seismogenetic belts, in central Iran, with a modest lateral escape of the Yazd and Tabas Block towards the Lut block along the Nayband Fault (Fig. 2.1), without the need of rigid block rotation. Significant, post-Miocene counter clockwise rotation (25–35°) has only been documented in the Lut and Tabas block, whereas no significant rotation has been detected north of the Doruneh Fault (Mattei et al., 2012).

In a recent study, Nozaem et al. (2013) documented important post-Neogene to Quaternary right-lateral strike-slip tectonics along the Kuh-e-Sarhangi Fault on north western edge of the Lut block (Fig. 2.1), less than 40 km south of the sub-parallel, active left-lateral Doruneh Fault (Farbod et al., 2011; Fattahi et al., 2007; Tchalenko et al., 1973). This post-Neogene faulting is proposed to have occurred due to the tectonic reactivation of the north-eastward prosecution of the late Neoproterozoic to early Paleozoic Kashmar–Kerman Tectonic Zone (Fig. 2.1; Ramezani and Tucker, 2003; Rossetti et al., 2014) in response to a kinematically induced stress field scenario (Nozaem et al., 2013). Similarly, Javadi et al. (2013) documented a polyphase kinematic history for the Doruneh Fault, with a major change from right- to left-lateral during the late Miocene-early Pliocene times. Furthermore, Farbod et al. (2011) suggested that the complex kinematic configuration of Central Iran may be due to kinematically induced spatial variation in the stress field orientation.

3.3 The study area

The study focuses on a linear mountainous ridge (~80 km long and ~10 km wide; maximum elevation of ~1700 m), associated with the E-W oriented Kuh-e-Faghan Fault (KFF, Fig. 2.1, 4.1). This fault system truncates the northern termination of the Kuh-e-Sarhangi fault system (Nozaem et al., 2013) and is located 25 km south of the Doruneh Fault, extending eastward for ca. 80 km (Fig. 4.1). The KFF system and the surrounding areas are seismically active (Fig. 4.1), with maximum-recorded magnitude between 4 and 5.5 and the focal depths <35 km (Farbod et al., 2011).

The KFF consists of E-W oriented brittle deformation zone, which cuts through pre-Neogene units (Paleozoic-Mesozoic carbonate and subordinate shale and arenitic deposits) and the unconformably overlying Neogene and Quaternary continental sequences (Behroozi et al., 1987; Eftekhari-Nezhad et al., 1976; Ghomashi et al., 2001; Jalilian et al., 1992). Fault kinematics along the KFF is poorly described, with strike-slip (Behroozi et al., 1987; Eftekhari-Nezhad et al., 1976; Ghomashi et al., 2001; Jalilian et al., 1992) vs. reverse (Hassami et al., 2003; Javadi et al., 2013) kinematics proposed so far.

The basement units exhibit a steeply-dipping ENE-WSW oriented planar fabric, also reported from the neighbouring Kuh-e-Sarhanghi Fault system (Nozaem et al., 2013). Conversely to the Kuh-e-Sarhang Fault, where the post-Neogene deformation has exploited the regional fabric, reactivating

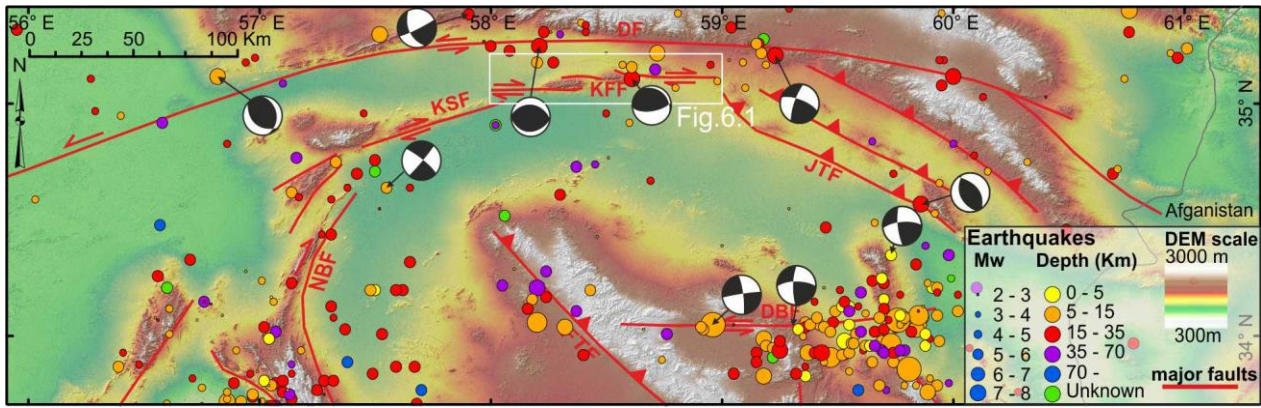


Figure 4.1 Simplified tectonic map of northern Central Iran, showing the historical and instrumental seismicity of the area. Focal mechanisms are taken from the Harvard catalog (<http://www.globalcmt.org/CMTsearch.html>). Epicentres are from the ISC EHB Bulletin (International Seismic Centre, Thatcham, United Kingdom, 2009, <http://www.isc.ac.uk>) and earthquake catalogue at Iranian Institute of Earthquake Engineering and Seismology; <http://www.iiess.ac.ir>. The white square indicates the location of the study area and the extent of the maps in figure 6.1.

the inherited structures (Nozaem et al., 2013), in the KFF the Neogene Quaternary deformation cuts across the ENE-WSW trending regional fabric and does not seem to exploit any pre-existing structure. Despite contrasting stratigraphic scenarios have been assigned to the Neogene successions, previous paleogeographic and sedimentological studies (Amini, 1997; Berberian and King, 1981) refer the Neogene deposits alongside the KFF to the Upper Red Formation of Central Iran. The Upper Red Formation is the first continental sequence above the marine, late Oligocene–middle Miocene Qom Formation (Ballato et al., 2008; Berberian, 1974; Daneshian and Dana, 2007; Hadavi et al., 2010) and consists of conglomerates, sandstones, siltstones, marls and evaporites (Amini, 1997; Ballato et al., 2008; Ballato et al., 2011; Morley et al., 2009). Due to the lack of biostratigraphical markers or radiometrically datable units, the age and duration of the Upper Red Formation are not well constrained. Based on the magnetostratigraphic study of the Eyvanekey section in southern Alborz Mountains, Ballato et al. (2008) proposed a Burdigalian to Tortonian (17.5–7.5 Ma) age.

Quaternary successions, made of alluvial fans and terraced alluvial plain deposits, unconformably overly the Neogene units. The stratigraphy of the alluvial deposits of the KFF region has not been studied yet. Walker and Fattahi (2011) reviewed the late Quaternary deposits of eastern Iran. The authors recognized that several generations of telescopic alluvial fans, as well as regional arrangement of river terraces and lake deposits could be explained by Late Pleistocene and Holocene environmental changes with aggradation phases occurring between ~30 and 13 ka and between ~9 and 7 ka, alternating with erosive phases, controlled by regional climatic forcing. As for the erosive phases, in-situ produced cosmogenic ^{10}Be provided surface abandonment ages for different Quaternary alluvial surfaces in the the Hormoz Strait area at 5.6 ± 0.6 , 8.4 ± 1.0 , 12.8 ± 1.0 , 20.1 ± 1.5 ,

and 44.0 ± 3.4 10Be ka (Regard et al., 2006). Similar generations of alluvial fans have been recognized in the neighbour regions and IRSL (infrared stimulated luminescence) age of ~ 10 ka (end of the Last Glacial Maximum) was obtained for the deposition of the Shesh–Taraz fan along the Doruneh fault (Fattahi et al., 2007).

4 METHODOLOGY

Through a multidisciplinary approach, the project integrates structural, geomorphological and stratigraphic field investigations with geochronological (OSL) and thermochronological (AFT, (U-Th)/He on Apatites and Hematite) analytical constrains.

4.1 Field work

Extensive fieldwork, data collection and sampling was carried out in order to reconstruct the overall Neogene to Quaternary structural and stratigraphic spatio-temporal evolution of the Kuh-e-Faghan Fault system (KFF). A new geological map detailing the KFF system and the distribution of the Neogene sedimentary cover has been produced integrating field mapping and aerial photointerpretation, together with the available published cartography, which has been reviewed and verified in the field. In particular, geological mapping was focused to characterize the Neogene stratigraphy, identifying the main sedimentary cycles and document their general geometry, stratigraphic relations and spatial distribution. Structural investigation was carried out in order to define the Neogene–Quaternary fault zone architecture and the style of brittle deformation along the KFF.

4.1.2 Structural survey

Structural data were collected in 59 sites, distributed along the three main fault strands (See appendix-B) in order to constrain the fault kinematics and architecture. A number of 501 faults occurring in the basement, the Neogene and Quaternary deposits were measured in the field. Fault kinematics was obtained based on classical criteria for brittle shear zones, such as fault offset, growth fibers, and Riedel shears e.g. (Doblas, 1998; Petit, 1987). Fault population analysis was performed through the software Daisy 3 (Salvini, 2004; <http://host.uniroma3.it/progetti/fralab>). Fault zones architecture were systematically described along the KFF in order to characterize potential along strike changes in the style of deformation.

4.1.3 Stratigraphic survey

Stratigraphic data were collected along 12 across-stake transects (approximately north south oriented) along the KFF in order to characterize the Neogene sedimentary deposits. Sedimentological characteristics were documented through a series of stick-logs that record sedimentary facies variations, paleo environmental indicators, unconformities, stratigraphic relationships and thicknesses variations through the Neogene sedimentary succession entire sedimentary.

4.1.4 Geomorphological survey

Geomorphological field-survey was carried out in order to characterize the Quaternary deposits and landform architecture. Different generations of Quaternary alluvial fans and fluvial

terraces were characterized and described. Morphostructural correlations of the described landforms and deposits was successively carried in order to reconstruct a relative generation history.

4.2 Digital Elevation Model and topographic analysis

A digital elevation model (DEM) of the study area was produced using data from topographic vector maps at 1:25000 scale in UTM coordinate system from the National Cartographic Center of Iran. Topographic contours, independent elevation points, and river networks data, were extracted from the topographic vector maps using a purposely-developed protocol which allowed to cross-check the three topographic datasets for errors. Successively the three datasets were interpolated using the Topo to Raster ArcGis10.1 tool to produce a DEM with 10x10m cell size.

The topographic analysis of relief is widely used to investigate the relationships among tectonics, climate and erosion (Burbank et al., 1996; Burbank, 1992; Mitchell and Montgomery, 2006; Montgomery et al., 2001; Whipple and Tucker, 1999). Ongoing refinement of techniques using digital elevation models (DEMs) allow the improvement of the analyses and the interpretation of the obtained results (Brocklehurst and Whipple, 2004; Grohmann, 2004; Hergarten et al., 2014; Troiani et al., 2014).

We performed a topographic analysis to produce:

- A river-network map (using the Hydrology Toolset of ArcGIS 10.1)
- A slope gradient map (using the Surface Toolset of ArcGIS 10.1)
- An aspect map (using the Surface Toolset of ArcGIS 10.1)
- A local relief map (Scotti et al., 2013; and references therein).
- 5 SWATH profiles (4 across and 1 along strike of the KFF, figure 5.3; Hergarten et al., 2014; Mitchell and Montgomery, 2006; Telbisz et al., 2013);
- A filtered topography analysis (e.g. Fig.5.2). This analysis is traditionally used to discern between crustal tectonics and mantle dynamics topographic signals (D'Agostino and McKenzie, 1999; Molin et al., 2012; Molin et al., 2004; Wegmann et al., 2007), with adopted wavelengths ranging from 50 to 300 km. We used it to assess the spatial distribution of different wavelengths topographic signals of the KFF system depending on different styles of crustal deformation. The analysis was performed with filters size ranging from 0 to 20 km in radius.
- A morphometric analysis of the slope angle of the northern Quaternary alluvial fans (see chapter 10). The analysis was performed to detect the geomorphic signal of fault-related uplift given by progressive tilting of alluvial fan surfaces (Bull, 1977; Giano, 2011). The procedure consisted in extracting the elevation data points of the top surfaces of single alluvial fans using a purposefully developed routine which allowed to exclude the areas of the fan which had been incised by erosion. The tool functioned following this steps:

- clip the DEM to the extent of a previously mapped single fan
- from the clipped DEM a curvature map of the fan was created
- from the curvature map the areas with positive and low curvature values were extracted (this areas represent the top surface of the fan)
- the area was than transformed into a point cloud containing the elevation data

This elevation data where than plotted along north-south transects (since the fans drain northward) and linear regressions were plotted along specified data intervals to capture the downstream changes in gradient angle along the fans. Furthermore, the DEM was used during the geomorphological-field survey to correlate surfaces and morphstructures.

4.3 Sampling and analytical work

Based on the new geological evidence, rock sampling was carried out for thermochronological and geocronological studies, in order to constrain the timing and patterns of exhumation and faulting in the study area. We applied low-temperature thermochronology (apatite fission track (AFT) thermochronology and apatite (AHe) and hematite (HeHe) (U–Th)/He dating) and optically stimulated luminescence (OSL) techniques to 31 samples collected along and across the strike of the KFF trace. In particular:

- (i) 17 samples were collected for AHe thermochronological analysis in order constrain the near-surface T–t paths (e.g. Fitzgerald et al., 2006) and the exhumation/denudation history along the KFF. The samples were collected from the arenitic portions of the Paleozoic units (6 samples) and the basal sandy intercalations of the Neogene deposits (11 samples);
- (ii) 7 samples from striated, hematite-coated fault surfaces within Neogene deposits were sampled for hematite AHe thermochronological analysis (Evans et al., 2014; Farley and Flowers, 2012);
- (iii) 9 samples of faulted Quaternary alluvial fan and fluvial terraces deposits were sampled for Optically Stimulated Luminescence (OSL) dating.

4.3.1 Apatite (U–Th)/He (AHe) and Apatite Fission Tracks (AFT) dating

AHe and AFT low thermochronology has been proven, by several studies, to be particularly effective in constraining fault related exhumation history along propagating strike-slip fault systems (Benowitz et al., 2011; Fitzgerald et al., 1995). Specially AFT and AHe analysis closure temperatures depend upon the cooling rate and composition of the sample and are typically around 110–120 and 60–70°C, respectively (Farley, 2000), readily allow the investigation of the near-surface T–t paths and the exhumation/denudation history.

The apatite (U–Th)/He data were acquired at the Scottish Universities Environmental Research Centre. Inclusion-free apatite were hand-picked under a high magnification binocular

microscope with cross-polarized light in order to avoid mineral inclusions in apatite crystals. Prior to analysis, grains were photographed and dimensions measured. Single crystals were packed into Pt foil capsules. Helium was extracted by heating the Pt-tubes at 600–700°C for 1–2 minutes using a laser diode following the procedures described by Foeken et al. (2006). ^4He concentrations were measured by comparison to a calibrated standard ^4He using a Hiden HAL3F quadrupole mass spectrometer equipped with an electron multiplier. The accuracy of measurements was checked by repeated measurements of an in-house He standard. System blank levels were trivial in comparison to measured He abundances and no correction was necessary.

Apatites were then dissolved in 5% HNO_3 with ^{235}U and ^{230}Th spikes and measured by VG Plasma Quad 2 ICP-MS. Correction for He recoil loss (F_t) was made using conventional procedure (Farley et al., 1996).

The AFT data were acquired at the Department of Geosciences, University of Arizona, USA. The analysis was performed in order to establish if during the Neogene development of the KFF system exhumation and/or burial were sufficient to affect the AFT system. The methodology follows that outlined in Thomson and Ring (2006). IRMM540R glass was used to monitor neutron fluence during irradiation at the Oregon State University Triga Reactor, Corvallis, USA. A IRMM540R apatite zeta calibration factor (Hurford and Green, 1983) of 368.1 ± 14.9 was used in age calculation. For apatite of typical Durango composition (0.4 wt% Cl) experimental and borehole data (Green et al., 1989; Ketcham et al., 1999) show that over geologic time tracks begin to anneal at a sufficient rate to be measurable above ca. 60°C, with complete annealing and total resetting of the apatite fission-track age occurring at between 100°C and 120°C. This range of temperatures is labeled the apatite fission-track partial annealing zone. For samples that have undergone moderate to fast cooling, a closure temperature of $110 \pm 10^\circ\text{C}$ can be reasonably assumed for the most common apatite compositions (e.g. Reiners and Brandon, 2006).

4.3.2 Hematite (U-Th)/He (HeHe) dating

The HeHe data were acquired at the Department of Geosciences, University of Arizona, USA. HeHe thermochronology is not commonly used to investigate fault related exhumation.

HeHe geo- and thermochronology can be applied to a range of Fe-oxides including botryoidal and specular hematite in hydrothermal veins (Evenson et al., 2014; Farley and Flowers, 2012; Lippolt et al., 1995; Wernicke and Lippolt, 1993), goethite cements and hematite in deep weathering horizons (Heim et al., 2006; Shuster et al., 2005; Vasconcelos et al., 2013), Fe- and Mn-oxides in sedimentary concretions (Reiners et al., 2014), and magnetite in mafic volcanic rocks (Blackburn et al., 2007).

The hematite He system closure temperature is estimated at ~200-300 °C (Bahr et al., 1994; Lippolt et al., 1993), while Farley and Flowers (2012) show that common polycrystalline hematite exhibits multi-domain diffusion behavior. The observed range in effective closure temperatures (~50-250 °C) within a single aliquot appears to correspond to the range of individual crystal grain sizes (Evenson et al., 2014; Farley and Flowers, 2012). This means that the individual crystal is likely the diffusion domain and closure temperatures increase with grain size.

Hematite films are also commonly found on fault surfaces, often exhibiting striated surfaces and high-metallic luster appearance.

Hematite He ages from fault surfaces may date three different processes:

- (i) record cooling caused by exhumation (Evenson et al., 2014). In this case, dates of aliquots with similar grain sizes and therefore effective bulk closure temperature should be uniform over relatively large length scales (e.g., > meter scales).
- (ii) Hematite from the sample formed below its closure temperature (e.g. Adams et al., 2013). In this case, the dates may represent either formation ages, before or during fault slip.
- (iii) dates may record rapid cooling from localized frictional heating or circulation of hot fluid along the surface during fault slip. Lachenbruch (1986), shows that slip surfaces can generate temperatures which exceed 700°C above ambient conditions, and flash heating to temperatures >500 °C may occur at geometric asperities (Beeler et al., 2008; Goldsby and Tullis, 2011; Rice, 2006). In this conditions, seismically induced shear heating is more than sufficient to reset the hematite (U-Th)/He system at the fault surface.

Therefore, hematite He dates represent either synkinematic formation ages or rapid cooling from shear heating or hot fluids associated with faulting giving direct constrain on the timing of fault slip.

4.3.3 OSL dating

Luminescence dating techniques – including OSL – are used to determine the period of time that has elapsed since quartz or feldspar mineral grains in sediments (amongst other constituents) were last exposed to sunlight or to heat, as heat and/or sunlight exposure for even a short time can cause the luminescence signal to be zeroed (Choi et al., 2009). After burial the OSL accumulates in response to natural ionising radiation (from radioactive isotopes in the Th, U series and ⁴⁰K, and from cosmic rays), received during the burial period of the sediment (Fattahi et al., 2006). Quartz and feldspar in the sediment have dosimetric properties. The level of OSL observed in these minerals is thus dependent on the absorbed radiation dose. For age determination two values are required: the equivalent dose D_e (which is the radiation level responsible for producing the luminescence signal) and the dose received per year (during burial).

A total of 9 samples were collected from faulted alluvial and fluvial deposits for OSL dating in order to constrain the timing faulting and of deposition of the Quaternary covers. The OSL data were acquired at the LABER OSL Lab, Waterville, Ohio (USA).

Sample preparation

For each sample pure quartz was extracted for De measurements. In OSL lab, the sample was treated firstly with 10% HCl and 30% H₂O₂ to remove organic materials and carbonates, respectively. After grain size separation, the fraction of 90-125 μ m is relatively abundant. As a result, this fraction was chosen for De determination. The grains were treated with HF acid (40%) for about 35 min, followed by 10% HCl acid to remove fluoride precipitates.

Measurement techniques

Quartz OSL measurements were performed using an automated Risø TL/OSL-20 reader. Stimulation was carried out by a blue LED ($\lambda=470\pm20$ nm) stimulation source for 40 s at 130 °C. Irradiation was carried out using a 90Sr/90Y beta source built into the reader. The OSL signal was detected by a 9235QA photomultiplier tube through a U-340 filter with 7.5 mm thickness.

Equivalent dose (De) measurement and age calculation

For De determination, SAR protocol was adopted. The preheat temperature is chosen to be 240 °C for 10 s and cut-heat is 180 °C for 10 s. The final De is the average of Des of all aliquots, and the error of the final De is the standard error of the De distribution. For each sample, 20 aliquots were measured for De determination.

The Quartz OSL was fast component dominated. Recycling ratios were between 0.90-1.1. Recuperation is negligible. The cosmic ray dose rate was estimated for each sample as a function of depth, altitude and geomagnetic latitude. The concentration of U, Th and K was measured by ICP-MS. The elemental concentrations were then converted into annual dose rate, taking into account of the water content effect. The final OSL age is then: De/dose-rate.

5 TOPOGRAPHIC SIGNATURE OF THE KFF

The structural architecture of the KFF system consists of three main broadly left stepping, E-W striking, fault strands, the Western Fault Strand (WFS), the Central Fault Strand (CFS) and the Eastern Fault Strand (EFS) (Fig 5.1a). Topographic analysis performed on a 10x10 m digital elevation model, derived from topographic maps, shows that the KFF deformation zone defines an E-W oriented, up to 17 Km wide, linear ridge reaching a maximum elevation of ~1700 m and thinning out to the east. The KFF associated ridge can be subdivided into two main topographic domains located west and east of the central southward draining active alluvial plain respectively (Fig. 5.1). The ~42 km long western domain prominently elevates above the southward Kavir-e-Namak salt plain, with the axial region characterized by rugged and steep terrains (slope angle $>15^\circ$) and high local relief (>100 m; Fig. 5.1b-c). Peripheral areas are characterized by less elevated and gentler dipping terrains (slope angle $\sim 2-5^\circ$) with lower local relief (<50 m; Fig. 5.1b-c). The linear topography of the western domain is interrupted by a low relief area, which dissects the ridge from north to south in a jagged fashion. West of this discontinuity, ENE-SSW oriented linear ridges and associated valleys tend to progressively bend northward and southward, towards the edges of the rugged central area (Fig. 5.1a and d). The boundaries between the axial and peripheral regions are marked by sharp breaks in slope, which seem to be located in correspondence of the main fault strands (Fig.5.1a and b). The ~23 Km long eastern domain shows an overall eastward narrowing and decreasing of the topography (Fig. 5.1c) and is dissected by a second southward draining active alluvial plain, which separates two sub-domains characterized by different topographic characters (Fig. 5.1 a). To the west a broadly E-W elongated oval hill, ~10 km long and 3.5 km wide, with discontinuous E-W oriented narrow ridges and associated valleys. To the East, a very narrow ~10 km long, E-W oriented linear ridge, marks the termination of the KFF. The whole KFF ridge shows a prominent, roughly E-W oriented divide that separates a broader and gentler northward draining slope from a narrower and steeper southward draining slope.

Figure 5.2 shows the filtered topography analysis performed on the regional DEM of the study area. From such analysis, it is possible to assess the topographic signal wavelength of the topographically prominent KFF. The local-scale topographic filtering quantifies the wavelength of the above described topographic domains, (Fig. 5.2). The western topographic domain starts to be picked up with the 10-km filter, while the eastern topographic domain has a 2-km wavelength. Representative across-strike and along-strike swath elevation profiles were also performed (Fig. 5.2; Hergarten et al., 2014; Mitchell and Montgomery, 2006; Telbisz et al., 2013). The above evidences are confirmed by the topographic data of the longitudinal swath profile (SWP5 in Fig. 5.3). This swath profile outlines very well the above described, fault-bounded longitudinal topographic

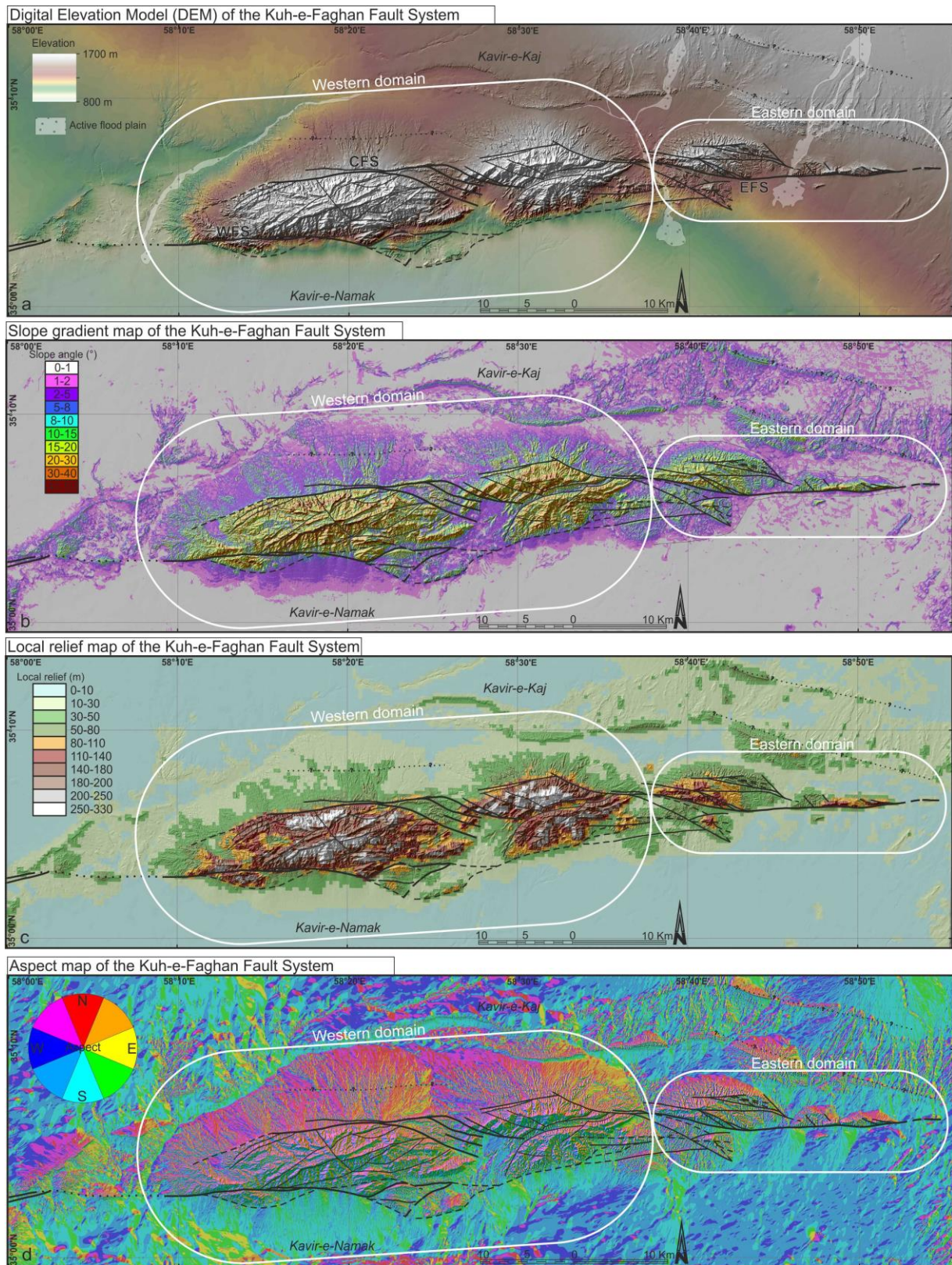


Figure 5.1 Maps of the study area extracted from a 10x10 m digital elevation model, with faults marked in black. (a) Topography by DEM. (b) Slope gradient map. Note the steep slope gradients along the boundary faults. (c) Local relief map. (d) Aspect map.

domains. The western one shows higher maximum topography, relief and a quite constant base level (minimum topography). Furthermore, an eastward increase of minimum topography of the range was observed, that corresponds to a progressively higher (i.e. transient) base level of erosion.

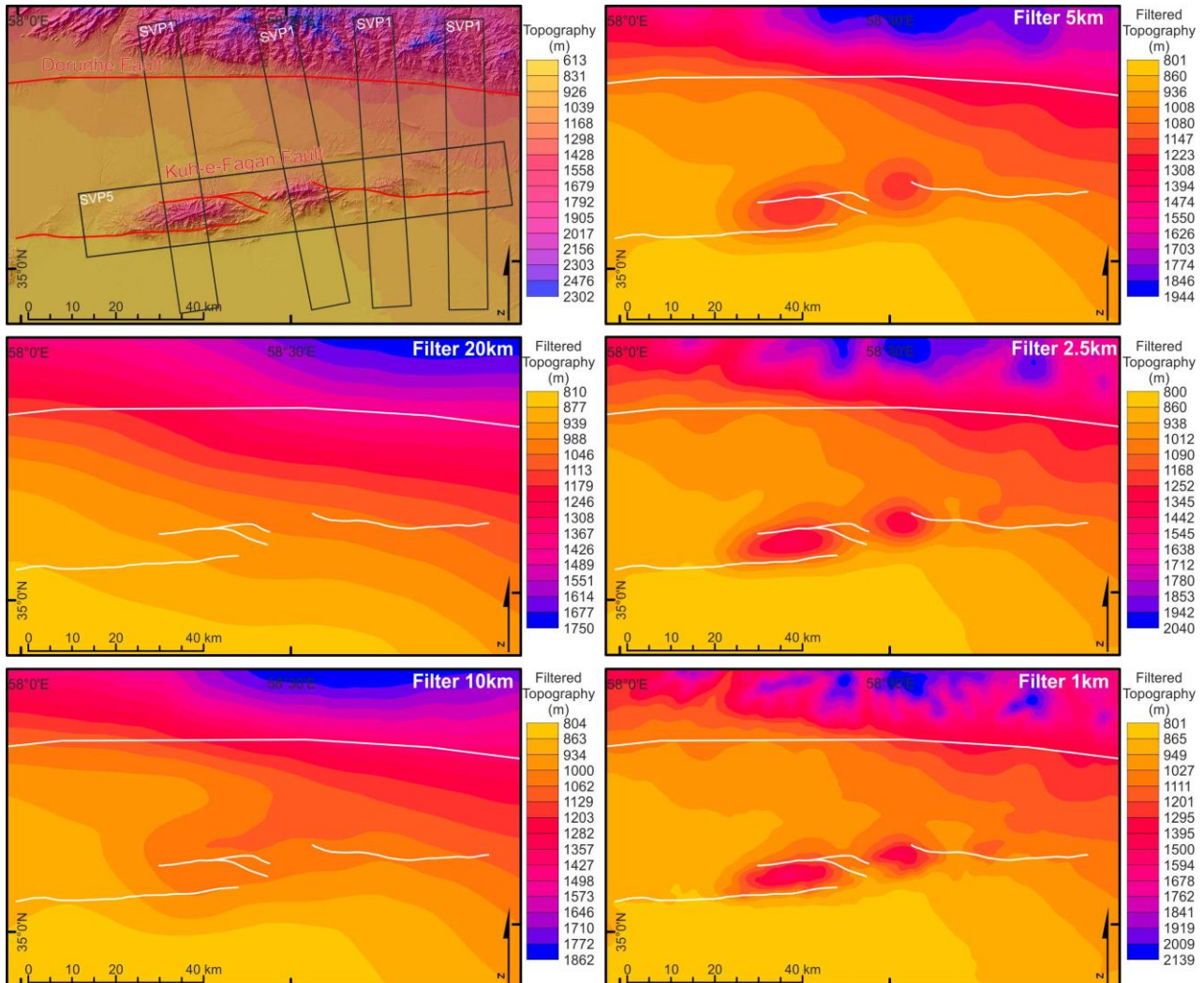


Figure 5.2. Filtered topography analysis performed on a 10x10 m (cell size) digital elevation model. Progressively smaller (from 20 to 1 km) radial filter was implemented.

The four across-strike oriented swath profiles outline the local topographic signal of the the KFF and Doruneh Fault, marked by sharp breaks in local relief (Fig. 5.3). Furthermore, they show that in the western part of the KFF the northern base level of the ridge is a well-developed flattish alluvial plain up to 170 m higher than the southern alluvial plain (Fig. 5.3). This plains are bordered by slightly-dipping alluvial fan systems which connect them to the slopes of both the Doruneh fault-related ridge and the KFF western topographic domain. Such alluvial plains progressively disappear eastward, where are partly covered by a southward dipping bajada of alluvial fans, likely feeded only by the Doruneh fault-related ridge (Fig. 5.1d).

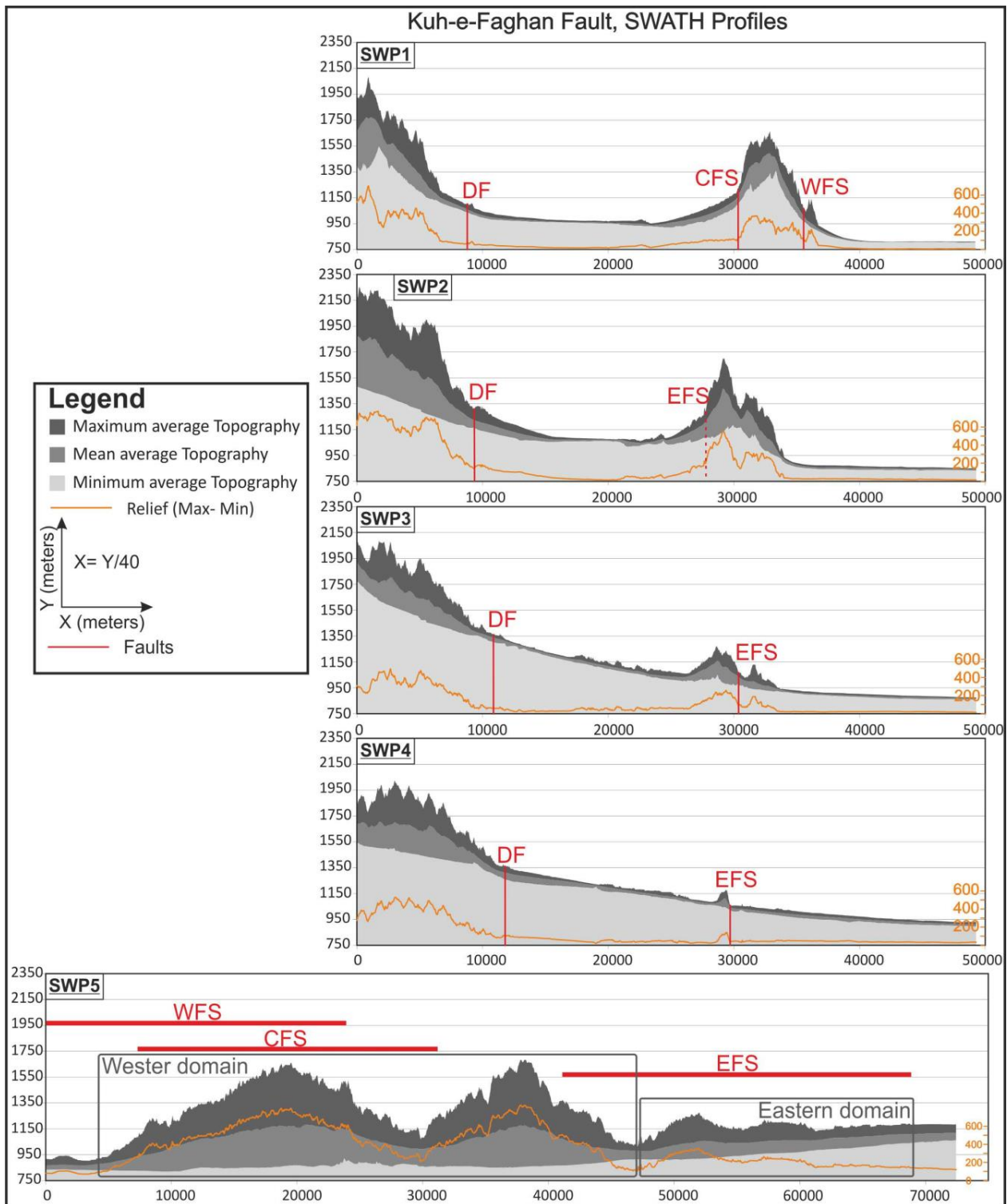


Figure 5.3 Swath profiles (40 times vertical exaggeration) across strike of the KFF (SWP1 to SWP4) and along strike of the KFF (SWP5) extracted from a 10x10 m digital elevation model. Locations of the swath is shown in Fig. 5.2

6 NEOGENE STRATIGRAPHY

The Neogene sedimentary units, belonging to the Upper Red Formation of Central Iran unconformably overlay the basement (Paleozoic and Mesozoic) units and consist of continental deposits comprising conglomerates, sandstones, siltstones, marls and evaporites (Fig. 6.1). In the KFF area a stratigraphic successions, comprising three main sedimentary cycles separated by angular unconformities, have been defined (Fig. 6.2). Figure 6.2a and 6.2b show two schematic generalized vertical sections (GVS) for the northern and southern area of the KFF respectively. The Neogene unit's estimated thicknesses variations along the system are reported in a series of stick-logs beside the GVSs, which have been measured along the relative geological cross-sections (Fig. 6.1). Figure 6.2c shows the diagram of the Neogene unit stratigraphic relations as reconstructed in the field.

From the geological map (Fig. 6.1), the cross-sections (Fig. 6.1) and the generalized vertical section of the KFF (Fig. 6.2a and b) it is evident that the overall lateral extent, geometry and thicknesses of the Neogene units and cycles vary spatially, along and across strike of the KFF system. Assessing and quantifying such lateral variations it is made more challenging by the fact that the units tend to outcrop along faulted segments and therefore often do not show continuous stratigraphic section. Furthermore, the basal units, in particular Ng C and Ng SSi contain facies (talus breccias and alluvial fan to fluvial facies) which are expected to have generated deposits with heterogeneous thicknesses. However, some general trends and relations are recognized and assessed.

In the following, the KFF system associated Neogene stratigraphy, belonging to the URF, will be described and interpreted.

6.1 Stratigraphic cycles and units

Cycle-1 unconformably overlies the basement units. The unconformity is characteristically angular and the Neogene inclined beds overlay the often verticalised basement units. It includes units Ng-B and Ng-C (Fig.6.2) and generally consists of breccias and red to pale brown conglomerates respectively. The clasts of all breccias and conglomerate deposits principally consist of yellow, grey and black fossiliferous limestone and dolomite with subordinate amounts of sandstone and shale. In the upper part of the cycle, minor amounts (<5%) quartz pebbles and clasts made of igneous and volcanoclastic sediments are found. The majority of the conglomerates and breccias are clast supported however; transitions into matrix supported conglomerates are not uncommon especially in the upper part of the cycle. The matrix (up to 25%) is usually made of dark red to pale grey mudstone and siltstone.

Geological map of the Kuh-e-Faghan Fault System

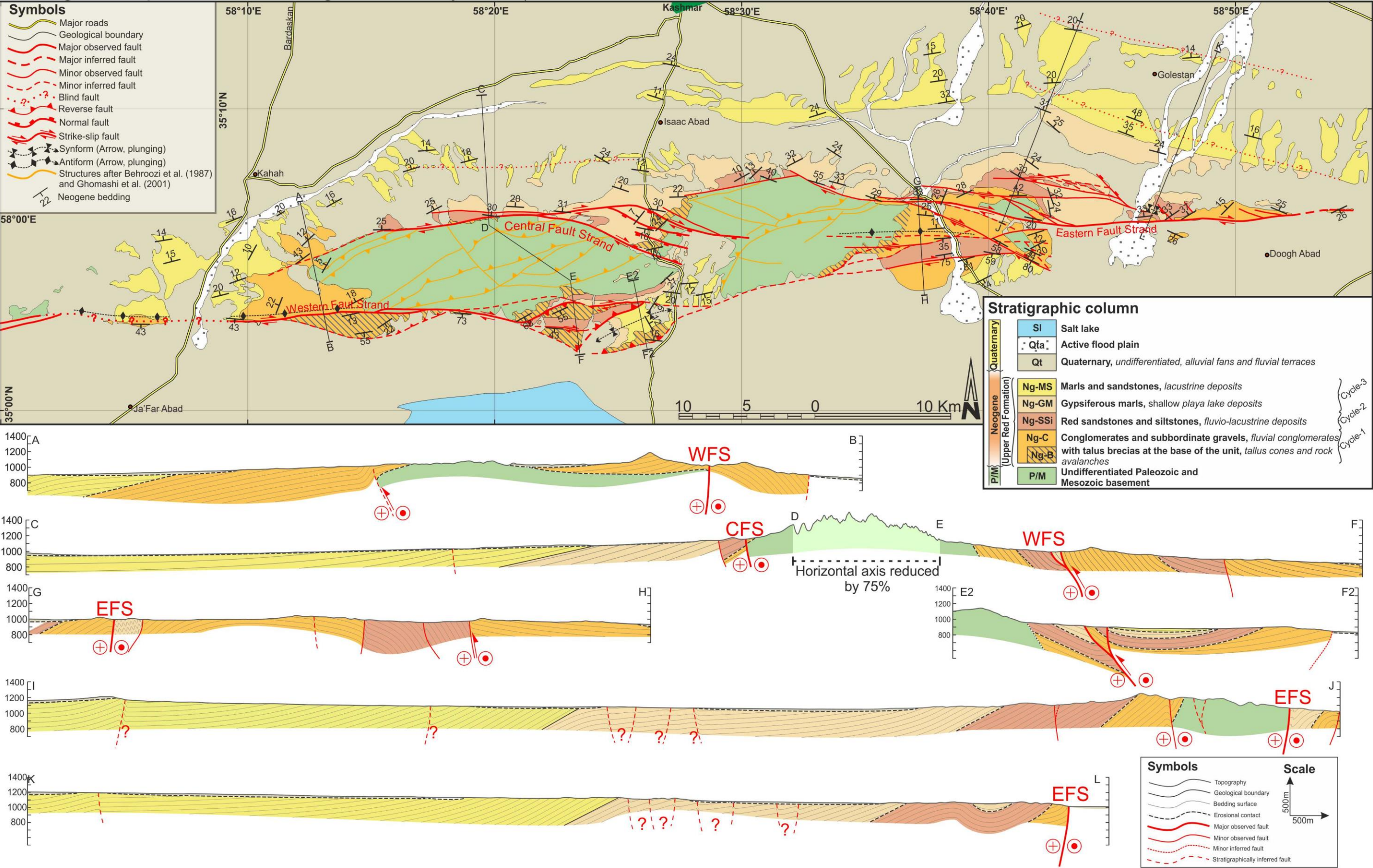


Figure 6.1 Geological map of the KFF system and geological cross-sections

The basal portion of cycle-1, unit Ng-B, consists of clasts supported, unstratified, extremely poorly sorted, breccias, with discontinuous and disorganized local extents. The clasts vary from boulder to cobble size (Fig. 6.2). In places the basal cycle include boulders up to 1 m in diameter made of the same lithology that contains it (intraformational boulders), indicating reworking of the older part of the deposit. Such basal breccias are only found along the WFS and along the CFS. Their presence, at the base of the cycle, is marked on the geological map on figure 6.1, by gray hatching.

Where the basal breccias are present, the transition to the upper part of cycle-1 varies from gradual to sharply on angular unconformity (e.g. Fig. 6.3a). Where basal breccias are absent the upper part of cycle-1, unit Ng-C unconformably overlies the basement units and is characterized by deposits consisting of clasts supported, crudely to well stratified, polymictic, conglomerates, with relatively rounded and sorted and in places imbricated clasts, arranged into 50 to 350 cm thick large scale lenticular and at times laterally discontinuous beds (Fig.6.3a). A distinction can be made however, between the western and eastern areas. Along the WFS and CFS the upper part of cycle-1 generally exhibits less rounded clasts and more chaotically bedded deposits with matrix rich horizons showing convoluted and at times folded bedding. By contrast along the EFS the conglomerate deposits are typically interbedded with subordinate, fining upwards, 10 to 50 cm thick gravelly sandstones packages. Concave upwards erosional surfaces and lenticular beds geometries are common. The deposits of cycle-1 often show progressive angular unconformities, throughout the area.

Cycle-1 is interpreted as a high-energy deposit. The poorly sorted, texturally immature and chaotic nature of the basal breccias, unit Ng-B, suggests very proximal deposition likely by block fall and avalanches resulting from deposition within proximal fans and/or as talus cones, on steep slopes. The presence of progressive angular unconformities and reworking of older parts of the deposit, may represent deposition along a tectonically active margin. In the western area, the chaotic and convoluted bedding and angular nature of the conglomerate deposits of the upper portion of cycle 1 indicative in depositions by debris flow dominated processes along a complex of alluvial fans. In the eastern area, the crudely stratified at times imbricated, and relatively texturally mature nature of the upper part of the cycle- and the presence of concave upward erosional surfaces are indicative of fluvial depositional environments. The widespread and laterally continuous nature of the upper part of cycle-, unit Ng-C, suggest that deposition occurred within an alluvial fan complex in the west area and a broad, well-fed alluvial plain in the east. The clasts lithologies and textures of the basal breccias deposits indicate that they have been sourced from the proximal basement units. Furthermore, the overlying upper conglomeratic units are also principally made-up of clasts belonging to the basement units of the KFF with some minor amounts of clasts made up of lithologies

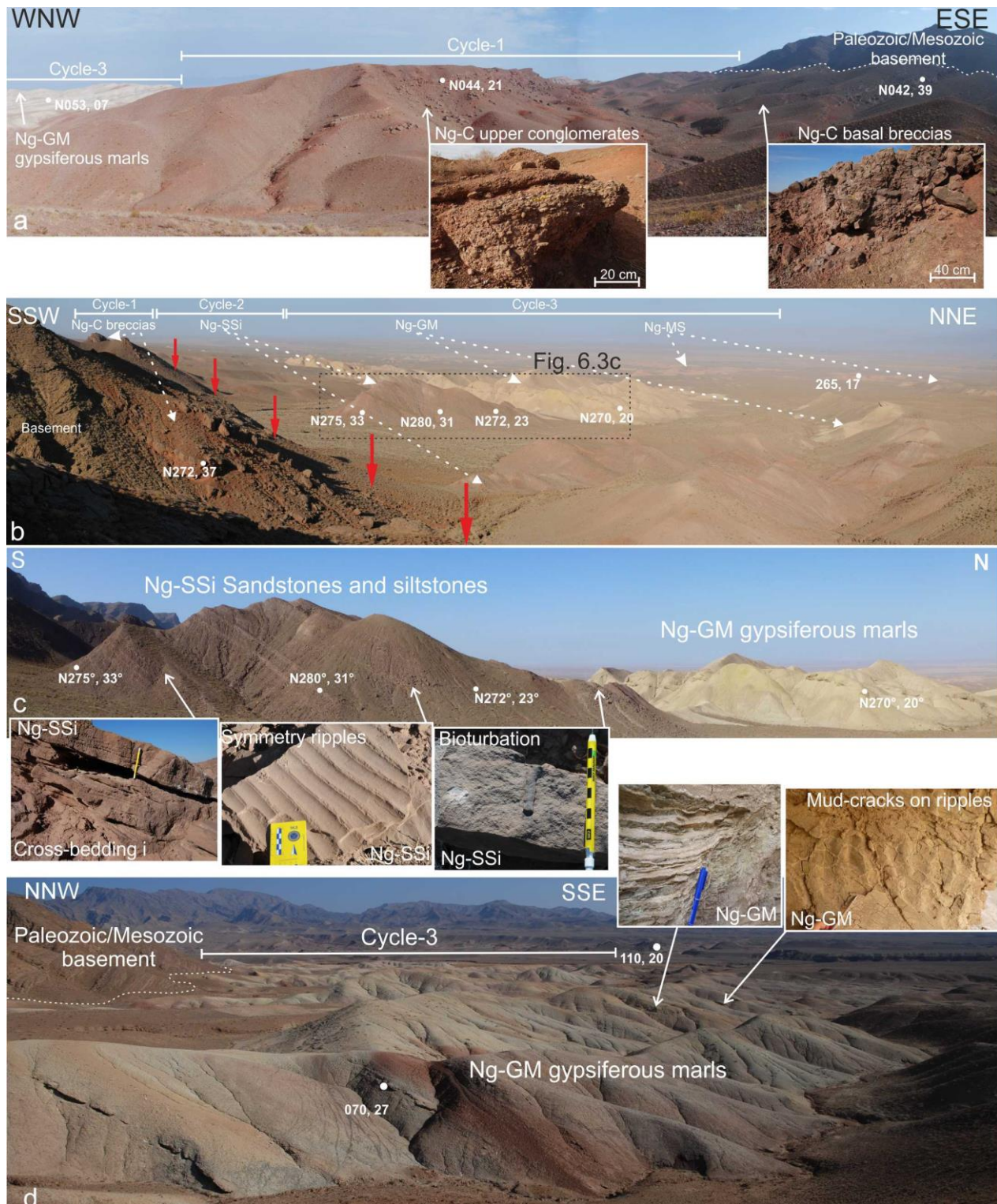


Figure 6.3 Field examples of the KFF Neogene deposits and their stratigraphic relations. (a) Panoramic view of cycle- deposits onlapping onto the Paleozoic and Mesozoic basement. Note the angular contact between the basal and upper portion of unit Ng-C consisting of fluvial conglomerates. Insert showing deposits characteristics. Cycle-3 onlaps directly onto cycle-. (b) Panoramic view showing the three sedimentary cycles and their stratigraphic relations. CFS fault trace marked by red arrows. (c) Progressive angular unconformities within cycle-2. The inserts show the range of sedimentary structure, observed within cycle-2 attesting for its fluvio-palustrine depositional environment. (d) panoramic view showing cycle-3 onlapping directly onto the Paleozoic and Mesozoic units. Bedding strike and dip measurement are marked by white dots. See figure A1 in appendix-A for location.

currently not represented in the study area. Overall cycle- shows large lateral thicknesses variations. Up to 450m of basal breccias are found in the southern side of the KFF, along the WFS, while along the CFS the exposed breccia deposits do not exceed 100m in thickness (Fig. 6.2a and b). The overlying upper deposits, consisting of fluvial conglomerates, show its greatest thickness (c.a. 500 m) along cross-section A-B, but more commonly does not exceed 300 meters in thickness as it can be observed in the EFS sector (Fig. 6.2a and b).

Cycle-2 overlays on angular unconformably Cycle-. It includes unit Ng-SSi (Fig. 6.2 and 6.7b) and consists of decimeter thick bedded, well sorted, mineralogically and texturally immature, planar to cross laminated, medium- to coarse-grained silty red sandstone. In places, the deposit shows cross-trough bedding alternating with subordinate horizons consisting of coarse gravelly sandstones. Straight crested symmetric, lunate and linguoid ripples are all common feature of the unit, together with locally bioturbated horizons and surfaces exhibiting mud cracks and casts (Fig. 6.3c). Progressive angular unconformities are very common especially in the lower part of cycle-2 (Fig. 6.3c).

The cross-trough bedding, the gravelly input and the lunate and linguoid ripple surface are indicative of a relatively turbulent fluvial environment. Nevertheless, the bioturbated horizons, the straight crested symmetric ripples and the presence of mud cracks and casts suggest a less turbulent and at times sub-aerial exposed fluvio/palustrine environment. The two types of the deposit represent the channel/bank and overbank deposits respectively within a fluvio/palustrine environment possibly proximal to a wide, well fed alluvial plain capable of supplying relatively well-sorted material but however unable to produce mineralogically and texturally mature sediments.

Cycle-2 is absent in the westernmost part of the KFF. It first outcrops along the western tip of the CFS and generally increase in thickness eastwardly to reach its maximum (575 m) in correspondence of the central part of the EFS to then thin out eastwardly once again. Overall Cycle-2 exhibits greater thicknesses to the north and south of the EFS, along cross-sections G-H and I-J (Fig. 6.1).

Cycle-3 unconformably overlays cycle-2 and generally have strongly discordant overlapping relationships with the underlying sedimentary and basement units, systematically marked by unconformity contacts. Cycle-3 includes units Ng-GM, and Ng-MS (Fig. 6.2). Unit Ng-GM is characterized by centimeter to tens of centimeter thick bedded, marls and silty-mudstone interbedded with centimeters thick of secondary gypsum horizons (Fig. 6.3d). Some infrequent planar to cross laminated, tens of centimeter thick fine sandstone beds are also present. Other horizons exhibit millimeter thick planar layering depicted by slight change in sediment color. Desiccation cracks and mud casts are also common. Several beds of marl and silty-mudstone exhibit bedding surfaces with

small-scale straight crested asymmetric ripples at times superimposed by mud-cracks (Fig. 6.3d). The gypsum is typically recrystallized/remobilized along bedding plane and fractures and in places it has deformed and disrupted the sediment layering. The basal and upper part of the unit are characterized by meter thick red marls and silts, relatively free of gypsum, interbedded with pale yellow gypsiferous silty marls; while the central part of the unit is characterized by continuous layering of yellow gypsiferous marls and mudstones (Fig. 6.2).

Ng-MS conformably overlays Ng-GM and consists of centimeter to tens of centimeter thick, pale red to beige, massively bedded, marls and silty-mudstone, with millimeter scale layering; interbedded by subordinate 0.5 to 2.5 m thick cross-bedded, at times laterally discontinuous, light brown, medium to coarse at times gravelly sandstones. Bedding surfaces exhibiting small-scale straight crested asymmetric ripples are rare but not uncommon.

Ng-GM units deposited under different conditions, ranging from evaporation dominated (secondary gypsum deposits), to suspension dominated (massive and layered marls and silty-mudstones), to relatively high energy tractional and unidirectional turbulent flow dominated (rippled silty-marls and fine sands) settings. Such characteristics are representative of playa mud flats and playa lake environments (Reading, 2009). The mud dominated portion of the deposits is associated with unconfined sheet flows during periods of widespread flooding on a low gradient flood plain capable of developing restricted ephemeral ponds that ultimately drained into a restricted shallow ephemeral saline lake where deposition occurred primarily by suspension settling. The frequent interbedding of silty-mud and gypsum are indicative of periodic flooding (silty-mud deposition), followed by subsequent dry periods dominated by evaporation (gypsum deposition), within the ponded areas, and mud cracks development along the sub-aerially exposed extents.

The thickly bedded marls and silty-mudstones, of units Ng-MS, mainly characterized by millimeter scale layering and some rare rippled surfaces, are indicative of deposition in a low energy shallow lacustrine environment, where deposition occurred primarily by suspension settling and secondarily by laminar and turbulent flow. The subordinate meters thick cross-bedded sandstone interbeds have been deposited by more turbulent and energetic flow and represent deposition during periods of increased sediment input and/or alluvial input from proximal fluvial channels.

Overall cycle-3 is mostly found in the northern areas of the KFF. The basal unit of Cycle-3, unit Ng-GM, behaves similarly to Cycle-2. It is absent in the western part of the KFF, it outcrops firstly in correspondence of the western tip of the CFS, it reaches its maximum thickness (~450m) north of the central portion of EFS to then thin out again eastwardly. The upper unit of Cycle-3, unit Ng-MS, extends throughout the northern KFF area and the maximum estimated thickness of non-

continuous section reaches ~1230m in correspondence of cross-section II. Throughout the area unit Ng-MS makes up almost half of the total thickness of the entire Neogene succession.

Collectively the sedimentary succession shows a general fining upwards trend: cycle- breccias and conglomerates, cycle-2 sandstones and cycle-3 mudstones, marls and gypsum. Such sedimentary architecture envisages that cycle-2 onlaps onto cycle- and cycle-3 onlaps onto cycle-2, during continuous synsedimentary tilting of the depocenter. Such geometry is clearly visible in the field as illustrated by figure 6.3b. In fact, the base of the succession outcropping closer to the fault system shows greater tilting which progressively decrease upward and away from the fault system. Such stratigraphic relations are generally valid in most areas, however in several places, cycle-3 onlaps directly onto cycle- (e.g. Fig. 6.3d).

Furthermore the three main cycles separated by angular unconformities, also show an upward decrease in synsedimentary deformation structures. Cycle- and 2 are characterized by progressive angular unconformities that gradually decrease towards the base of cycle-3 where unit Ng-GM show synsedimentary faulting which progressively disappear towards the top of the unit. The upper unit of cycle-3 (unit Ng-MS), which constitutes more than a half of the total stratigraphic succession does not show any syndepositional deformation structures and generally it onlaps onto the units and cycles below. Additionally, cycle-1, 2, and the base of cycle-3 show greater lateral thickness variations than the upper part of cycle-3 with an overall increase in thicknesses towards the eastern and northeastern areas. Important to notice is also that the basal and proximal breccia deposits of cycle- are only reported in the western area and are completely absent along the EFS.

The KFF Neogene stratigraphic succession and along strike changes, in sedimentary facies, depositional architectures and deposits thicknesses, reflect a history of deposition strongly influenced by tectonics and modulated by regional and local environmental changes.

7 QUATERNARY LANDFORMS AND DEPOSITS

The Quaternary morpho-evolution of the KFF mountainous ridge is dominated by the erosional/depositional dynamics of the drainage network developed on the exhuming relief. In such a climatic environment, alluvial fan and alluvial plain development is generally spectacular due to: (i) lack of vegetation cover favoring channel shifting; (ii) occasional thunderstorms capable of revitalize the streams and make them capable of evacuating large volumes of sediments; (iii) availability of large quantities of debris produced by weathering processes (Bull, 1977; Cooke et al., 1993; Harvey, 1997).

Although in the present KFF desert environment the entire drainage network is ephemeral, most likely its dynamics developed over a climate-changing time span and was controlled by local base levels given by the two northern and southern large plains bounding the ridge, with a difference in elevation of up to 170 m. Presently, the northern plain is drained by two major competing rivers that dissect the ridge connecting the northern Kavir-e-Kaj alluvial plain to the southern Kavir-e-Namak alluvial-to-salt lake plain (Fig.7.1). The two rivers mark the western and eastern boundaries of the western topographic domain of the KFF ridge (see chapter 6) and their upper reaches are westward- and eastward-flowing respectively, with a very low-relief divide, clearly closer to the eastern boundary (Fig. 7.1). This means that the westward-flowing river exerted the most effective headward erosion and progressively captured the streams flowing on the northern slope of the ridge, as testified by their progressive curvature towards the confluence with the main river (Fig. 7.1). This evidence is in agreement with the progressive eastward decrease of the elevation difference between the northern and southern plains, that gave higher stream power to the westward-flowing river

Three generations of Quaternary deposits have been recognized, which unconformably overlay the Neogene continental units of the Upper Red Formation. Similar generations of Quaternary deposits, first studied in other Iranian sites, have been interpreted as having developed during Quaternary cold periods (see Beaumont (1972) for the southern piedmont of the Alborz Mountains, and Dufaure et al. (1978) for the Zendan fault area in southeast Iran). Recently, Walker and Fattahi (2011) reviewed the late Quaternary deposits of eastern Iran. The authors recognized that several generations of telescopic alluvial fans, as well as regional arrangement of river terraces and lake deposits could be explained by Late Pleistocene and Holocene environmental changes with aggradation phases occurring between ~30 and 13 ka and between ~9 and 7 ka, alternating with erosive phases, all controlled by regional climatic forcing. As for the erosive phases, in-situ produced cosmogenic ^{10}Be provided surface abandonment ages for different Quaternary alluvial surfaces in the the Hormoz Strait area at 5.6 ± 0.6 (offset of the mid-Holocene humid period), 8.4 ± 1.0 , 12.8 ± 1.0 (onset of the dry Younger Dryas cold and dry episode), 20.1 ± 1.5 (end of the Last Glacial Maximum),

River network of the Kuh-e-Faghan Fault System

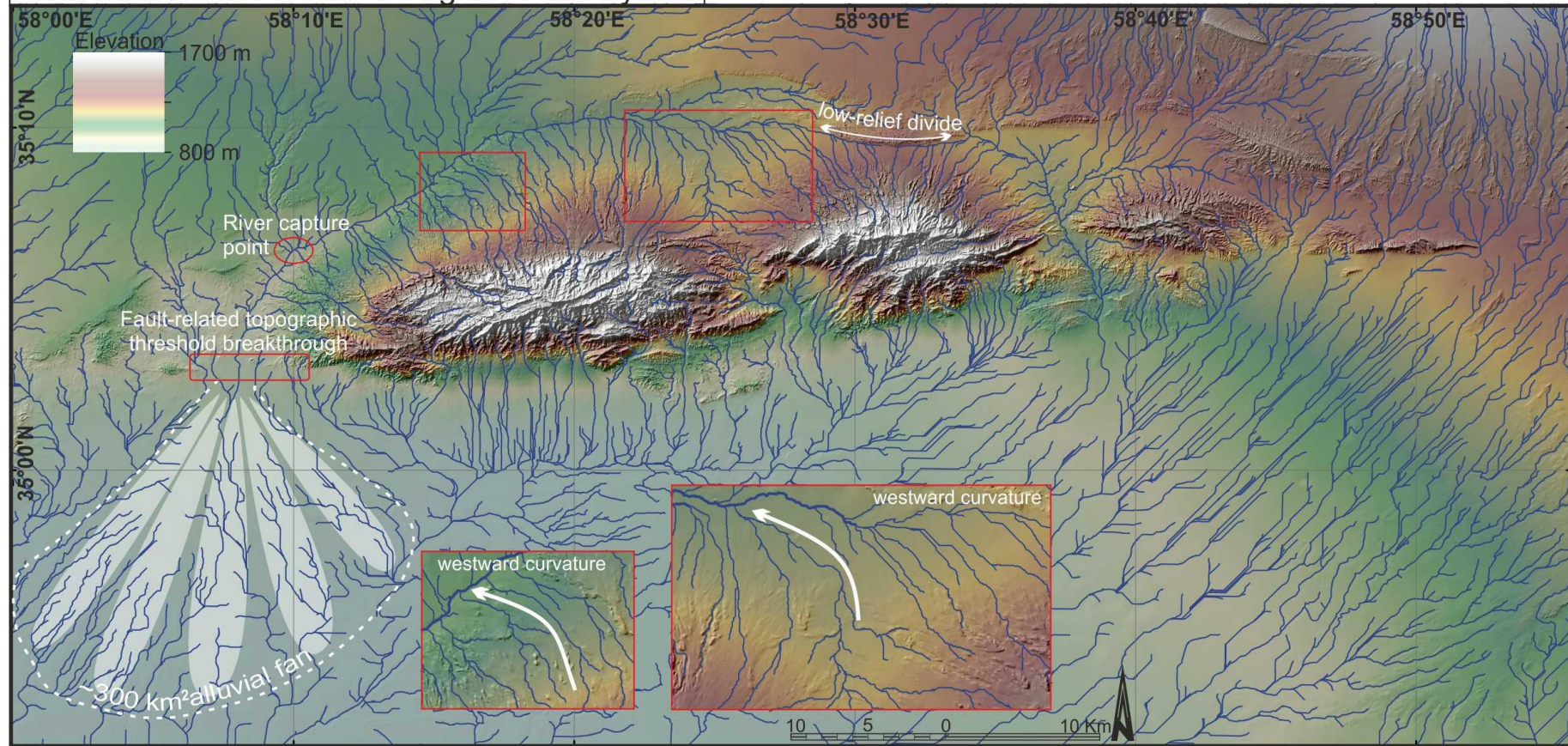


Figure 7.1 River network on DEM of the KFF area. Geomorphic evidence of drainage evolution are outlined. River capture point

and 44.0 ± 3.4 10Be ka (Regard et al., 2006). Similar generations of alluvial fans have been recognized in the neighbor regions and IRSL (infrared stimulated luminescence) age of ~ 10 ka was obtained for the deposition of the Shesh–Taraz fan along the Doruneh fault (Fattahi et al., 2007).

The quaternary deposits of the KFF area have been mapped integrating geomorphological field survey with DEM terrain analysis and aerial photointerpretation. Figure 7.2 and 7.3 show the satellite image and the lithological map of the different generations of Quaternary deposits associated with the KFF system respectively. The contact between the Neogene and Quaternary deposits is characterized by a regional erosive angular unconformity, which extends throughout the area and is identifiable both to the north (Fig. 7.4a and b) and south (Fig. 7.4c and d) of the KFF mountainous ridge. The unconformity surface is represented by a paleo-pediment that can be traced tens of kilometers both along and away from the KFF, especially to the north of the KFF ridge (Fig. 7.4a and b). Such pediment surface strikes sub-parallel to, and dips away from the KFF prominent linear topography and exhibits slopes angles $< 7^\circ$ which generally tend to decrease away from the KFF structure. The pediment has been heavily incised and eroded by subsequent fluvial processes. In fact, it is typically found 20 to 35 m meters above the active alluvial plains in areas proximal to the fault system (e.g. Fig. 7.4b).

The Quaternary deposits consist of alluvial fans and alluvial plain deposits made of a wide array of conglomerates, gravels and sands, exhibiting various degree of consolidation. The clasts making up the deposits principally consist of yellow, grey and black fossiliferous limestone, dolomite, sandstone and shale, belonging to the basement units indicating that the deposits have been sourced from the basement and Neogene units. Principally along the terraced alluvial and fluvial deposits, subordinate amounts of quartz pebbles and volcanoclastic sediments are also present. Most probably such subordinate amounts have been sourced from the Doruneh Fault area and transported to the KFF by the southward draining alluvial systems. Three major geomorphological zone are recognized in the KFF area, based on the landforms and deposits type associations. Zone 1 is located in northern side of the KFF mountainous ridge and extends from the western to the central southward draining active alluvial plain (Fig. 6.1 and 7.2a and 7.3a). Zone 2 is located to the south of the KFF mountainous ridge and extends from the western to the eastern southward draining active alluvial plain. Zone 3 includes the area north of the EFS, east of the central southward draining active alluvial plain, and the area south of the eastern end of the EFS, east of the eastern southward draining active alluvial fan.

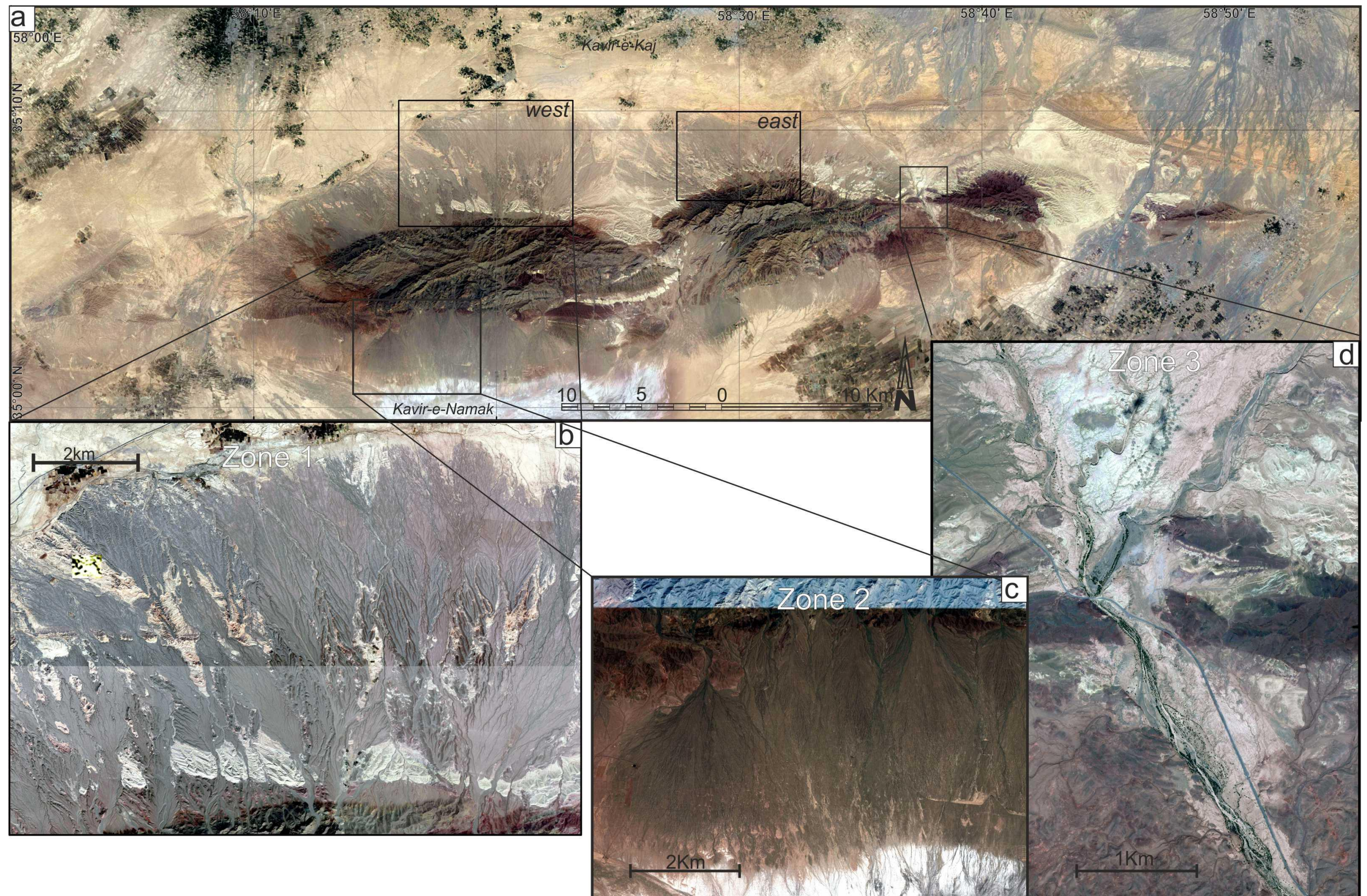


Figure 7.2. (a) Satellite image of the KFF area. The squares marked “west” and “east” indicate the areas where morphometric analysis was performed. (b) Blow-up of the north-western telescopically arranged quaternary alluvial fan deposits. (c) Blow-up of detailing the southern stacked quaternary alluvial fan deposits (d) Blow-up detailing the different generations of Quaternary terraced alluvial plain deposits. See figure 7.3 for details on the distribution of the different Quaternary alluvial deposits.

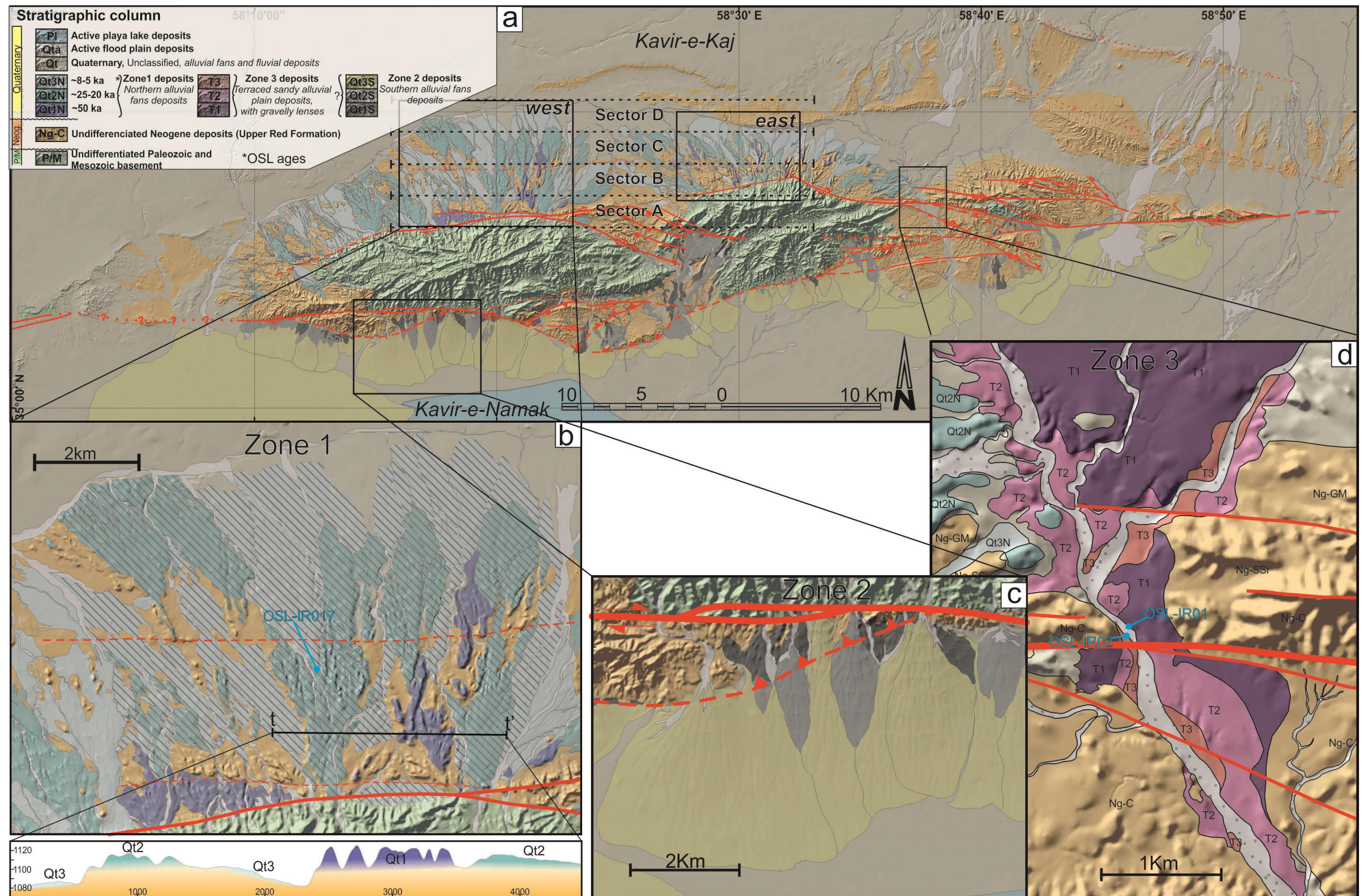


Figure 7.3. (a) Map of the KFF area showing the distribution of Quaternary alluvial deposits. The squares marked “west” and “east” indicate the areas where morphometric analysis was performed. The black dotted lines represent the boundaries of sectors in which morphometric analysis and statistics were performed (see chapter 10). (b) Blow-up of the north-western quaternary alluvial fan deposits (Zone 1 deposits) with topographic section t-t' across Qt1N, Qt2N and Qt3N deposits. Black hatched areas mark the alluvial fans used for the morphometric analysis. (c) Blow-up of detailing the distribution of the southern stacked quaternary alluvial fan deposits (Zone 2 deposits). (d) Map on shaded-relief detailing the distribution of the different generations of Quaternary terraced alluvial plain deposits (Zone 3 deposits).

7.1 Sedimentological characters

Two main type of deposits are recognized in the three zones: (i) alluvial fan deposits, found in Zone 1 and 2 and (ii) and alluvial plain deposits principally found in Zone 3.

The alluvial fan generally exhibit different deposits characteristics from the apex to the distal part. Chaotic, clast supported, highly angular, proximal breccia and conglomerate deposits characterize the apex area (the first 200 to 300 m) with maximum particle size of 35 cm (Fig. 7.4e). The central part of the fan system is characterized by relatively more texturally mature and rounded, matrix supported conglomerates agemented into 30 to 100 cm thick beds exhibiting normal grading and infrequent cross-stratification in the upper part of the beds. In this area clast sizes are up to 15cm (Fig. 7.4f). The distal portion of the fan deposits are characterized by cross-stratified and at times clinostatified gravelly sands exhibiting normal grading and infrequent concave upwards erosional surfaces. The deposits can contain clasts with maximum particle size of 5 cm (Fig. 7.4g). The alluvial fan deposits distally merge and interfinger with alluvial plain deposits. The alluvial fan deposits are arranged in a broad up to 7km wide bajada that extend from the KFF main fault strands to the surrounding alluvial plains.

The alluvial plain deposits principally consist of sandy large-scale lenticular beds, exhibiting some cross-stratification and concave upward erosional surfaces with gravelly horizons (Fig. 7.4h).

7.2 Morphological characters

In Zone 1 three generations of alluvial fan have been identified (Qt1N, Qt2N and Qt3N, Fig. 7.2 and 7.3). The three alluvial fan generation can be distinguished from their degree of surface incision and their relative top and bottom surface elevation which systematically decrease from Qt1N to Qt3N (e.g. cross-section t-t', figure 7.3b). In particular the Qt1N alluvial fan deposits are generally poorly preserved and their fan geometry is often fragmented (Fig. 7.2b 7.3b). They are always found lying above the paleo-pediment surface and the top surface exhibit extremely incised and rugged topography (Figure 7.4b). The Qt2N alluvial fan deposits geometries are better preserved and exhibit relatively less incised top surfaces. They are found entrenched in Qt1N, often also into the paleo-pediment surface with their bottom and top surface generally located at lower elevation than the Qt1N's. The Qt3N alluvial fan deposits geometries are the most well preserved and exhibit very little top surface incision. They are relatively deeply entrenched into both Qt1N and Qt2N fans and they lie further below the paleo-pediment surface. Collectively the three fan generations displays geometric relations and characteristics typical of telescopically arranged fan system. Nevertheless, the three fan generations make up a wide bajada which generally drains northward into alluvial plains,

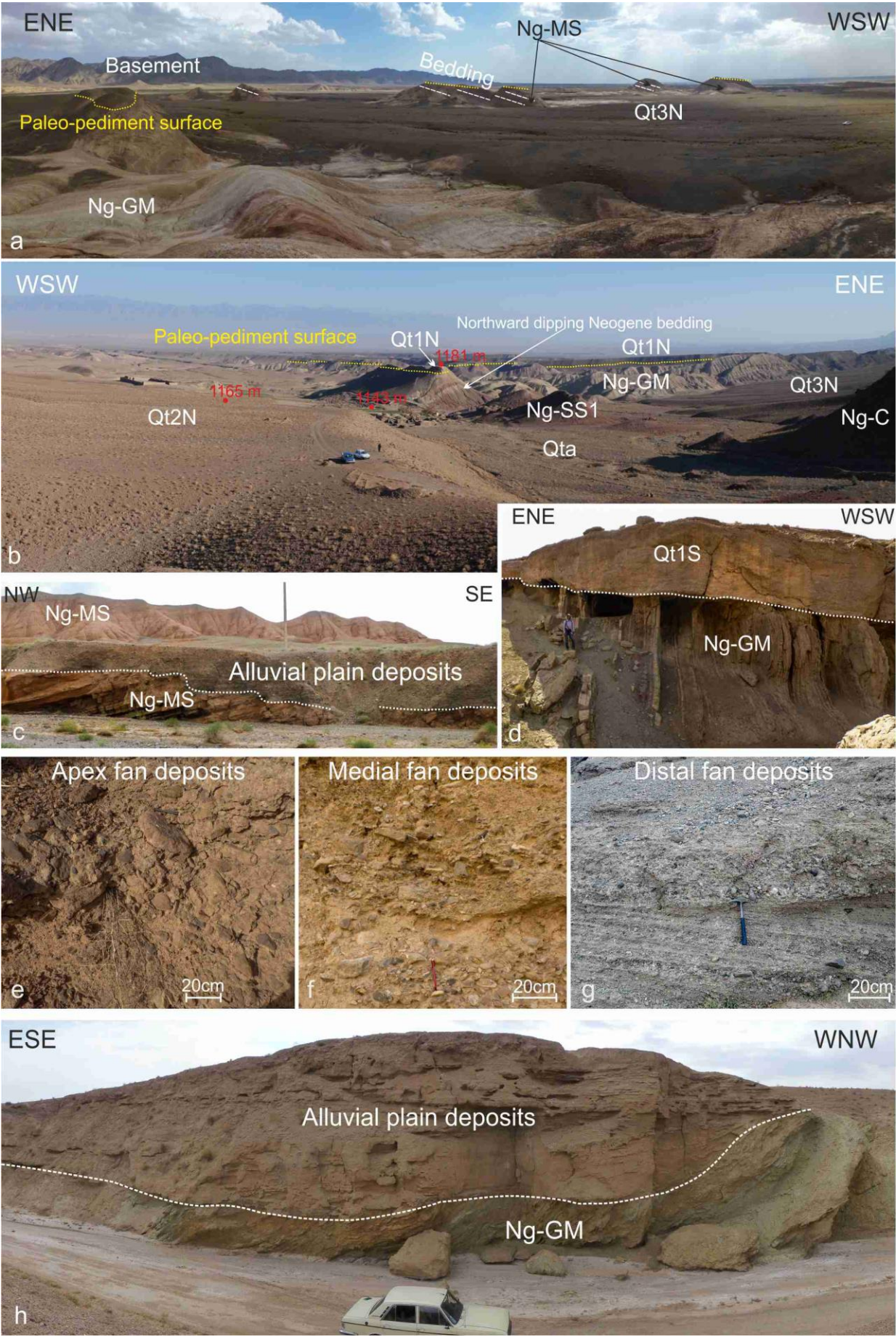


Figure 7.4. Outcrop examples of the Quaternary alluvial fan and fluvial deposits. Panoramic views of the alluvial fan deposits and their stratigraphic relations with the Neogene deposits in the geomorphological Zone 1 (see text), viewed from the northern alluvial plain towards the fault system (a) and from the fault system (the CFS) towards the alluvial plain (b). (c) Example of the Neogene-Quaternary angular unconformity tens of kilometers north of the fault system. (d) Example of the Neogene-Quaternary angular unconformity to the south of the KFF. Example of Quaternary fan deposits characteristics from the fan apex region (e) to the fan medial (f) and distal region (g). (h) Outcrop example of the alluvial plain deposits in the geomorphological Zone 3. See figure A1 in appendix-A for locations.

that are currently drained by the two above mentioned competing ephemeral fluvial systems flowing to the west-southwest and east-southeast respectively (Fig.7.3a and b).

In Zone 2 three other generation of alluvial fans are documented (Qt1S, Qt2S and Qt3S, Fig.7.2 and 7.3). The three fan generations make up a wide bajada, which generally drains southward into the southern alluvial-to-salt lake alluvial plain. Qt1S and Qt2S deposits are restricted to proximal regions of the bajada, close to the southern mountain front. They represent remnants of alluvial fan apexes which are now suspended tens of meters above the present thalweg. Qt3S alluvial fans make up most of the southern bajada and extend from the mountain front to the southern plain (Fig. 7.2c and 7.3c). Collectively the three fan generations of Zone 2 exhibit a stacked architecture.

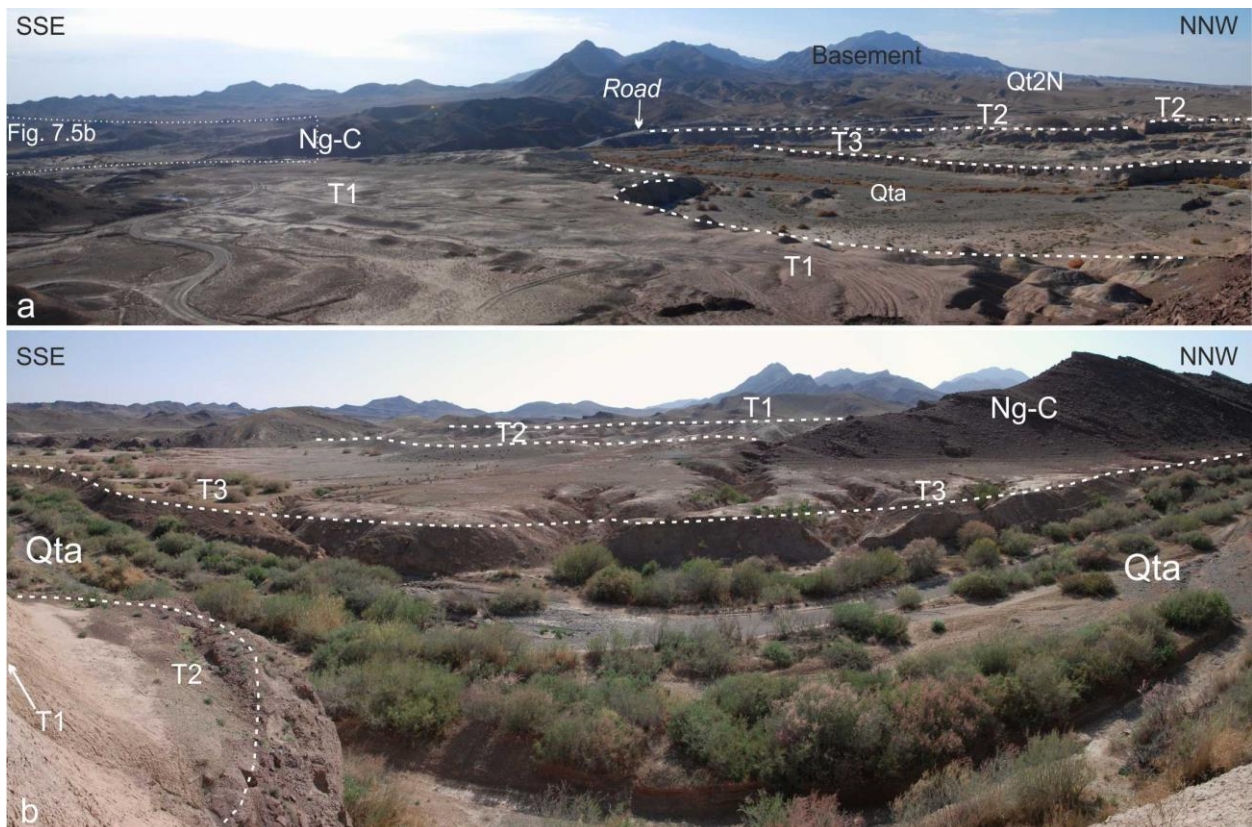


Figure 7.5. Panoramic view of the Quaternary fluvial terraces and their relation with the northern alluvial fan deposits (a). (b) Detail of the geometric relationship between the three generations of fluvial terraces. See figure A1 in appendix-A for locations.

Zone 3 is characterized by three generations of terraced fluvial deposits, which extend throughout the zone. These alluvial plain deposits were sourced both from the KFF topographically prominent linear ridge and the Doruneh fault area (to the north) as attested by the presence of mixed clasts population of KFF basement rocks and volcanoclastic, quartz rich from the Doruneh fault area. An example of the three generations of fluvial terraces comes from the central southward draining river (Fig. 7.2d 7.3d), where the terraces (T1, T2, T3) are hanging at different elevation above the active alluvial plain (Fig. 7.5). The oldest terrace (T1), lies directly onto the pediment sculpted in the Neogene bedrock, while the T2 and T3 are mainly entrenched within the T1 deposits. The alluvial terraces T1, T2, and T3, lie at 18, 5 and 3 m respectively above the active alluvial plain. Furthermore, to the northwest the T2 and Qt2N deposits seem to interfinger and their top surfaces to be morphologically correlated, plausibly indicating their synchronous generation (Fig. 7.5a).

In order to constrain better the ages and the relations among the different generations of Quaternary deposits, they have been sampled and dated through OSL analyses, whose results will be presented in the following chapters.

8 STRUCTURAL DATA AND FAULT KINEMATICS

Structural investigations were focused on the three main, left –stepping KFF fault strands (WFS, CFS and EFS), and their associated fault damage zones which cut through the Neogene sedimentary cover often involving the overlying Quaternary deposits (Fig 6.1). Results are presented in the structural map in Figure 6.1 as derives from both Author's revised mapping and existing literature data. In particular, the map includes the basement faults as derived from Behroozi et al. (1987) and Ghomashi et al. (2001). These basement fault generally consist of broadly NE-SW oriented reverse faults and their extent is limited by the KFF major fault strands.

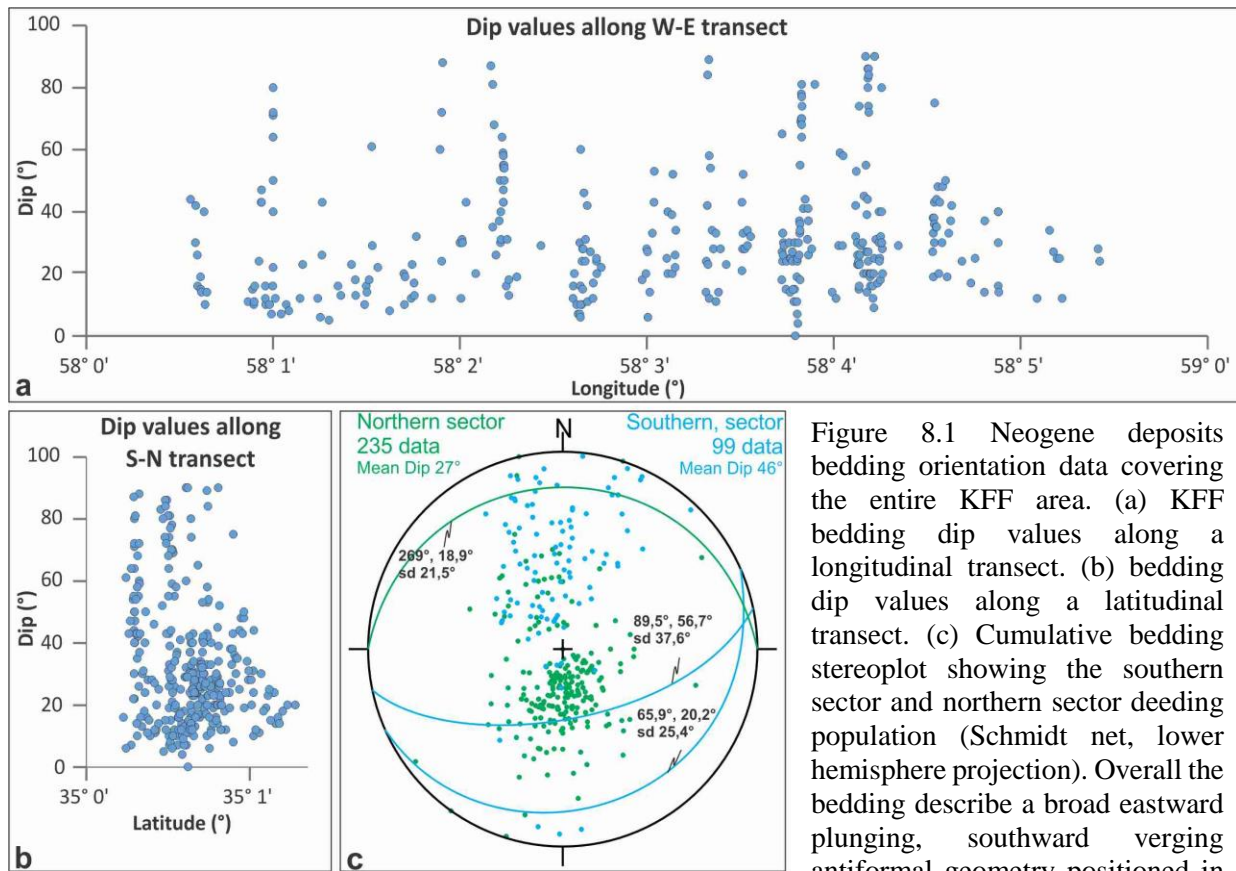


Figure 8.1 Neogene deposits bedding orientation data covering the entire KFF area. (a) KFF bedding dip values along a longitudinal transect. (b) bedding dip values along a latitudinal transect. (c) Cumulative bedding stereoplot showing the southern sector and northern sector bedding population (Schmidt net, lower hemisphere projection). Overall the bedding describe a broad eastward plunging, southward verging antiformal geometry positioned in correspondence of the KFF system

The Neogene deposits show bedding attitudes steeply dipping away (mean 46°) to the south and less (mean 27°) to the north, and striking sub-parallel to the axis of linear ridge (Fig. 8.1). Collectively they are arranged to form a broad eastward plunging, southward verging antiformal geometry positioned in correspondence of the KFF system. Moreover, the bedding dip angle of the Neogene deposits generally decreases away from the boundary fault system (Fig. 6.1). Such regional architecture, picked-out by the Neogene strata, is clearly identifiable from the western sector (e.g. along cross-section A-B, Fig. 6.1) to the central part of the EFS (e.g. cross-section G-H and I-J, Fig. 6.1). From there onwards (eastward) only the monocline northern limb is clearly exposed to the north of the EFS (cross-section K-L, Fig. 6.1)

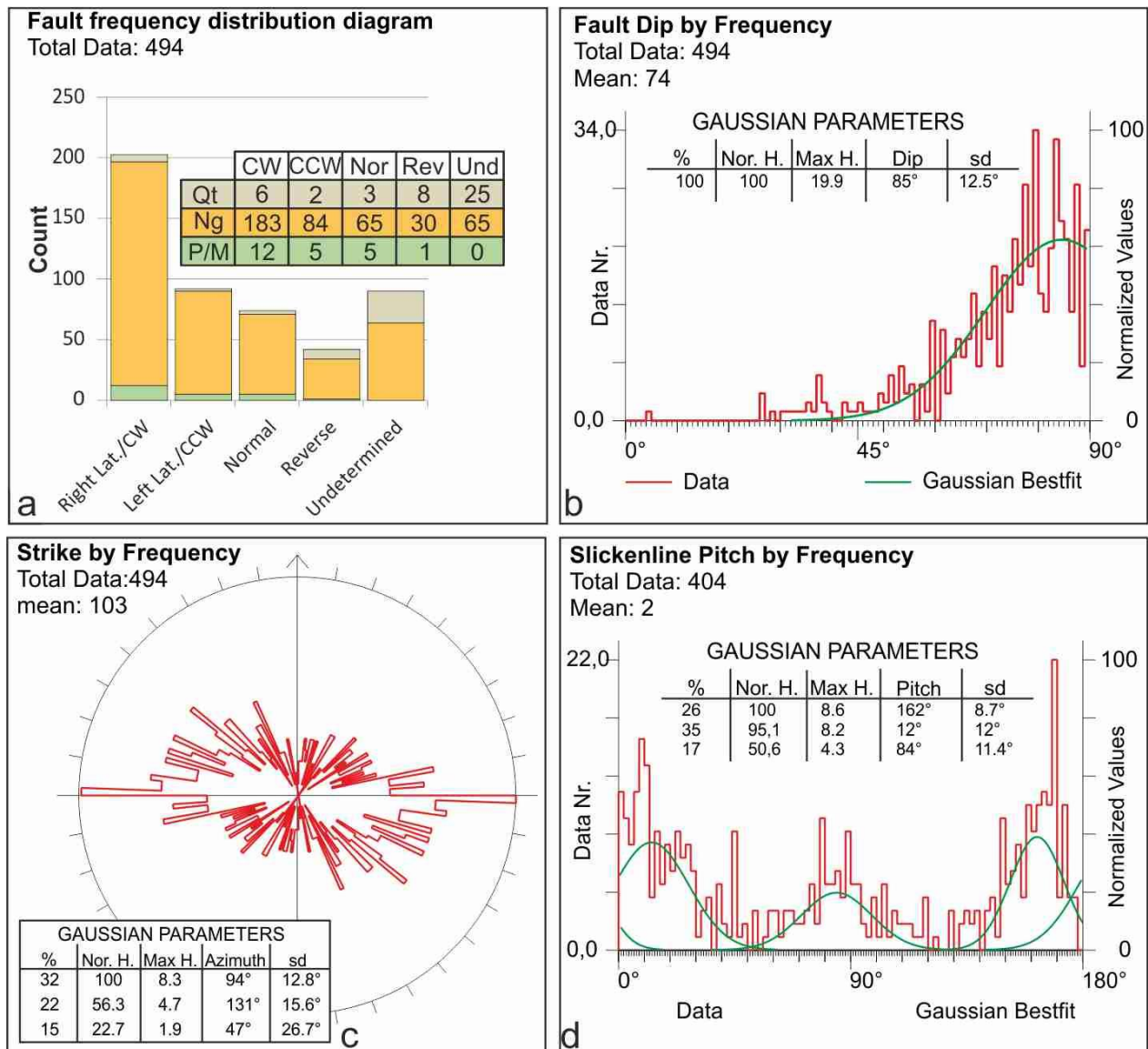


Figure 8.2 (a) Frequency histogram of cumulative fault types and kinematics as collected in the different lithological units exposed in the study area (b) Polymodal Gaussian distribution statistics of the fault dips. (c) Rose diagram and polymodal Gaussian distribution statistics of the fault strikes (d) Polymodal Gaussian distribution statistics of the slickenline pitch values. Data processing through the Daisy3 software. The histogram of the original data distribution and the Gaussian best-fit curves are shown. In the table: %, percent of data fitted by each Gaussian curve; Nor H., normalized height of the Gaussian peak with respect to the highest peak; Max H., maximum height of the Gaussian peak; s.d., standard deviation.

A number of 494 striated fault surfaces (over a total number of 1040 structural data; see in appendix-B for complete dataset) occurring in the basement, the Neogene and Quaternary deposits were measured in the field (Fig. 8.2a). Fault kinematics was obtained based on classical criteria for brittle shear zones, such as fault offset, growth fibers, and Riedel shears e.g. (Doblas, 1998; Petit, 1987). Fault population analysis was performed through the software Daisy 3 (Salvini, 2004; <http://host.uniroma3.it/progetti/fralab>). The cumulative fault data set shows high-to sub-vertical dips,

with a maximum frequency distribution at 85° and a mean dip value of 74° (Fig. 8.2b). The maximum frequency distribution of fault strikes shows a maximum at $N94^\circ$, with subordinate $N131^\circ$ and $N47^\circ$ (Fig. 8.2c). The frequency distribution of the pitch angle of the measured slickenlines attests for dominant strike-slip kinematics with maxima at 12° and 162° and subordinate dip-slip population (84°). In particular, the analysis shows that $\sim 72\%$ of the slickenline pitches are sub-horizontal (0° to 45° and 135° to 180°) and less than 28% exhibit sub-vertical (45° to 135°) pitches. The mean pitch values is 2° (Fig. 8.2d) that further attests for the dominant strike-slip tectonics in the study area.

In the following, a systematic description of the fault system architecture and kinematics is provided for each fault strand. The location of field pictures is reported in Figure 6.1

8.1 Western fault strand

The WFS runs W-E for more than 35 Km on the southern side of the KFF (Fig.6.1), with distinct along-strike fault zone architecture when moving eastward from the western fault tip. The western fault tip is defined by a broad (wavelength of ca. 5 km), E-W striking, south-verging antiformal fold that affect the basal Ng-C deposits with a monocline geometry. The fold axial trace maps out ca. 20 km and separates shallow dipping ($< 20^\circ$) strata to the north from steeply dipping ($> 40^\circ$) strata to the south, with an eastward periclinal geometry (Fig. 6.1). The fault surfaces rarely cuts through the monocline and it is therefore considered as a blind fault (Fig. 6.1). The few measured fault surfaces define two main sets of subvertical planes, striking E-W and NW-SE, both showing dominant right-lateral strike-slip kinematics (Fig. 8.3a).

Moving eastward along the WFS trace, the southern limb of the monocline becomes increasingly steeper to overturned and is dissected by numerous subvertical fault strands (see the geological cross section A-B, Fig.6.1). These fault strand define a ca. 100 m. thick fault damage zone, made of verticalised, E-W striking fractured rock panels along which the abrupt contact between the basal Neogene conglomerates (Ng-C) and the gypsiferous marls (Ng-GM) occur. (Fig. 8.3b). The fault slip is characterised by dextral and reverse kinematics, attesting for partitioning between strike-slip and contractional deformation during a dominant transpressional regime of shearing (Stereoplot, Fig. 8.3).

Further to the east the WFS bends NE to form a major restraining bend seen to affect the Neogene deposits, with positive flower structures in cross-section and a contractional strike-slip duplex (Woodcock and Fischer, 1986) in map view (see Fig.6.1 and geological cross sections E-F and E2-F2 in Fig. 6.1). The duplex bounding faults are developed within the Neogene deposits; however faults are seen to affect also the Quaternary alluvial deposits (see below). The contractional jog is associated with development of a tight NE-SW trending syncline, mapping out subparallel to the main fault trace and affecting the Ng-C and the unconformable Ng-GM and Ng-MS deposits. The

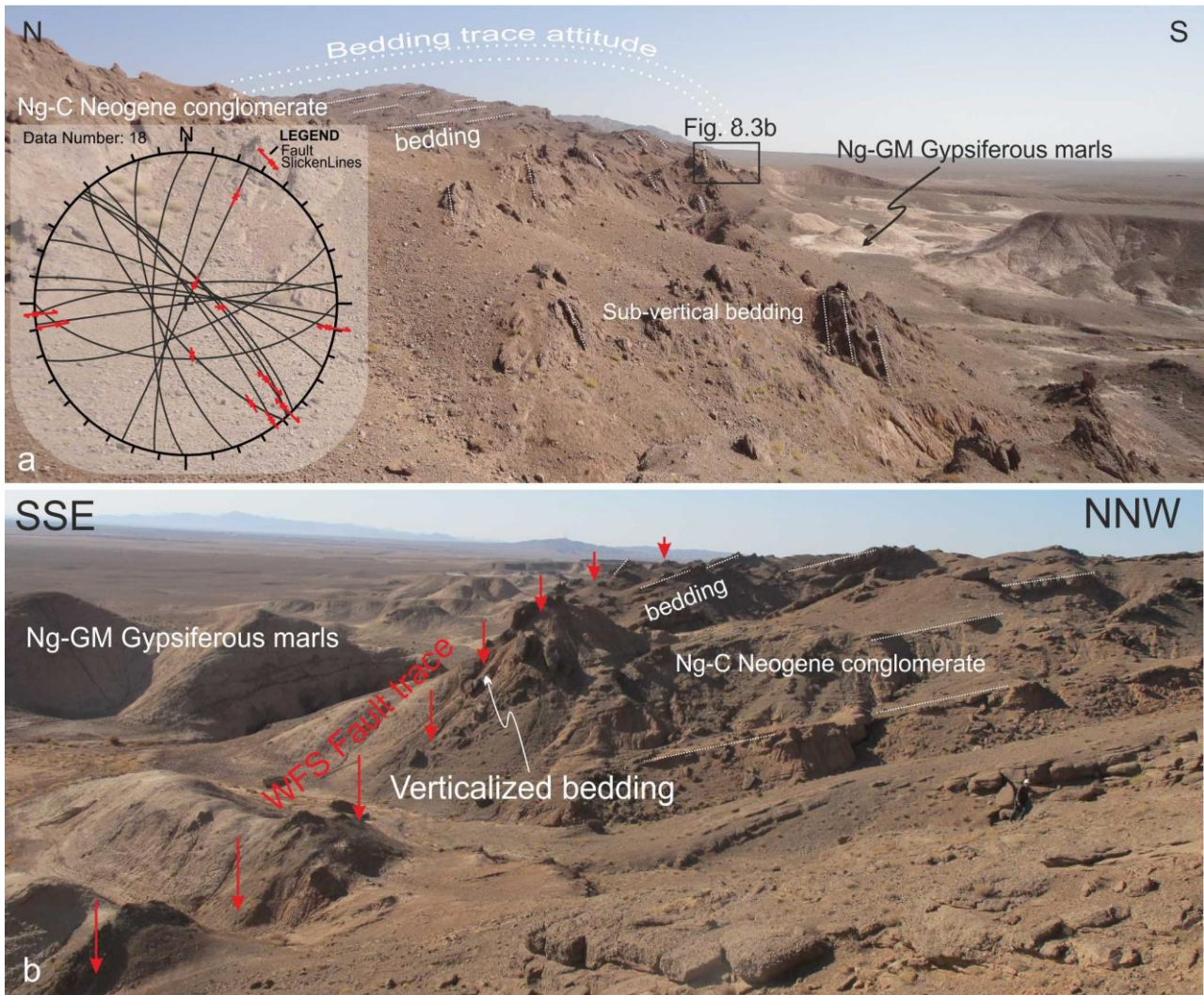


Figure 8.3. The western portion of the WFS. (a) Panoramic view (looking eastward), showing the core of the antiformal structure defined by arrangement of the Neogene conglomerates (Ng-C). Note steepening of the southward limb approaching the WFS trace. Faulting is accomplished by distributed NW-SE and E-W striking fault segments. The stereonet shows the collected fault data (Schmidt net, lower hemisphere projection). (b) The fault zone is defined by verticalized panels of cataclastic conglomerates (Ng-C) in tectonic contact with the gypsiferous marls (Ng-GM). The stereonet details the collected fault data set (Schmidt net, lower hemisphere projection). See figure A1 in appendix-A for locations.

fold profile shows a moderately north dipping southeastern flank with a steep to overturned northwestern flank, with a periclinal doubly plunging geometry (Fig. 6.1). The northwestern fold limb is dissected by major, NE striking sub-vertical fault strands that cause the tectonic repetitions among the Neogene units. The duplex-bounding faults are subvertical, with major fault slip localization occurring along the northwestern boundary fault zone. This fault zone consists of ca. 300 m thick damage zone, defined by subvertical panels of cataclastic fault rocks and cohesive fault breccias (Fig 8.4a). Dextral kinematics is attested by drag folding of the Neogene strata along the

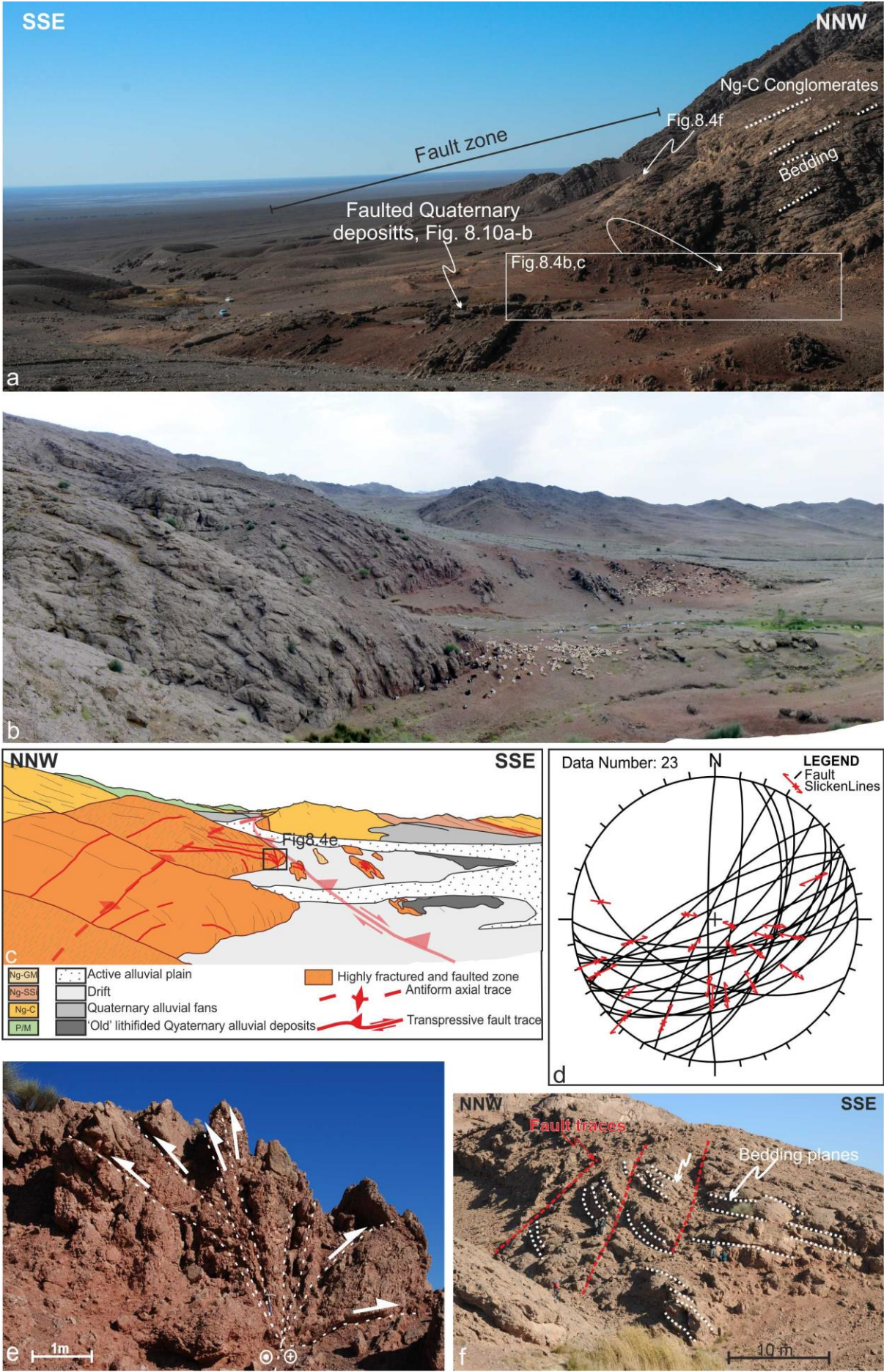


Figure 8.4 The eastward termination of the WFS. (a) Panoramic view (looking westward), showing the sub-vertical, ~500 meter thick damage zone associated with the NE bending of the WFS, which abruptly interrupts the monoclinial attitude of the Ng-C deposits. The fault zone involves the Quaternary alluvial and terraced deposits. (b) Hectometer-scale drag folding and interpretative line drawing (c) in the Ng-C deposits when approaching the trace of the WFS. The fold is E/SE-plunging with an axial trace at an angle to the fault trace. (d) Stereoplot showing the collected fault data (Schmidt net, lower hemisphere projection). Fault slip is dominated by dextral and reverse kinematics. (e) Outcrop-scale positive flower structure (see Fig. Xc for location) developed within the cataclastic core of the fault zone. (f) Meter-thick S-C structures within the Ng-C deposits. See figure A1 in appendix-A for locations.

principal displacement zone, which documents for the dominant right-lateral shear component of the contractional strike-slip duplex (Figs. 8.4b-c). Measured fault surfaces strike NE-SW; offset bedding truncations, Riedel shears and calcite slickenfiber, systematically document either right-lateral oblique strike-slip or reverse kinematics (Fig. 8.4d). At the meso-scale, the slip surfaces converge at depth to resemble a flower structure and dominantly exhibit subhorizontal and dip-slip slickenlines (Fig. 8.4 e). In many instances, the Neogene strata are re-oriented to form structures that resemble meter-sized S-C fabrics; the S-C fabrics are compatible with dextral/reverse shear senses (Fig. 8.4f).

Based on the field evidence, in cross-section the sub-vertical attitude of the duplex-bounding faults are depicted as upward-divergent fault strands that converge at depth towards the northwestern boundary fault to define a flower structure (see cross section E-F in Fig. 6.1).

8.2 Central fault strand

The CFS runs W-E for about 20 Km on the northern side of the KFF associated linear mountain ridge defining a sharp break in slope between the topographically elevated basement rock sequences and the Neogene-Quaternary sedimentary covers (Fig.6.1). Several associated minor faults (reported on the geological map on figure 6.1 as a single fault) run sub-parallel and eventually join up to the CFS.

In the central part of the CFS, basement-cover relations are well preserved, with fault zone localization occurring within the basement units and only marginally within the basal Neogene conglomeratic (Ng-C) units (Fig. 8.5a; see also the geological cross sections A-B and C-D in Fig. 6.1). In the field, they generally appear as 50-200 m wide deformation zones associated with verticalised rock panels affected by diffuse brittle deformation. The shear deformation is principally accommodated within the weaker basement shale and silt beds, while the stronger sandstone and siltstones remain partially coherent to define fault lithons (Fig. 8.5a and b). The slip zones are typically delocalized, defined by meter to tens of meter thick bands of cataclastic material. As in the WFS, well-developed fault surfaces with striations and kinematic indicators are rare but not uncommon, and localized slip zones and fault gouges are extremely rare. Brittle deformation in the

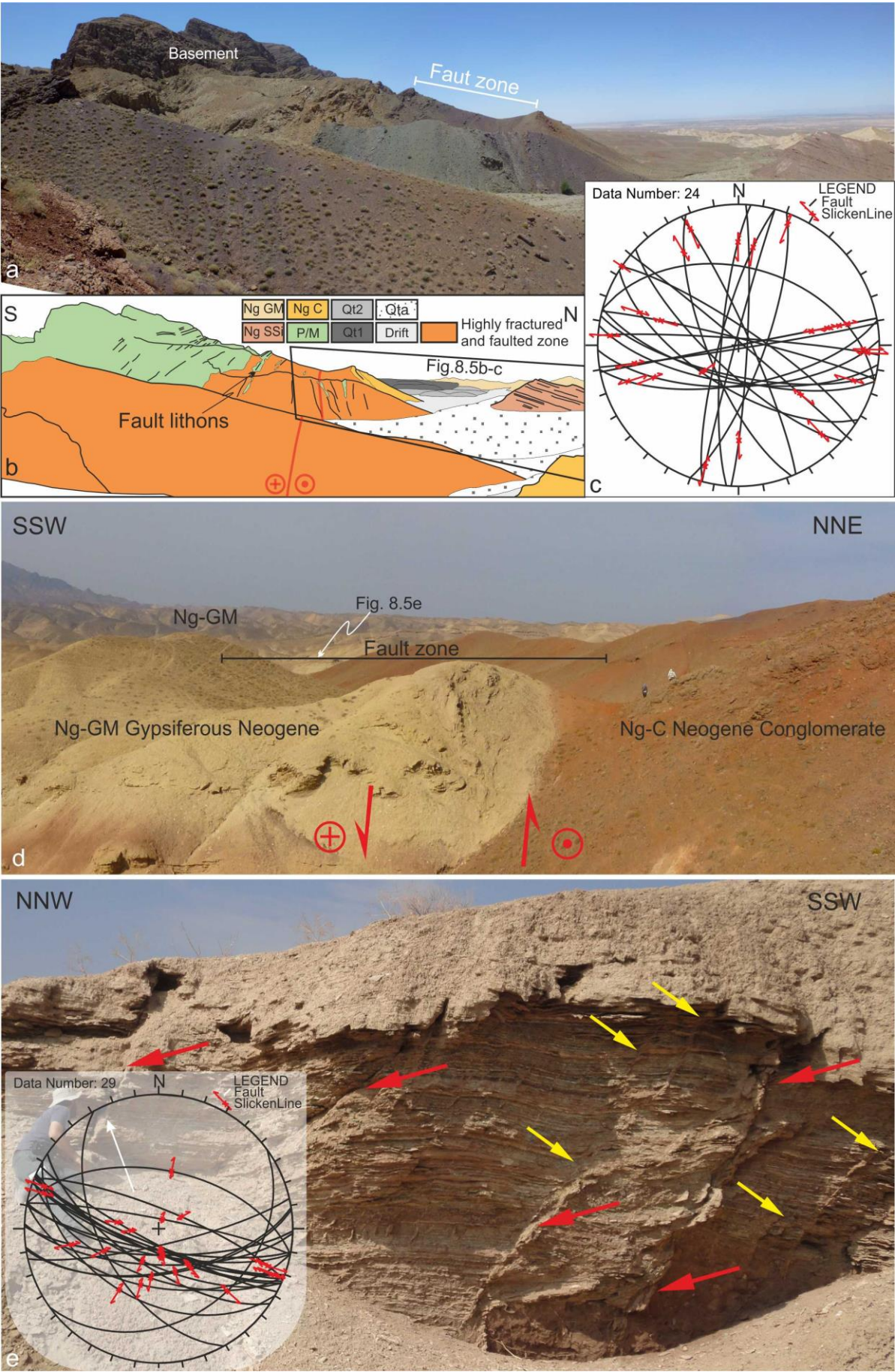


Figure 8.5. (a) The basement-Neogene fault contact along the CFS (looking westward). (b) Interpretative line drawing of Figure 8.5a, showing the fault zone architecture and fault zone localisation along the verticalised weaker basement shale units. (c) The stereoplot details the collected fault data set (Schmidt net, lower hemisphere projection). (d) Panoramic view (looking northwest) of a decameter-thick fault damage zone associated with a NW-SE striking transtensional splay of the CFS. The fault zone puts into contact the basal Ng-C with the Ng-GM deposits. (e) Mesoscale NW-SE striking fault systems in the Ng-GM deposits along the northwestern prosecution of the fault shown in Figure Bd. Note the syn-sedimentary character of faulting: the faults (red arrow) die out upwards into the sediments (yellow arrow), which are progressively sealed. The stereoplot details the collected fault data set (Schmidt net, lower hemisphere projection). See figure A1 in appendix-A for locations.

Ng-C deposits is characterized by a dominant set of sub-vertical E-W striking cataclastic zones, generally with less of 1 m of thickness. Striated fault surfaces provide sub-horizontal pitch values and the fault kinematics is systematically right-lateral. Subsidiary, steeply-dipping NW-SE dextral and NNE-SSW left-lateral faults are also reported (see the stereoplot in Fig. 8.5c).

Continuing to the east, the CFS bends southward and branches out into four main NW-SE oriented subvertical fault segments arranged to form a trailing extensional imbricate fan (Woodcock and Fischer, 1986), also referred as to “horsetail-type” transtensive termination (Granier, 1985) (Fig. 6.1). The dominant strike-slip motion along the CFS passes into a lozenge-shaped extensional/transtensional basins at its tip, consistent with dextral offset, that are filled up by the Ng-GM deposits (Fig. 6.1). The NW-SE striking basin sidewall faults form up to 100 m thick, subvertical damage zones made up of the coalescence of slip surfaces and anastomosing lenses of cataclastic cohesive fault rocks and decameter-thick fault cores (Fig. 8.5d). Striated fault surfaces either show dip-slip normal or oblique-to-strike-slip dextral kinematics, attesting for the dominant transtensional regime of faulting. Within the Ng-GM deposits, faulting is accommodated by diffuse zones of deformation, hundreds of meters wide, characterized by evenly spaced (meters apart) sets of NW-SE striking faults that accommodate oblique-slip and normal dip-slip displacements (Fig. 8.5e). The fault surfaces are often decorated by cm-thick fibrous shear veins that attest for polyphase slip/opening. It is worth nothing that many of these mesoscale faults show vertically decreasing offsets and some of them vertically die out in the sediment, clearly indicating syn-depositional faulting (Fig. 8.5e).

8.3 Eastern fault strand

The EFS is a ca. 40 km long, sub-vertical fault zone, made of the coalescence of several synthetic faults to form a major curvilinear slip zone and prominent range front, striking from NW-SE to E-W at its eastward termination (Fig. 6.1). The fault zone shows a decameter-to-hectometer thick damage zone that comprises numerous mesoscale fault segments cutting through the pre-Neogene basement units that are tectonically juxtaposed with the Ng-GM sequences. In particular, the NW segment abruptly cuts an E-W striking Neogene basin boundary fault strand. It continues

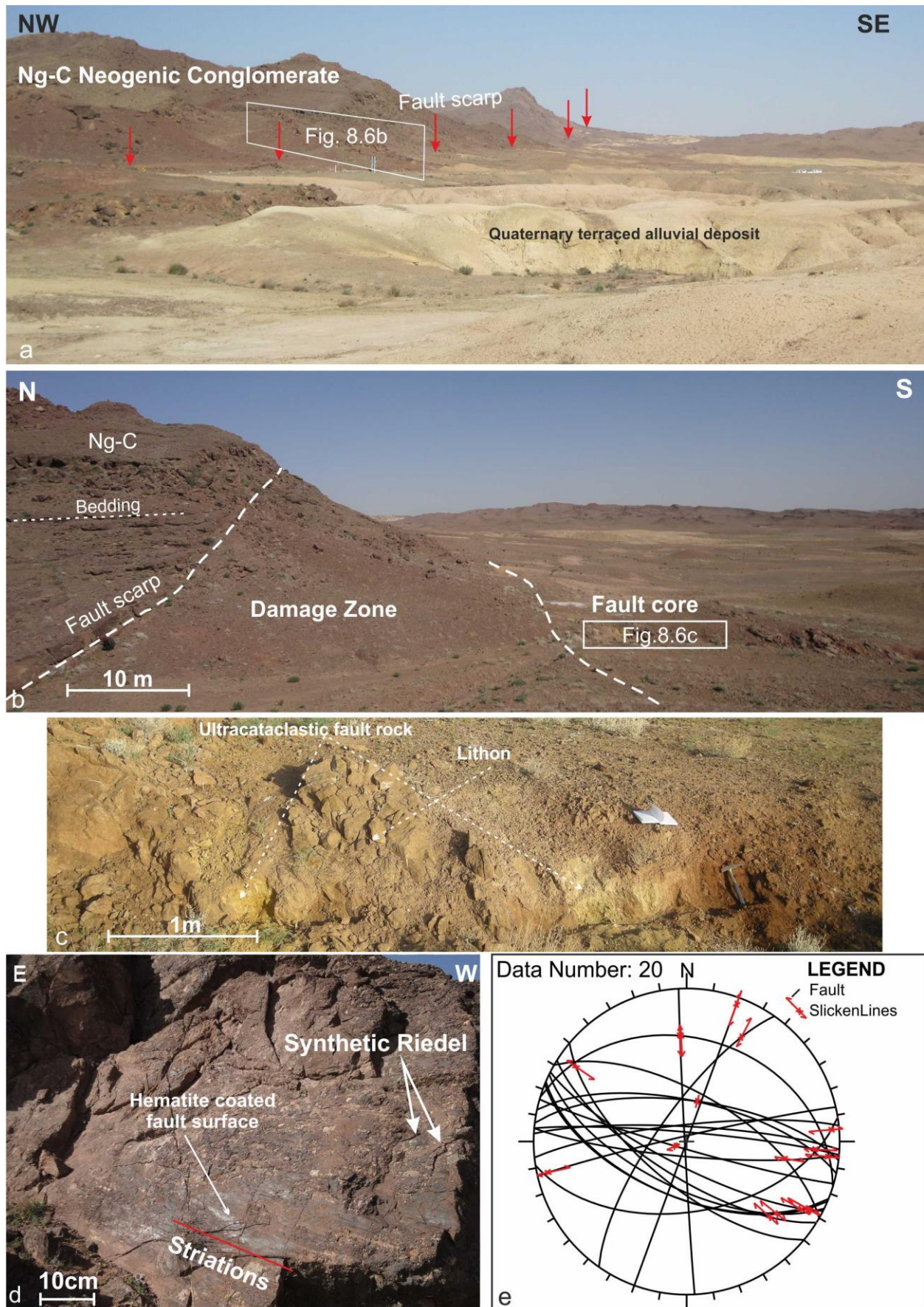


Figure 8.6. (a) Panoramic view (looking north-eastward) of the prominent break in slope that defines the trace of the of the EFS, bounding Neogene and Quaternary deposits. (b) Structural architecture of the fault

zone across the EFS, exhibiting decametre-thick, sub-vertical damage zone and fault core. (c) Outcrop-scale characteristics of the fault core, showing bands of ultracataclastic fault rocks (fault gouge) and sheared lithons. Lateral colour variations are due to secondary fault rock alteration. (d) Example of a polished, hematite-coated fault surface, exhibiting prominent sub-horizontal striations. The kinematic indicators as provided by synthetic Riedel shears, lunate fractures and abrasion steps attest for right-lateral kinematics. (e) Stereoplot showing the collected fault data set (Schmidt net, lower hemisphere projection). See figure A1 in appendix-A for locations.

eastward bending to E-W direction and cutting through a relatively leveled area, showing a prominent linear fault scarp in the Neogene deposits that can be traced continuously eastward for more than 20 km in the alluvial Quaternary plain (Fig. 8.6a). The fault zone bending to the E-W direction corresponds to a widening of the fault damage zone, reaching thickness in excess of 400 m and prominent up-to-tens of meter thick fault cores (Fig. 8.6b). The fault cores consist of ultraclastic bands and fault gouges, separated by brecciated fault rocks and sheared lithons (Fig. 8.6c). Their minimum thickness observed in the field ranges from 20 to 100 meters. Major fault surfaces are typically sub-vertical, NW-SE and E-W striking and exhibit sub-horizontal slickenlines (pitch: 5-15°). Typically, most of the striated fault surfaces are decorated by hematite coatings. Fault kinematics as deduced by synthetic Riedel shear planes, together with calcite slickenfibers, grain grooves and lunate fractures systematically point to dominant right-lateral slip (Figs. 8.6 d and e).

In the Neogene Ng-GM deposits, transition to the main displacement zone is typified by increasing fracture density and by trains of upright open to chevron folds, trending ENE-WSW to WNW-ESE. The fold shapes are getting close to tight when entering the fault damage zone with their axial planes getting almost always parallel to the main fault strikes. There, cataclastic bands cut across and transpose the folds within the main slip zones (Fig. 8.7).

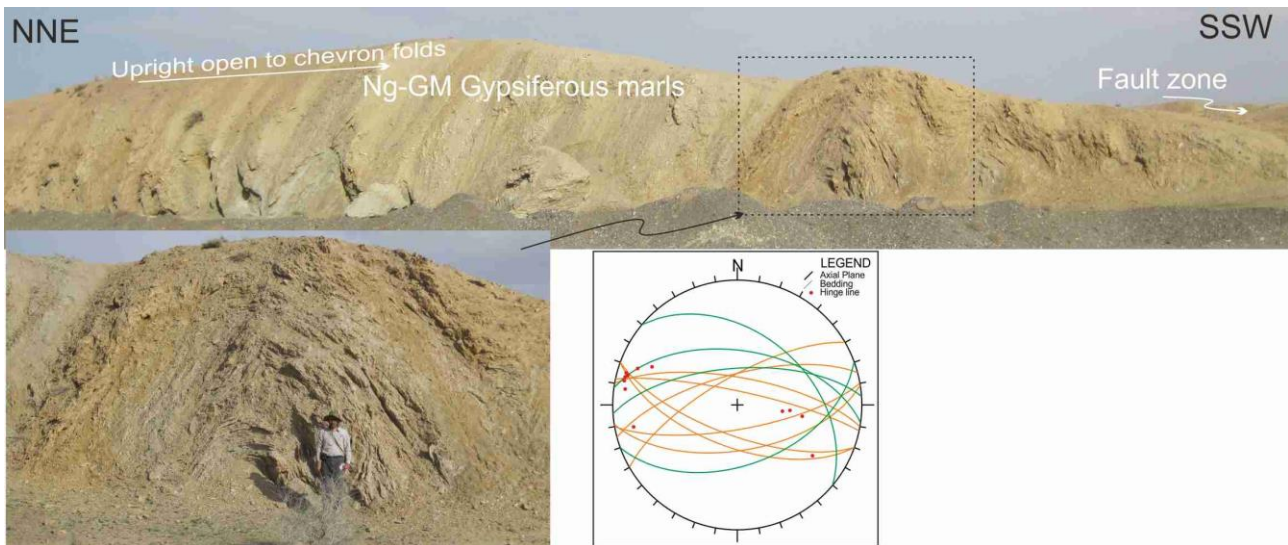


Figure 8.7 Panoramic view (looking eastward) showing upright, mesoscopic fold trains in Ng-GM deposits, ~1 km northward of the main fault trace. The stereoplot (Schmidt net, lower hemisphere projection) details the bedding and fold attitudes. See figure A1 in appendix-A for locations.

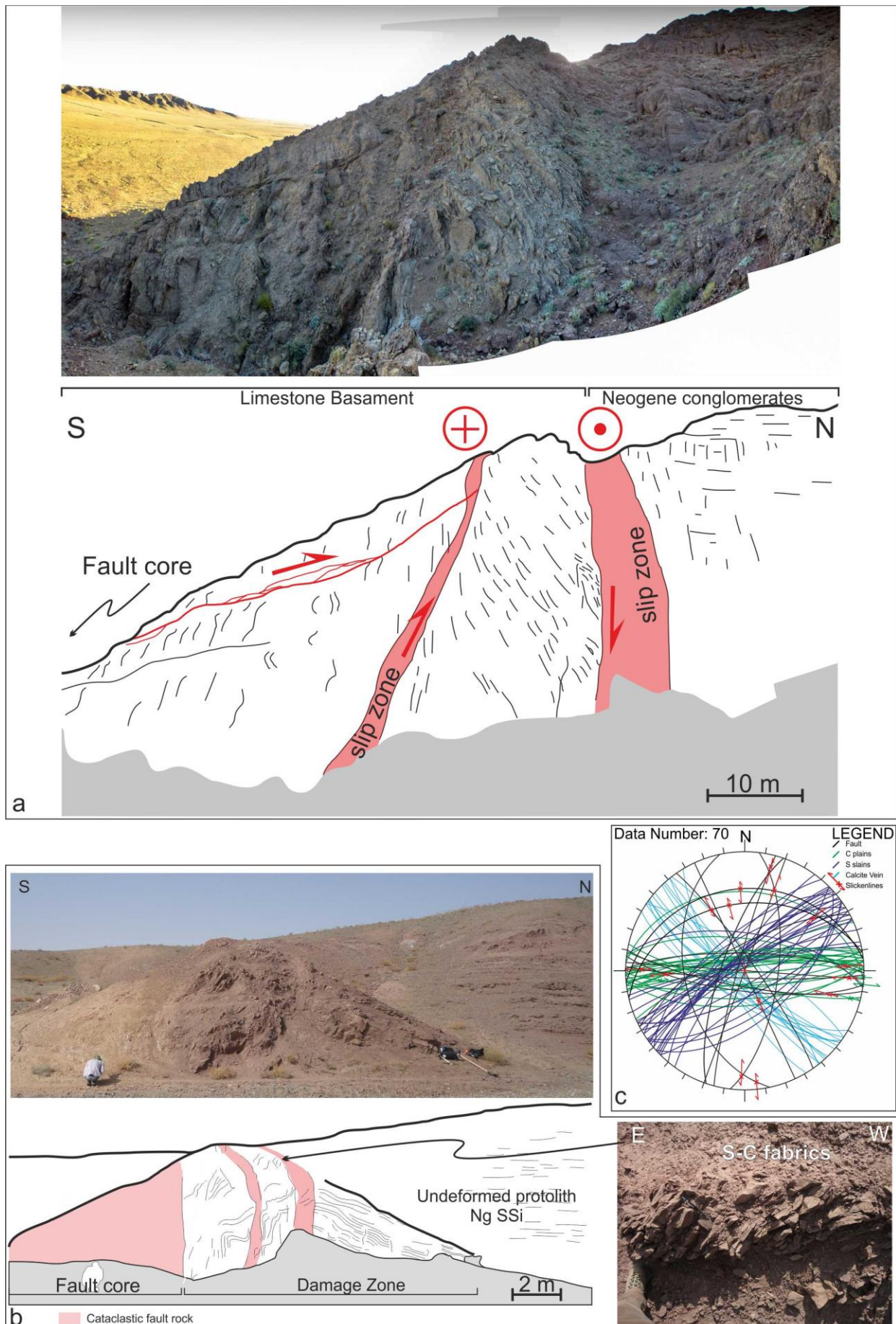


Figure E - Field examples of S-C fabric development along the main trace of the EFS. (a) Outcrop-scale, S-C tectonites developed along the main trace of the EFS bounding the basement-Neogene (Ng-C) contact.

Note the occurrence of meter-thick, E-W striking sub-vertical ultracataclastic right-lateral slip zones that control the fault zone architecture and bound the main fault rock types. (b) S-C tectonites developed within the Ng-SSi deposits. The fault zone transition from the undeformed protolith to the fault core is defined by decameter-thick damage zone, with external folding and an inner portion characterised by anastomosing slip zones and foliated fault rocks. The inset shows a detail of the S-C fabrics within the damage zone (c) Stereoplot (Schmidt net, lower hemisphere projection) showing the angular relationships between the S-C fabrics, the vein array and the main strike-slip fault surfaces. See figure A1 in appendix-A for locations.

Significantly, spectacular decameter-scale, S-C fabrics are observed along coherent tracts of the principal displacement zone of the EFS and continue over significant distances (> 300 m), both along the basement-Neogene contacts and within the Neogene deposits (Figs. 8.8a-b). Within these deformation zones, S surfaces are defined by dissolution seams and strike NW-SE, the C-surfaces strike roughly E-W to ENE-SSW. Lineations are provided by slickenlines on the C-surfaces that systematically are sub-horizontal. The S-C fabrics are associated with NW-SE striking, steeply dipping extensional fractures and calcite- and gypsum-bearing vein sets. Overall, the geometric relationships among the different structural elements are compatible with right-lateral shearing (Figs. 8.8c). Finally, meter-thick coesive and foliated cataclasites are seldom observed to form the fault rocks along the slip zones developed within the Neogene deposits.

8.4 Minor Faults

Minor fault strands are documented to the north and to the south of the EFS. The main fault systems strike E-W and interfere with shorter WNW-ESE fault strands (Fig. 6.1).

In the northern sector, the major E-W striking faults are characterized by up-to-decameter-thick fault damage zones and, locally, by hematite-coated striated fault surfaces showing dominant right-lateral slip (Figs. 8.9a-b). A population of NW-SE calcite-filled fracture arrays is associated with faulting (Fig. 8.9c). The fault population measured within the fault damage zones show a complex fault pattern dominated by NW-SE and E-W right lateral faults and, subordinate, NNE-SSW sinistral/oblique strike-slip faults (Fig. 8.9d). An apparent horizontal right-lateral offset of more than a thousand meters can be reconstructed across the major fault system (see figure A1 in appendix-A for locations). The NW-SE fault systems consist of extensional and right-lateral oblique-slip faults, which mainly involve the Ng-GM deposits and the Quaternary alluvial covers. In such area, a set of NW-SE gypsum filled fractures is documented (Figs. 8.9e-f).

In the southern area, the E-W striking right-lateral faults are truncated by a trough-going system of NW-SE oriented transtensional faults, splaying out of the EFS (Fig. 6.1).

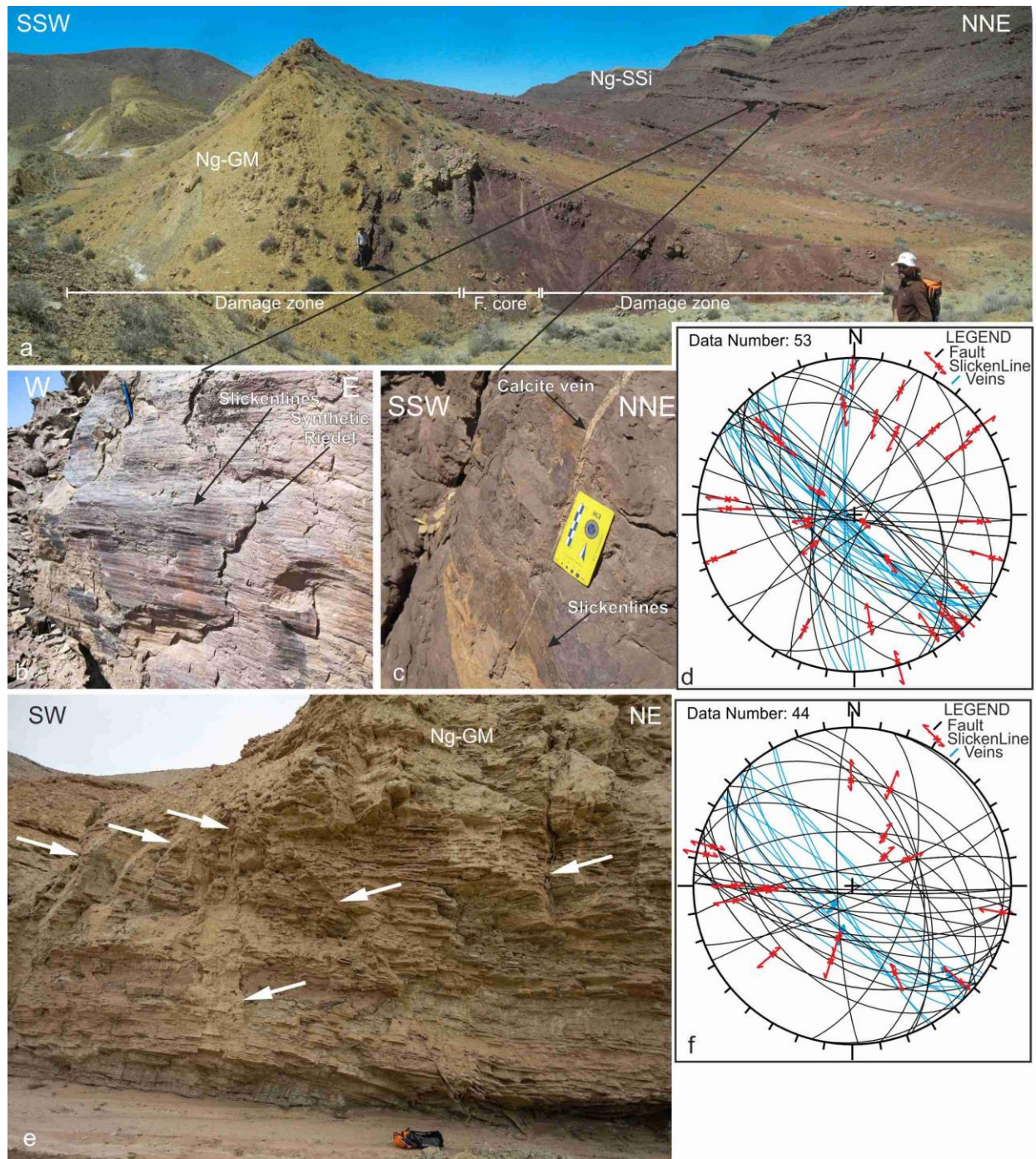


Figure 8.9 - (a) Decametre thick, sub vertical fault zone bounding the tectonic contact between Ng-GM and Ng-SSi. (b) E-W striking hematite-coated fault surface, with sub-horizontal slickenlines. The fault kinematics is right-lateral as defined by synthetic Riedel shears and abrasion steps. (c) NW-SE striking, calcite-filled tension gashes at an angle with the fault surface, compatible with right-lateral shear. (d) Stereoplot (Schmidt net, lower hemisphere projection) of the structural data collected within the fault damage zone. (e) River cut outcrop within Ng-GM showing diffuse NW-SE extensional faults associated with E-W striking right-lateral ones (white arrows). (f) Stereoplot (Schmidt net, lower hemisphere projection) of the structural data collected along the outcrop shown in Figure 8.9 f. See figure A1 in appendix-A for locations.

8.5 Fault zone architecture

The fault zone architecture varies substantially along and across the KFF system. In general, fault zones show distinct structural characteristics when moving eastward along the KFF (Fig. 6.1).

Fault zones developed along the CFS and the WFS have wider (up to 100 m in thickness) damage zones in their central portions, thinning out westward and splaying out eastward into contractional or extensional terminations (Fig. 6.1). In the western sector, slip zones are typically delocalized, zones of verticalised bedding, defined by meter to tens of meter thick bands of relatively more cataclastic non-cohesive and cohesive fault rocks; fault gouges are extremely rare (Fig. 8.4b and 8.5b-c).

The EFS is characterized by shear localised along a major slip zone with well-developed and discrete damage zones and fault cores, exhibiting a higher degree of fault zone localization (mature fault zones). Deformation is more pervasive in the Neogene units and it occurs along a 50 to 150 m thick fault zones consisting of 50 to 140 m thick damage zones and 5 to 50 m fault cores, which cut sharply through the Neogene inclined deposits (Fig. 8.6b). The fault cores consist of bands of ultra-cataclastic cohesive and non-cohesive fault rock, bounded by fault gouge rich slip zones, intercalated with lithons exhibiting sigmoidal fracture patterns. The damage zones typically consist of a coalescence of slip zones and fractures, in between which “S-C type” fabric are easily picked out by the rearranged cataclastic material and reoriented bedding surfaces (Fig. 8.8). Overall there is an observed eastward increase in fault localization within the main fault zones, from broad distributed deformation characterized by cataclastic fault rocks in the west (the WFS and CFS) to localized fault zone characterized by ultracataclastic fault gouges in the east (the EFS).

8.6 Quaternary faulting

The Quaternary successions along the KFF consist of a wide array of alluvial and fluvial deposits, made of conglomerates, gravels and sands exhibiting various degree of consolidation. Evidence of Quaternary faulting (and fracturing) have been documented along the WFS and the EFS (see figure A1 in appendix-A for locations), where faulting is dominated by strike-slip fault zones.

Along the contractional bending that terminates the WFS to the east, right-lateral and oblique-slip faults cut through the Quaternary terraced deposits, juxtaposing and squeezing together lenses of Quaternary and Neogene sediments (Figs. 8.4a and 8.10a-b). Such faults show transpressive right-lateral kinematics, compatible with what found to affect the Neogene deposits (Fig. 8.10c).

Along the EFS, Quaternary faulting is documented both along the principal displacement zone and along subsidiary, synthetic fault strands (Fig. 6.1). Along the prominent E-W striking fault scarp that defines the geomorphic expression of the EFS (Fig. 8.6a), Quaternary deposits are extensively affected by E-W and WNW-ESE oriented set of sub-vertical fracture arrays. Further to the east, along

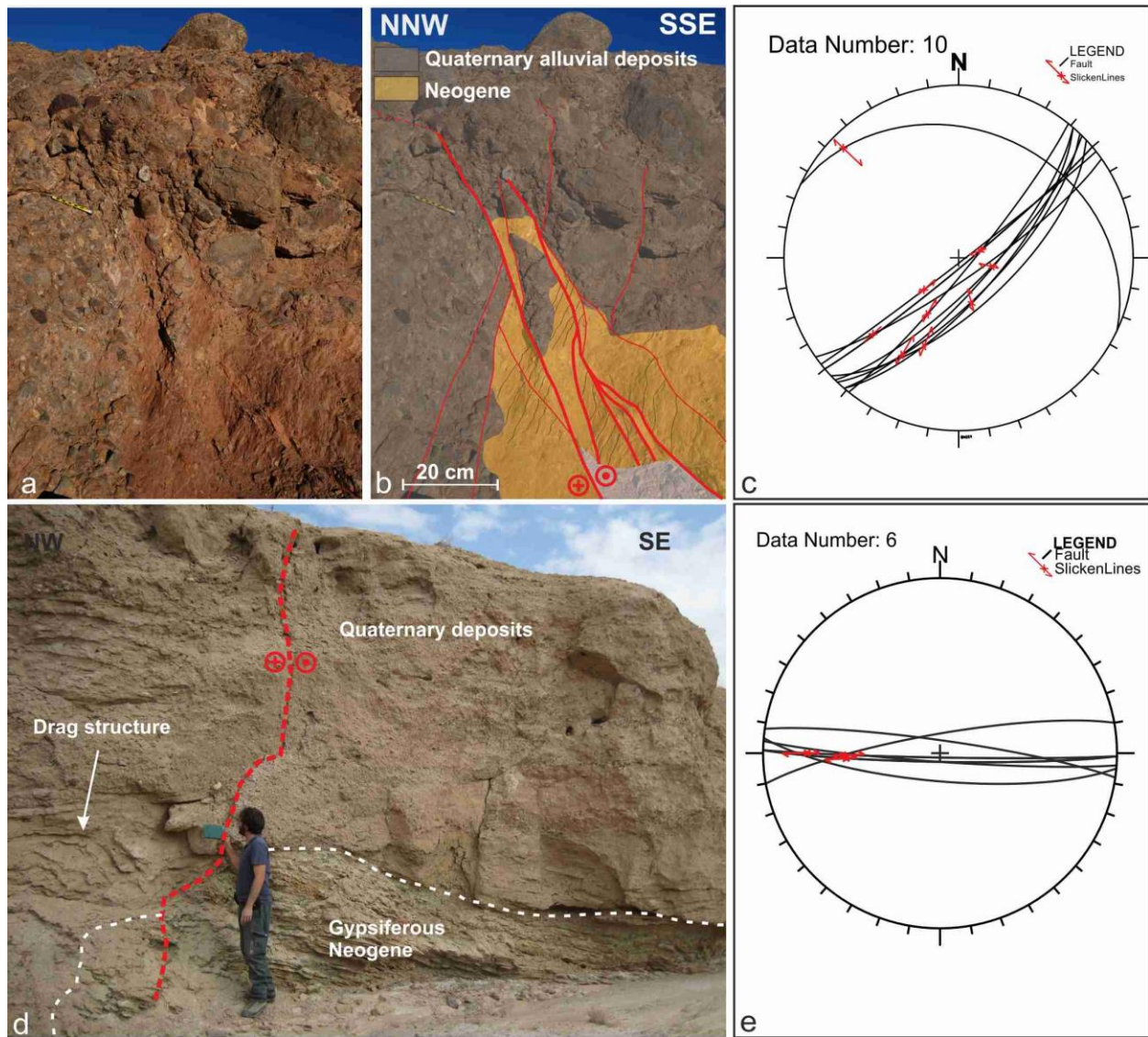


Figure 8.10 Details of the faulted Quaternary alluvial deposits shown in Fig. 8.4a, b and c (a)-(b) Steeply-dipping Fault sets cutting through and involving Neogene and Quaternary deposits. (c) Stereoplot showing the collected fault data (Schmidt net, lower hemisphere projection). The faults strike NE-SW and show dextral and reverse kinematics. (d) River cut exposure showing a subvertical right-lateral fault system cutting across the Neogene-Quaternary contact. (e) The stereoplot (Schmidt net, lower hemisphere projection) details the fault attitude and kinematics. See figure A1 in appendix-A for locations.

the NW-SE fault systems that make up the transtensional trailing imbricate fan of a major fault right-lateral segment to the north of the EFS, extensional and right-lateral oblique-slip faults involve the Ng-GM deposits and the Quaternary alluvial covers (Fig. 6.1). Evidence of Quaternary faulting is documented along an E-W striking, minor fault strand. In this area, E-W oriented sub-vertical faults cut through the gypsiferous Neogene units and into the Quaternary alluvial deposits, displaying calcite slickenlines and small-scale drag fold compatible with right-lateral kinematics (Fig. 8.10 d and e).

9 MORPHOMETRIC ANALYSIS

In the previous chapters, the study has documented that the KFF has been interested by right-lateral strike-slip faulting and related topographic growth and exhumation. Such faulting has mainly interested the Neogene deposits. Nevertheless, faulted Quaternary deposits have been documented both along the major KFF strands and along the associated minor faults. The documented Quaternary faults show the same orientation and kinematics of those cutting the Neogene deposits. Furthermore, the study showed that the Neogene deposits belonging to the Upper Red Formation have been affected by sin-sedimentary faulting and tilting as attested by the progressive angular unconformities found within the Neogene deposits. Further post-sedimentary tilting of the Neogene deposit has also been documented both to the north and south of the KFF. This is well illustrated by the regional erosional pediment that separates the Neogene from the Quaternary (e.g. Figure 7.4).

However, what it is not clear is if sin and/or post sedimentary fault-related uplift also occurred during the Quaternary.

Geomorphic processes on alluvial fans and pediments are considered as proxies for base-level changes and tectonic activity along faulted mountain front (Bull, 1984). In particular, in tectonically active regions the arrangement of alluvial fan generations along a mountain front is the result of the competition among uplift rate, channel downcutting rate and pediment aggradation/degradation rate. Typically, stacked generations of alluvial fans develop with dominant aggradation where uplift is the main base-level process. On the other hand, telescopic alluvial fans develop if the apex of fan deposition shifts down where stream-channel downcutting is the dominant base-level process (Bull, 2007). According to the alluvial fan architecture observed in geomorphological *Zone 1* (telescopic alluvial fans) and *Zone 2* (stacked alluvial fans) it seems that the northern front of the KFF ridge could have experienced more important stream-channel downcutting than the southern one. This is in agreement with the drainage network evolution, and in particular with the evidence that rivers draining the northern plain are considerably entrenched due to headward erosion that likely propagated to the streams draining the northern slope. On the other hand, *Zone 2* corresponds to the steepest limb (dip angle $>40^\circ$) of the broad, E-W striking, asymmetric and south-verging antiformal fold, closer to the localized active deformation zone of the WFS (Fig. 6.1).

Furthermore, even in the case of channel downcutting rate as main base-level process, the eventual ongoing uplift can be testified by progressive tilting of alluvial fan surfaces (Bull, 1977; Giano, 2011)

In order to assess if any fault-related uplift tilted the Quaternary deposits in the KFF system, ideally it is necessary to reconstruct the original bottom and top surfaces of the deposits, that means using them as geomorphic markers. This is not an easy task since in most cases such surfaces are not

exposed and/or have been incised and reshaped by erosion. Nevertheless, geomorphological *Zone 1* with its telescopically arranged alluvial fan deposits provides the best area to asses if the tilting continued during the Quaternary times. In this area three generation of alluvial fans, entrenched into each other are documented.

Table 9.1: Northern Quaternary alluvial fans slope angle analysis

	Sector A			Sector B			Sector C			Sector D		
	m^* (m)	slope (°)	C_{endA+} (m)	m^* (m)	slope (°)	C_{endB+} (m)	m^* (m)	slope (°)	C_{endC+} (m)	m^* (m)	slope (°)	C_{endD+} (m)
<i>"west"</i>												
Qt1_1	0.0677	3.87	1050									
Qt1_2	0.0909	5.19	1087									
Qt1_3	0.0787	4.50	1119									
Qt1_4	0.0891	5.09	1117									
Qt1_5	0.1024	5.85	1141									
Qt1_6	0.0823	4.71	1124	0.0373	2.14	1041						
Qt1_7				0.0412	2.36	1048	0.0341	1.95	977			
mean	0.0852	4.87	1106	0.04	2.25	1045	0.03	1.95	977			
ds	0.0118	0.67	33	0.0028	0.16	5						
Qt2_1	0.0572	3.27	1040	0.0490	2.80	937						
Qt2_2	0.0470	2.69	1050	0.0449	2.57	966						
Qt2_3				0.0288	1.65	1009						
Qt2_4	0.1099	6.27	1069	0.0301	1.73	1006						
Qt2_5	0.0572	3.28	1110	0.0433	2.48	1030						
Qt2_6	0.0482	2.76	1113	0.0345	1.97	1042	0.0244	1.40	991			
Qt2_7				0.0330	1.89	960						
Qt2_8				0.0602	3.45	1011	0.0306	1.75	952	0.0181	1.03	886
Qt2_9							0.0321	1.84	963	0.0226	1.30	922
Qt2_10				0.0367	2.10	1042	0.0310	1.77	980	0.0304	1.74	911
Qt2_11				0.0368	2.11	1046	0.0336	1.92	985			
Qt2_12							0.0254	1.45	983			
Qt2_13				0.0322	1.85	1052	0.0314	1.80	982			
Qt2_14							0.0262	1.50	988	0.0264	1.51	938
Qt2_15				0.0040	0.23	1040	0.0309	1.77	978			
Qt2_16							0.0365	2.09	980			
Qt2_17							0.0251	1.44	989	0.0226	1.30	943
Qt2_18							0.0362	2.07	982			
mean	0.0639	3.65	1076	0.0361	2.07	1012	0.0303	1.73	979	0.0240	1.38	920
ds	0.0261	1.49	34	0.0136	0.78	38	0.0042	0.24	11	0.0046	0.27	23
Qt3_1	0.0680	3.89	1024	0.0437	2.50	937						
Qt3_2	0.0469	2.69	1040	0.0659	3.77	908						
Qt3_3				0.0347	1.99	972	0.0299	1.71	911			
Qt3_4	0.0519	2.97	1047	0.0425	2.43	967						
Qt3_5	0.0583	3.34	1087	0.0403	2.31	999	0.0255	1.46	948			
Qt3_6	0.0599	3.43	1101	0.0324	1.85	1027						
Qt3_7				0.0377	2.16	1031	0.0287	1.64	969	0.0251	1.44	919
Qt3_8							0.0226	1.29	968	0.0265	1.52	913

Qt3_9							0.0246	1.41	973	0.0214	1.22	929
Qt3_10							0.0247	1.42	983	0.0245	1.41	928
Qt3_11							0.0209	1.20	988	0.0191	1.09	949
Qt3_12										0.0175	1.00	952
Qt3_13							0.0177	1.01	989	0.0181	1.03	952
Qt3_14			0.0299	1.71	1041		0.0259	1.49	980			
Qt3_15							0.0232	1.33	990	0.0245	1.41	940
Qt3_16							0.0133	0.76	990	0.0185	1.06	951
Qt3_17							0.0199	1.14	990	0.0161	0.92	958
Qt3_18	0.0412	2.36	1103	0.0350	2.01	1033	0.0222	1.27	986	0.0145	0.83	959
Qt3_19							0.0145	0.83	987	0.0156	0.90	957
mean	0.0544	3.11	1067	0.0402	2.30	991	0.0224	1.28	975	0.0201	1.15	942
ds	0.0078	0.55	34	0.0113	0.61	47	0.0048	0.28	22	0.0041	0.24	16
"east"												
Qt1_1				0.0899	5.14	1189						
Qt1_2							0.0513	2.94	1069			
Qt1_3							0.0763	4.36	1048			
Qt1_4							0.0407	2.33	1077			
Qt1_5							0.0573	3.28	1071			
Qt1_6				0.0888	5.07	1196	0.0742	4.24	1041			
Qt1_7							0.0518	2.96	1050			
Qt1_8							0.0787	4.50	1027			
mean				0.0893	5.10	1193	0.0614	3.52	1055			
ds				0.0008	0.04	5	0.0149	0.85	18			
Qt2_1				0.0845	4.83	1185	0.0593	3.39	1065			
Qt2_2							0.0460	2.64	1065	0.0313	1.80	998
Qt2_3							0.0543	3.11	1080	0.0396	2.27	999
Qt2_4							0.0680	3.89	1036			
Qt2_5				0.0727	4.16	1166						
Qt2_6				0.1071	6.12	1174						
Qt2_7							0.0684	3.91	1047			
Qt2_8							0.0543	3.11	1056			
mean				0.0881	2.62	1175	0.0584	1.14	1058	0.0355	0.33	999
ds				0.0175	1.00	10	0.0087	0.50	15	0.0058	0.33	1
Qt3_1							0.0424	2.43	1067	0.0318	1.82	1003
Qt3_2							0.0582	3.33	1057			
Qt3_3							0.0351	2.01	1078			
Qt3_4							0.0292	1.67	1071	0.0283	1.62	1011
Qt3_5							0.0465	2.66	1072			
Qt3_6							0.0505	2.89	1074	0.0316	1.81	1007
Qt3_7							0.0351	2.01	1087	0.0397	2.27	1007
Qt3_8							0.0337	1.93	1084	0.0362	2.07	1011
Qt3_9							0.0467	2.68	1082	0.0352	2.02	1006
Qt3_10			0.0535	3.06	1176		0.0514	2.94	1067	0.0261	1.49	1008
Qt3_11							0.0296	1.70	1059	0.0219	1.26	1016
mean			0.0535	3.06	1176		0.0417	0.54	1073	0.0313	0.27	1009
ds							0.0097	0.56	10	0.0058	0.33	4

* m is the elevation/N-S distance ratio, from which the angle is calculated

+ C_{endA} is the elevation at the end of each sector (the northern end)

Table 9.1. Northern Quaternary alluvial fans slope angle analysis, for area “west” and “east” (Fig. 7.3a and 7.2a). Data are extracted from a 10x10 DEM.

9.1 Alluvial fan slope analysis

The fan slope angle analysis focused on two areas of Zone 1 where the fan systems are approximately oriented N-S. Those two areas are marked on figure 7.3a by black dotted boxes as “west” and “east” respectively. The analysis used a purposely-developed routine to extract, from the DEM of the area (Fig. 6.1) the elevation data points of the top surfaces of single alluvial fans excluding the areas of the fan which had been incised by erosion (refer to chapter 4 for the methodology). For each mapped alluvial fan the slope (inclination) angle has been measured along the N-S direction by plotting a linear regressions through the extracted elevation point-cloud data, at 2 km intervals, for Sectors A, B, C, D (figure 7.3a). An example of the extracted alluvial fan top surface elevation data, the resulting linear regressions and the obtained fan parameters, for a single alluvial fan are presented in figure 9.1.

A total of 71 alluvial fans were analyzed using this method in area “west” and “east”. The results of this analysis are presented in table 9.1.

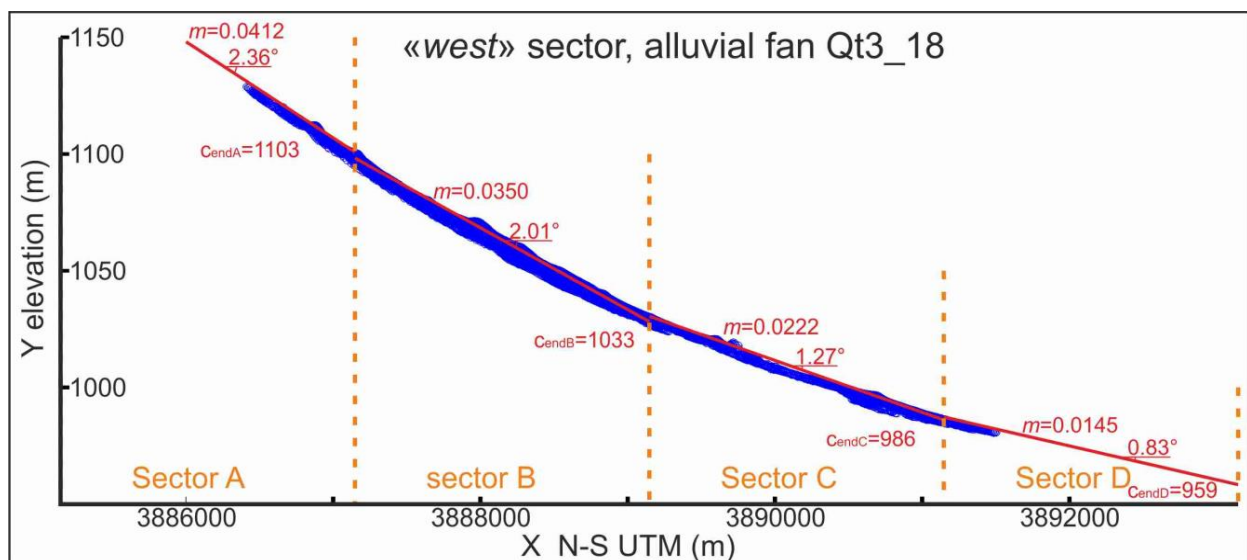


Figure 9.1. Example of extracted alluvial fan data plotted on a N-S transect and the calculated slope for each sector. m = slope gradient, C_{endX} = fan elevation at the end of sector x .

9.1 Results

Figure 9.2 shows the fan slope angle analysis results for the three alluvial fan generation within “west” and “east” areas (Fig. 7.2a and 7.3a). The plot shows the mean slope angle of each

alluvial fan generation, located at their average elevation, along the four sectors (A, B, C and D, figure 7.3a) for the two selected area. The northing range of fault segments position is also indicated. The analysis clearly shows that there are differences in slope angle and elevation both between different fan generation (within the same sector) and the two selected areas.

It may be argued that the different alluvial fans top surface angles reflect the deposits grain size changes both between the three fan generations and along each fan (changes in grain size and consequently in slope angle from fan apex to the distal portions of the fan). Nevertheless the three generation of alluvial fan deposits exhibit similar maximum particle size for comparable distances from the mountain front. Furthermore, comparing the obtained alluvial fan slope angle with those found on alluvial fans in semi-arid settings (e.g. Blissenbach, 1954) it is very clear that our data consistently exceeded the expected slope angles (Fig. 9.3). Moreover, the observed maximum grain size of the KFF alluvial fans (~35 cm at the apex, 15 cm in the central part, 5 cm in the distal part) seem to be much smaller than the expected one. This indicates that the Quaternary alluvial fans top surfaces slope do not represent the original depositional slope, demonstrating therefore, that post depositional tilting has occurred.

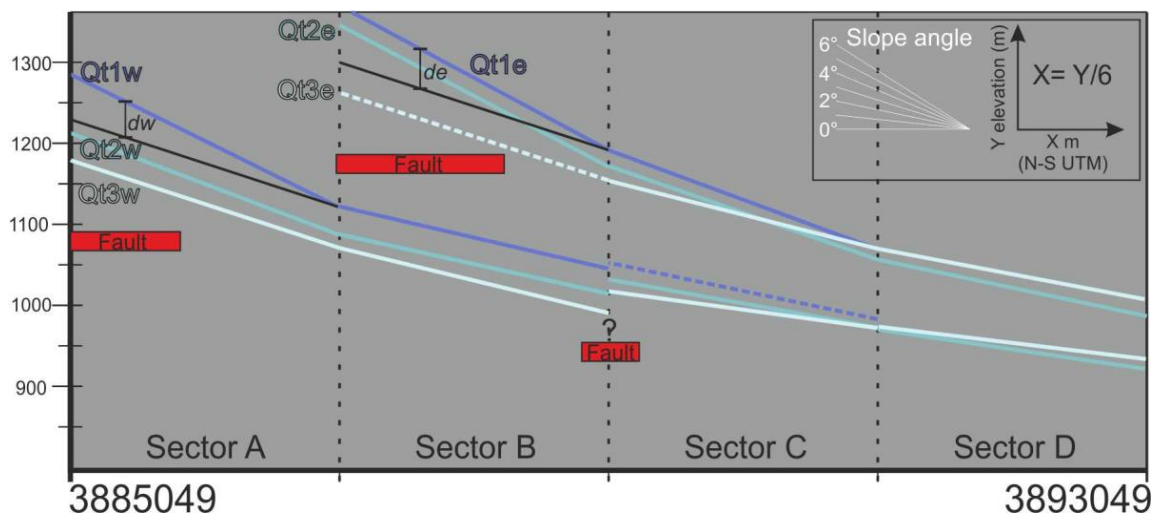


Figure 9.2. Results of the northern Quaternary alluvial fan slope angle analysis for area “west” and “east” (Fig. 7.3a). The diagram shows the mean alluvial fan slope angles and elevation for the four sectors (A, B, C and D). The projected fault location extent is shown in red. *dw* and *de* marks the a conservative estimate of the Qt1N surface uplift for the two area.

From the fan slope angle analysis results in figure 9.2, it is possible to appreciate some general trends: i) fan tilting is greater towards the faults and seems to decrease proportionally away from it; ii) tilting is generally greater in Qt1 fans and progressively decreases in Qt2 and Qt3. The tilting and the elevation of the three alluvial fan generation is greater in the “east” area. Furthermore, in the “west” area the three fan generation show generally decreasing slopes from Qt1w to Qt3w, their profiles seem to be disturbed in correspondence of an inferred fault at the end of Sector B and

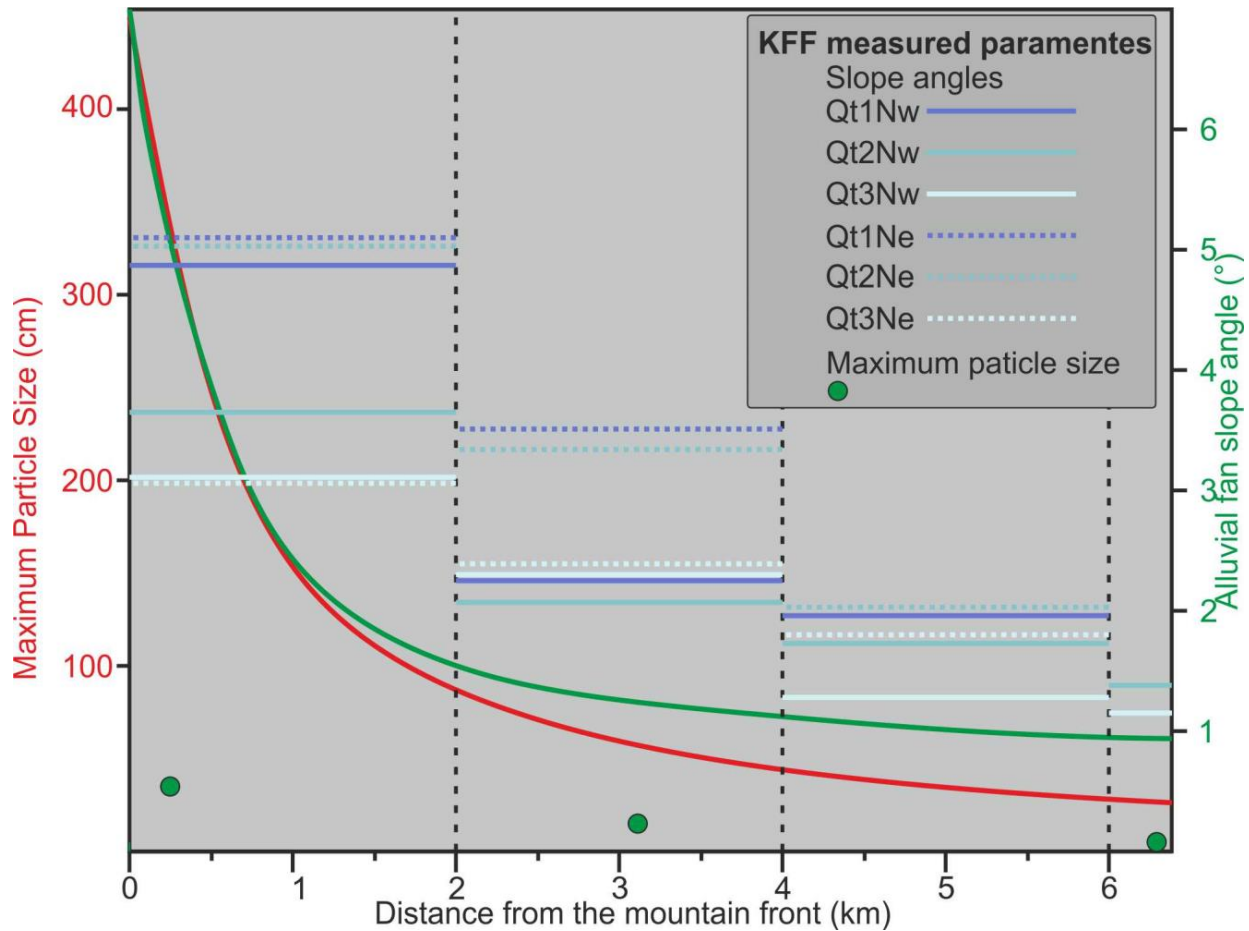


Figure 9.3 Comparison between the obtained mean slope angle results of the KFF and the mean fan surface slope angle (green), along a radial profile on alluvial fans in semi-arid settings. The expected mean, maximum particle sizes (red) is also reported for alluvial fans in semi-arid settings. Particle size and slope angle curves after Blissenbach (1954).

generally merge at the end of sector C. By contrast in the “east” area Qt1e and Qt2e show approximately parallel slope profiles though located at different elevations. Qt3e is less tilted and its profile crosses Qt1w and 2w at the end of Sector C. In both the “west” and “east” area Qt3 in Sector D seems to be less tilted but at a higher elevation than the other two alluvial fan generations.

The fact that the tilting generally decreases away from the principal faults indicates that the driver of such tilting are the fault themselves. The slope profile geometries of the Quaternary fans in area “west” indicate that tilting occurred at least since the time of deposition of Qt1W fans. On the other hand, the slope profile geometries of the Quaternary fans in area “east” indicate that tilting occurred after the deposition of Qt2e onwards.

10 THERMOCHRONOLOGY AND GEOCHRONOLOGY

The results from AHe and HeHe thermochronology and OSL geochronological analysis and their sample location are shown in figure 10.1.

10.1 Apatite (U-Th)/He (AHe) and Apatite Fission Tracks (AFT) dating

A total number of 17 rock samples, 6 from the basement unit and 11 from the basal units of the Neogene deposits were collected for AHe thermochronological analysis from an approximate constant elevation transect parallel to the KFF trace (Fig.10.1). The samples are from the arenitic portions of the Paleozoic and Mesozoic basement and the Neogene basal sandy intercalations of cycle- and 2. Due to the detrital origin, the quantity and quality of apatite grains is highly variable. In most samples, apatite consisted of rounded grains with frosted surfaces making the identification of inclusion-free grains difficult. Eight samples were excluded from the analysis due to their apatites pore quality.

AHe thermochronology was performed on 9 samples. The analytical protocol adopted in this study follows Foeken et al. (2006). For detail on the analysis methodology, refer to section 4.3.1. Single grain ages corrected for α -ejection (Farley et al., 1996) generally show a good within-sample reproducibility (Table 10.1).

Mean ages and standard deviation are plotted in figure 10.1. Three samples show single grain ages that does not overlap within two standard deviations with the other ages of the same sample. Because these three grains have low U and Th content, we consider them outlier and they were not included in the mean age calculation. All samples have mean and single grain AHe ages younger than the stratigraphic age, indicating that all were reset and their ages indicate a Miocene to Pliocene cooling/exhumation history. Mean ages range from 2.9 ± 1.5 Ma to 20 ± 2.6 Ma, defining two mean age populations, clustering at ~ 18 and ~ 4 Ma.

The spatial distribution of the AHe ages shows two broad areas with common cooling history: (i) the western area, comprising the topographically prominent basement ridge bordered to the south by the WFS, to the north by the CFS and to the northwest by the westernmost EFS and (ii) the eastern area, located along and to the north and south of the EFS (Fig. 10.1).

The AHe ages distribution in the western area shows that the southern and central zones of the linear mountainous ridge shear a similar cooling age, ranging from 20.0 to 16.5 Ma, broadly clustering at ~ 18 Ma. At odd with this clustering sample IR 10 exhibit a much younger cooling age (2.9 Ma).

The AHe ages distribution in the eastern area shows a cooling ages, broadly clustering at ~ 4 Ma with the exception of sample IR 17 which shows an age of 7.9 Ma.

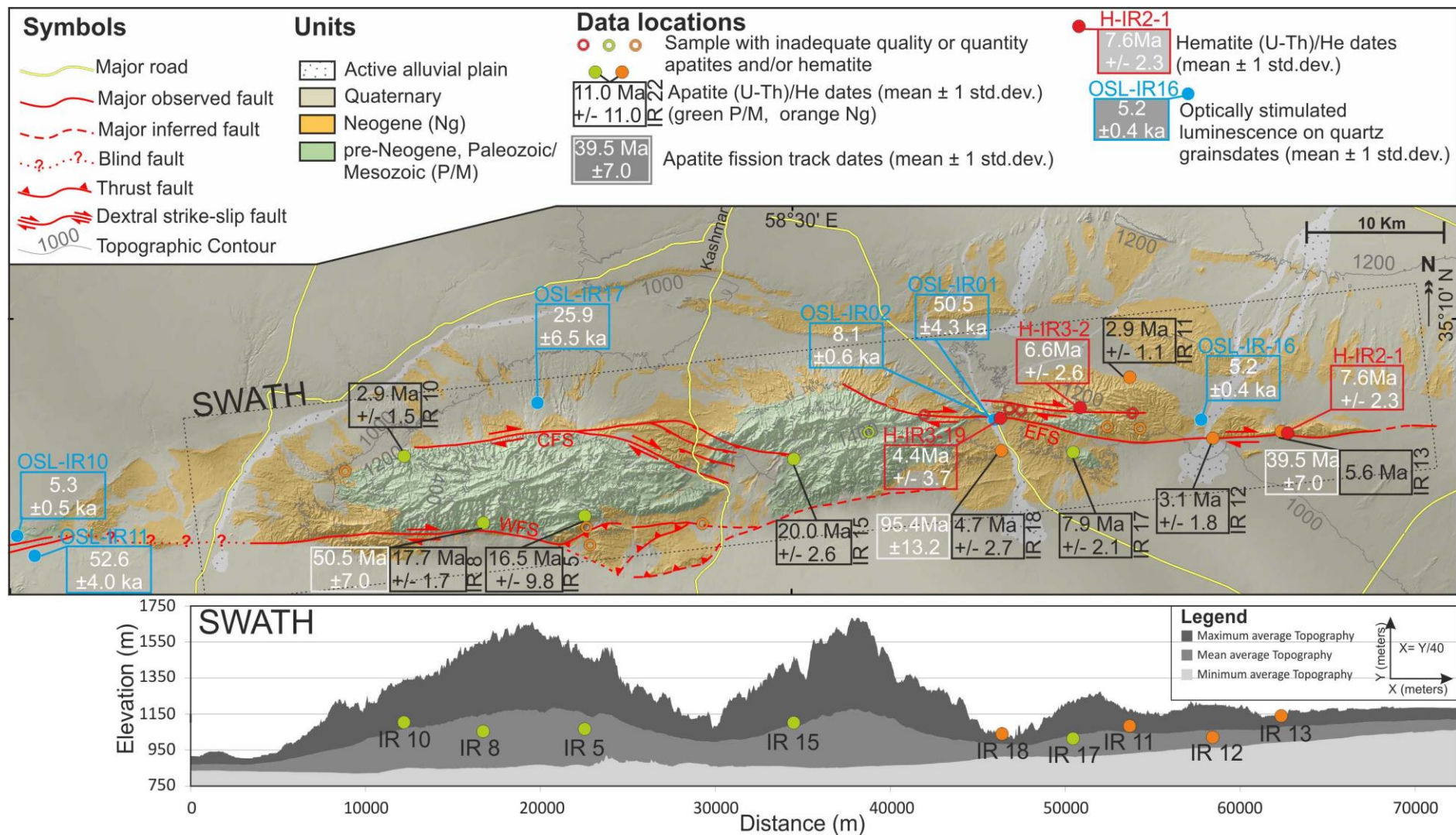


Figure 10.1. Structural map of the KFF on shaded relief. Location of the samples used for AHe, HeHe thermochronology and OSL geochronology together with mean age results and standard deviation for each sample are also indicated. Samples, which were rejected during analysis for their poor material quality or quantity, are also shown by empty circles. Note that swath profile shows that the AHe data were taken approximately along an equal elevation profile.

Table 10.1 APATITE (U-Th)/He DATA

Sample	Rock unit	Location		Altitude (m)	Aliquot name	U	Th	He	He Age	Corrected He age	uncert ^a	mean age	uncert st. dev.
		Lat (°N)	Long (°E)			(ng)	(ng)	(cc)	(Ma)	(Ma)			
IR-8	Pre-Neogene	35.060867°	58.316167°	1054	IR-8.1	0.0166	0.106	2.91E-11	5.44	7.1*	0.2	17.7	± 1.7
					IR-8.2	0.0124	0.189	9.23E-11	12.81	17.5	0.4		
					IR-8.3	0.0627	0.248	1.71E-10	11.38	15.4	0.3		
					IR-8.4	0.297	0.507	7.62E-10	14.95	19.5	0.4		
					IR-8.5	0.212	0.559	6.01E-10	14.26	18.4	0.4		
IR-15	Pre-Neogene	35.096801°	58.494049°	1102	IR-15.1	0.059	0.392	2.30E-10	12.30	17.4	0.4	20.0	± 2.6
					IR-15.2	0.031	0.139	6.89E-11	8.53	11.1*	0.3		
					IR-15.4	0.227	2.591	1.91E-09	18.66	22.6	0.5		
					IR-15.5	0.044	2.496	1.37E-09	17.77	20.0	0.5		
IR-10	Pre-Neogene	35.095326°	58.254287°	1104	IR-10.1	0.001	0.302	4.21E-12	0.46	0.7*	0.3	2.9	± 1.5
					IR-10.2	0.009	0.105	1.21E-11	2.78	3.9	0.2		
					IR-10.3	0.003	0.125	5.03E-12	1.19	1.8	0.2		
IR-11	Neogene Ng-SSi	35.132007°	58.688542°	1084	IR-11.1	0.003	0.056	5.09E-12	2.28	3.6	0.3	2.9	± 1.1
					IR-11.2	0.003	0.049	4.60E-12	2.20	3.5	0.3		
					IR-11.3	0.004	0.033	1.72E-12	1.02	1.6	0.8		
IR-13	Neogene Ng-C	35.100512°	58.673708°	1140	IR-13.1	0.005	0.081	1.34E-11	4.18	5.6	0.5	5.6	
IR-18	Neogene Ng-C	35.101207°	58.634732°	1049	IR-18.1	0.002	0.043	3.93E-12	2.16	3.1	0.4	4.7	± 2.7
					IR-18.2	0.014	0.039	1.63E-11	5.27	7.8	0.4		
					IR-18.3	0.004	0.042	4.56E-12	2.27	3.1	0.3		
IR-5	Pre-Neogene	35.061950°	58.369084°	1067	IR-5.1	0.022	0.190	3.97E-11	4.73	6.2	0.2	16.5	± 9.8
					IR-5.2	0.195	0.198	5.07E-10	17.09	25.9	0.5		
					IR-5.3	0.060	0.164	1.75E-10	14.24	17.5	0.4		
IR-17	Pre-Neogene	35.100512°	58.673708°	1014	IR-17.1	0.007	0.034	1.50E-11	7.14	9.4	0.6	7.9	± 2.1
					IR-17.2	0.007	0.054	1.24E-11	4.71	6.4	0.3		
IR-12	Neogene Ng-C	35.104742°	58.771337°	1021	IR-12.1	0.003	0.032	8.51E-13	0.56	1.0	0.7	3.1	± 1.8
					IR-12.2	0.008	0.08	1.17E-11	3.28	4.5	0.2		
					IR-12.3	0.060	0.07	2.71E-11	2.81	3.8	0.2		

* single age excluded by mean age calculation; ^a 1-sigma errors propagated from U, Th and He measurement uncertainties

The preliminary AFT ages from detrital apatites from one pre-Neogene and two Neogene basin samples yield ages of 50.5 ± 7.0 Ma, and 95.4 ± 13.2 Ma and 39.5 ± 7.0 Ma, respectively (Fig. 10.1). The analytical results are shown in table 10.2. These data fail a χ^2 test and are considered “mixed ages”. AFT ages from Neogene samples IR13 and IR18 that are *older* than the stratigraphic age of the Neogene sediments indicate that these samples were not reheated to temperatures greater than 100 °C.

Table 10.2: Apatite Fission-track Data

Sample No.	No. of Crystals	Track Density ($\times 10^6$ tr cm^{-2})			$\rho_s/\rho_i \pm 1\sigma$	Mean Dpar (μm)	Age Dispersion ($P\chi^2$)	Central Age $\pm 1\sigma$ (Ma)
		ρ_s (N_s)	ρ_i (N_i)	ρ_d (N_d)				
IRFT 8	20	0.4006 (270)	1.720 (1159)	1.111 (3554)	0.2330 ± 0.0188	1.99	46.86% ($<0.01\%$)	50.54\pm7.00 mixed age
IRFT 13	11	0.2292 (60)	1.287 (3525)	1.102 (3525)	0.1780 ± 0.0261	2.03	27.41% (10.24%)	39.54\pm6.98 mixed age
IRFT 18	20	0.2294 (133)	0.4898 (284)	1.093 (3497)	0.4683 ± 0.0533	2.50	29.40% (12.40%)	95.42\pm13.24 mixed age

Notes:

(i). Analyses by external detector method using 0.5 for the $4\pi/2\pi$ geometry correction factor;

(ii). Ages calculated using dosimeter glass: IRMM540R with $\zeta_{540R} = 368.1 \pm 14.9$ (apatite);

(iii). $P\chi^2$ is the probability of obtaining a χ^2 value for v degrees of freedom where $v = \text{no. of crystals} - 1$;

These ages are significantly older than AHe ages acquired from the same samples, which suggests that although the detrital apatites have been reset with respect to He system, they have not been “reset” with respect to the AFT system. Unfortunately, the low number of track lengths that could be measured meant that it was challenging to determine whether any shortened track lengths due to the crystal’s previous source time-temperature history or to Neogene burial/partial reset.

Taken together, the AHe and AFT data from the Neogene basin sediments imply burial temperatures in excess of ~ 60 °C and less than 100 °C.

10.2 Hematite (U-Th)/He (HeHe) dating

A total number of 7 samples from, hematite-coated fault surfaces within Neogene deposits were collected along the EFS and associated minor faults for HeHe thermochronological analysis in order to directly date fault slip events and/or fault related exhumation and fluid circulation during the propagation and growth of the KFF. All the hematite coated fault surfaces exhibited slickenlines striations (e.g. Fig. 8.6d and 8.9b). Four samples were excluded from the analysis due to the hematite inadequate quality. HeHe thermochronology was performed on 3 samples (H-IR2-1, H-IR3-2 and H-

Table 10.3. Hematite (U-Th)/He ages from hematite-coated fault surfaces

Sample	location		U (ng)	$\pm 1\sigma$	Th (ng)	$\pm 1\sigma$	Th/U (ng)	⁴ He (fmol)	$\pm 1\sigma$	Date (Ma)	Error (Ma) ^a
	Lat (N)	Long (°E)									
H-IR2-1A	35.106045°	58.814844°									
H1			0.050	0.001	0.058	0.001	1.195	3.586	0.108	10.405	0.341
H2			0.042	0.001	0.079	0.001	1.932	1.716	0.093	5.237	0.291
H3			0.041	0.001	0.101	0.001	2.547	1.600	0.094	4.592	0.275
H4			0.033	0.000	0.108	0.002	3.360	1.196	0.100	3.796	0.321
H5			0.033	0.001	0.056	0.001	1.733	0.980	0.099	3.947	0.399
									Avg.	5.60	
									Std. Dev.	2.75	
H-IR2-1B	35.106045°	58.814844°									
H1			0.026	0.000	0.032	0.001	1.256	1.392	0.091	7.730	0.517
H2			0.027	0.000	0.031	0.001	1.174	1.533	0.096	8.172	0.522
H3			0.029	0.000	0.023	0.000	0.809	1.657	0.104	8.835	0.565
H4			0.025	0.000	0.029	0.000	1.193	1.499	0.097	8.855	0.585
H5			0.021	0.000	0.023	0.000	1.131	1.177	0.097	8.434	0.704
									Avg.	8.41	
									Std. Dev.	0.47	
H-IR2-1C	35.106045°	58.814844°									
H1			0.273	0.004	0.150	0.002	0.564	14.913	0.142	8.964	0.139
H2			0.155	0.002	0.093	0.001	0.616	9.505	0.116	9.929	0.173
H3			0.214	0.003	0.126	0.002	0.602	11.512	0.187	8.755	0.184
H4			0.249	0.004	0.078	0.001	0.322	13.265	0.176	9.195	0.172
									Avg.	9.211	
									Std. Dev.	0.511	
									Sample Avg.	7.63	
									Sample Std. Dev.	2.25	
H-IR3-2	35.118348°	58.686581°									
H1			0.082	0.001	0.178	0.003	2.217	4.093	0.157	6.094	0.242
H2			0.086	0.001	0.284	0.004	3.390	2.342	0.111	2.837	0.138
H3			0.094	0.001	0.322	0.005	3.501	3.743	0.113	4.073	0.129
H4			0.056	0.001	0.089	0.001	1.626	5.172	0.129	12.361	0.337
H5			0.075	0.001	0.223	0.003	3.052	4.527	0.144	6.574	0.220
H6			0.118	0.002	0.441	0.006	3.845	9.167	0.192	7.658	0.180
H7			0.091	0.001	0.320	0.005	3.622	6.105	0.150	6.800	0.180
H8			0.159	0.002	0.270	0.004	1.749	8.237	0.155	6.863	0.151
H9			0.085	0.001	0.157	0.002	1.905	4.122	0.116	6.272	0.190
									Sample Avg.	6.61	
									Sample Std. Dev.	2.63	
H-IR3-19	35.115870°	58.631777°									
H1			0.030	0.000	0.113	0.002	3.886	1.151	0.063	3.776	0.209
H2			0.021	0.000	0.092	0.001	4.461	0.453	0.055	1.948	0.239
H4			0.022	0.000	0.078	0.001	3.641	0.473	0.048	2.170	0.221
H5			0.097	0.001	0.181	0.003	1.915	1.582	0.067	2.099	0.091
H6			0.111	0.002	0.257	0.004	2.365	4.256	0.115	4.580	0.133
H7			0.061	0.001	0.158	0.002	2.641	6.247	0.125	11.701	0.265
									Sample Avg.	4.38	
									Sample Std. Dev.	3.74	

^a1 σ propagated error from analytical uncertainties on U, Th, and He analyses.

IR3-19). Aliquots of hematite were extracted from striated fault surfaces of each selected sample. The aliquots comprise an aggregate of individual hematite crystals and are, on average ~100 μm -thick. These crystals are not neoformed, plate-like specularite crystals but rather appear comminuted, or grain-size reduced. Single aliquot ages generally show a good within-sample reproducibility (Table

10.3) Mean ages, standard deviation and their sample location are reposted in figure 10.1. HeHe ages from three hematite coated fault surfaces – IR2-1, IR3-2, and IR3-19 – yield ages of 7.6 ± 2.3 Ma, 6.6 ± 2.6 Ma, and 4.4 ± 3.7 Ma, respectively and average at c.a. ~ 6 Ma. However, in each HeHe sample, the single aliquots dates range from 10-12 Ma down to ~ 2 Ma. This spread in data strongly suggests that: (1) Aliquots from each sample comprise a variety of crystal sizes and thus closure temperatures and (2) variability in dates reflect different proportions of highly retentive (coarser grained) and less retentive (finer grained) diffusion domains in each of the aliquots within a given sample. Ultimately, this observation implies that some of the less retentive domains within an aliquot are open to He diffusion (i.e., lower closure temperature) after hematite formation, and are thus recording cooling during exhumation. In other words, in each sample the HeHe age population may reflect both of formation ages (the aliquots with more retentive, coarser grained and therefore higher closure temperature hematite) and exhumation ages (the aliquots with less retentive, finer grained and therefore lower closure temperature hematite).

10.3 Optically Stimulated Luminescence (OSL) dating

A total of 9 samples from Quaternary alluvial deposits and alluvial fans (see OSL supplementary material) were collected for Optically Stimulated Luminescence (OSL) dating of quartz grains. Sampling of Quaternary alluvial deposits for OSL dating was carried out in the frame of a wider research project. As a result, 4 sample were collected from the KFF area (samples IR01, 02, 16 and 17 see table 10.4 and figure 10.1), 2 samples from the area between the KFF and the neighbouring Kuh-e-Sarhangi Fault (samples IR11 and 12; see table 10.4 and figure 10.1) and 3 from the Kuh-e-Sarhangi Fault area (Samples IR05, 06 and 07; see table 10.4). In the KFF area, sample IR01, 02, 10, 11 and 16 were collected in faulted Quaternary alluvial deposits while sample IR17 was collected from Quaternary alluvial fan deposits (Fig.10.1). Sample IR01 is from a mostly sandy alluvial deposit, with gravelly lenses. The top surface of the deposit lies at ~ 980 m a.s.l and corresponds to the highest (T1) of three generations of fluvial terraces (Fig. 8.6a and 10.2). Sample IR02 is from a sandy layer of an alluvial deposit entrenched in the previous one. The top surface of the deposit lies at ~ 965 m a.s.l and corresponds to the lowest (T3) of the above mentioned fluvial terraces (Fig.10.2). The Quaternary deposits from which IR01 and 02 were extensively affected by E-W and WNW-ESE oriented set of sub-vertical fracture arrays (see section 8.6).

Sample IR10 is from a silty-sandy terraced alluvial deposit. The Top surface of the deposit lies at ~ 875 m a.s.l.. The deposit from which the sample was collected shows evidences of quaternary faulting and topographically prominent linear fault scarps (Fig.10.2) along the CFS western fault splay. Sample IR11 is from a silty-sandy terraced alluvial deposit with gravelly beds. The Top surface of the deposit lies at ~ 858 m a.s.l.. The deposit from which the sample was collected, exhibit a

relatively more cemented gravelly upper horizon which shows pervasive fracturing and faulting with strike-slip right-lateral kinematics and NE-SW orientation (Fig. 10.2).

Sample OSL16 is from a sandy-gravelly alluvial deposit from the terraced alluvial plain of the easternmost river dissecting the KFF ridge. The top of the deposit is 5 m above the present thalweg and lies at ~1040 m a.s.l. The deposit from which this sample was collected it has been cut through by E-W oriented right-lateral strike-slip faults (see section 8.6 and figures 8.10d and 10.2). Sample IR17 is from a silty- to sandy matrix supported terraced alluvial fan deposit with gravelly lenses and it belongs to the Qt2N alluvial fan generation (Fig. 10.2). The Top surface of the deposit lies at ~1050 m a.s.l.

All the alluvial deposits mainly derive from the dismantling of Neogene units and the quartz grains used for OSL dating originally come from the pre-Neogene bedrock. For any site we sampled at a depth > 1m below the top depositional surface or below eventual cut-in-fill erosional surfaces within the deposit, in order to avoid the risk of rejuvenated ages. The three samples from the Kuh-e-Sarhangi Fault area (Samples IR05, 06 and 07) were also collected from faulted alluvial quaternary deposits, but their results are used in this study only to constrain the overall Quaternary deposit generation in the region.

10.3.1 Results

The OSL dating results are shown in Table 10.4 and the results from the samples taken within the KFF area are shown in figure 10.1. The sampled Quaternary deposits of the KFF provided ages between Late Pleistocene and Holocene (Table 10.4). Collectively the ages range from ~5 to ~56 ka, defining three mean age populations, clustering at ~6, ~24 and ~53 ka.

These ages are coherent with the OSL and IRSL ages obtained regionally for the Quaternary alluvial deposits in eastern Iran (Walker and Fattahi, 2011; and references therein), and with the ^{10}Be surface abandonment ages obtained by Regard et al. (2006).

In particular, in the KFF area three generations of Quaternary deposits with ages clustering at ~6ka and one at ~53ka are cut by major and minor faults with documented right lateral strike-slip kinematics and orientations compatible with the overall KFF system. Furthermore, the oldest fluvial terrace of the western river, is 50.49 ± 4.34 ka and the youngest in the same valley is 8.06 ± 0.60 ka. The sample from the easternmost river valley is 5.16 ± 0.41 ka. Moreover, the fact that the youngest fluvial terrace (as well as the the corresponding active river bed), located more to the east, is at higher elevation, with respect to the oldest one to the west, is consistent with the regional topography of the KFF deformation zone and in particular with the eastward increase of the minimum elevation.

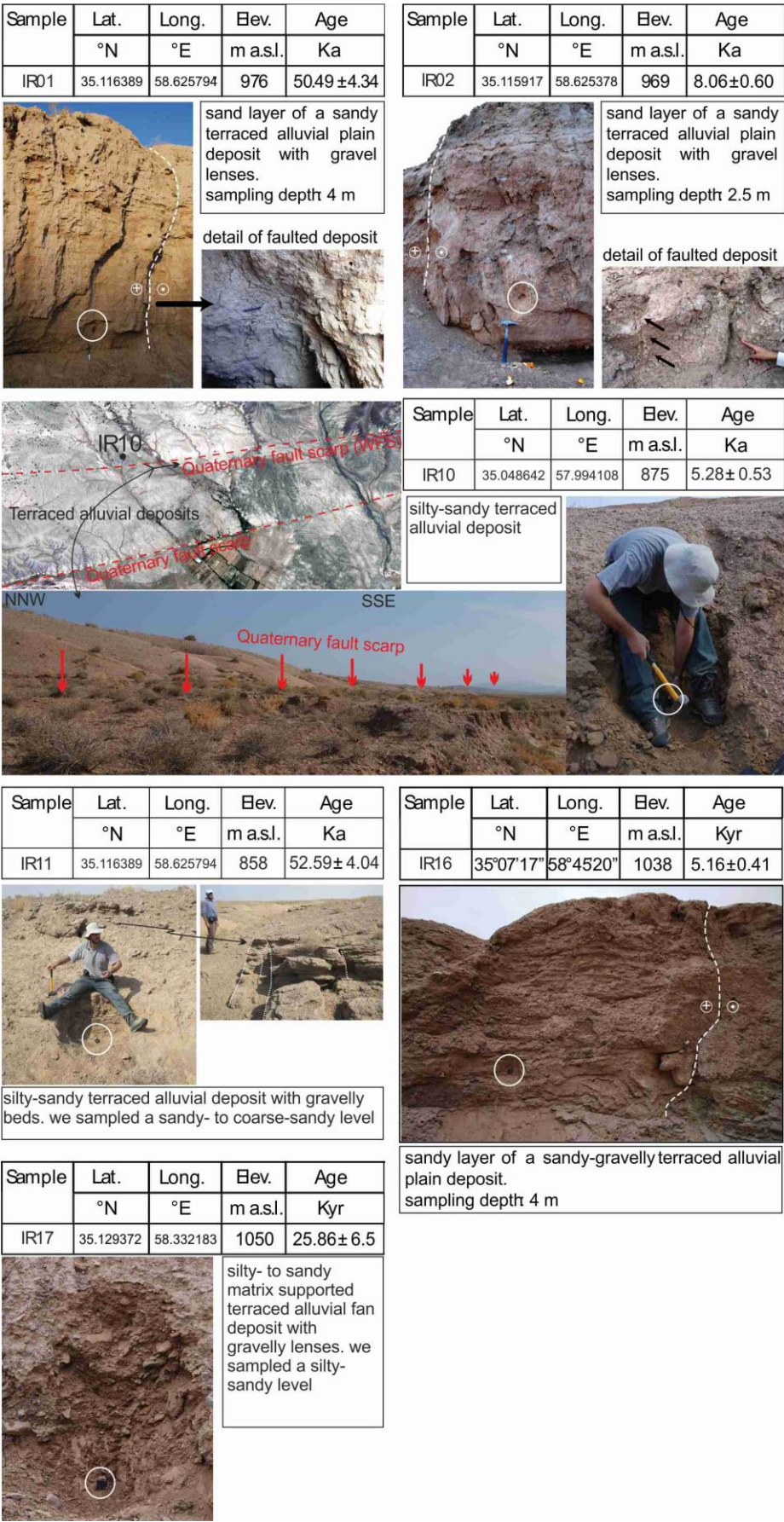


Figure 10.2. OSL sampling and analysis summary figures, exhibiting the deposits from which the samples were collected, their coordinates (latitude, longitude, and elevation) and the dating result.

Table 10.3. OSL dating results

Sampl e	Deposit type	location		Elevation	K	U	Rb	Th	Moisture	Depth	Dose Rate	E.Dose	Age	Error
	(fom map)	Lat (°N)	Long (°E)	(m)	%	ppm	ppm	ppm	%	m	Gy/Kyr	Gy ($\pm 1 \sigma_s$)	Kyr	s1
IR16	Qt	35.121461°	58.755644°	1038	1.45	1.7	57.9	6	10+/-5	4	2.13±0.12	10.99±0.54	5.16	0.41
IR10	Qt	35.048642°	57.994108°	875	1.43	2.1	53.8	6.1	10+/-5	1.5	2.25±0.12	11.89±0.55	5.28	0.53
IR02	T3	35.115917°	58.625378°	969	1.7	0.26	60.2	6.82	10+/-5	2.5	2.104±0.132	16.97±0.48	8.06	0.6
IR05	Qt/KSF	34.973111°	57.970306°	850	1.05	0.14	56.3	4.27	10+/-5	1.5	1.386±0.085	29.71±1.09	21.43*	1.65
IR06	Qt/KSF	34.973583°	57.969694°	860	1.05	0.11	48.2	2.08	10+/-5	2	1.23±0.10	30.58±0.41	25.54	1.43
IR17	Qt2N	35.129372°	58.332183°	1050	2.01	2.3	108.5	10.7	10+/-5	6	3.02±0.17	78.09±19.08	25.86*	6.5
IR01	T1	35.116389°	58.625794°	967	1.67	0.25	55.3	6.21	10+/-5	4	2.059±0.129	103.95±5.31	50.49	3.34
IR11	Qt	35.037828°	58.016147°	858	1.25	1.7	46.4	4.7	10+/-5	1.5	1.92±0.11	100.90±4.59	52.59	4.04
IR07	Qt/KSF	34.936777°	57.847815°	901	1.87	0.02	45.7	7.1	10+/-5	2	2.231±0.143	126.75±1.92	56.82	4.1

* Low signal, may not be reliable age

11 DISCUSSION

The multidisciplinary dataset presented in this study offers significant spatial and temporal constraints on the geological history and evolution of the KFF system at the northern edge of the Lut Block, Central Iran. These results may elucidate the way strike-slip faulting enucleates and propagates, by linking structures, stratigraphy and thermochronology to the long-term response of crustal deformation in intraplate settings.

11.1 Structural synthesis

The geological investigation shows that the KFF consists of a broad, E-W striking deformation zone made of a complex array of fault strands, where three main, broadly left stepping, right-lateral fault segments are recognised to cut through the Paleozoic and Mesozoic basement units and the Neogene-Quaternary sedimentary covers (Fig. 6.1). These fault zones are tens of kilometre long and cut at high angle the basement NE-SW striking planar fabric (Fig. 6.1), ruling out a major contribution of tectonic reactivation during the KFF development. As such, the cumulative fault population analysis may provide insights into the stress regimes and strain conditions during the KFF development (cf. Davis et al., 2000; Storti et al., 2006). The right-lateral fault population (215 data over a total of 495) provides a mean strike cluster at $N91^\circ$, which is interpreted as the mean strike of the principal displacement zone (PDZ) (Fig. 11.1). The normal faults and extensional veins (111 data) strike data cluster at $N135^\circ$ (Fig. 11.1b). These angular relationships suggest fault zone development in response to a (local) regional direction of the maximum principal stress ($R\sigma_1$) trending NW-SE, at an angle of $\sim 44^\circ$ from the PDZ. This direction of $R\sigma_1$ (i) bisects the dihedral angle of *ca.* 60° made between the conjugate systems as defined by main left-lateral fault and the secondary right-lateral fault population strikes, striking $N191^\circ$ and $N311^\circ$, respectively; and (ii) is orthogonal to the main reverse fault strikes at $N47^\circ$ (Fig. 11.1). This result attests for simple shear dominated strike-slip deformation (simple shear wrenching in Fossen et al. (1994)) during the KFF development, in agreement with the mean pitch angle (2°) of the fault slickenlines as obtained from the cumulative data set (Fig. 11.1a). Within this general scenario, the along-strike spatial variations of the fault population orientation, kinematics and strain regimes (restraining and releasing areas; figure 11.1a) reflect the different ways by which the overall E-W right lateral shear is accommodated, distributed and partitioned along the principal and minor fault strands of the KFF system (Fig. 6.1, 8.2 and 11.1).

Fault zone architecture and structural characteristics markedly varies along-strike of the KFF. Overall, there is an observed eastward increase in shear localization within the main fault zones, from distributed deformation characterized by cataclastic fault rocks in the west (the WFS and CFS) to

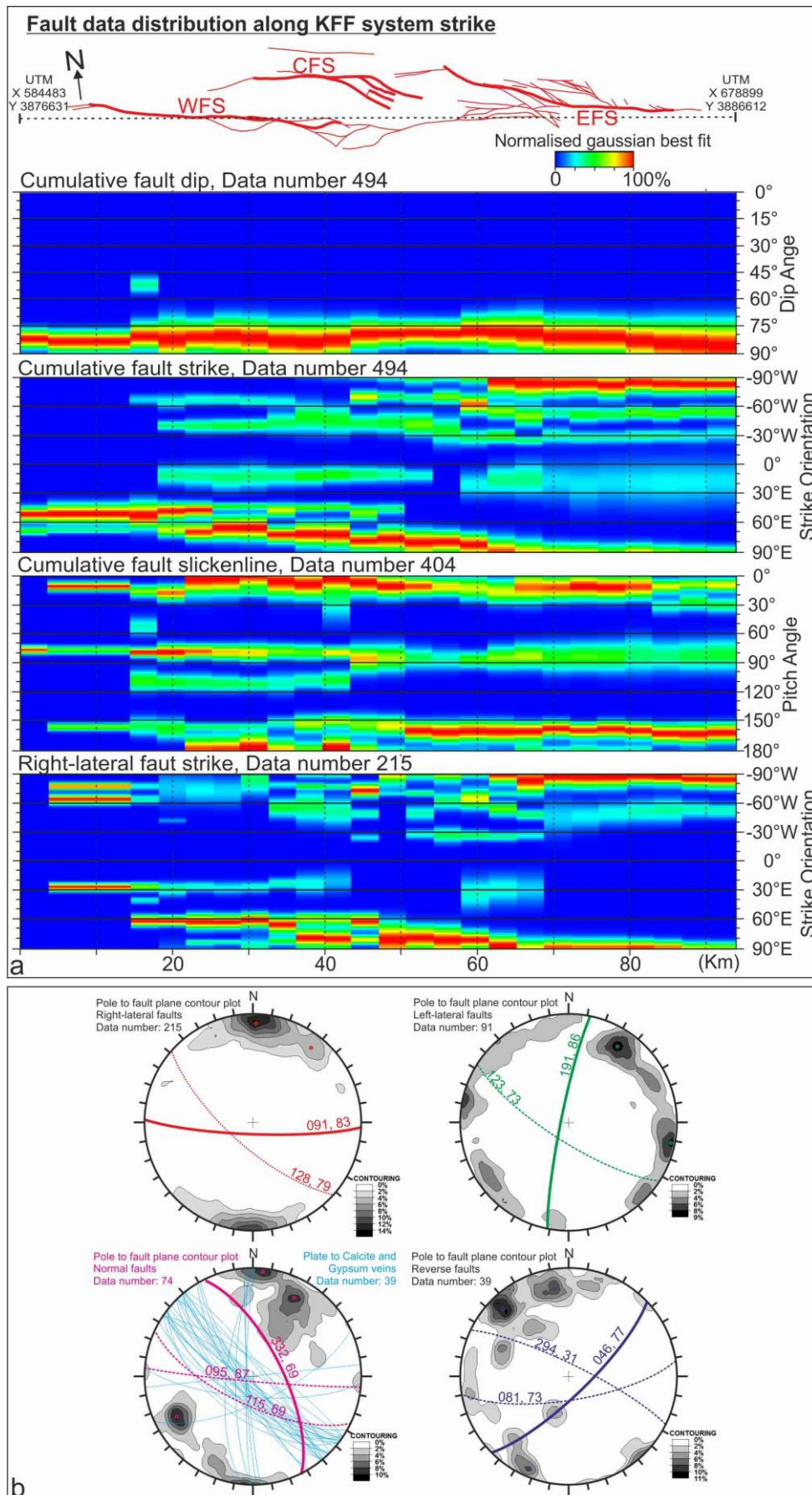


Figure 11.1 (a) Structural data plotted along E-W transect as normalized Gaussian best-fit values. (b) Cumulative contour stereo plots of fault plate orientation divided by kinematics. Fault population analysis was performed through the software Daisy 3 (Salvini, 2004; <http://host.uniroma3.it/progetti/fralab>).

localized and mature fault zones characterized by ultracataclastic fault gouges (distributed cataclastic flow) and S-C fabrics in the east (the EFS). It is known that porous rocks such those that make up the basal deposits of the faulted Neogene strata along the KFF, display a transition from dilatant, brittle behaviour to shear-enhanced compaction and macroscopically ductile behaviour with increasing effective pressure at constant temperature (Paterson et al., 2005; Rutter and Hadizadeh, 1991; Wong and Baud, 2012). This general scenario is documented along the KFF by deformation mechanisms varying eastward from pure brittle fracturing to coupled cataclastic flow and dissolution creep during S-C fabric development. This is also in agreement with occurrence of hematite-coated fault surfaces systematically observed on the EFS, which attest for focused fluid flow during fault zone localisation, a process that can not occur at shallow (< 3 km) crustal depths (Caine et al., 1996; Rowland and Sibson, 2004; Sheldon et al., 2006). Such lines of evidence suggest shear deformation occurred under different confining pressure conditions moving eastward. Differential lithostatic loading between the western and the eastern areas is supported by the stratigraphic and thermochronological data (see below), which shows an overall eastward increase in the Neogene sediment thickness (up to 3.8 km) and fault-related exhumation, postdating Neogene sedimentation.

Faulting is intimately associated with regional bulging (antiformal folding) of the Neogene deposits (Fig 6.1 and 8.1), providing further constrains on the KFF growth and evolution. In particular, the along-strike space-time overprinting relationships between fault-parallel folding along the KFF can be reconstructed (at various scales) from field observations. It is inferred that early folding was caused by the upward fault nucleation and propagation, accompanied by pervasive fracturing aided by the dilatant behaviour of the shallower (< 4 km) rocks. Folding was then amplified by fault zone propagation (fault-related folding; both vertically and along-strike) in the Neogene deposits. With increasing shearing, deformation zones matures into discrete through-going fault zones, which localize deformation, preventing further fold amplification. This overall antiformal geometry is better preserved along the western region (see geological cross sections A-B and C-F in Figure 6.1), while it dies out eastward and is abruptly interrupted by the EFS (Fig 6.1).

Major strike-slip faults such as the KFF typically accommodate large displacement via an array of evolving strands. Estimation of the fault offset along the KFF is hampered by lack of homologous markers cut across the major fault strands. Nevertheless, qualitative estimates from the single fault strands can be obtained from empirically-derived scaling law for faults, relating fault displacement (D) to fault length (L) (e.g. Schlische et al., 1996), fault damage zone (DT) and fault core (CT) thickness (Fossen, 2010). Based on the field observation from the KFF, the D - L diagram provides displacement values ranging from 10^2 to 10^4 m. These estimates are in the range of what obtained from the DT - D and CT - D diagrams (Fig. 11.2). A further indication of the magnitude of the

apparent horizontal offset along the fault strands that make up the KFF can be derived from the basement outcrop pattern across the NW-SE striking trace of the EFS (Fig 6.1). The basement block to the north of the EFS could have been displaced south-eastward from its original position. In this scenario, a horizontal displacement of 8-10 km can be proposed, which fits well with the above estimates. Based on these estimates, it is therefore plausible to assume that the cumulative displacement accumulated along the right-lateral KFF deformation zone should have been in the order of few tens of km.

11.2 Stratigraphic architecture: linking faulting to sedimentation

The Neogene stratigraphy associated with the KFF consist of an up to 3.8 km thick fining-upward succession, comprising three main sedimentary cycles, separated by angular unconformities. Field observations document a progressive up-section decline in syn-depositional tilting, recorded by the gradual disappearance of progressive angular unconformities, together with a progressive waning of synsedimentary faulting from Cycle-1 to the base of Cycle-3 (Fig. 6.3a, b and c). The presence of synsedimentary faulting, together with the overall syn-depositional architecture of the Neogene sequences indicate that the tilting must have been produced by localized uplift along KFF system suggesting fault-related topographic growth during the fault system propagation. In such scenario, the texturally immature and proximally sourced breccias and conglomerates of Cycle-1, are the stratigraphic marker for the beginning of the growing linear topography associated with the KFF development.

Furthermore, the Neogene deposits show variation in facies distribution and thicknesses along-strike of the KFF. In particular: (i) the lower portion of Cycle-1, consisting of talus breccias, is only present in the western areas (WFS and CFS; marked on the geological map on figure 6.1, by gray hatching) with greatest preserved thicknesses documented along the central WFS (Fig. 6.2). This indicates that the fault-related topographic high, from which the breccia deposits were sourced, was initially confined to the western region. The greatest thickness of talus breccia deposits along the WFS also indicate that the southern side of the KFF experienced greater sediment supply influx and/or greater accommodation space.

The upper part of cycle-, cycle-2 and the lower unit of cycle-3, generally show significant lateral thickness variations, reflecting sedimentation under the influence of active tectonics. In particular, the increase in their thickness towards the east may reflect a structurally controlled eastward migrating depocenter, developed during the eastward propagation and evolution of the KFF. By contrast, the upper part of Cycle-3 deposits is the thickest (constituting more than half of the total

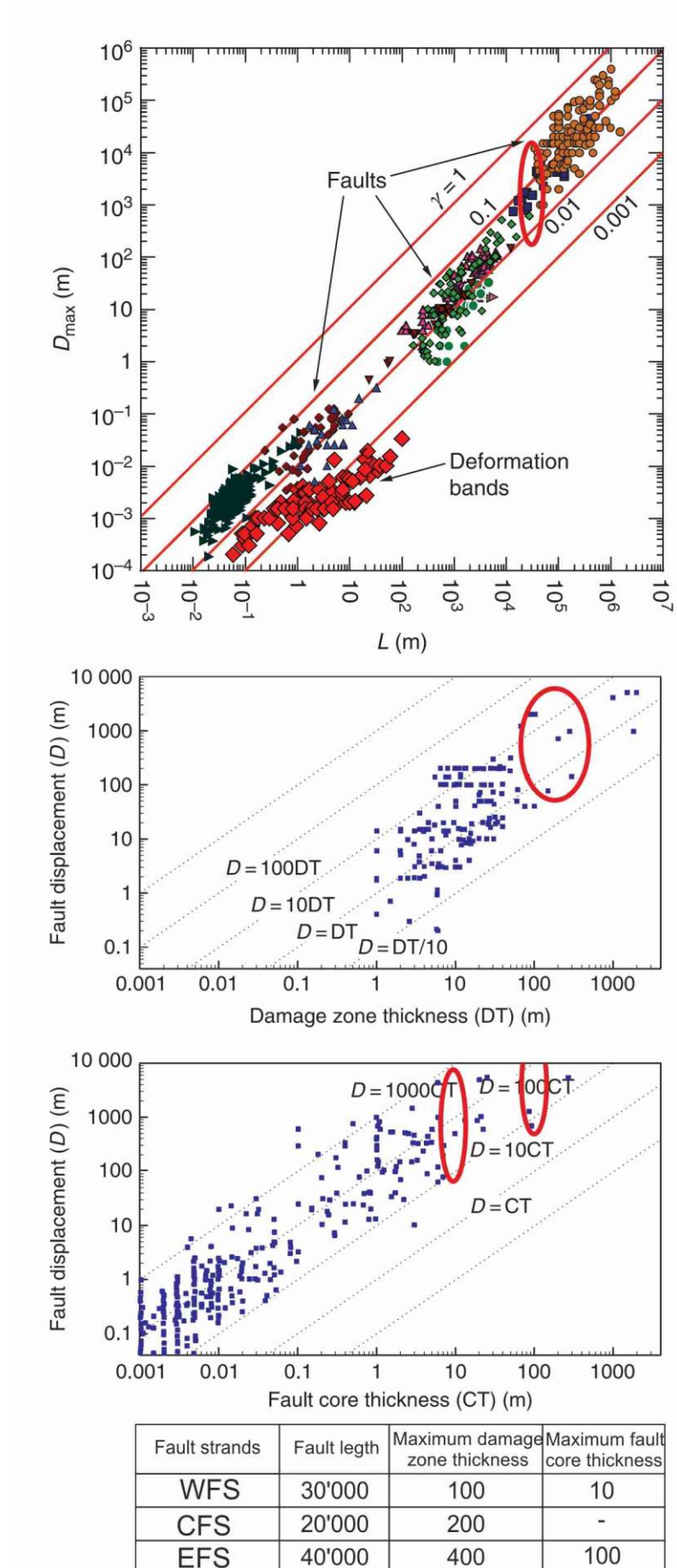


Figure 11.2 Displacement-length, damage zone thickness-length and fault core thickness-length diagrams for faults from a number of localities and settings are plotted. The measured fault parameters for the KFF

are reported in the table, red circles mark the measured fault parameters for the KFF. Figure after (Fossen, 2010).

stratigraphic succession) and the most laterally continuous. Its thickness, lateral stratigraphic continuity, and lack of synsedimentary deformation moving up-section, indicate that it was deposited during a period of tectonic quiescence and most probably of regional subsidence.

Overall, the KFF Neogene stratigraphic succession and the along strike changes in sedimentary facies, depositional architectures and deposits thicknesses reflect a history of deposition strongly influenced by tectonics and modulated by regional and local environmental changes. The increase in Neogene deposits thickness towards the east may reflect an eastward migrating depocenter, controlled by the eastward propagation and evolution of the KFF during the Neogene.

11.3 A two stage exhumation history

A thermochronological investigation was carried out for the KFF system integrating apatite (U-Th)/He and fission track dating on detrital apatites, together with hematite (U-Th)/He dating from hematite coated fault surfaces, in order to constrain the overall spatio-temporal fault related exhumation history of the KFF.

11.3.1 AHe and AFT dating

The low closure temperature for the AHe and AFT system, usually quoted as 110–120 and 60–70°C, respectively for typical rates of cooling and grain sizes (Farley, 2000) makes AHe and AFT thermochronology particularly useful for assessing age of the late-stage deformation/exhumation history affecting the uppermost portions of the crust where brittle deformation and faulting predominates.

The AHe thermochronological data defines two mean age populations, clustering at ~18 and ~4 Ma, respectively. Their spatial distribution is markedly different along the strike of the KFF. In particular, the first Early Miocene exhumation episode is recorded by the basement samples IR5, IR8 and IR15, located along the southern and central zones of the KFF. The second, early Pliocene, exhumation episode is chiefly recorded from the Neogene deposits along the EFS (Fig. 10.1).

The AFT data from detrital apatites from one pre-Neogene and two Neogene basin samples exhibit mixed ages ranging from ~95 to ~40 Ma. This indicates that the basement units, that now outcrop at the surface, were most probably below the closure temperature (100-120 °C) of the AFT system during the first exhumation event (at ~18 Ma), implying maximum exhumation depths of less than 4 km. Similarly, the basement and Neogene units have not been reset for the AFT system by Miocene burial (>4 Ma), implying maximum burial depths prior to exhumation of less than 4 km. Collectively, the AHe and AFT data from the Neogene basin sediments, imply burial temperatures in

excess of ~ 60 °C and less than 100 °C, which depending on the geothermal gradient translate to burial depths varying between ~ 2 to ~ 4 km, for the two events.

In this framework the first Early Miocene episode is interpreted as the beginning of faulting, topographic growth and exhumation along the KFF. A source-to-sink scenario is inferred for this time lapse, when the fault-related topographic growth caused the synchronous erosion/exhumation of the topographically prominent basement units and deposition of the eroded material in the surrounding lowland depocenter, located alongside the growing structure. This is supported by previously mentioned (i) proximal nature of the basal Ng-C conglomerates; (ii) presence of progressive angular unconformities in the basal portion of the Neogene sedimentary successions (Cycle-1 and -2); and (iii) the bedding steepness that gradually decreases up section and away from the boundary fault systems. In this source-to-sink scenario, the continental Neogene successions along the KFF is compatible with the Burdigalian-Messinian of the Upper Red Formation (Ballato et al., 2008) and, consequently, can be considered as their lateral equivalent in Central Iran. The fact that Neogene samples coming from the EFS systematically show AHe ages younger than their source rocks (the Paleozoic and Mesozoic basement) indicate that they have been thermally reset. Indeed, the reconstructed Neogene stratigraphy indicates that the succession is up to 3.8 km thick (Fig. 6.2), well above the thickness needed to reset the AHe system at the base of the succession in normal continental settings with and flat geothermal gradient. (e.g. 25 ± 2.5 °C/km, Chapman, 1986). It is therefore inferred that with the exception of the western and central area of the KFF zone (i.e., samples IR-5, IR-8 and IR-15 in Fig. 10.1) the thickness of these Neogene deposits was sufficient to reset the (U-Th)/He system of the detrital apatite grains hosted within both the pre-Neogene and the basal Neogene successions. Renewed fault activity and fault-related exhumation occurred at ~ 4 Ma, which is only recorded in those area where the AHe system was previously reset (IR-10, IR-11, IR-12, IR-13 and IR 18; Fig. 10.1). This second exhumation episode is further documented by the northward and southward post-depositional tilting of the Neogene units (particularly the Ng-GM deposits), to the north and south of the KFF respectively.

This event was characterized by widespread erosion that preferentially targeted the lithologically weaker Cycle-3 units, consisting of marls and gypsiferous marls deposits. Differently to the first event, there is no stratigraphic record (at least in the study area) documenting the topographic growth and general unroofing along the KFF. In fact, a major erosional and angular unconformity separates the Neogene successions from the Quaternary alluvial deposits, suggesting a long period of non-deposition lasting until ~ 56 ka as attested by OSL ages (refer to section 10.3). Within this general scenario, sample IR-17 that exhibits an average age that lies between the two mean age clusters, is interpreted to have been partially reset. Finally, occurrence of the second

exhumation episode along the KFF allows to constrain the maximum age for the topmost Neogene successions as >4 Ma, still compatible with a stratigraphic position equivalent to that of the Upper Red Formation (e.g. Ballato et al., 2008).

11.3.2 HeHe dating

The observed range in effective closure temperatures for the hematite (U-Th)/He system ranges from ~50 to 250 °C within a single aliquot appears to correspond to the range of individual crystal grain sizes (Evenson et al., 2014; Farley and Flowers, 2012). This means that the individual crystal is likely the diffusion domain and closure temperatures increase with grain size. Hematite He ages from fault surfaces may record the timing of ambient cooling from tectonic exhumation, constrain pre- or syn-kinematic hematite formation, or rapid cooling from hot fluids or localized friction during fault slip.

The HeHe results from samples collected along the EFS area, show mean ages ranging from ~4 to ~8 Ma with standard deviation errors that overlap with the ~4 Ma event of the AHe derived ages. The AFT ages of the Neogene sediments are not reset by Miocene burial. This suggests that temperatures in the basins were not significant enough to reset the hematite (U-Th)/He ages if the hematite had indeed formed prior to the initiation of basin exhumation along the strike-slip fault systems. Nevertheless in each hematite (U-Th)/He sample, the aliquot dates range from 10-12 Ma down to ~2 Ma. Given that, it has been demonstrated that hematite exhibits “multi-domain diffusion” behavior (e.g. Farley and Flowers, 2012), because an aliquot of hematite is an aggregate of individual crystals, it is reasonable to assume that the observed range of closure temperatures in any given aliquot is a function of the range of grain sizes in that aliquot. This assumption appears to true for data presented in Farley and Flowers (2012), Reiners et al. (2014), Evenson et al. (2014) and Farley and Flowers (2012), Reiners et al., (2014) and Evenson et al., (2014). This implies that the coarser is the mean hematite grains population, the more retentive and the higher the closure temperature and the older the resulting mean age.

A conservative interpretation of the HeHe ages might be that the oldest individual hematite He ages may record hematite formation from the fluids circulating through the basin ca. 10-12 Ma. These fluids are precipitating hematite in fractures and faults likely during active faulting (i.e., creation of permeability). Alternatively, these ages could also reflect the initial stage of cooling from exhumation, requiring hematite formation between ~15-12 Ma. The other ages from each of the samples record rapid cooling due to fault-related exhumation. The clustering of individual ages between 9 and 6 Ma from samples IR2-1 and IR3-2 implies rapid cooling during that discrete time interval, likely linked to activity on the strike-slip fault system. Sample IR3-19 includes individual ages between ~4-2 Ma. These aliquots likely contain a higher proportion of lower retentivity domains

and are thus capturing a more recent part of the exhumation history complementary to the AHe data. Furthermore it is worth emphasizing that on-going slip on these slip surfaces and the possibly progressive grain-size reduction may influence the diffusion domain lengthscale, making the samples progressively less retentive to helium.

The HeHe results reveal a apparently complex thermal history, mainly caused by the closure temperature-grain size dependence of the HeHe system and by all the processes which may control the temporal evolution of hematite grain size population in active faults system.

AHe thermochronology results indicate KFF system propagation was punctuated in time and space, and associated with two major episodes of fault-related exhumation, at ~18 Ma (Early Miocene) and ~4 Ma (Early Pliocene), respectively. The AHe and AFT data from the Neogene basin sediments imply burial temperatures in excess of ~60 °C and less than 100 °C. This indicated that the HeHe single aliquots ages register both formation ages at the end of first exhumation event (>6-4Ma) and exhumation ages during the second exhumation event (<6-4 Ma).

10.4 Quantifying and comparing exhumation and slip rates

From the above discussion, it emerges that the KFF experienced a punctuated history of fault-related exhumation consisting of two major events. This first fault-related exhumation event started at ~18 Ma and progressively waned to a period of relative tectonic quiescence and inferred generalised subsidence during deposition of Cycle-3, some time before ~4 Ma. This time lapse probably corresponded to the time when syn-sedimentary faulting and tilting ended (mainly during the deposition of the Cycle-3 Ng-GM deposits). In absence of any age constrain on the Neogene stratigraphy and therefore on the time laps of the event, the exhumation rate associated with the first exhumation episode cannot be estimated.

The second exhumation event started in early Pliocene (at ~4 Ma) and it is interpreted to be responsible for the present overall structural architecture of the KFF. For each sample that records the early Pliocene event, AHe ages were converted to exhumation rates using a typical continental geothermal gradient of 25 ± 2.5 °C/km (e.g. Chapman, 1986), an mean ambient surface temperature of 16 °C (average annual temperature for Kashmar; <http://en.climate-data.org/location/5127/>) and a closure temperature of 70 °C (Farley, 2000). Accordingly, depth of the base of the apatite Partial Retention Zone (PRZ) prior to the onset of denudation is therefore assumed at ~2.1 km. Assuming closure isotherms are roughly parallel to local mean elevation and taken into consideration that samples were collected from approximately the same mean elevation at each location (see SWATH profile in figure 10.1), exhumation rates were not adjusted for local sample elevation. The calculated exhumation rates vary between 0.4 and 0.7 km/Ma, with a mean exhumation rate of 0.6 km/Ma. Not

having a constrain on the regional mean surface elevation during the early Pliocene, a reliable rock uplift or surface uplift rate cannot be estimated.

Slip-rates can be also estimated for the KFF early Pliocene event along the EFS. Assuming that the faulting started at ~4 Ma and continued at a constant rate, resulting in a cumulative slip displacement ranging from 8-10 km (see section 6.2); the slip rate for the EFS range from 2 to 2.5 mm/yr. The calculated slip rate is comparable with those obtained for the E-W oriented strike-slip Doruneh Fault ranging from 1.3-2.5 mm/yr (Farbod et al., 2011; Fattahi et al., 2007; Walpersdorf et al., 2014) and Dasht-e-Bayaz fault ranging from 1-2.5 mm/yr (Berberian and Yeats, 1999; Walker et al., 2004).

Exhumation rates along regional strike-slip fault systems have been shown to vary greatly both from fault to fault, but also along the same fault systems. For example, along the San Andreas Fault system, exhumation rates span from 0.03 to 10 km/Ma, with mean values of 0.4 km/Ma (Buscher and Spotila, 2007; Niemi et al., 2013; Spotila et al., 1998; Spotila et al., 2001; Spotila et al., 2007a; Spotila et al., 2007b). Furthermore, Spotila et al. (2007b) show that the uplift rates variations along the San Andreas Fault did not simply correlate with the degree of transpression (plate obliquity) precipitations or rock erodibility. Mean exhumation rates seem to be somewhat higher in the Alaskan Range fault system, in the order ~1km/Ma (Fitzgerald et al., 1995), possibly because affected by highly erosive glacial processes (Headley et al., 2013). Therefore, the calculated long-term exhumation rates for the KFF system in intraplate Central Iran are comparable with those found along major plate boundaries associated strikes-slip systems.

Finally, the calculated exhumation rates are comparable with those obtained for the Alborz (0.2-0.7 km/Ma; Axen et al. (2001) Ballato et al. (2013), and the Zagros (~ 0.2-0.6 km/Ma; Mouthereau (2011), for the same time frame. The fact that regional exhumation along major orogenic belts and focused exhumation located along intraplate strike-slip fault systems exhibit comparable rates of exhumation during the same time lapse, suggests similar denudation rates despite the tectonic setting or the scale of the exhuming area. This seems to suggest that the rate of denudation/exhumation is likely mainly climate-controlled, but its location and scale is strongly controlled by tectonic processes.

11.5 The long-term evolution of the Kuh-e-Faghan Fault: enucleation, propagation, and topographic growth

Deformation in intraplate settings is generally not confined to narrow linear belts, but it is often distributed along broad zones of diffuse deformation (e.g. McKenzie and Jackson, 1983; Molnar and Tapponnier, 1975; Storti et al., 2003). In such settings, analogue modeling studies have shown

that strike-slip fault systems enucleate and evolve from distributed to localized, through-going fault strands (for review Dooley and Schreurs, 2012).

Within this general framework, and in the assumption that the long-term topographic evolution and stratigraphic response was structurally controlled during the documented two-stage history (at ~18 and ~4 Ma, respectively) of fault zone development, a five-step model is proposed for the long-term evolution of the KFF. The fault system enucleated in the west and propagated eastward, accompanied by topographic growth and syn- to post-tectonic sedimentation.

11.5.1 Fault system nucleation

The fault nucleation stage is characterized by the initial topographic growth and basement exhumation, in a scenario of diffuse deformation at ~18 Ma (Fig.11.3; point 1*). Such topographic growth is inferred to have been achieved by a combination of: (a) local transpressive regimes (e.g. Cunningham, 2013; Fossen and Tikoff, 1993; Robin and Cruden, 1994; Sanderson and Marchini, 1984), (b) structural irregularities such as stepovers (Aydin, 1985; Carne and Little, 2012; Finzi et al., 2009; Hilley and Arrowsmith, 2008), (c) local variations in master fault dip (Dair and Cooke, 2009), (d) pervasive, tectonically induced, fracturation and associated volume increase accommodated (between 5 to 10% volume increase; Braun, 1994; Le Guerroué and Cobbold, 2006; Schopfer and Steyrer, 2001; Schrank and Cruden, 2010). The net result of these processes operating together and over different spatial and temporal scales is the growth of a topographically prominent bulge along the evolving fault zone (Fig.11.3; point 1*). In absence of well-developed drainage networks the eroded material is deposited into the adjacent less elevated areas by rock avalanches, to form thick packages of proximally-sourced talus deposits at the base of Cycle-, which are typical of tectonically active terrains (Fig. 11.3 point 2*).

11.5.2 Fault localization and propagation

Expectedly, faulting is initially accommodated by a network of distributed *en-echelon* Riedel shears that successively merged by sideways propagation or linkage to form major, through-going master faults. In addition, due to the strain hardening and velocity-strengthening properties of poorly consolidated syn-tectonic sediments (e.g. Scholz, 2002), fault propagation is inhibited within the newly deposited material. This has the effect of favoring faulting along areas free of unconsolidated sediments, causing faulting activity to migrate inwards, gradually localizing along sub-vertical fault zones at the basement-sediment interface (Le Guerroué and Cobbold, 2006; Fig. 11.4 points 3*). This positive feedbacks between topographic growth, erosion, sedimentation and inward fault migration is the primary driver for the progressive narrowing of the fault system and of its topographic growth. As a result, syn-sedimentary faulting accompanies the topographic growth and the progressive tilting of the deposits (Fig.11.4 point 4*). The progressively more developed drainage network produced

increasingly texturally mature sediments, transitioning into the fluvial conglomerates of the upper part of Cycle-1 (Fig.11.4 point 5*).

The across-strike thickness variations within Cycle-1 deposits (thicker and more proximal to the south) suggests an overall asymmetric topographic growth of the developing fault system. This evidence may be explained in a scenario of partitioned transpressive regime, between the northern (strike-slip dominated) and southern (reverse and oblique-slip dominated) sectors of the developing KFF system (cf. Woodcock and Rickards, 2003; Figure 11.4 point 6*).

With continuous deformation, the principal fault strands propagate length ward and become increasingly localized, resulting in the development of progressively larger damage zones. The drainage network develops further, creating larger catchments capable of producing yet more texturally mature sediments of Cycle-2. Such conditions produce proximal alluvial fans deposits consisting of gravelly sandstones, intermediate alluvial plains consisting of clinostratified and cross-bedded channel fill and bar sandstones deposits, which distally evolve into fluvio-palustrine facies (Fig.11.4 point 7*). Distribution of the Cycle-2 deposits indicates increasing thicknesses towards the NE, suggesting preferred sediment influx/rooting towards this region (Fig.11.4 point 8*).

11.5.3 Fault termination and tectonic quiescence

Development of trailing extensional imbricate fan terminations at the eastern fault tips (Woodcock and Fischer, 1986) attests for strike-slip shear dissipation at fault zone terminations. The extensional/transtensional faulting and the associated tectonically-controlled subsiding depocenters (cf. Wu et al., 2009) occurs synchronous with deposition of the basal part of Cycle-3 (Ng-GM). Their distribution and the syn-tectonic character of its deposition allow to define the distribution and geometries of the subsiding areas and basin boundary faults (Fig.11.5 point 9*). Tectonic activity progressively wanes during the deposition of unit Ng-GM as attested by the gradual up-section disappearance syn-sedimentary faulting and tilting. Successively, the Ng-MS deposits cover the entire KFF area. Their thickness, lateral stratigraphic continuity and lack of synsedimentary deformation indicate that they are deposited during a period of tectonic quiescence and, most probably, of regional subsidence. (Fig.11.6 point 10*). The change in lithology between the lower and upper part of Cycle-3, from lacustrine gypsiferous marls to lacustrine marls with subordinate sandstones might reflect an environmental/climatic change from less to more humid conditions.

11.5.4 Renewed faulting

Deformation and faulting activity resumes at ~4 Ma, reactivating most of the preexisting faults strands and creating new ones that propagates further eastward (e.g. the EFS Fig.11.7 point 11*). This renewed fault activity is considered to be responsible for the current fault zone architecture, developed in a regime of simple shear dominated strike-slip faulting.

The EFS propagates from west to east, underneath the thickest part of the previously formed Neogene stratigraphic succession. At depths, below the Neogene deposits, the EFS propagate upwards from the basement into the Neogene continental covers. The fault zone quickly localizes in its deepest levels, where sufficient confining pressure from the lithostatic load is provided by the Neogene deposits (up to 3.8 km). This allows the formation of discrete damage zones and fault cores characterized by cataclastic flow and dissolution creep deformation processes, resulting in the development of localized cataclastic and ultracataclastic sub-vertical shear zones, separated by bands exhibiting S-C fabric. Towards shallower levels, due to the reduced confining pressure, the fault zone is more delocalized and characterized by dilatant brittle behaviour, which causes broad zones of pervasively fractured rock, associated with volume increase and accommodated by vertical bulging. This causes the Neogene sediment to bulge into broad anticlinal structures with axial trace parallel to the fault zone essentially driving topographic growth. Such distributed style of deformation occurs also along the WFS and CFS, where the Neogene overburden thickness is less important than along the EFS. The renewed topography growth of the entire KFF system is accompanied by widespread erosion and unroofing as attested. In the western area topographic growth is also achieved by the left-stepping geometry between the right-lateral WFS and the CFS. As this second faulting event progresses, unroofing and exhumation are greater along the EFS because of the high edibility and greater thicknesses of the overlaying Cycle-3 deposits (Ng-GM and Ng-MS) but also because the greater fault activity of the EFS. This greater exhumation allows deeper levels of the fault zone to be exposed to the surface (in the EFS), accounting for more localized nature of the EFS fault zone with respect to the WFS and CFS. In the western area, along the WFS and CFS, fault activity is relatively less than in along the EFS with topographic growth also achieved by the left-stepping geometry between the right-lateral WFS and the CFS.

The fact that no syntectonic deposits are preserved in the proximity (tens of kilometers) of the KFF during this second event suggest that the eroded material could be efficiently transported away from the KFF area. Right-lateral deformation during this second event, is mostly accommodated along the EFS which exhibits apparent displacements of up to 10 km (Fig.11.7 point 12*)

Fault system nucleation at ~18 Ma
Deposition of Cycle 1 (basal unit)

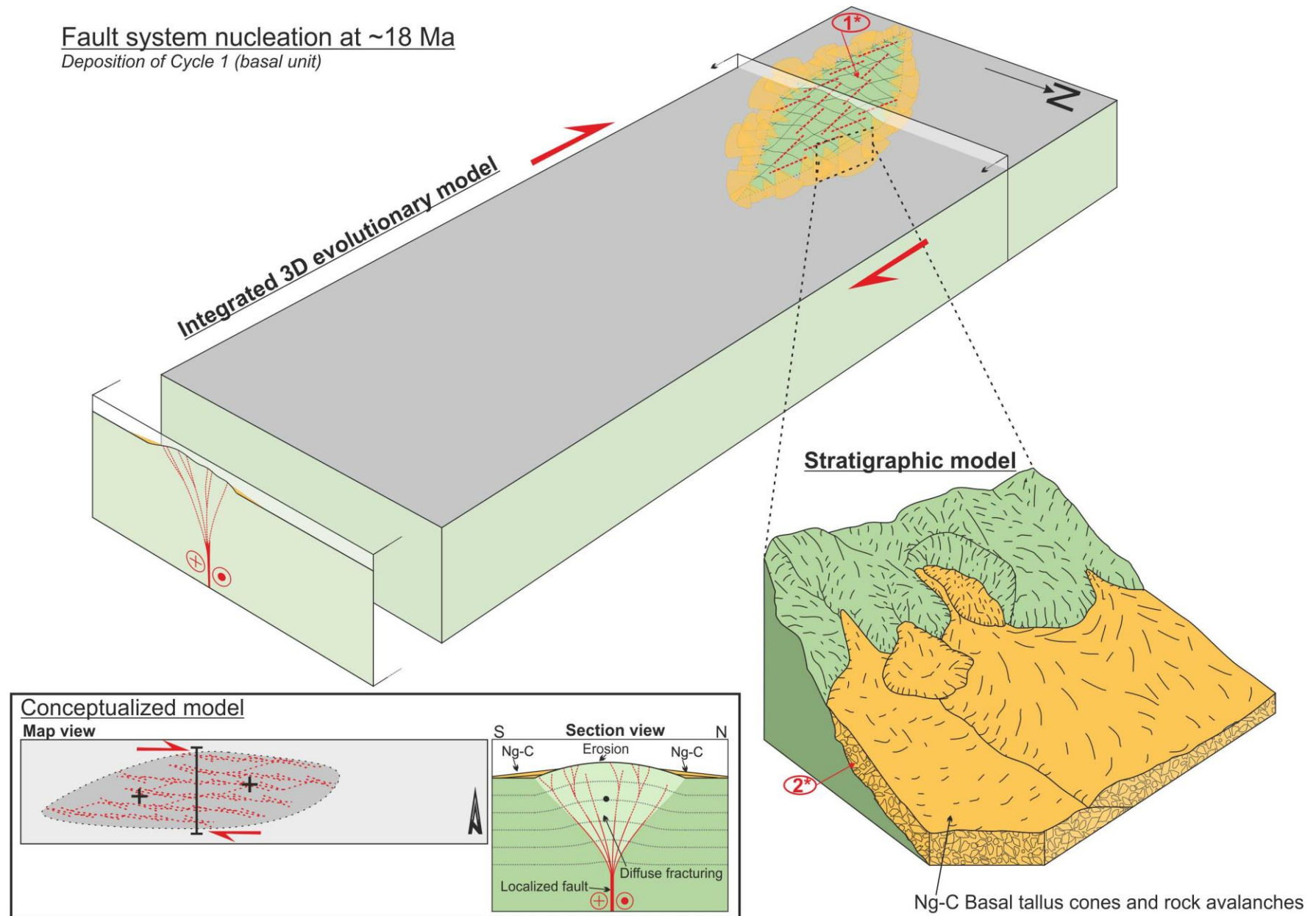


Figure 11.3. Step 1 of the proposed spatio-temporal evolutionary model for the KFF.

Fault localization and propagation *Deposition of upper Cycle1 and Cycle 2*

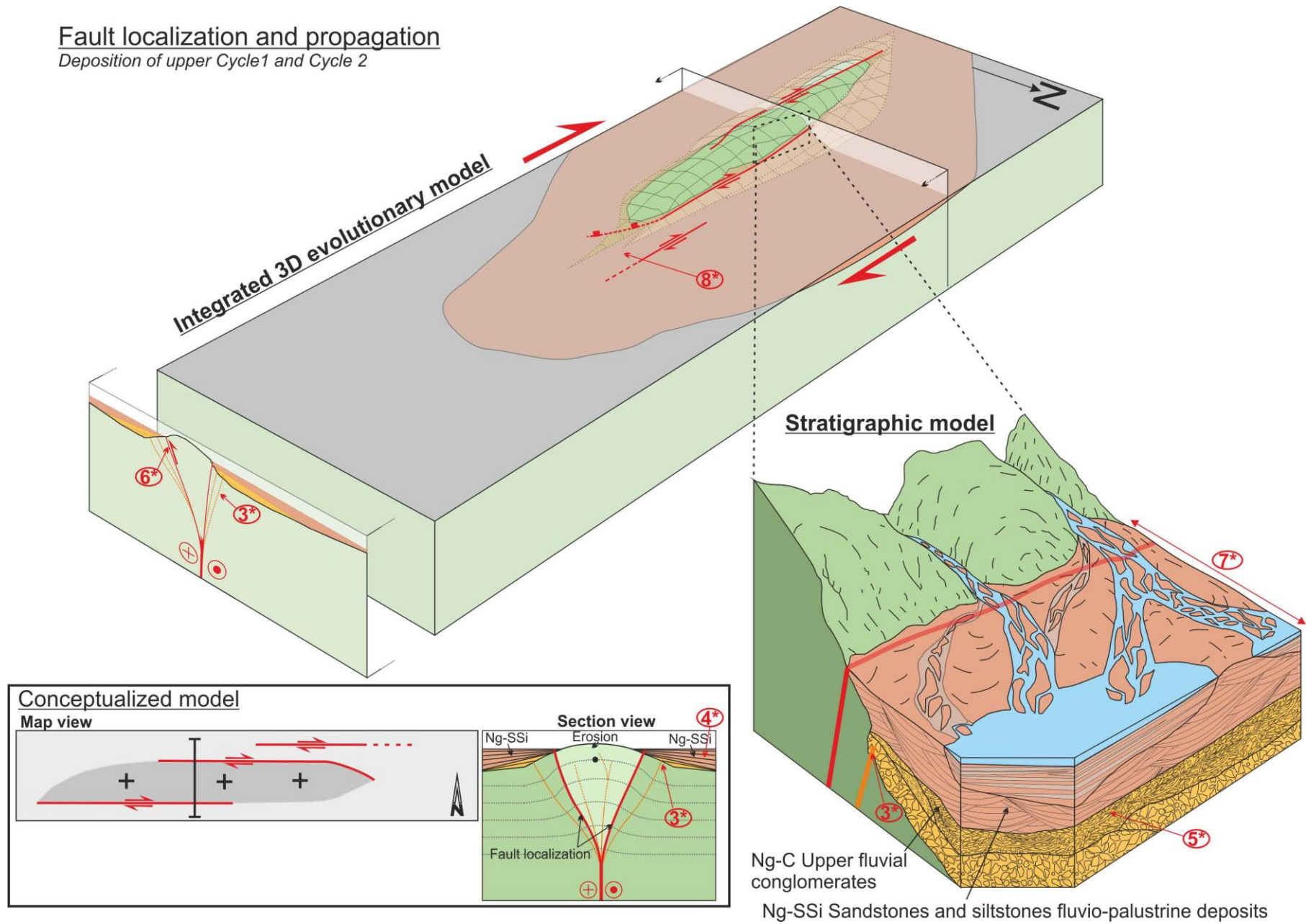


Figure 11.4. Step 2 of the proposed spatio-temporal evolutionary model for the KFF.

Fault termination
Deposition of Cycle 3 (basal unit)

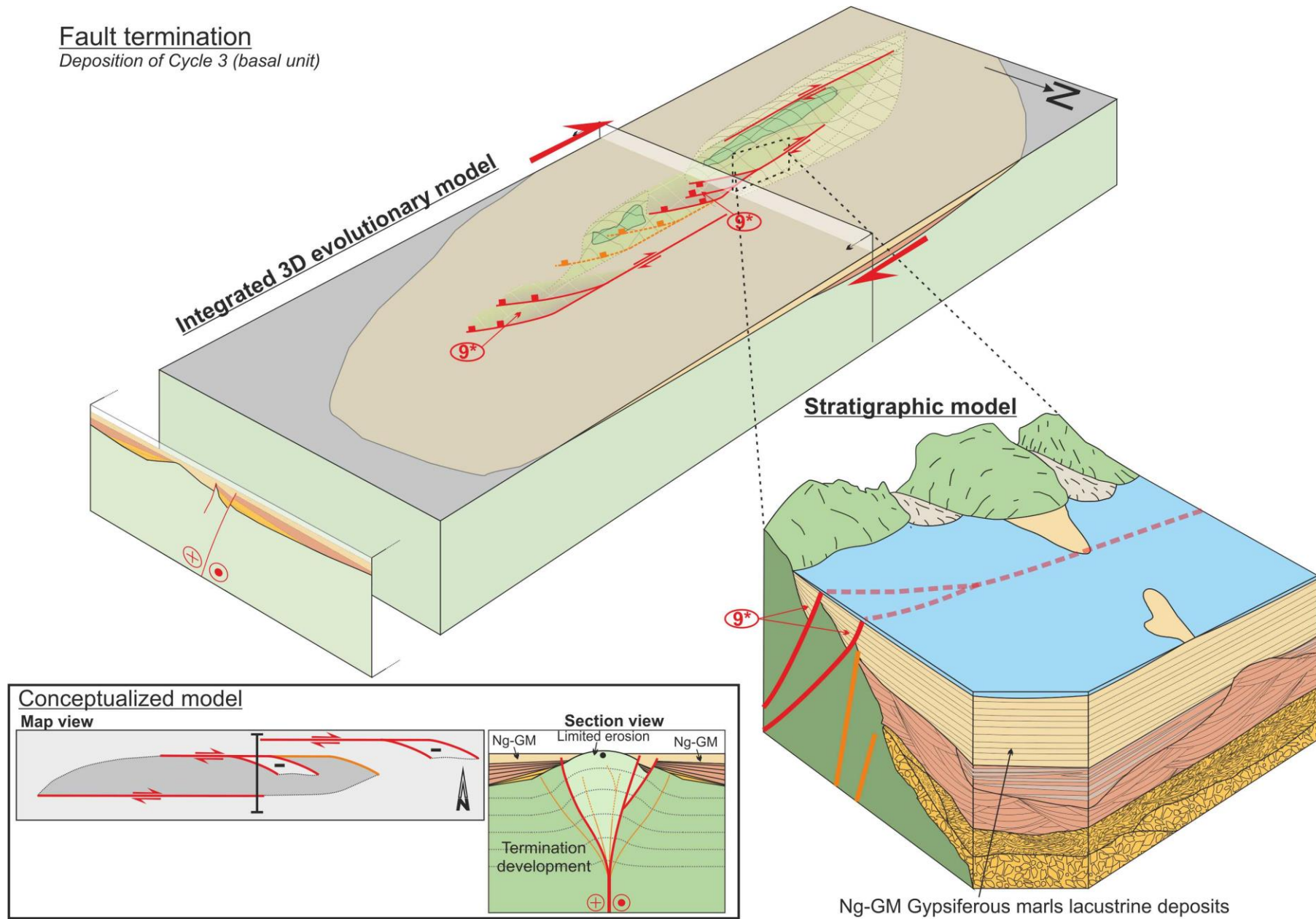


Figure 11.5. Step 3 of the proposed spatio-temporal evolutionary model for the KFF.

Tectonic quiescence
Deposition of Cycle 3 (upper unit)

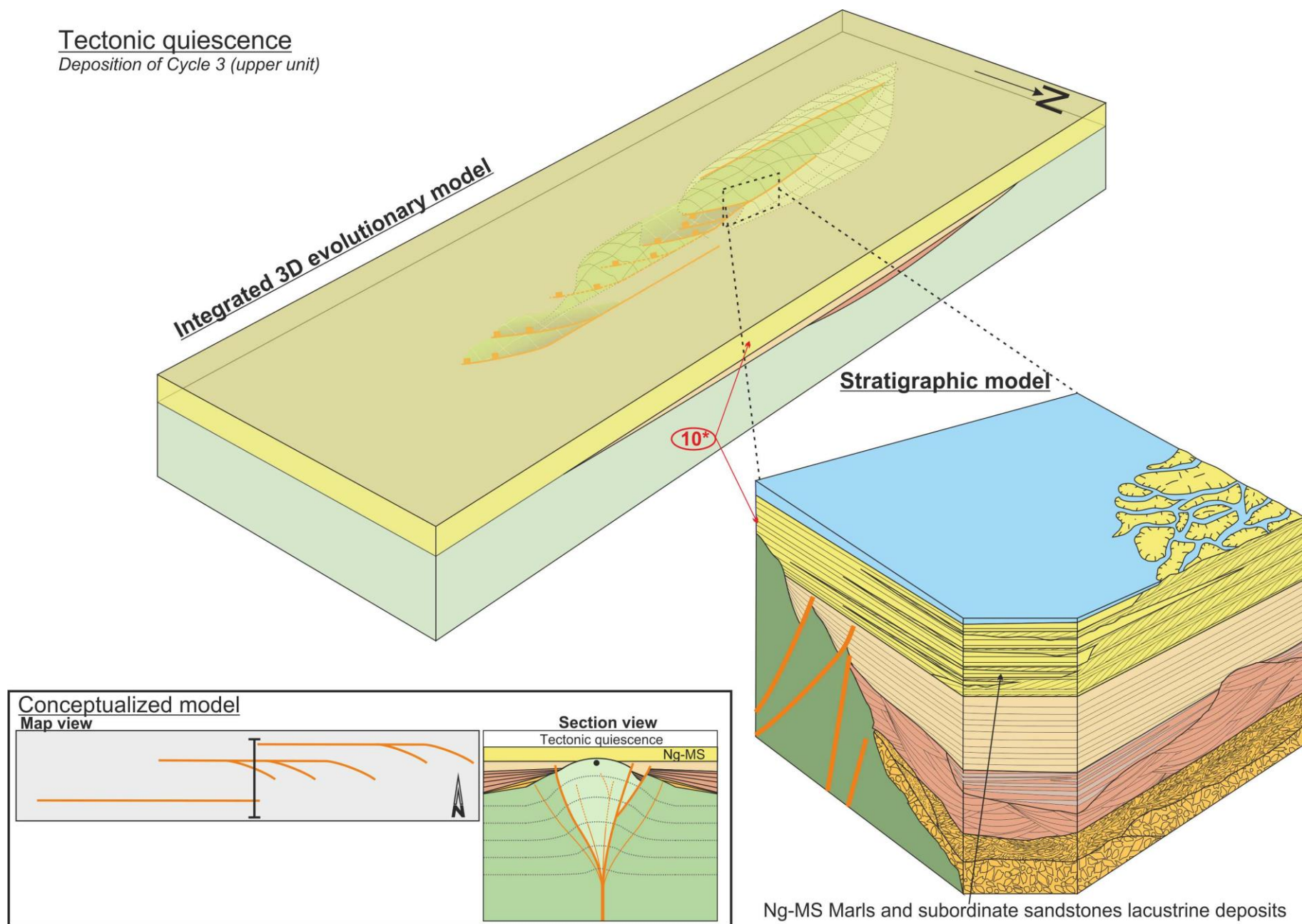


Figure 11.6. Step 4 of the proposed spatio-temporal evolutionary model for the KFF.

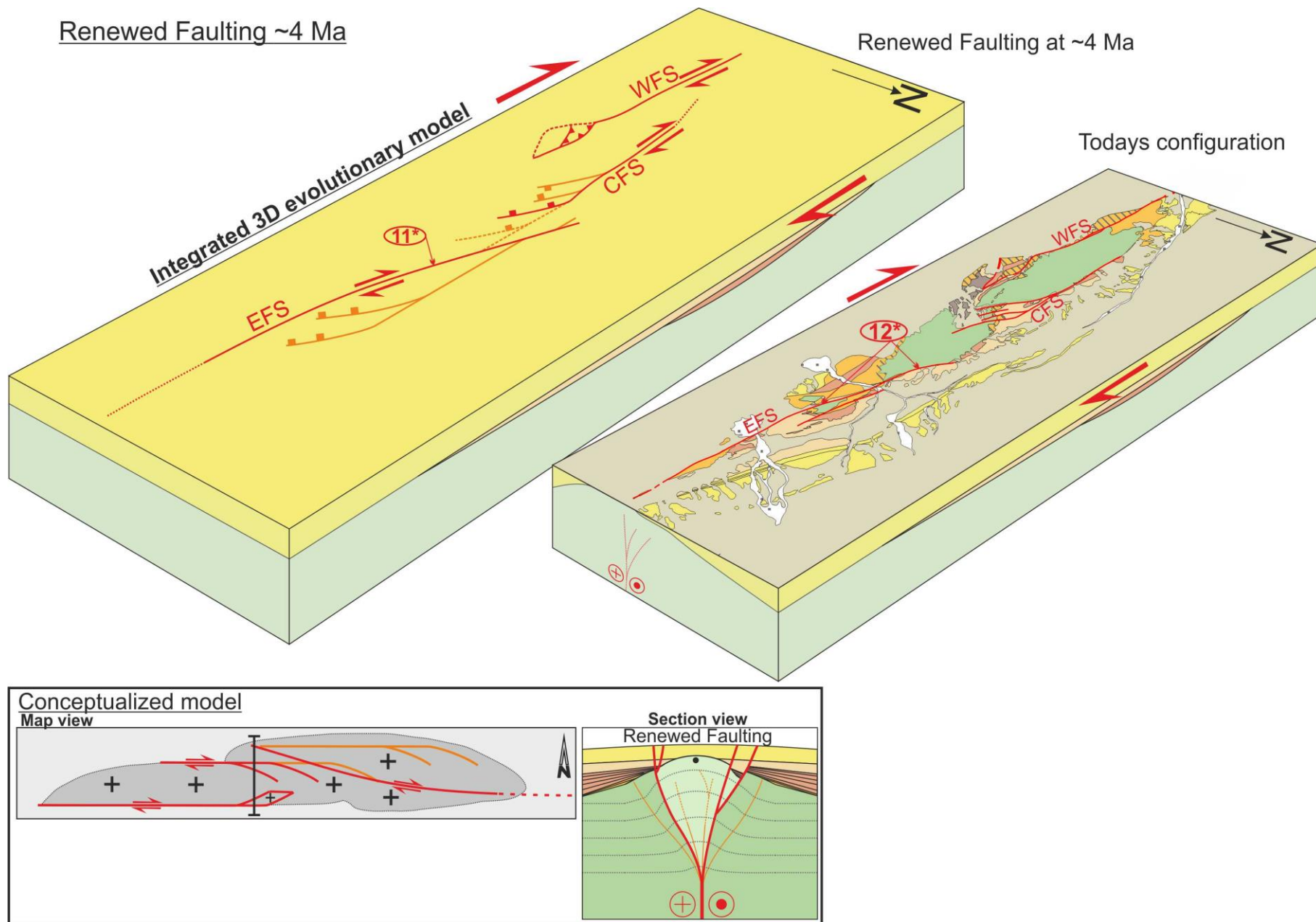


Figure 11.7. Step 5 of the proposed spatio-temporal evolutionary model for the KFF.

11.6 Topographic signal of KFF and geomorphic response to active tectonics

Form the above paragraphs it is clear that the right-lateral strike-slip KFF system, enucleated, propagated and evolved from west to east accompanied by two episodes of fault related topographic growth and exhumation starting at and ~ 18 and ~ 4 Ma. The second episode in particular it is responsible for the current fault system configuration. A link can be found between the topographic signal and the two-phase exhumation history and style of deformation in the eastward propagating KFF system. Furthermore, climatic vs. tectonic inputs to the Late Quaternary morpho-evolution of the area can be decrypted through the above described geomorphic signature.

11.6.1 Linking exhumation history, style of deformation and topographic signal of KFF

The Early Miocene (~ 18 Ma) fault nucleation stage likely left its fingerprint in the initial topographic growth and exhumation of the pre-Neogene basement, in a scenario of diffuse deformation evolving into fault localization (along the WFS and CFS, figures 11.3 11.4). The net result of these processes has to be expected in a wide topographically prominent bulge along the evolving fault zone. The partial dismantling of this first morpho-structure occurred in a source-to-sink scenario, in which an up to 3.8 km thick fining-upward syntectonic Neogene continental succession, comprising three major sedimentary cycles. They deposited all around the first 10-km wavelength relief corresponding to the ~ 42 km long western topographic domain, which thus can be identified as the remnant topographic signal of the first exhumation event (~ 18 Ma). More to the east the basal breccias of cycle- are absent and the Neogene succession starts with alluvial facies, indicating that the EFS was not yet producing topographic growth.

Strike-slip shear dissipation at fault zone terminations is testified by the development of trailing extensional imbricate fan terminations at the eastern fault tips of the CFS and to the north of the EFS (see section 11.5.3). The extensional/transensional faulting and the associated tectonically-controlled subsiding depocenters are recorded in the internal topographic discontinuity of the western domain, given by a low relief area, which dissects the ridge from north to south in a jagged fashion. Tectonic activity progressively waned during the deposition of the upper Neogene units as attested by the gradual up-section disappearance of syn-sedimentary faulting and tilting.

After this phase of tectonic quiescence, deformation and fault activity renewed at ~ 4 Ma, reactivating most of the preexisting fault strands and creating new ones that propagated further eastward (e.g. the EFS). The EFS propagated from west to east, underneath the thickest part of the previously formed Neogene stratigraphic succession. The fault zone quickly localized in its deepest levels, where sufficient confining pressure from the lithostatic load was provided by the Neogene deposits (up to 3.8 km). Towards shallower levels, due to the reduced confining pressure, the fault zone was again more delocalized and whole characterized by dilatant brittle behavior, which caused

the Neogene sediment to bulge into a broad anticlinal structure, with axial trace parallel to the fault zone. This essentially caused renewed topographic growth of the western domain and new bulging to the east. The renewed topographic growth of the entire KFF system was accompanied by widespread erosion and unroofing. This exhumation event was greater along the EFS because of the high erodibility and greater thicknesses of the cycle3 deposits but also because of the greater fault activity of the EFS (see section 11.5.4). This greater exhumation allowed deeper levels of the fault zone to be exposed to the surface. The topographic signal of such an exhumed deep fault zone is given by the ~23 Km long eastern topographic domain, showing an overall eastward narrowing and decreasing of elevation and relief.

11.6.2 Constraints on Quaternary morpho-evolution

The fact that no syn-tectonic deposits are preserved in the proximity (tens of kilometers) of the KFF during the second event suggests that it was followed by an important Plio-Pleistocene erosional phase, testified by the regional paleo-pediment cutting the tilted Neogene deposits (Fig. 7.4a-d and h). The progressive eastward topographic growth of the KFF deformation zone is confirmed by the eastward increase of minimum topography of the range, that corresponds to a progressively higher (i.e. transient) relict base level of erosion, roughly corresponding to the paleo-pediment surface. This fault-related topographic arrangement strongly conditioned the Quaternary drainage network evolution in the area, in response to base-level changes and consequently the architecture of the three alluvial fan generations developed around the KFF ridge. The telescopic arrangement of alluvial fans on the northern piedmont of the KFF ridge and the stacked arrangement on the southern one can be related to: i) the asymmetric growth of the ridge according to the position of the fault strands along which fault localization occurred; ii) the re-arrangement of the drainage network in response to- and with the effect of local base-levels changes.

Field surveys outlined three generation of telescopically arranged alluvial fan deposits of geomorphological Zone 1 (Fig. 7.2 and 7.3), progressively younger from Qt1N to Qt3N. Similarly the terraced alluvial deposits in Zone 3 progressively younger from T1 to T3. OSL ages indicate that T1 and T3 are 8.06 ± 0.6 and 50.49 ± 3.34 ka respectively and Qt2N is 25.86 ± 6.5 ka. It is inferred therefore, that the three generation of alluvial fans and the three orders of alluvial terraced deposits are coeval and therefore have inferred ages of ~53, ~24 and ~6 ka. Accordingly, the Plio-Pleistocene erosive phase likely continued until ~53 ka. Thus, although a tectonic control was exerted on the architecture of the alluvial fans in different sectors of the KFF ridge, the coherence of the three age populations of Quaternary deposits with the OSL and IRSL ages obtained regionally for the Quaternary alluvial fan deposits in eastern Iran (Walker and Fattahi, 2011; and references therein), and with the ^{10}Be surface abandonment ages obtained by Regard et al. (2006) suggests that alluvial

deposition dynamics in the KSF and KFF area is most likely the result of Late Quaternary and Holocene, climate-driven aggradation phases that affected the entire Iranian Plateau.

11.6.3 Constraints on fault-related Quaternary uplift

As documented by the quantitative alluvial fan slope analysis performed in geomorphological Zone1 (Fig.9.2), tilting of the alluvial deposits, interpreted to be associated with the fault-related topographic growth of the KFF, has been active throughout the Quaternary time.

Tentatively the total surface uplift and the surface uplift rate, in correspondence of the main faults, can be calculated. The observed difference in elevation between the fan profiles of the three generations is potentially due to a combination of tectonic uplift, erosion/deposition dynamics and thus possibly to differently dominated base-level changes. Nevertheless, a conservative estimation of the tectonic uplift rate can be performed by taking into account only the fraction of elevation difference due to slope angle difference between Qt1 and Qt3 for the sector closer to the major faults. Thus, we just measured this elevation difference in correspondence of the mean N-S projected fault location (elevation differences is marked by dw and de in Fig. 9.2). The obtained dw and de values are 44 and 49 m respectively. However, from the fan profiles geometries it is clear that in “west” area a progressive tilting of Qt1, Qt2 and Qt3 occurred since the deposition of Qt1N whereas in “east” area since the deposition of Qt2N (parallel to Qt1N). Therefore, the uplift rate in correspondence of the fault is 0.9 and 2.6 mm/yr for the “west” and “east” areas, respectively. It is worth to note that these considerably different uplift rates are not to be considered as representative over the long-time scale, but it is likely that the single fault strands of the KFF evolved through punctuated, diachronous and likely in some cases coseismic events.

Finally, the eastward propagation of the KFF system up to present is testified also by: i) the eastward increase of top surface elevation of the same generation of alluvial landforms and particularly for the youngest generation of terraced alluvial plain deposits (~6 ka), whose elevation ranges from 869 m a.s.l. in the westernmost KFF area to 1038 m a.s.l. in the easternmost; ii) the documented Late Pleistocene (KSF and KFF) to Holocene (KFF) right-lateral strike-slip faulting. This evidence together with the elevated seismicity of the area indisputably implies that KSF and KFF are major active right-lateral fault systems in the northern edge of the Lut Block.

Overall, the study shows that, the generation and development of the Quaternary alluvial deposits were primarily controlled by Late Quaternary and Holocene, climate-driven aggradation phases recognized throughout the Iranian plateau (e.g. Regard et al., 2006; Walker and Fattahi, 2011); nevertheless their geometric configuration and style of deposition documented along the KFF have been strongly influenced by the fault system tectonic activity.

11.7 Implications

This study has reconstructed the spatio-temporal evolution of the KFF system in Central Iran through an integrated approach that combined structural stratigraphic and geomorphological field investigation with thermochronological and geochronological analysis. The results from such reconstruction bear important implications, on both the Neogene-Quaternary tectonic history of Central Iran, and on the understanding of the processes involved during intraplate strike-slip faulting.

11.7.1 Regional tectonics

Despite the challenge posed by the apatite quality and preservation potential, the data presented above document that KFF experienced two main episodes of fault-related exhumation and topographic growth, dated early Miocene (at ~18 Ma) and early Pliocene (~4 Ma), respectively. This two-fold exhumation history well fit with the major stages of formation of the Iranian plateau.

The first tectonic/exhumation event recognized in the KFF during the early Miocene is nearly coincident with thermochronological results obtained from the Zagros, Alborz, Talesh orogenic belts (Axen et al., 2001; Ballato et al., 2013; Gavillot et al., 2010; Guest et al., 2006; Madanipour et al., 2013). It also correlates well with the late-stage, early Miocene exhumation of the Kashmar-Kerman Tectonic Zone (Fig. 2.1), which is interpreted as the transition from extension to compression in the region (Verdel et al., 2007). This timing is furthermore in agreement with the inferred “hard” continent-continent Arabia-Eurasia collision (Ballato et al., 2011) and closure of the Neotethys Ocean sea way (Okay et al., 2010).

The second event dated as early Pliocene is instead coeval with the widespread tectonic reorganization of the Iranian Plateau, as inferred from the recognized acceleration in uplift rates in the Alborz and Talesh orogenic belts and by fault kinematic changes in the Kopeh Dag and in the Zagros–Makran Transfer Zone (Axen et al., 2001; Hollingsworth et al., 2010; Madanipour et al., 2013; Rezaeian et al., 2012; Shabanian et al., 2009a). It is worth noting that this age is also in agreement with previous inference on the onset of the intraplate strike-slip tectonics in the region (e.g. Allen et al., 2004). Finally, the Miocene-Pliocene boundary also corresponds to the time lapse when the Zagros collisional zone has been inferred to have become too overthickened to sustain further shortening (Allen et al., 2004; Austermann and Iaffaldano, 2013). Despite the ultimate cause of the Pliocene regional tectonic re-organization across the Iranian Plateau is still uncertain, the AHe age data presented in this study constitute the first direct documentation of such Pliocene event in Central Iran.

Nevertheless, our findings do not support the regional kinematic model of Central Iran firstly proposed by Jackson and McKenzie (1984) and successively adopted and modified by other authors (e.g. Allen et al., 2011; Farbod et al., 2011; Fattahi et al., 2007; Walker and Jackson, 2004; Walker

et al., 2004; Walker and Khatib, 2006). In particular, evidence of Neogene-Quaternary NW-SE to E-W right-lateral strike-slip kinematics (Nozaem et al., 2013; this study) acting at rates compatible with the regional average values (see chapter 11.4) along the northern edge of the Lut Block to the south of the Doruneh Fault are not compatible with the current kinematic configuration proposed for Central Iran. This is commonly framed into a scenario of dynamic rupture achieved through N-S dextral and E-W sinistral slip zones, associated with rigid block rotations and strain partitioning (e.g., Allen et al., 2004; Walker and Jackson, 2004; Mattei et al., 2013; Walpersdorf et al., 2014). In particular, modeling of GPS data with a block rotation model suggests that the rotations have been going on at a similar rate ($1 \pm 0.4^\circ/\text{Ma}$) over the last 12 Ma (Walpersdorf et al., 2014). This is in disagreement with the estimated ~5 to ~7 Ma onset of strike-slip tectonics in south Central Iran (Allen et al., 2004; Allen et al., 2011; Walker and Jackson, 2004). Furthermore this steady-state scenario contrasts with the Neogene-Quaternary kinematic configuration recently recognized for the northern boundary of the Lut Block, where punctuated events of fault zone (re)activation and kinematic shift in space and time have been documented (Farbod et al., 2011; Javadi et al., 2013; this study; Nozaem et al., 2013; this study).

Attempts have been made by Regard et al. (2005b) and Bonini et al. (2003) to model the evolution of the Iranian continental collision. Regard et al. (2005b), through 3D laboratory experiments, using sand–silicone plates floating on glucose syrup modeled the tectonic regime that governed the indentation of Arabia within Eurasia. Although the study gives important insight into how the dynamics of indentation process are affected by the evolution at depth of the oceanic and continental subductions. In particular, the model predicts that all the deformation is distributed along the plate boundary with little or no deformation in the intraplate domains. Bonini et al. (2003) through an analogue modelling study shows that the deformation pattern observed in Iran, is compatible with partitioning of the N-directed Arabia indentation into a composite system of: (i) collision-oblique seismogenetic belts, with two main conjugate transpressive belts (the dextral NW–SE-trending Zagros belt and the NE–SW-trending sinistral Alborz-Aran-Torud belt) and (ii) collision-parallel seismogenetic belts, in central Iran, with a modest lateral escape of the Yazd and Tabas Block towards the Lut block along the Nayband Fault (Fig. 2.1), without the need of rigid block rotation. Nevertheless their model fails to the complex kinematic configuration documented along the northern (this study) and north-western margin (Nozaem et al., 2013) of the Lut Block.

Furthermore, Farbod et al. (2011) suggested that the complex kinematic configuration of Central Iran may be due to kinematically induced/perturbed (from the fault system themselves) spatial variation in the stress field orientation. This seems to be very likely especially in the light of the new GPS data on eastern Iran (; Fig. 2.1 Walpersdorf et al., 2014) which clearly show velocity vectors

change orientations from NNE in the south Lut Block, to north in the Tabas and central Lut Block to NNW in the in the northern Lut Blok (north of the Dasht-e Bayaz fault).

As a result, a reappraisal of the spatio-temporal kinematic evolution of Central Iran in the aftermath of the Arabia-Eurasia convergence history is necessary.

It is here proposed that the Neogene-Quaternary deformation in Iran has been primarily controlled by the spatial and temporal variations in the degree of coupling along the Arabia-Eurasia collision interface. The degree of coupling, together with the capacity of accommodating convergence along the collision zone, controlled the amount of northward convergence that was transferred to the intraplate domain and therefore controlled the deformation distribution in space and time (Fig. 11.8). The intra-plate response to such variations were in turn influenced by structural inheritances, which ultimately constrained the location, orientation and development of the deformation zones.

In this scenario, as the Arabia-Eurasia convergence history culminates in oblique continent-continent collision during early Miocene, the degree of coupling at the collision boundary transitioned from partially to fully coupled (from subduction to continental collision dominated), causing more convergence to be transferred northward. Such convergence was mostly accommodated by crustal thickening and northeastward expansion of the Zagros collisional zone, and, in part, was transferred northward through central Iran to the Alborz and Kopeh Dagh deformation belts. The Makran convergence zone, however, maintained a partially coupled collision boundary, accommodating the majority of the convergence by oceanic subduction and hence transferring less residual convergence northward of this region. This imposed a southeastward decreasing convergence velocity gradient within the intraplate domain of Central Iran (Fig. 11.8a). At the same time, the oblique geometry of the collision front enforced a northeastward escape component to the intraplate domain that resulted in the reactivation of the Kerman-Kashmar Tectonic Zone as documented along the KSF, KFF, and the DF (Javadi et al., 2013; Fig. 11.8a; Nozaem et al., 2013; Verdel et al., 2007). Within this context, the reconstructed source-to-sink scenario along the KFF places onset of deposition of Neogene continental successions of the Upper Red Formation in Central Iran at the early Miocene. This age is compatible with the Burdigalian-Messinian age of the Upper Red Formation (Ballato et al., 2008), but contrasts with the recently proposed Burdigalian-Serravallian age for the “e” member of the Qom Formation (Hadavi et al., 2010), which instead implies a possible post-Serravallian onset of the continental deposition of the Upper Red Formation. This suggests a diachronic distribution of the Neogene continental deposits and the control operated by regional tectonics on the Neogene sedimentary facies distribution and stratigraphy in Central Iran.

At the Miocene-Pliocene boundary, the Zagros collisional zone became overthickened to sustain further shortening (Allen et al., 2004; Austermann and Iaffaldano, 2013). This likely caused

a gradual decrease in the capacity to accommodate convergence along the Zagros collisional zone, resulting in an overall advancing convergent plate margin with a further increase in the intraplate residual convergence. As a result, the faster northward migration of the Zagros collisional zone with

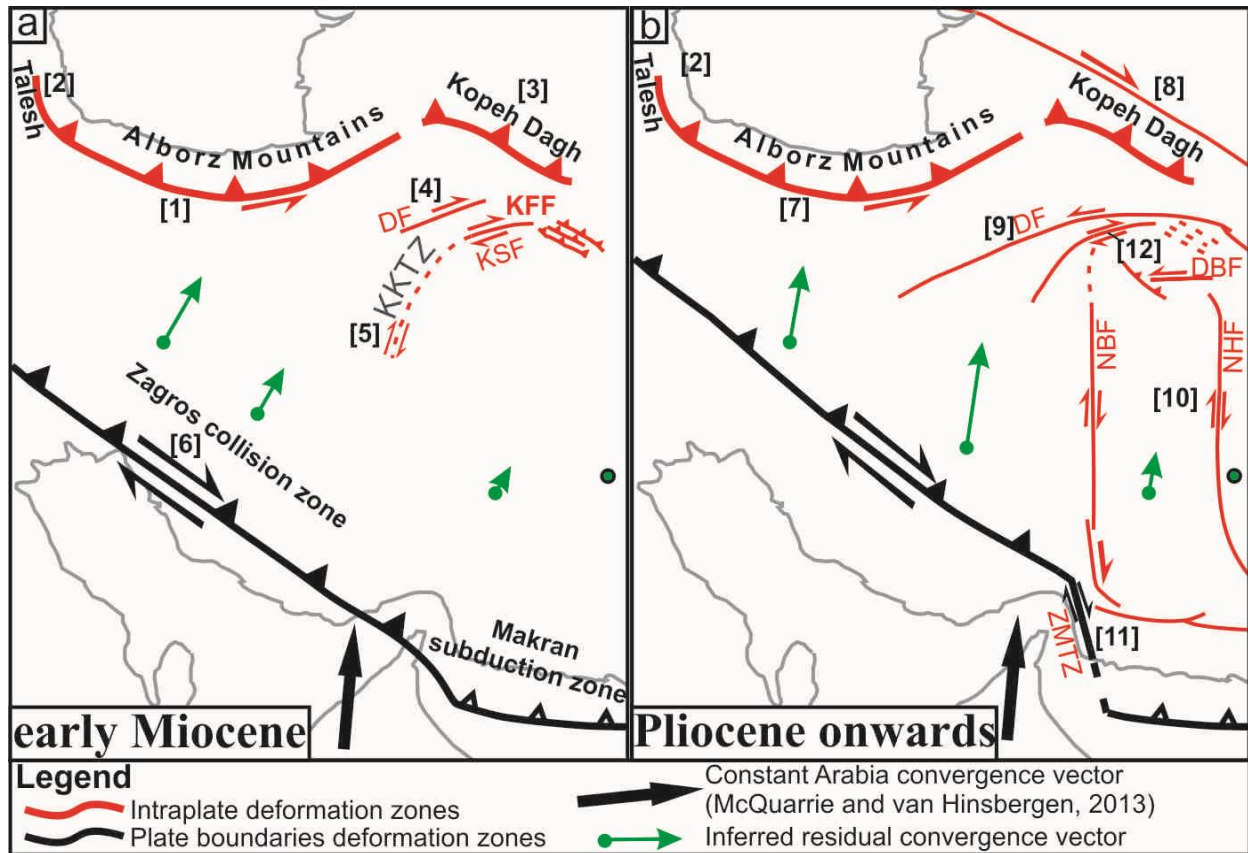


Figure 11.8 Conceptual spatio-temporal evolutionary model for the intraplate response to the Arabia-Eurasia convergence history during the last 20 Ma in Iran. (a) The early Miocene stage. (b) Pliocene onwards. Numbers refer to available time constraints on the collision-related events: [1] Ballato et al. (2013); [2] Madanipour et al. (2013); [3] Hollingsworth et al. (2010); [4] Javadi et al. (2013); [5] Verdel et al. (2007); [6] Gavillot et al. (2010), Okay et al. (2010); [7] Axen et al. (2001), Rezaeian et al. (2012); [8] Shabanian et al. (2009a); [9] Farbod et al. (2011), Javadi et al. (2013); [10] Allen et al. (2004); Walker and Jackson (2004); [11] Regard et al. (2005a); [12] Nozaem et al. (2013).

respect to the Makran subduction zone caused the formation of the dextral Zagros-Makran Transfer Zone (Regard et al., 2005). This allowed the efficient northward transfer of the Arabia convergence across the eastern margin of Iran through the development of N-S striking dextral strike-slip fault localized along the preexisting tectonic boundaries of the CIMC microblocks. This kinematic rearrangement, resulted into new configuration of the intraplate residual convergence (Fig. 11.8b). The faster northward moving intra-fault block bordered by the Doruneh Fault to the north and the Nayband Fault to the south, resulted in sinistral and dextral kinematic reactivation of the Doruneh, and Kuh-e-Sarhangi/KFF, respectively. The later dextral movement of the Kuh-e-Sarhangi/KFF has been enhanced by rapid westward propagation of the Dasht-e-Bayaz Fault across the Lut Block (Nozaem et al., 2013; Fig. 11.8b). Ultimately, convergence was transferred to the Kopeh Dag where

dextral strike-slip faulting began (e.g. Shabanian et al., 2009a). In Central Iran, this new kinematic configuration resulted in northward convergence velocities that decreased away from the Zagros-Makran Transfer Zone. This later kinematic configuration remained unchanged since then. In fact, the current GPS vector velocities show northward convergence vectors that generally decreased away from (to the northwest and east) the Zagros-Makran Transfer Zone (e.g. Vernant et al., 2004; Walpersdorf et al., 2014; Fig. 2.1).

In the light of the above paragraphs, it is worth to mention that it would be extremely interesting and valuable to model the evolution of this region (either with a numerical or analogical approach), integrating all the new findings and evidence.

11.7.2 Implications for topographic growth along intraplate strike-slip faults

Integration of the multidisciplinary data set presented in this study shows that the long-term intraplate strike-slip fault system evolution characterized by spatially and temporally punctuated fault propagation-related topography growth.

Based on the regional scenario and synchronicity with the regional deformation events leading to the growth of the Iran Plateau the reason for this nonlinear temporal evolution is partially imputable to changes in the regional (far field) stress field through time. Tectonic stresses and forces are generated at the plate margins and are transferred to the intraplate domains where they interact with preexisting structures and local (near-field) dynamically and kinematically induced stress fields. The temporal changes in those interactions and, the resulting changes in the way plate boundary stresses are transferred to the intraplate domains, may ultimately be responsible for the punctuated development of intraplate deformation. Several other near-field process that operate at the scale of the fault system, also contribute to such punctuated evolution. The nonlinear spatial variation in fault development and fault zone maturity of intraplate strike-slip fault system, reflects there diachronous propagation history and hence there along and across strike changes in the degree of fault development.

The spatio-temporal changes in far and near field processes, regulate the way plate boundary stresses are transferred to the intraplate domains and may ultimately be together responsible for the punctuated development of intraplate deformation and associated topographic growth.

Finally, from this study, it emerges that the intraplate response to regional convergence is likely a function of the degree of tectonic coupling at the collisional boundaries. In particular, it seems that the intraplate response is particularly sensitive to major tectonic changes occurring at the plate boundaries, and, as such, intraplate deformation zones can be regarded as a gage for plate-tectonics induced state of stress changes at the plate boundaries.

12 SUMMARY AND CONCLUSIONS

A multidisciplinary approach that integrates structural, stratigraphic and geomorphological field investigations with geochronological (OSL) and thermochronological (AFT, AHe and HeHe) analyses is adopted to reconstruct the spatio-temporal evolution of the Kuh-e-Faghan Fault (KFF), in northeaster Central Iran. This study was aimed at understanding (i) feedbacks among the long-term evolution of natural intraplate strike-slip systems and associated topographic growth, erosion/exhumation and syn-tectonic sedimentation history, and vice versa, how these feedback relationships influence the fault zone propagation, and (ii) any linkage between the intraplate response to the far field plate boundaries evolution.

The main results can be summarized in the following points:

1. The KFF consists of a major E-W striking, 80 km long right-lateral strike-slip brittle deformation zone, made up of three broadly left stepping, E-W striking, right-lateral, strike-slip fault strands which cut through the Neogene sedimentary cover and unconformably overlying Quaternary deposits;
2. The structural investigation reveals the KFF is characterized simple shear dominated right-lateral strike-slip deformation. The documented along-strike spatial variations of the fault population orientation, kinematics and strain regimes (restraining and releasing areas) reflect the different ways by which the overall E-W right lateral shear is accommodated, distributed and partitioned along the principal and minor fault strands of the KFF system.
3. The AFT and AHe results, together with the independently estimated maximum stratigraphic thickness of 3.8 km of the Neogene successions, implies burial temperatures in excess of ~60 °C and less than 100 °C.
4. AHe thermochronology results indicate KFF system propagation was punctuated in time and space, and associated with two major episodes of fault-related exhumation, at ~18 Ma (Early Miocene) and ~4 Ma (Early Miocene), respectively.
5. The first faulting/exhumation episode is chiefly recorded by the structural and depositional architecture of the Neogene deposits along the KFF, where a source-to-sink scenario can be reconstructed for this time frame. Topographic growth caused the synchronous erosion/exhumation of the pre-Neogene units and deposition of the eroded material in the surrounding fault-bounded continental depocenters.
6. The reconstructed source-to-sink scenario for the Early Miocene attests for the control operated by regional intraplate tectonics on the Neogene sedimentary facies distribution and stratigraphy in Central Iran.

7. Successively, the KFF gradually entered a period of relative tectonic quiescence and, probably, regional subsidence during which a thick pile of fine-grained onlapping sediments were deposited, caused the resetting of the (U-Th)/He system of the detritic apatite grains hosted both within the pre-Neogene and the basal Neogene successions.
8. The second faulting episode at ~4 Ma, recorded by the AHe and HeHe dating and by the further tilting of the Neogene deposits, caused the final fault zone exhumation of the fault system, resulting in the current fault zone and topographic architecture.
9. Collectively the stratigraphic, structural and thermochronological datasets shows that the KFF enucleated in the west and propagated eastward in two punctuated events.
10. Topographic analysis of the Kuh-e-Faghan fault-related ridge reveals that the two Neogene fault propagation and exhumation events that shaped the structural and stratigraphic architecture of the fault system can be recognized in the current topographic signal of the KFF. In particular, a first 10-km wavelength signal, corresponding to the ~42 km long western topographic domain, is likely the topographic fingerprint of the first diffuse-to-localized deformation event (~18 Ma). The overall eastward narrowing, decreasing in elevation and relief and ~23 km long eastern topographic domain, is instead identified as the remnant topographic signal of the second (~4 Ma) exhumation event.
11. Geomorphological analysis and OSL dating show that the generation and development of the of the KFF Quaternary alluvial deposits were primarily controlled by Late Pleistocene and Holocene, climate-driven aggradation phases, previously recognized throughout the Iranian Plateau by other studies. Nevertheless, their geometric configuration and style of deposition documented along the KFF indicate that they have been strongly influenced by the fault activity and by the consequent drainage network re-arrangement.
12. The presented structural and geochronological (OSL) data indisputably document Quaternary WSW-ENE to W-E oriented right-lateral strike-slip tectonics along the north-western edge of the Lut block, through Late Pleistocene to Holocene activity of the Kuh-e-Faghan fault systems.
13. The statistical alluvial fan slope angle analysis furthermore indicates that the KFF is still producing fault-related topographic growth. This growth is recorded by fan surfaces that are over-steepened with respect to slope angles predictable through maximum particle size of the deposits. Furthermore, a progressive increase of tilting with alluvial fan age and proximity to fault zones was recorded.
14. For the same time lapse (>4Ma), the estimated exhumation rates for the KFF exhibit comparable rates with major orogenic belts in the region, despite the tectonic setting. This

seems to suggest that the rate of denudation/exhumation is likely mainly climate-controlled, but its location and scale is strongly controlled by tectonic processes.

15. Furthermore the two fault related exhumation events are nearly coincident with (i) the well documented acceleration of collision-related uplift in the early Miocene, recorded along Iran major orogenic belts, and with (ii) the inferred tectonic reorganization of central Iran and the beginning of strike slip tectonics in central-eastern Iran.

From the study, it emerges that intraplate strike-slip fault systems propagation and evolution is accompanied by substantial topographic growth, exhumation erosion and production of syn-tectonic deposits, which distribution, geometry and facies characteristics are strongly influenced by the spatio-temporal propagation history and structural evolution of the fault system. Additionally, the study recognizes that due to the strain hardening and velocity-strengthening properties of poorly consolidated syn-tectonic sediments, fault propagation is inhibited within the newly deposited material. This has the effect of favoring faulting along areas free of unconsolidated sediments, causing faulting activity to migrate inwards, gradually localizing along sub-vertical fault zones at the “basement-sediment” interface. These positive feedbacks between topographic growth, erosion, sedimentation and inward fault migration is the primary driver for the progressive narrowing of the fault system and of its topographic growth.

Moreover, the study shows that the documented long term evolution history of the KFF system of intraplate Iran is characterized by punctuated events nearly coincident with major tectonic events at the plate boundaries. This strongly suggests that the intraplate response along strike-slip fault systems is particularly sensitive to major (far-field) tectonic changes occurring at the plate boundaries, and, as such, intraplate deformation zones can be regarded as a gage for plate-tectonics induced state of stress changes at the plate boundaries.

Finally, the study argues that if the new findings are contextualized into their regional tectonic framework and, together with the outcomes from recently published studies, a reappraisal of the spatio-temporal kinematic evolution of Central Iran in the aftermath of the Arabia-Eurasia convergence history is necessary. It is proposed, through a conceptualized tectonic model, that the Neogene-Quaternary deformation in Iran has been primarily controlled by the spatial and temporal variations in the degree of coupling along the Arabia-Eurasia collision interface. The intra-plate response to such variations was modulated by dynamic and kinematic effects that where in turn influenced by structural inheritances, which ultimately constrained the location, orientation and development of the deformation zones. The spatio-temporal changes in the degree of coupling, together with the capacity of accommodating convergence along the collision zone, controlled the

amount of northward convergence that was transferred to the intraplate domain and therefore controlled the deformation distribution kinematic configuration in space and time.

The revised tectonic/kinematic model needs to be improved and validated by further studies to be carried out along the major fault system of south-central Iran, in order to verify their persistence, distribution, kinematics and overall evolution.

References

- Adams, B. A., Hodges, K. V., van Soest, M. C., and Whipple, K. X., 2013, Evidence for Pliocene-Quaternary normal faulting in the hinterland of the Bhutan Himalaya: *Lithosphere*, v. 5, no. 4, p. 438-449.
- Agard, P., Omrani, J., Jolivet, L., and Mouthereau, F., 2005, Convergence history across Zagros (Iran): constraints from collisional and earlier deformation: *International Journal of Earth Sciences*, v. 94, no. 3, p. 401-419.
- Agard, P., Omrani, J., Jolivet, L., Whitechurch, H., Vrielynck, B., Spakman, W., Monié, P., Meyer, B., and Wortel, R., 2011, Zagros orogeny: a subduction-dominated process: *Geological Magazine*, v. 148, no. 5-6, p. 692-725.
- Aghanabati, A., 2004, *Geology of Iran*, Geological Survey of Iran.
- Ahlgren, S. G., 2001, The nucleation and evolution of Riedel shear zones as deformation bands in porous sandstone: *Journal of Structural Geology*, v. 23, no. 8, p. 1203-1214.
- Allen, M., Jackson, J., and Walker, R., 2004, Late Cenozoic reorganization of the Arabia-Eurasia collision and the comparison of short-term and long-term deformation rates: *Tectonics*, v. 23, no. 2.
- Allen, M. B., and Armstrong, H. A., 2008, Arabia-Eurasia collision and the forcing of mid-Cenozoic global cooling: *Palaeogeography, Palaeoclimatology, Palaeoecology*, v. 265, no. 1, p. 52-58.
- Allen, M. B., Kheirikhah, M., Emami, M. H., and Jones, S. J., 2011, Right-lateral shear across Iran and kinematic change in the Arabia-Eurasia collision zone: *Geophysical Journal International*, v. 184, no. 2, p. 555-574.
- Amini, A., 1997, *Provenance and Depositional Environment of the Upper Red Formation, Central Zone Iran*: The University of Manchester.
- Antonellini, M., and Aydin, A., 1995, Effect of faulting on fluid flow in porous sandstones: geometry and spatial distribution: *AAPG bulletin*, v. 79, no. 5, p. 642-670.
- Araujo, M. N. C., Vasconcelos, P. M., da Silva, F. C. A., de Sa, E. F. J., and Sa, J. M., 2005, Ar-40/Ar-39 geochronology of gold mineralization in Brasiliano strike-slip shear zones in the Borborema province, NE Brazil: *Journal of South American Earth Sciences*, v. 19, no. 4, p. 445-460.
- Arbolea, M. L., and Engelder, T., 1995, Concentrated slip zones with subsidiary shears: their development on three scales in the Cerro Brass fault zone, Appalachian valley and ridge: *Journal of Structural Geology*, v. 17, no. 4, p. 519-532.
- Atmaoui, N., Kukowski, N., Stöckhert, B., and König, D., 2006, Initiation and development of pull-apart basins with Riedel shear mechanism: insights from scaled clay experiments: *International Journal of Earth Sciences*, v. 95, no. 2, p. 225-238.
- Austermann, J., and Iaffaldano, G., 2013, The role of the Zagros orogeny in slowing down Arabia-Eurasia convergence since ~5 Ma: *Tectonics*, v. 32, no. 3, p. 351-363.
- Axen, G. J., Lam, P. S., Grove, M., Stockli, D. F., and Hassanzadeh, J., 2001, Exhumation of the west-central Alborz Mountains, Iran, Caspian subsidence, and collision-related tectonics: *Geology*, v. 29, no. 6, p. 559.
- Aydin, A., 1985, The types and role of stepovers in strike slip tectonics.
- Aydin, A., and Nur, A., 1982, Evolution of pull-apart basins and their scale independence: *Tectonics*, v. 1, no. 1, p. 91-105.
- Bahr, R., Lippolt, H. J., and Wernicke, R. S., 1994, Temperature-induced ^4He degassing of specularite and botryoidal hematite: A ^4He retentivity study: *Journal of Geophysical Research*, v. 99, p. 17695-17707.
- Ballato, P., Nowaczyk, N. R., Landgraf, A., Strecker, M. R., Friedrich, A., and Tabatabaei, S. H., 2008, Tectonic control on sedimentary facies pattern and sediment accumulation rates in the Miocene foreland basin of the southern Alborz mountains, northern Iran: *Tectonics*, v. 27, no. 6, p. n/a-n/a.

- Ballato, P., Stockli, D. F., Ghassemi, M. R., Landgraf, A., Strecker, M. R., Hassanzadeh, J., Friedrich, A., and Tabatabaei, S. H., 2013, Accommodation of transpressional strain in the Arabia-Eurasia collision zone: new constraints from (U-Th)/He thermochronology in the Alborz mountains, north Iran: *Tectonics*, v. 32, no. 1, p. 1-18.
- Ballato, P., Uba, C. E., Landgraf, A., Strecker, M. R., Sudo, M., Stockli, D. F., Friedrich, A., and Tabatabaei, S. H., 2011, Arabia-Eurasia continental collision: Insights from late Tertiary foreland-basin evolution in the Alborz Mountains, northern Iran: *Geological Society of America Bulletin*, v. 123, no. 1-2, p. 106-131.
- Barka, A., and Kadinsky-Cade, K., 1988, Strike-slip fault geometry in Turkey and its influence on earthquake activity: *Tectonics*, v. 7, no. 3, p. 663-684.
- Bayasgalan, A., Jackson, J., Ritz, J. F., and Carretier, S., 1999, Field examples of strike-slip fault terminations in Mongolia and their tectonic significance: *Tectonics*, v. 18, no. 3, p. 394-411.
- Beaumont, P., 1972, Alluvial fans along the foothills of the Elburz Mountains, Iran: *Palaeogeography, Palaeoclimatology, Palaeoecology*, v. 12, no. 4, p. 251-273.
- Beeler, N. M., Tullis, T. E., and Goldsby, D. L., 2008, Constitutive relationships and physical basis of fault strength due to flash heating: *Journal of Geophysical Research*, v. 113, p. B01401.
- Behroozi, A., Sahbaei, M., Etemadi, N., Zedeh, A. A., Ghomashi, A., and Moghtader, M., 1987, Feyz Abad: Geological Survey of Iran, scale 1:100000.
- Benowitz, J. A., Layer, P. W., Armstrong, P., Perry, S. E., Haeussler, P. J., Fitzgerald, P. G., and VanLaningham, S., 2011, Spatial variations in focused exhumation along a continental-scale strike-slip fault: The Denali fault of the eastern Alaska Range: *Geosphere*, v. 7, no. 2, p. 455-467.
- Berberian, M., 1974, A brief geological description of north-central Iran: *Materials for the Study of the Seismotectonics of Iran; North-Central Iran: Geol. Survey of Iran Report*, v. 29, p. 127-138.
- Berberian, M., 2014, *Earthquakes and Coseismic Surface Faulting on the Iranian Plateau*, Elsevier Science.
- Berberian, M., and King, G., 1981, Towards a paleogeography and tectonic evolution of Iran: *Canadian journal of earth sciences*, v. 18, no. 2, p. 210-265.
- Berberian, M., and Yeats, R. S., 1999, Patterns of historical earthquake rupture in the Iranian plateau: *Bulletin of the Seismological Society of America*, v. 89, no. 1, p. 1.
- Biddle, K. T., 1985, Glossary—Strike-slip deformation, basin formation, and sedimentation.
- Blackburn, T. J., Stockli, D. F., and Walker, J. D., 2007, Magnetite (U-Th)/He dating and its application to the geochronology of intermediate to mafic volcanic rocks: *Earth and Planetary Science Letters*, v. 259, p. 360-371.
- Blair, T. C., and Bilodeau, W. L., 1988, Development of tectonic cyclothems in rift, pull-apart, and foreland basins - sedimentary response to episodic tectonism: *Geology*, v. 16, no. 6, p. 517-520.
- Blissenbach, E., 1954, Geology of alluvial fans in semiarid regions: *Geological Society of America Bulletin*, v. 65, no. 2, p. 175-190.
- Bonini, M., Corti, G., Sokoutis, D., Vannucci, G., Gasperini, P., and Cloetingh, S., 2003, Insights from scaled analogue modelling into the seismotectonics of the Iranian region: *Tectonophysics*, v. 376, no. 3, p. 137-149.
- Boulton, S. J., and Robertson, A. H., 2007, The Miocene of the Hatay area, S Turkey: Transition from the Arabian passive margin to an underfilled foreland basin related to closure of the Southern Neotethys Ocean: *Sedimentary Geology*, v. 198, no. 1, p. 93-124.
- Braun, J., 1994, Three-dimensional numerical simulations of crustal-scale wrenching using a non-linear failure criterion: *Journal of Structural Geology*, v. 16, no. 8, p. 1173-1186.
- Brocard, G., Van Der Beek, P., Bourlès, D., Siame, L., and Mugnier, J.-L., 2003, Long-term fluvial incision rates and postglacial river relaxation time in the French Western Alps from< sup>

- ¹⁰Be dating of alluvial terraces with assessment of inheritance, soil development and wind ablation effects: *Earth and Planetary Science Letters*, v. 209, no. 1, p. 197-214.
- Brocklehurst, S. H., and Whipple, K. X., 2004, Hypsometry of glaciated landscapes: *Earth Surface Processes and Landforms*, v. 29, no. 7, p. 907-926.
- Brown, E. T., Stallard, R. F., Larsen, M. C., Raisbeck, G. M., and Yiou, F., 1995, Denudation rates determined from the accumulation of in situ-produced ¹⁰Be in the Luquillo experimental forest, Puerto Rico: *Earth and Planetary Science Letters*, v. 129, no. 1, p. 193-202.
- Bull, W. B., 1977, The alluvial-fan environment: *Progress in physical geography*, v. 1, no. 2, p. 222-270.
- , 1984, *Tectonic Geomorphology* *Journal of Geological Education*, v. 32, p. 310.
- , 2007, *Tectonic geomorphology of mountains: a new approach to paleoseismology*, Oxford, Blackwell Publishing, 320 p.:
- Burbank, D., Meigs, A., and Brozović, N., 1996, Interactions of growing folds and coeval depositional systems: *Basin Research*, v. 8, no. 3, p. 199-223.
- Burbank, D. W., 1992, Causes of recent Himalayan uplift deduced from deposited patterns in the Ganges basin: *nature*, v. 357, no. 6380, p. 680-683.
- Burbank, D. W., and Anderson, R. S., 2011, *Tectonic geomorphology*, John Wiley & Sons.
- Burbidge, D. R., and Braun, J., 1998, Analogue models of obliquely convergent continental plate boundaries: *Journal of Geophysical Research: Solid Earth* (1978–2012), v. 103, no. B7, p. 15221-15237.
- Buscher, J. T., and Spotila, J. A., 2007, Near-field response to transpression along the southern San Andreas fault, based on exhumation of the northern San Gabriel Mountains, southern California: *Tectonics*, v. 26, no. 5.
- Cabrera, L., Roca, E., and Santanach, P., 1988, Basin formation at the end of a strike-slip fault: the Cerdanya Basin (eastern Pyrenees): *Journal of the Geological Society*, v. 145, no. 2, p. 261-268.
- Caine, J. S., Evans, J. P., and Forster, C. B., 1996, Fault zone architecture and permeability structure: *Geology*, v. 24, no. 11, p. 1025-1028.
- Carne, R., and Little, T., 2012, Geometry and scale of fault segmentation and deformational bulging along an active oblique-slip fault (Wairarapa fault, New Zealand): *Geological Society of America Bulletin*, v. 124, no. 7-8, p. 1365-1381.
- Castelltort, S., Goren, L., Willett, S. D., Champagnac, J.-D., Herman, F., and Braun, J., 2012, River drainage patterns in the New Zealand Alps primarily controlled by plate tectonic strain: *Nature Geoscience*, v. 5, no. 10, p. 744-748.
- Catalano, S., Monaco, C., Tortorici, L., and Tansi, C., 1993, Pleistocene strike-slip tectonics in the Lucanian Apennine (southern Italy): *Tectonics*, v. 12, no. 3, p. 656-665.
- Chapman, D., 1986, *Thermal gradients in the continental crust*: Geological Society, London, Special Publications, v. 24, no. 1, p. 63-70.
- Choi, J., Kim, J., Murray, A., Hong, D., Chang, H., and Cheong, C.-S., 2009, OSL dating of marine terrace sediments on the southeastern coast of Korea with implications for Quaternary tectonics: *Quaternary International*, v. 199, no. 1, p. 3-14.
- Christie-Blick, N., 1985, Deformation and basin formation along strike-slip faults.
- Cloos, H., 1928, Experimente zur inneren Tektonik: *Centralblatt für Mineralogie*, v. 12, p. 609-621.
- Cobbold, P., and Davy, P., 1988, Indentation tectonics in nature and experiment. 2: Central Asia, *Bull. Geol. Inst. Univ. Uppsala*, v. 14, p. 143-162.
- Cooke, R., Warren, A., and Goudie, A., 1993, *Desert geomorphology*: University College of London Press, London.
- Cowgill, E., Yin, A., Arrowsmith, J. R., Feng, W. X., and Shuanhong, Z., 2004, The Akato Tagh bend along the Altyn Tagh fault, northwest Tibet 1: Smoothing by vertical-axis rotation and the effect of topographic stresses on bend-flanking faults: *Geological Society of America Bulletin*, v. 116, no. 11-12, p. 1423-1442.

- Cowie, P. A., and Scholz, C. H., 1992, Physical explanation for the displacement-length relationship of faults using a post-yield fracture mechanics model: *Journal of Structural Geology*, v. 14, no. 10, p. 1133-1148.
- Cox, S. C., Stirling, M. W., Herman, F., Gerstenberger, M., and Ristau, J., 2012, Potentially active faults in the rapidly eroding landscape adjacent to the Alpine Fault, central Southern Alps, New Zealand: *Tectonics*, v. 31.
- Cox, S. F., 1999, Deformational controls on the dynamics of fluid flow in mesothermal gold systems: *Fractures, Fluid Flow and Mineralization*, v. 155, p. 123-140.
- Cox, S. F., and Ruming, K., 2004, The St Ives mesothermal gold system, Western Australia - a case of golden aftershocks?: *Journal of Structural Geology*, v. 26, no. 6-7, p. 1109-1125.
- Cunningham, D., 2013, Mountain building processes in intracontinental oblique deformation belts: Lessons from the Gobi Corridor, Central Asia: *Journal of Structural Geology*, v. 46, p. 255-282.
- Cunningham, W., and Mann, P., 2007, *Tectonics of strike-slip restraining and releasing bends*: Geological Society, London, Special Publications, v. 290, no. 1, p. 1-12.
- Cunningham, W. D., 1993, Strike-slip faults in the southernmost andes and the development of the Patagonian orocline: *Tectonics*, v. 12, no. 1, p. 169-186.
- Cyr, A. J., Granger, D. E., Olivetti, V., and Molin, P., 2010, Quantifying rock uplift rates using channel steepness and cosmogenic nuclide-determined erosion rates: Examples from northern and southern Italy: *Lithosphere*, v. 2, no. 3, p. 188-198.
- D'Agostino, N., and McKenzie, D., 1999, Convective support of long-wavelength topography in the Apennines (Italy): *Terra Nova-Oxford*, v. 11, no. 5, p. 228-233.
- d'Alessio, M. A., and Martel, S. J., 2004, Fault terminations and barriers to fault growth: *Journal of Structural Geology*, v. 26, no. 10, p. 1885-1896.
- Dair, L., and Cooke, M. L., 2009, San Andreas fault geometry through the San Geronio Pass, California: *Geology*, v. 37, no. 2, p. 119-122.
- Daneshian, J., and Dana, L. R., 2007, Early Miocene benthic foraminifera and biostratigraphy of the Qom Formation, Deh Namak, central Iran: *Journal of Asian Earth Sciences*, v. 29, no. 5, p. 844-858.
- Davis, G., 1984, *Structural geology of rocks and regions*.
- Davis, G. H., Bump, A. P., García, P. E., and Ahlgren, S. G., 2000, Conjugate Riedel deformation band shear zones: *Journal of Structural Geology*, v. 22, no. 2, p. 169-190.
- Della Seta, M., 2003, L'analisi geomorfica quantitativa nello studio dell'evoluzione morfotettonica recente della fascia peri-adriatica marchigiano-abruzzese.
- Dewey, J., Hempton, M., Kidd, W., Saroglu, F. t., and Şengör, A., 1986, Shortening of continental lithosphere: the neotectonics of Eastern Anatolia—a young collision zone: Geological Society, London, Special Publications, v. 19, no. 1, p. 1-36.
- Di Bucci, D., and Mazzoli, S., 2003, The October–November 2002 Molise seismic sequence (southern Italy): an expression of Adria intraplate deformation: *Journal of the Geological Society*, v. 160, no. 4, p. 503-506.
- Di Vincenzo, G., Rossetti, F., Viti, C., and Balsamo, F., 2013, Constraining the timing of fault reactivation: Eocene coseismic slip along a Late Ordovician ductile shear zone (northern Victoria Land, Antarctica): *Geological Society of America Bulletin*, v. 125, no. 3-4, p. 609-624.
- Doblas, M., 1998, Slickenside kinematic indicators: *Tectonophysics*, v. 295, no. 1, p. 187-197.
- Dooley, T., and McClay, K., 1997, Analog modeling of pull-apart basins: *AAPG bulletin*, v. 81, no. 11, p. 1804-1826.
- Dooley, T., McClay, K., and Bonora, M., 4D evolution of segmented strike-slip fault systems: applications to NW Europe, *in Proceedings Geological Society, London, Petroleum Geology Conference series 1999, Volume 5*, Geological Society of London, p. 215-225.

- Dooley, T. P., and Schreurs, G., 2012, Analogue modelling of intraplate strike-slip tectonics: A review and new experimental results: *Tectonophysics*, v. 574, p. 1-71.
- Dufaure, J., Thibault, C., Kadjar, M., and Mercier, J., 1978, La zone de failles du Zendan (Iran du Sud-Est): I—Géomorphologie et Stratigraphie du Quaternaire, paper presented at Réunion Annuelle des Sciences de la Terre (6th RAST): Soc. Geol. de Fr., Orsay, France.
- Eftekhari-Nezhad, J., Aghanabati, A., Hamzehpour, B., and Baroyant, V., 1976, Kashmar: Geological Survey of Iran, scale 1:250000.
- Ellis, S., 1996, Forces driving continental collision: Reconciling indentation and mantle subduction tectonics: *Geology*, v. 24, no. 8, p. 699-702.
- Ellis, S. M., 1995, Continental convergence: length-scales, aspect ratios, and styles of crustal deformation [PhD].
- England, P., and McKenzie, D., 1982, A thin viscous sheet model for continental deformation: *Geophysical Journal International*, v. 70, no. 2, p. 295-321.
- England, P., and Molnar, P., 1990, Surface uplift, uplift of rocks, and exhumation of rocks: *Geology*, v. 18, no. 12, p. 1173-1177.
- Ershov, A. V., Brunet, M.-F., Nikishin, A. M., Bolotov, S. N., Nazarevich, B. P., and Korotaev, M. V., 2003, Northern Caucasus basin: thermal history and synthesis of subsidence models: *Sedimentary Geology*, v. 156, no. 1, p. 95-118.
- Evans, J. P., Prante, M. R., Janecke, S. U., Ault, A. K., and Newell, D. L., 2014, Hot faults: Iridescent slip surfaces with metallic luster document high-temperature ancient seismicity in the Wasatch fault zone, Utah, USA: *Geology*.
- Evenson, N. S., Reiners, P. W., Spencer, J., and Shuster, D. L., 2014, Hematite and Mn oxide (U-Th)/He dates from the Buckskin-Rawhide detachment system, western Arizona: constraining the timing of mineralization and hematite (U-Th)/He systematics: *American Journal of Science*.
- Farbod, Y., Bellier, O., Shabanian, E., and Abbassi, M. R., 2011, Geomorphic and structural variations along the Doruneh Fault System (central Iran): *Tectonics*, v. 30.
- Farley, K., 2000, Helium diffusion from apatite: General behavior as illustrated by Durango fluorapatite: *Journal of Geophysical Research: Solid Earth* (1978–2012), v. 105, no. B2, p. 2903-2914.
- Farley, K., Wolf, R., and Silver, L., 1996, The effects of long alpha-stopping distances on (U-Th)/He ages: *Geochimica et Cosmochimica Acta*, v. 60, no. 21, p. 4223-4229.
- Farley, K. A., and Flowers, R. M., 2012, (U-Th)/Ne and multidomain (U-Th)/He systematics of a hydrothermal hematite from eastern Grand Canyon: *Earth and Planetary Science Letters*, v. 359-360, p. 131-140.
- Fattahi, M., Walker, R., Hollingsworth, J., Bahroudi, A., Nazari, H., Talebian, M., Armitage, S., and Stokes, S., 2006, Holocene slip-rate on the Sabzevar thrust fault, NE Iran, determined using optically stimulated luminescence (OSL): *Earth and Planetary Science Letters*, v. 245, no. 3-4, p. 673-684.
- Fattahi, M., Walker, R. T., Khatib, M. M., Dolati, A., and Bahroudi, A., 2007, Slip-rate estimate and past earthquakes on the Doruneh fault, eastern Iran: *Geophysical Journal International*, v. 168, no. 2, p. 691-709.
- Faulkner, D., Mitchell, T., Healy, D., and Heap, M., 2006, Slip on 'weak' faults by the rotation of regional stress in the fracture damage zone: *nature*, v. 444, no. 7121, p. 922-925.
- Fialko, Y., Rivera, L., and Kanamori, H., 2005, Estimate of differential stress in the upper crust from variations in topography and strike along the San Andreas fault: *Geophysical Journal International*, v. 160, no. 2, p. 527-532.
- Finnegan, N. J., Schumer, R., and Finnegan, S., 2014, A signature of transience in bedrock river incision rates over timescales of 104-107 years: *nature*, v. 505, no. 7483, p. 391-394.

- Finzi, Y., Hearn, E. H., Ben-Zion, Y., and Lyakhovsky, V., 2009, Structural properties and deformation patterns of evolving strike-slip faults: Numerical simulations incorporating damage rheology: *Pure and Applied Geophysics*, v. 166, no. 10-11, p. 1537-1573.
- Fitzgerald, P., Baldwin, S., Webb, L., and O'sullivan, P., 2006, Interpretation of (U-Th)/He single grain ages from slowly cooled crustal terranes: a case study from the Transantarctic Mountains of southern Victoria Land: *Chemical Geology*, v. 225, no. 1, p. 91-120.
- Fitzgerald, P. G., Sorkhabi, R. B., Redfield, T. F., and Stump, E., 1995, Uplift and denudation of the central Alaska ange - a case-study in the use of apatite fission-track thermochronology to determine absolute uplift parameters: *Journal of Geophysical Research-Solid Earth*, v. 100, no. B10, p. 20175-20191.
- Fitzgerald, P. G., Stump, E., and Redfield, T. F., 1993, Late Cenozoic uplift of Denali and its relation to relative plate motion and fault morphology: *Science*, v. 259, no. 5094, p. 497-499.
- Foeken, J., Stuart, F. M., Dobson, K. J., Persano, C., and Vilbert, D., 2006, A diode laser system for heating minerals for (U-Th)/He chronometry: *Geochemistry, Geophysics, Geosystems*, v. 7, no. 4.
- Fossen, H., 2010, *Structural geology*, Cambridge University Press.
- Fossen, H., and Tikoff, B., 1993, The deformation matrix for simultaneous simple shearing, pure shearing and volume change, and its application to transpression-transension tectonics: *Journal of Structural Geology*, v. 15, no. 3, p. 413-422.
- Fossen, H., Tikoff, B., and Teyssier, C., 1994, Strain modeling of transpressional and transtensional deformation: *Norsk Geologisk Tidsskrift*, v. 74, no. 3, p. 134-145.
- Foster, D. A., Doughty, P. T., Kalakay, T. J., Fanning, C. M., Coyner, S., Grice, W. C., and Vogl, J., 2007, Kinematics and timing of exhumation of metamorphic core complexes along the Lewis and Clark fault zone, northern Rocky Mountains, USA: *Geological Society of America Special Papers*, v. 434, p. 207-232.
- Foster, D. A., and Gleadow, A. J., 1992, Reactivated tectonic boundaries and implications for the reconstruction of southeastern Australia and northern Victoria Land, Antarctica: *Geology*, v. 20, no. 3, p. 267-270.
- Françolin, J., Cobbold, P., and Szatmari, P., 1994, Faulting in the Early Cretaceous Rio do Peixe basin (NE Brazil) and its significance for the opening of the Atlantic: *Journal of Structural Geology*, v. 16, no. 5, p. 647-661.
- Frostick, L. E., and Reid, I., 1989, Climatic versus tectonic controls of fan sequences: lessons from the Dead Sea, Israel: *Journal of the Geological Society*, v. 146, no. 3, p. 527-538.
- Gapais, D., Fiquet, G., and Cobbold, P., 1991, Slip system domains, 3. New insights in fault kinematics from plane-strain sandbox experiments: *Tectonophysics*, v. 188, no. 1, p. 143-157.
- Gavillot, Y., Axen, G. J., Stockli, D. F., Horton, B. K., and Fakhari, M. D., 2010, Timing of thrust activity in the High Zagros fold-thrust belt, Iran, from (U-Th)/He thermochronometry: *Tectonics*, v. 29, no. 4.
- Ghomashi, A., Masoomi, R., Hosseiny, S. Z., Taheri, J., Shamanian, G., Kaveh, N. S., Baheremad, M., and Razavi, M. A., 2001, *Kashmar: Geological Survey of Iran*, scale 1:100000.
- Giano, S., 2011, Quaternary alluvial fan systems of the Agri intermontane basin (southern Italy): tectonic and climatic controls: *Geologica Carpathica*, v. 62, no. 1, p. 65-76.
- Gioia, D., Gallicchio, S., Moretti, M., and Schiattarella, M., 2014, Landscape response to tectonic and climatic forcing in the foredeep of the southern Apennines, Italy: insights from Quaternary stratigraphy, quantitative geomorphic analysis, and denudation rate proxies: *Earth Surface Processes and Landforms*, v. 39, no. 6, p. 814-835.
- Goldsby, D. L., and Tullis, T. E., 2011, Flash Heating Leads to Low Frictional Strength of Crustal Rocks at Earthquake Slip Rates: *Science*, v. 334, no. 6053, p. 216-218.
- Gordon, R. G., 1998, The plate tectonic approximation: Plate nonrigidity, diffuse plate boundaries, and global plate reconstructions: *Annual Review of Earth and Planetary Sciences*, v. 26, no. 1, p. 615-642.

- Gordon, S. M., Whitney, D. L., Miller, R. B., McLean, N., and Seaton, N. C. A., 2010, Metamorphism and deformation at different structural levels in a strike-slip fault zone, Ross Lake fault, North Cascades, USA: *Journal of Metamorphic Geology*, v. 28, no. 2, p. 117-136.
- Granier, T., 1985, Origin, damping, and pattern of development of faults in granite: *Tectonics*, v. 4, no. 7, p. 721-737.
- Green, P., Duddy, I., Laslett, G., Hegarty, K., Gleadow, A. W., and Lovering, J., 1989, Thermal annealing of fission tracks in apatite 4. Quantitative modelling techniques and extension to geological timescales: *Chemical Geology: Isotope Geoscience Section*, v. 79, no. 2, p. 155-182.
- Grohmann, C. H., 2004, Morphometric analysis in geographic information systems: applications of free software GRASS and R: *Computers & Geosciences*, v. 30, no. 9, p. 1055-1067.
- Guest, B., Stockli, D. F., Grove, M., Axen, G. J., Lam, P. S., and Hassanzadeh, J., 2006, Thermal histories from the central Alborz Mountains, northern Iran: implications for the spatial and temporal distribution of deformation in northern Iran: *Geological Society of America Bulletin*, v. 118, no. 11-12, p. 1507-1521.
- Hadavi, F., Moghaddam, M. N., and Mousazadeh, H., 2010, Burdigalian–serravalian calcareous nannoplanktons from Qom Formation, north-center Iran: *Arabian Journal of Geosciences*, v. 3, no. 2, p. 133-139.
- Hafkenscheid, E., Wortel, M., and Spakman, W., 2006, Subduction history of the Tethyan region derived from seismic tomography and tectonic reconstructions: *Journal of Geophysical Research: Solid Earth* (1978–2012), v. 111, no. B8.
- Harding, T., 1985, Seismic characteristics and identification of negative flower structures, positive flower structures, and positive structural inversion: *AAPG bulletin*, v. 69, no. 4, p. 582-600.
- , 1990, Identification of Wrench Faults Using Subsurface Structural Data: Criteria and Pitfalls (1): *AAPG bulletin*, v. 74, no. 10, p. 1590-1609.
- Harrison, T. M., and Zeitler, P. K., 2005, Fundamentals of noble gas thermochronometry: *Reviews in Mineralogy and Geochemistry*, v. 58, no. 1, p. 123-149.
- Harvey, A., 2004, The response of dry-region alluvial fans to late Quaternary climatic change: Desertification in the third millenium, p. 83-98.
- Harvey, A. M., 1997, The role of alluvial fans in arid zone fluvial systems: *Arid Zone Geomorphology: Processes, Form and Change in Drylands*, p. 231-259.
- Hassami, K., Jamali, F., and Tabassi, H., 2003, Major active faults of Iran: International institute of earthquake engineering and seismology of Iran Press.
- Hatzfeld, D., and Molnar, P., 2010, Comparisons of the kinematics and deep structures of the Zagros and Himalaya and of the Iranian and Tibetan plateaus and geodynamic implications: *Reviews of Geophysics*, v. 48, no. 2.
- Headley, R. M., Enkelmann, E., and Hallet, B., 2013, Examination of the interplay between glacial processes and exhumation in the Saint Elias Mountains, Alaska: *Geosphere*, v. 9, no. 2, p. 229-241.
- Heidbach, O., Tingay, M., Barth, A., Reinecker, J., Kurfeß, D., and Müller, B., 2001, World stress map: *Naturwissenschaften*, v. 88, p. 357-371.
- Heidbach, O., Tingay, M., Barth, A., Reinecker, J., Kurfeß, D., and Müller, B., 2008, The world stress map database release 2008, doi: 10.1594/GFZ: WSM. Rel2008.
- Heim, J. A., Vasconcelos, P. M., Shuster, D. L., Farley, K. A., and Broadbent, G., 2006, Dating paleochannel iron ore by (U-Th)/He analysis of supergene goethite, Hamersley province, Australia: *Geology*, v. 34, p. 173-176.
- Hempton, M. R., and Neher, K., 1986, Experimental fracture, strain and subsidence patterns over en echelon strike-slip faults: implications for the structural evolution of pull-apart basins: *Journal of Structural Geology*, v. 8, no. 6, p. 597-605.
- Hergarten, S., Robl, J., and Stüwe, K., 2014, Extracting topographic swath profiles across curved geomorphic features: *Earth Surface Dynamics*, v. 2, no. 1, p. 97-104.

- Hessami, K., KOYL, H. A., Talbot, C. J., Tabasi, H., and Shabanian, E., 2001, Progressive unconformities within an evolving foreland fold–thrust belt, Zagros Mountains: *Journal of the Geological Society*, v. 158, no. 6, p. 969-981.
- Hilley, G. E., and Arrowsmith, J. R., 2008, Geomorphic response to uplift along the Dragon's Back pressure ridge, Carrizo Plain, California: *Geology*, v. 36, no. 5, p. 367-370.
- Holdsworth, R., Handa, M., Miller, J., and Buick, I., 2001a, Continental reactivation and reworking: an introduction: *Geological Society, London, Special Publications*, v. 184, no. 1, p. 1-12.
- Holdsworth, R., Stewart, M., Imber, J., and Strachan, R., 2001b, The structure and rheological evolution of reactivated continental fault zones: a review and case study: *Geological Society, London, Special Publications*, v. 184, no. 1, p. 115-137.
- Holdsworth, R. E., Strachan, R. A., and Dewey, J. F., 1998, Continental transpressional and transtensional tectonics, *Geological Society*.
- Hollingsworth, J., Fattahi, M., Walker, R., Talebian, M., Bahroudi, A., Bolourchi, M. J., Jackson, J., and Copley, A., 2010, Oroclinal bending, distributed thrust and strike-slip faulting, and the accommodation of Arabia-Eurasia convergence in NE Iran since the Oligocene: *Geophysical Journal International*, p. no-no.
- Homke, S., Vergés, J., Serra-Kiel, J., Bernaola, G., Sharp, I., Garcés, M., Montero-Verdú, I., Karpuz, R., and Goodarzi, M. H., 2009, Late Cretaceous–Paleocene formation of the proto–Zagros foreland basin, Lorestan Province, SW Iran: *Geological Society of America Bulletin*, v. 121, no. 7-8, p. 963-978.
- Homke, S., Vergés, J., Van Der Beek, P., Fernández, M., Saura, E., Barbero, L., Badics, B., and Labrin, E., 2010, Insights in the exhumation history of the NW Zagros from bedrock and detrital apatite fission-track analysis: evidence for a long-lived orogeny: *Basin Research*, v. 22, no. 5, p. 659-680.
- Hurford, A. J., and Green, P. F., 1983, The zeta age calibration of fission-track dating: *Chemical Geology*, v. 41, p. 285-317.
- Ioganson, L. I., 2005, Pull-apart basins: a review: *Geotectonics*, v. 39, no. 2, p. 156-168.
- Jackson, J., and McKenzie, D., 1984, Active tectonics of the Alpine—Himalayan belt between western Turkey and Pakistan: *Geophysical Journal International*, v. 77, no. 1, p. 185-264.
- Jalilian, M., Etemadi, N., Zadeh, A. A., Manouchehri, M., Pour, M. J. V., Tehrani, N. A., Behrouzi, A., Kholghi, M. H., and Naini, M. A., 1992, Torbat-e-Heydarieh: *Geological Survey of Iran*, scale 1:250000.
- Jamison, W. R., and Stearns, D. W., 1982, Tectonic deformation of Wingate Sandstone, Colorado National Monument: *AAPG bulletin*, v. 66, no. 12, p. 2584-2608.
- Javadi, H. R., Ghassemi, M. R., Shahpasandzadeh, M., Guest, B., Ashtiani, M. E., Yassaghi, A. L. I., and Kouhpeyma, M., 2013, History of faulting on the Doruneh Fault System: implications for the kinematic changes of the Central Iranian Microplate: *Geological Magazine*, v. 150, no. 04, p. 651-672.
- Johansson, M., Olvmo, M., and Söderström, M., 1999, Application of digital elevation and geological data in studies of morphotectonics and relief—a case study of the sub-Cambrian peneplain in SW Sweden: *Zeitschrift für Geomorphologie*, v. 43, p. 505-520.
- Jolivet, L., and Faccenna, C., 2000, Mediterranean extension and the Africa-Eurasia collision: *Tectonics*, v. 19, no. 6, p. 1095-1106.
- Keller, E. A., and Pinter, N., 1996, *Active tectonics*, Prentice Hall Upper Saddle River.
- Ketcham, R. A., Donelick, R. A., and Carlson, W. D., 1999, Variability of apatite fission-track annealing kinetics: III. Extrapolation to geological time scales: *American Mineralogist*, v. 84, p. 1235-1255.
- Khadivi, S., Mouthereau, F., Larrasoana, J. C., Vergés, J., Lacombe, O., Khademi, E., Beamud, E., Melinte-Dobrinescu, M., and Suc, J. P., 2009, Magnetochronology of synorogenic Miocene foreland sediments in the Fars arc of the Zagros Folded Belt (SW Iran): *Basin Research*.

- Kocyigit, A., and Beyhan, A., 1998, A new intracontinental transcurrent structure: the Central Anatolian Fault Zone, Turkey: *Tectonophysics*, v. 284, no. 3-4, p. 317-336.
- Koons, P., Zeitler, P., Chamberlain, C., Craw, D., and Meltzer, A., 2002, Mechanical links between erosion and metamorphism in Nanga Parbat, Pakistan Himalaya: *American Journal of Science*, v. 302, no. 9, p. 749-773.
- Lachenbruch, A. H., 1986, Simple models for the estimation and measurement of frictional heating by an earthquake: U.S. Geological Survey Open File Report 86-508, p. 13 p.
- Lavé, J., and Avouac, J., 2001, Fluvial incision and tectonic uplift across the Himalayas of central Nepal: *Journal of Geophysical Research: Solid Earth* (1978–2012), v. 106, no. B11, p. 26561-26591.
- Lazarte, C., and Bray, J., 1996, A study of strike-slip faulting using small-scale models: *ASTM geotechnical testing journal*, v. 19, no. 2, p. 118-129.
- Le Guerroué, E., and Cobbold, P. R., 2006, Influence of erosion and sedimentation on strike-slip fault systems: insights from analogue models: *Journal of Structural Geology*, v. 28, no. 3, p. 421-430.
- Lippolt, H. J., Wernicke, R. S., and Bahr, R., 1995, Paragenetic specularite and adularia (Elba, Italy): concordant (U+Th)-He and K-Ar ages: *Earth and Planetary Science Letters*, v. 132, p. 43-51.
- Lippolt, H. J., Wernicke, R. S., and Boschmann, W., 1993, ⁴He diffusion in specular hematite: *Physics and Chemistry of Minerals*, v. 20, p. 415-418.
- Little, T. A., Cox, S., Vry, J. K., and Batt, G., 2005, Variations in exhumation level and uplift rate along the oblique-slip Alpine fault, central Southern Alps, New Zealand: *Geological Society of America Bulletin*, v. 117, no. 5-6, p. 707-723.
- Lowell, J. D., 1985, Structural styles in petroleum exploration, Oil & Gas Consultants International.
- Madanipour, S., Ehlers, T. A., Yassaghi, A., Rezaeian, M., Enkelmann, E., and Bahroudi, A., 2013, Synchronous deformation on orogenic plateau margins: Insights from the Arabia–Eurasia collision: *Tectonophysics*, v. 608, p. 440-451.
- Mandl, G., 2000, *Faulting in brittle rocks: an introduction to the mechanics of tectonic faults*, Springer.
- Mann, P., 2007, Global catalogue, classification and tectonic origins of restraining-and releasing bends on active and ancient strike-slip fault systems: Geological Society, London, Special Publications, v. 290, no. 1, p. 13-142.
- Marshak, S., Karlstrom, K., and Timmons, J. M., 2000, Inversion of Proterozoic extensional faults: An explanation for the pattern of Laramide and Ancestral Rockies intracratonic deformation, United States: *Geology*, v. 28, no. 8, p. 735-738.
- Marshak, S., Nelson, W. J., and McBride, J. H., 2003, Phanerozoic strike-slip faulting in the continental interior platform of the United States: examples from the Laramide Orogen, Midcontinent, and Ancestral Rocky Mountains, *in* Storti, F., Holdsworth, R. E., and Salvini, F., eds., *Intraplate Strike-Slip Deformation Belts*, Volume 210, p. 159-184.
- Martel, S. J., and Pollard, D. D., 1989, Mechanics of slip and fracture along small faults and simple strike-slip fault zones in granitic rock: *Journal of Geophysical Research: Solid Earth* (1978–2012), v. 94, no. B7, p. 9417-9428.
- Massonnet, D., Rossi, M., Carmona, C., Adragna, F., Peltzer, G., Feigl, K., and Rabaute, T., 1993, The displacement field of the Landers earthquake mapped by radar interferometry: *nature*, v. 364, no. 6433, p. 138-142.
- Mattei, M., Cifelli, F., Muttoni, G., Zanchi, A., Berra, F., Mossavvari, F., and Eshraghi, S. A., 2012, Neogene block rotation in central Iran: Evidence from paleomagnetic data: *Geological Society of America Bulletin*, v. 124, no. 5-6, p. 943-956.
- McClay, K., and Bonora, M., 2001, Analog models of restraining stepovers in strike-slip fault systems: *AAPG bulletin*, v. 85, no. 2, p. 233-260.

- McClusky, S., Reilinger, R., Mahmoud, S., Sari, D. B., and Tealeb, A., 2003, GPS constraints on Africa (Nubia) and Arabia plate motions: *Geophysical Journal International*, v. 155, no. 1, p. 126-138.
- McKenzie, D., and Jackson, J., 1983, The relationship between strain rates, crustal thickening, palaeomagnetism, finite strain and fault movements within a deforming zone: *Earth and Planetary Science Letters*, v. 65, no. 1, p. 182-202.
- McKenzie, D. P., and Parker, R. L., 1967, The North Pacific: an example of tectonics on a sphere: *nature*, v. 216, p. 1276-1280.
- McQuarrie, N., Stock, J., Verdel, C., and Wernicke, B., 2003, Cenozoic evolution of Neotethys and implications for the causes of plate motions: *Geophysical research letters*, v. 30, no. 20.
- Merritts, D., and Ellis, M., 1994, Introduction to special section on tectonics and topography: *Journal of Geophysical Research: Solid Earth (1978–2012)*, v. 99, no. B6, p. 12135-12141.
- Mitchell, S. G., and Montgomery, D. R., 2006, Polygenetic topography of the Cascade Range, Washington State, USA: *American Journal of Science*, v. 306, no. 9, p. 736-768.
- Mitra, S., and Paul, D., 2011, Structural geometry and evolution of releasing and restraining bends: Insights from laser-scanned experimental models: *AAPG bulletin*, v. 95, no. 7, p. 1147-1180.
- Molin, P., Fubelli, G., Nocentini, M., Sperini, S., Ignat, P., Grecu, F., and Dramis, F., 2012, Interaction of mantle dynamics, crustal tectonics, and surface processes in the topography of the Romanian Carpathians: A geomorphological approach: *Global and Planetary Change*, v. 90, p. 58-72.
- Molin, P., Pazzaglia, F. J., and Dramis, F., 2004, Geomorphic expression of active tectonics in a rapidly-deforming forearc, Sila Massif, Calabria, Southern Italy: *American Journal of Science*, v. 304, no. 7, p. 559-589.
- Molnar, P., 1988, Continental tectonics in the aftermath of plate tectonics: *nature*, v. 335, no. 6186, p. 131-137.
- Molnar, P., Anderson, R. S., and Anderson, S. P., 2007, Tectonics, fracturing of rock, and erosion: *Journal of Geophysical Research-Earth Surface*, v. 112, no. F3.
- Molnar, P., and Tapponnier, P., 1975, Cenozoic tectonics of Asia: effects of a continental collision: *Science*, v. 189, no. 4201, p. 419-426.
- Montgomery, D. R., Balco, G., and Willett, S. D., 2001, Climate, tectonics, and the morphology of the Andes: *Geology*, v. 29, no. 7, p. 579-582.
- Moore, J. M., 1979, Tectonics of the Najd transcurrent fault system, Saudi Arabia: *Journal of the Geological Society*, v. 136, no. 4, p. 441-452.
- Morgan, W. J., 1968, Rises, trenches, great faults, and crustal blocks: *Journal of Geophysical Research*, v. 73, no. 6, p. 1959-1982.
- Morisawa, M., and Hack, J. T., 1985, Tectonic Geomorphology: *Proceedings of the 15th Annual Binghamton Geomorphology Symposium*, September 1984, Allen & Unwin.
- Morley, C., 2002, A tectonic model for the Tertiary evolution of strike-slip faults and rift basins in SE Asia: *Tectonophysics*, v. 347, no. 4, p. 189-215.
- Morley, C. K., 2007, Variations in Late Cenozoic–Recent strike-slip and oblique-extensional geometries, within Indochina: The influence of pre-existing fabrics: *Journal of Structural Geology*, v. 29, no. 1, p. 36-58.
- Morley, C. K., Kongwung, B., Julapour, A. A., Abdolghafourian, M., Hajian, M., Waples, D., Warren, J., Otterdoom, H., Srisuriyon, K., and Kazemi, H., 2009, Structural development of a major late Cenozoic basin and transpressional belt in central Iran: The Central Basin in the Qom-Saveh area: *Geosphere*, v. 5, no. 4, p. 325-362.
- Mouthereau, F., 2011, Timing of uplift in the Zagros belt/Iranian plateau and accommodation of late Cenozoic Arabia–Eurasia convergence: *Geological Magazine*, v. 148, no. 5-6, p. 726-738.
- Mouthereau, F., Lacombe, O., and Vergés, J., 2012, Building the Zagros collisional orogen: Timing, strain distribution and the dynamics of Arabia/Eurasia plate convergence: *Tectonophysics*, v. 532-535, p. 27-60.

- Mouthereau, F., Tensi, J., Bellahsen, N., Lacombe, O., De Boisgrollier, T., and Kargar, S., 2007, Tertiary sequence of deformation in a thin-skinned/thick-skinned collision belt: The Zagros Folded Belt (Fars, Iran): *Tectonics*, v. 26, no. 5, p. n/a-n/a.
- Naylor, M., Mandl, G. t., and Supesteijn, C., 1986, Fault geometries in basement-induced wrench faulting under different initial stress states: *Journal of Structural Geology*, v. 8, no. 7, p. 737-752.
- Niemi, N. A., Buscher, J. T., Spotila, J. A., House, M. A., and Kelley, S. A., 2013, Insights from low-temperature thermochronometry into transpressional deformation and crustal exhumation along the San Andreas fault in the western Transverse Ranges, California: *Tectonics*, v. 32, no. 6, p. 1602-1622.
- Nilforoushan, F., Masson, F., Vernant, P., Vigny, C., Martinod, J., Abbassi, M., Nankali, H., Hatzfeld, D., Bayer, R., Tavakoli, F., Ashtiani, A., Doerflinger, E., Daignières, M., Collard, P., and Chéry, J., 2003, GPS network monitors the Arabia-Eurasia collision deformation in Iran: *Journal of Geodesy*, v. 77, no. 7-8, p. 411-422.
- Nozaem, R., Mohajjel, M., Rossetti, F., Della Seta, M., Vignaroli, G., Yassaghi, A., Salvini, F., and Eliassi, M., 2013, Post-Neogene right-lateral strike-slip tectonics at the north-western edge of the Lut Block (Kuh-e-Sarhangi Fault), Central Iran: *Tectonophysics*.
- Okay, A. I., Zattin, M., and Cavazza, W., 2010, Apatite fission-track data for the Miocene Arabia-Eurasia collision: *Geology*, v. 38, no. 1, p. 35-38.
- Paterson, M. S., Wong, T.-f., Paterson, M. S., Geologist, A., and Géologue, A., 2005, *Experimental rock deformation: the brittle field*, Springer.
- Pederson, J. L., Anders, M. D., Rittenhour, T. M., Sharp, W. D., Gosse, J. C., and Karlstrom, K. E., 2006, Using fill terraces to understand incision rates and evolution of the Colorado River in eastern Grand Canyon, Arizona: *Journal of Geophysical Research: Earth Surface* (2003–2012), v. 111, no. F2.
- Pedraza, A., Pérez-Peña, J. V., Galindo-Zaldívar, J., Azañón, J. M., and Azor, A., 2009, Testing the sensitivity of geomorphic indices in areas of low-rate active folding (eastern Betic Cordillera, Spain): *Geomorphology*, v. 105, no. 3, p. 218-231.
- Pérez-Peña, J., Azañón, J., and Azor, A., 2009, CalHypso: an ArcGIS extension to calculate hypsometric curves and their statistical moments. Applications to drainage basin analysis in SE Spain: *Computers & Geosciences*, v. 35, no. 6, p. 1214-1223.
- Petit, J., 1987, Criteria for the sense of movement on fault surfaces in brittle rocks: *Journal of Structural Geology*, v. 9, no. 5, p. 597-608.
- Petrinin, A. G., and Sobolev, S. V., 2008, Three-dimensional numerical models of the evolution of pull-apart basins: *Physics of the Earth and Planetary Interiors*, v. 171, no. 1-4, p. 387-399.
- Pinheiro, R. V. L., and Holdsworth, R. E., 1997, Reactivation of Archaean strike-slip fault systems, Amazon region, Brazil: *Journal of the Geological Society*, v. 154, no. 1, p. 99-103.
- Ramezani, J., and Tucker, R. D., 2003, The Saghand region, central Iran: U-Pb geochronology, petrogenesis and implications for Gondwana tectonics: *American Journal of Science*, v. 303, no. 7, p. 622-665.
- Reading, H. G., 2009, *Sedimentary environments: processes, facies and stratigraphy*, Wiley.
- Redfield, T. F., and Fitzgerald, P. G., 1993, Denali fault system of southern Alaska - an interior strike-slip structure responding to dextral and sinistral shear coupling: *Tectonics*, v. 12, no. 5, p. 1195-1208.
- Regard, V., Bellier, O., Braucher, R., Gasse, F., Bourlès, D., Mercier, J., Thomas, J. C., Abbassi, M. R., Shabanian, E., and Soleymani, S., 2006, ¹⁰Be dating of alluvial deposits from Southeastern Iran (the Hormoz Strait area): *Palaeogeography, Palaeoclimatology, Palaeoecology*, v. 242, no. 1-2, p. 36-53.
- Regard, V., Bellier, O., Thomas, J. C., Abbassi, M., Mercier, J., Shabanian, E., Feghhi, K., and Soleymani, S., 2004, Accommodation of Arabia-Eurasia convergence in the Zagros-Makran

- transfer zone, SE Iran: A transition between collision and subduction through a young deforming system: *Tectonics*, v. 23, no. 4.
- Regard, V., Bellier, O., Thomas, J. C., Bourlès, D., Bonnet, S., Abbassi, M. R., Braucher, R., Mercier, J., Shabanian, E., Soleymani, S., and Feghhi, K., 2005a, Cumulative right-lateral fault slip rate across the Zagros-Makran transfer zone: role of the Minab-Zendan fault system in accommodating Arabia-Eurasia convergence in southeast Iran: *Geophysical Journal International*, v. 162, no. 1, p. 177-203.
- Regard, V., Faccenna, C., Martinod, J., and Bellier, O., 2005b, Slab pull and indentation tectonics: insights from 3D laboratory experiments: *Physics of the Earth and Planetary Interiors*, v. 149, no. 1, p. 99-113.
- Reilinger, R., McClusky, S., Vernant, P., Lawrence, S., Ergintav, S., Cakmak, R., Ozener, H., Kadirov, F., Guliev, I., and Stepanyan, R., 2006, GPS constraints on continental deformation in the Africa-Arabia-Eurasia continental collision zone and implications for the dynamics of plate interactions: *Journal of Geophysical Research: Solid Earth* (1978–2012), v. 111, no. B5.
- Reiners, P. W., and Brandon, M. T., 2006, Using thermochronology to understand orogenic erosion: *Annu. Rev. Earth Planet. Sci.*, v. 34, p. 419-466.
- Reiners, P. W., Chan, M. A., and Evenson, N. S., 2014, Radiogenic helium dating and chemistry of diagenetic Fe- and Mn-oxides in Mesozoic sandstones of the Colorado Plateau: *Geological Society of America Bulletin*, v. 126, no. 9-10, p. 1363-1383.
- Rezaeian, M., Carter, A., Hovius, N., and Allen, M. B., 2012, Cenozoic exhumation history of the Alborz Mountains, Iran: New constraints from low-temperature chronometry: *Tectonics*, v. 31, no. 2, p. n/a-n/a.
- Rice, J. R., 2006, Heating and weakening of faults during earthquake slip: *Journal of Geophysical Research*, v. 111, no. B5.
- Richard, P., and Cobbold, P., Experimental insights into partitioning of fault motions in continental convergent wrench zones, *in Proceedings Annales Tectonicae* 1990, Volume 4, p. 35-44.
- Richard, P., and Krantz, R. W., 1991, Experiments on fault reactivation in strike-slip mode: *Tectonophysics*, v. 188, no. 1, p. 117-131.
- Richard, P., Mocquet, B., and Cobbold, P., 1991, Experiments on simultaneous faulting and folding above a basement wrench fault: *Tectonophysics*, v. 188, no. 1, p. 133-141.
- Richard, P., Naylor, M., and Koopman, A., 1995, Experimental models of strike-slip tectonics: *Petroleum Geoscience*, v. 1, no. 1, p. 71-80.
- Riedel, W., 1929, Zur mechanik geologischer brucherscheinungen: *Zentralblatt für Mineralogie, Geologie und Paläontologie B*, v. 1929, p. 354-368.
- Ritter, J. B., Miller, J. R., Enzel, Y., and Wells, S. G., 1995, Reconciling the roles of tectonism and climate in Quaternary alluvial fan evolution: *Geology*, v. 23, no. 3, p. 245-248.
- Robertson, A. H., Ustaömer, T., Parlak, O., Ünlügenç, U. C., Taşlı, K., and Inan, N., 2006, The Berit transect of the Tauride thrust belt, S Turkey: Late Cretaceous–Early Cenozoic accretionary/collisional processes related to closure of the Southern Neotethys: *Journal of Asian Earth Sciences*, v. 27, no. 1, p. 108-145.
- Robin, P. Y. F., and Cruden, A. R., 1994, STRAIN AND VORTICITY PATTERNS IN IDEALLY DUCTILE TRANSPRESSION ZONES: *Journal of Structural Geology*, v. 16, no. 4, p. 447-466.
- Rockwell, T., Keller, E., Clark, M., and Johnson, D., 1984, Chronology and rates of faulting of Ventura River terraces, California: *Geological Society of America Bulletin*, v. 95, no. 12, p. 1466-1474.
- Roe, G. H., Stolar, D. B., and Willett, S. D., 2006, Response of a steady-state critical wedge orogen to changes in climate and tectonic forcing: *Geological Society of America Special Papers*, v. 398, p. 227-239.
- Roeske, S. M., Till, A. B., Foster, D. A., and Sample, J. C., 2007, Introduction: *Geological Society of America Special Papers*, v. 434, p. vii-x.

- Rossetti, F., Nozaem, R., Lucci, F., Vignaroli, G., Gerdes, A., Nasrabadi, M., and Theye, T., 2014, Tectonic setting and geochronology of the Cadomian (Ediacaran-Cambrian) magmatism in Central Iran, Kuh-e-Sarhangi region (NW Lut Block): *Journal of Asian Earth Sciences*, no. 0.
- Rossetti, F., Storti, F., and Läufer, A. L., 2002, Brittle architecture of the Lanterman Fault and its impact on the final terrane assembly in north Victoria Land, Antarctica: *Journal of the Geological Society*, v. 159, no. 2, p. 159-173.
- Rowland, J., and Sibson, R., 2004, Structural controls on hydrothermal flow in a segmented rift system, Taupo Volcanic Zone, New Zealand: *Geofluids*, v. 4, no. 4, p. 259-283.
- Royden, L., and Taylor Perron, J., 2013, Solutions of the stream power equation and application to the evolution of river longitudinal profiles: *Journal of Geophysical Research: Earth Surface*, v. 118, no. 2, p. 497-518.
- Rutter, E., and Hadizadeh, J., 1991, On the influence of porosity on the low-temperature brittle—Ductile transition in siliciclastic rocks: *Journal of Structural Geology*, v. 13, no. 5, p. 609-614.
- Rutter, E., Holdsworth, R., and Knipe, R., 2001, The nature and tectonic significance of fault-zone weakening: an introduction: *Geological Society, London, Special Publications*, v. 186, no. 1, p. 1-11.
- Salvini, F., 2004, Daisy 3 The Structural Data Integrated System Analyzer., p. Available at Software University of Roma Tre, Roma: <http://host.uniroma3.it/progetti/fralab>.
- Salvini, F., Brancolini, G., Busetti, M., Storti, F., Mazzarini, F., and Coren, F., 1997, Cenozoic geodynamics of the Ross Sea region, Antarctica: Crustal extension, intraplate strike-slip faulting, and tectonic inheritance: *Journal of Geophysical Research: Solid Earth* (1978–2012), v. 102, no. B11, p. 24669-24696.
- Sanderson, D. J., and Marchini, W., 1984, Transpression: *Journal of Structural Geology*, v. 6, no. 5, p. 449-458.
- Schiattarella, M., Di Leo, P., Beneduce, P., Giano, S. I., and Martino, C., 2006, Tectonically driven exhumation of a young orogen: an example from the southern Apennines, Italy: *Geological Society of America Special Papers*, v. 398, p. 371-385.
- Scholz, C. H., Dawers, N. H., Yu, J. Z., and Anders, M. H., 1993, FAULT GROWTH AND FAULT SCALING LAWS - PRELIMINARY-RESULTS: *Journal of Geophysical Research-Solid Earth*, v. 98, no. B12, p. 21951-21961.
- Schopfer, M. P., and Steyrer, H. P., 2001, Experimental modeling of strike-slip faults and the self-similar behavior: *MEMOIRS-GEOLOGICAL SOCIETY OF AMERICA*, p. 21-28.
- Schrank, C. E., and Cruden, A. R., 2010, Compaction control of topography and fault network structure along strike-slip faults in sedimentary basins: *Journal of Structural Geology*, v. 32, no. 2, p. 184-191.
- Schreurs, G., 2003, Fault development and interaction in distributed strike-slip shear zones: an experimental approach, *in* Storti, F., Holdsworth, R. E., and Salvini, F., eds., *Intraplate Strike-Slip Deformation Belts*, Volume 210: Bath, Geological Soc Publishing House, p. 35-52.
- Schreurs, G., and Colletta, B., 1998, Analogue modelling of faulting in zones of continental transpression and transtension: *Geological Society, London, Special Publications*, v. 135, no. 1, p. 59-79.
- Schreurs, G., and Colletta, B., 2002, Analogue modelling of continental transpression: *Journal of the virtual Explorer*, v. 6, p. 67-78.
- Scotti, R., Brardinoni, F., Alberti, S., Frattini, P., and Crosta, G. B., 2013, A regional inventory of rock glaciers and protalus ramparts in the central Italian Alps: *Geomorphology*, v. 186, p. 136-149.
- Segall, P., and Pollard, D. D., 1983, Nucleation and growth of strike slip faults in granite: *Journal of Geophysical Research*, v. 88, no. B1, p. 555-568.
- Sella, G. F., Dixon, T. H., and Mao, A., 2002, REVEL: A model for recent plate velocities from space geodesy: *J. geophys. Res.*, v. 107, no. 10.1029, p. 209-226.

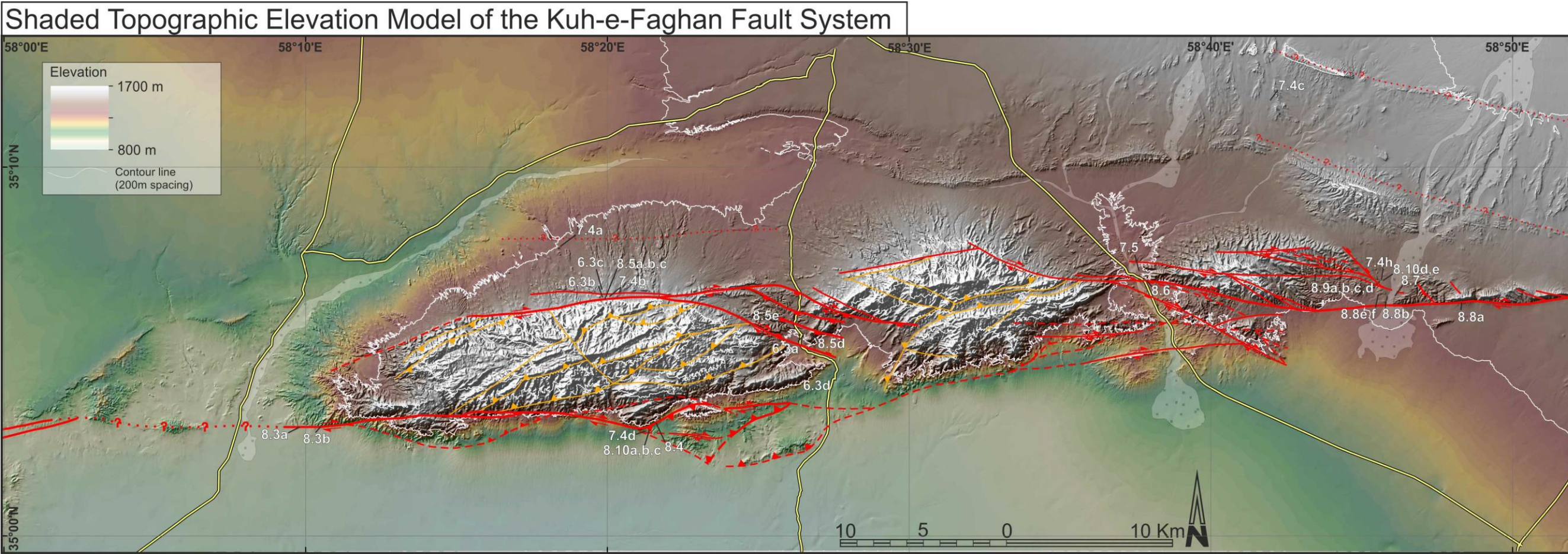
- Sengor, A. M. C., Tuysuz, O., Imren, C., Sakinc, M., Eyidogan, H., Gorur, G., Le Pichon, X., and Rangin, C., 2005, The North Anatolian Fault: A new look: *Annual Review of Earth and Planetary Sciences*, v. 33, p. 37-112.
- Serpelloni, E., Faccenna, C., Spada, G., Dong, D., and Williams, S. D., 2013, Vertical GPS ground motion rates in the Euro-Mediterranean region: New evidence of velocity gradients at different spatial scales along the Nubia-Eurasia plate boundary: *Journal of Geophysical Research: Solid Earth*, v. 118, no. 11, p. 6003-6024.
- Shabanian, E., Bellier, O., Abbassi, M. R., Siame, L., and Farbod, Y., 2010, Plio-Quaternary stress states in NE Iran: Kopeh Dag and Allah Dag-Binalud mountain ranges: *Tectonophysics*, v. 480, no. 1-4, p. 280-304.
- Shabanian, E., Bellier, O., Siame, L., Arnaud, N., Abbassi, M. R., and Cochemé, J.-J., 2009a, New tectonic configuration in NE Iran: Active strike-slip faulting between the Kopeh Dag and Binalud mountains: *Tectonics*, v. 28, no. 5.
- Shabanian, E., Siame, L., Bellier, O., Benedetti, L., and Abbassi, M. R., 2009b, Quaternary slip rates along the northeastern boundary of the Arabia-Eurasia collision zone (Kopeh Dag Mountains, Northeast Iran): *Geophysical Journal International*, v. 178, no. 2, p. 1055-1077.
- Sheldon, H., Barnicoat, A., and Ord, A., 2006, Numerical modelling of faulting and fluid flow in porous rocks: an approach based on critical state soil mechanics: *Journal of Structural Geology*, v. 28, no. 8, p. 1468-1482.
- Shuster, D. L., Vasconcelos, P. M., Heim, J. A., and Farley, K. A., 2005, Weathering geochronology by (U-Th)/He dating of goethite: *Geochimica et Cosmochimica Acta*, v. 69, p. 659-673.
- Spotila, J. A., Farley, K. A., and Sieh, K., 1998, Uplift and erosion of the San Bernardino Mountains associated with transpression along the San Andreas fault, California, as constrained by radiogenic helium thermochronometry: *Tectonics*, v. 17, no. 3, p. 360-378.
- Spotila, J. A., Farley, K. A., Yule, J. D., and Reiners, P. W., 2001, Near-field transpressive deformation along the San Andreas fault zone in southern California, based on exhumation constrained by (U-Th)/He dating: *Journal of Geophysical Research: Solid Earth*, v. 106, no. B12, p. 30909-30922.
- Spotila, J. A., House, M. A., Niemi, N. A., Brady, R. C., Oskin, M., and Buscher, J. T., 2007a, Patterns of bedrock uplift along the San Andreas fault and implications for mechanisms of transpression: *Geological Society of America Special Papers*, v. 434, p. 15-33.
- Spotila, J. A., Niemi, N., Brady, R., House, M., Buscher, J., and Oskin, M., 2007b, Long-term continental deformation associated with transpressive plate motion: The San Andreas fault: *Geology*, v. 35, no. 11, p. 967-970.
- Stock, J. D., and Montgomery, D. R., 1999, Geologic constraints on bedrock river incision using the stream power law: *Journal of Geophysical Research: Solid Earth* (1978–2012), v. 104, no. B3, p. 4983-4993.
- Storti, F., Holdsworth, R. E., and Salvini, F., 2003, Intraplate strike-slip deformation belts: *Geological Society, London, Special Publications*, v. 210, no. 1, p. 1-14.
- Storti, F., Rossetti, F., Läufer, A. L., and Salvini, F., 2006, Consistent kinematic architecture in the damage zones of intraplate strike-slip fault systems in North Victoria Land, Antarctica and implications for fault zone evolution: *Journal of Structural Geology*, v. 28, no. 1, p. 50-63.
- Storti, F., Rossetti, F., and Salvini, F., 2001, Structural architecture and displacement accommodation mechanisms at the termination of the Priestley Fault, northern Victoria Land, Antarctica: *Tectonophysics*, v. 341, no. 1, p. 141-161.
- Sutton, J., and Watson, J. V., 1986, Architecture of the continental lithosphere: *Philosophical Transactions of the Royal Society of London. Series A, Mathematical and Physical Sciences*, v. 317, no. 1539, p. 5-12.
- Sylvester, A. G., 1984, Wrench fault tectonics: selected papers reprinted from the AAPG Bulletin and other geological journals, *Amer Assn of Petroleum Geologists*, v. 28.

- Sylvester, A. G., 1988, Strike-Slip Faults: Geological Society of America Bulletin, v. 100, no. 11, p. 1666-1703.
- Tan, O., Tapirdamaz, M. C., and Yörük, A., 2008, The earthquake catalogues for Turkey: Turkish Journal of Earth Sciences, v. 17, no. 2, p. 405-418.
- Tapponnier, P., and Molnar, P., 1976, Slip-line field theory and large-scale continental tectonics: nature, v. 264, no. 5584, p. 319-324.
- Tarboton, D. G., Bras, R. L., and Rodriguez-Iturbe, I., 1991, On the extraction of channel networks from digital elevation data: Hydrological processes, v. 5, no. 1, p. 81-100.
- Tchalenko, J., 1970, Similarities between shear zones of different magnitudes: Geological Society of America Bulletin, v. 81, no. 6, p. 1625-1640.
- Tchalenko, J., and Ambraseys, N. N., 1970, Structural analysis of the Dasht-e Bayaz (Iran) earthquake fractures: Geological Society of America Bulletin, v. 81, no. 1, p. 41-60.
- Tchalenko, J., and Berberian, M., 1975, Dasht-e Bayaz fault, Iran: earthquake and earlier related structures in bed rock: Bulletin of the Geological Society of America, v. 86, no. 5, p. 703.
- Tchalenko, J., Berberian, M., and Behzadi, H., 1973, Geomorphologic and seismic evidence for recent activity on the Doruneh Fault, Iran: Tectonophysics, v. 19, no. 4, p. 333-341.
- Telbisz, T., Kovács, G., Székely, B., and Szabó, J., 2013, Topographic swath profile analysis: a generalization and sensitivity evaluation of a digital terrain analysis tool: Zeitschrift für Geomorphologie, v. 57, no. 4, p. 485-513.
- Thomson, S. N., and Ring, U., 2006, Thermochronologic evaluation of postcollision extension in the Anatolide orogen, western Turkey: Tectonics, v. 25, no. 3.
- Till, A. B., 2007, Exhumation associated with continental strike-slip fault systems, Geological Society of America.
- Troiani, F., and Della Seta, M., 2008, The use of the Stream Length–Gradient index in morphotectonic analysis of small catchments: A case study from Central Italy: Geomorphology, v. 102, no. 1, p. 159-168.
- Troiani, F., and Della Seta, M., 2011, Geomorphological response of fluvial and coastal terraces to Quaternary tectonics and climate as revealed by geostatistical topographic analysis: Earth Surface Processes and Landforms, v. 36, no. 9, p. 1193-1208.
- Troiani, F., Galve, J. P., Piacentini, D., Della Seta, M., and Guerrero, J., 2014, Spatial analysis of stream length-gradient (SL) index for detecting hillslope processes: A case of the Gállego River headwaters (Central Pyrenees, Spain): Geomorphology, v. 214, p. 183-197.
- Tuckwell, G. W., Bull, J. M., and Sanderson, D. J., 1999, Mechanical control of oceanic plate boundary geometry: Tectonophysics, v. 313, no. 3, p. 265-270.
- Vasconcelos, P. M., Heim, J. A., Farley, K. A., Monteiro, H., and Waltenberg, K., 2013, $^{40}\text{Ar}/^{39}\text{Ar}$ and $(\text{U-Th})/\text{He} - ^4\text{He}/^3\text{He}$ geochronology of landscape evolution and channel iron deposits genesis at Lynn Peak, Western Australia: Geochimica et Cosmochimica Acta, v. 117, p. 283-312.
- Vauchez, A., and Tommasi, A., 2003, Wrench faults down to the asthenosphere: geological and geophysical evidence and thermomechanical effects: Geological Society, London, Special Publications, v. 210, no. 1, p. 15-34.
- Verdel, C., Wernicke, B. P., Ramezani, J., Hassanzadeh, J., Renne, P. R., and Spell, T. L., 2007, Geology and thermochronology of Tertiary Cordilleran-style metamorphic core complexes in the Saghand region of central Iran: Geological Society of America Bulletin, v. 119, no. 7-8, p. 961-977.
- Vermilye, J. M., and Scholz, C. H., 1998, The process zone: A microstructural view of fault growth: Journal of Geophysical Research, v. 103, no. B6, p. 12223-12212, 12237.
- Vernant, P., Nilforoushan, F., Hatzfeld, D., Abbassi, M. R., Vigny, C., Masson, F., Nankali, H., Martinod, J., Ashtiani, A., Bayer, R., Tavakoli, F., and Chéry, J., 2004, Present-day crustal deformation and plate kinematics in the Middle East constrained by GPS measurements in Iran and northern Oman: Geophysical Journal International, v. 157, no. 1, p. 381-398.

- Vincent, S. J., Allen, M. B., Ismail-Zadeh, A. D., Flecker, R., Foland, K. A., and Simmons, M. D., 2005, Insights from the Talysh of Azerbaijan into the Paleogene evolution of the South Caspian region: *Geological Society of America Bulletin*, v. 117, no. 11-12, p. 1513-1533.
- Vincent, S. J., Morton, A. C., Carter, A., Gibbs, S., and Barabadeze, T. G., 2007, Oligocene uplift of the Western Greater Caucasus: an effect of initial Arabia–Eurasia collision: *Terra Nova*, v. 19, no. 2, p. 160-166.
- Walker, R., and Jackson, J., 2002, Offset and evolution of the Gowk fault, SE Iran: a major intra-continental strike-slip system: *Journal of Structural Geology*, v. 24, no. 11, p. 1677-1698.
- , 2004, Active tectonics and late Cenozoic strain distribution in central and eastern Iran: *Tectonics*, v. 23, no. 5.
- Walker, R., Jackson, J., and Baker, C., 2004, Active faulting and seismicity of the Dasht-e-Bayaz region, eastern Iran: *Geophysical Journal International*, v. 157, no. 1, p. 265-282.
- Walker, R. T., and Fattahi, M., 2011, A framework of Holocene and Late Pleistocene environmental change in eastern Iran inferred from the dating of periods of alluvial fan abandonment, river terracing, and lake deposition: *Quaternary Science Reviews*, v. 30, no. 9, p. 1256-1271.
- Walker, R. T., and Khatib, M. M., 2006, Active faulting in the Birjand region of NE Iran: *Tectonics*, v. 25, no. 4.
- Walpersdorf, A., Manighetti, I., Mousavi, Z., Tavakoli, F., Vergnolle, M., Jadidi, A., Hatzfeld, D., Aghamohammadi, A., Bigot, A., and Djamour, Y., 2014, Present-day kinematics and fault slip rates in eastern Iran, derived from 11 years of GPS data: *Journal of Geophysical Research: Solid Earth*, v. 119, no. 2, p. 1359-1383.
- Wannamaker, P. E., Caldwell, T. G., Jiracek, G. R., Maris, V., Hill, G. J., Ogawa, Y., Bibby, H. M., Bennie, S. L., and Heise, W., 2009, Fluid and deformation regime of an advancing subduction system at Marlborough, New Zealand: *nature*, v. 460, no. 7256, p. 733-U790.
- Wegmann, K. W., and Pazzaglia, F. J., 2009, Late Quaternary fluvial terraces of the Romagna and Marche Apennines, Italy: Climatic, lithologic, and tectonic controls on terrace genesis in an active orogen: *Quaternary Science Reviews*, v. 28, no. 1, p. 137-165.
- Wegmann, K. W., Zurek, B. D., Regalla, C. A., Bilardello, D., Wollenberg, J. L., Kopczynski, S. E., Ziemann, J. M., Haight, S. L., Apgar, J. D., and Zhao, C., 2007, Position of the Snake River watershed divide as an indicator of geodynamic processes in the greater Yellowstone region, western North America: *Geosphere*, v. 3, no. 4, p. 272-281.
- Wernicke, R. S., and Lippolt, H. J., 1993, Botryoidal hematite from the Schwarzwald (Germany): heterogeneous uranium distributions and their bearing on the helium dating method: *Earth and Planetary Science Letters*, v. 114, p. 287-300.
- Whipple, K. X., 2001, Fluvial landscape response time: how plausible is steady-state denudation?: *American Journal of Science*, v. 301, no. 4-5, p. 313-325.
- , 2004, Bedrock rivers and the geomorphology of active orogens: *Annu. Rev. Earth Planet. Sci.*, v. 32, p. 151-185.
- Whipple, K. X., and Tucker, G. E., 1999, Dynamics of the stream-power river incision model: Implications for height limits of mountain ranges, landscape response timescales, and research needs: *Journal of Geophysical Research: Solid Earth* (1978–2012), v. 104, no. B8, p. 17661-17674.
- Whittaker, A. C., Attal, M., Cowie, P. A., Tucker, G. E., and Roberts, G., 2008, Decoding temporal and spatial patterns of fault uplift using transient river long profiles: *Geomorphology*, v. 100, no. 3, p. 506-526.
- Whittaker, A. C., Cowie, P. A., Attal, M., Tucker, G. E., and Roberts, G. P., 2007, Bedrock channel adjustment to tectonic forcing: Implications for predicting river incision rates: *Geology*, v. 35, no. 2, p. 103-106.
- Wilkinson, M., McCaffrey, K., Roberts, G., Cowie, P., Phillips, R., Michetti, A. M., Vittori, E., Guerrieri, L., Blumetti, A., and Bubeck, A., 2010, Partitioned postseismic deformation

- associated with the 2009 Mw 6.3 L'Aquila earthquake surface rupture measured using a terrestrial laser scanner: *Geophysical research letters*, v. 37, no. 10.
- Willett, S. D., McCoy, S. W., Perron, J. T., Goren, L., and Chen, C.-Y., 2014, Dynamic reorganization of river basins: *Science*, v. 343, no. 6175, p. 1248765.
- Willett, S. D., Schlunegger, F., and Picotti, V., 2006, Messinian climate change and erosional destruction of the central European Alps: *Geology*, v. 34, no. 8, p. 613-616.
- Wilson, J. T., 1965, A new class of faults and their bearing on continental drift: *nature*, v. 207, no. 4995, p. 343-347.
- Wong, T.-f., and Baud, P., 2012, The brittle-ductile transition in porous rock: A review: *Journal of Structural Geology*, v. 44, p. 25-53.
- Woodcock, N., and Schubert, C., 1994, Continental strike-slip tectonics: *Continental deformation*, p. 251-263.
- Woodcock, N. H., and Fischer, M., 1986, Strike-slip duplexes: *Journal of Structural Geology*, v. 8, no. 7, p. 725-735.
- Woodcock, N. H., and Rickards, B., 2003, Transpressive duplex and flower structure: Dent Fault System, NW England: *Journal of Structural Geology*, v. 25, no. 12, p. 1981-1992.
- Wu, J. E., McClay, K., Whitehouse, P., and Dooley, T., 2009, 4D analogue modelling of transtensional pull-apart basins: *Marine and Petroleum Geology*, v. 26, no. 8, p. 1608-1623.
- Ziegler, P. A., Cloetingh, S., and van Wees, J.-D., 1995, Dynamics of intra-plate compressional deformation: the Alpine foreland and other examples: *Tectonophysics*, v. 252, no. 1, p. 7-59.
- Ziegler, P. A., Van Wees, J.-D., and Cloetingh, S., 1998, Mechanical controls on collision-related compressional intraplate deformation: *Tectonophysics*, v. 300, no. 1, p. 103-129.
- Zoback, M. L., 1992, First-and second-order patterns of stress in the lithosphere: The world stress map project: *Journal of Geophysical Research: Solid Earth (1978–2012)*, v. 97, no. B8, p. 11703-11728.
- Zolnai, G., 1991, Continental Wrench-Tectonics and Hydrocarbon Habitat, *American Association of Petroleum Geologists, Tectonique Continentale en Cisaillement*, 55 p.:

Appendix
Appendix A Figure location map



A. Structural map of the KFF on shaded Topographic Elevation Model. Numbers in black report the figures location.

Appendix-B Structural data

Structural data								
UTM WGS84				Element type	Azimut (°)	Dip (°)	Pich (°)	Sense
Station	Lat. E°	Long. N°	Z (m)					
IR_1_2b_12	665255	3886556	-	Fault	104	60	162	Left Lat./CCW
IR_1_2b_12	665255	3886556	-	Fault	144	65	25	Left Lat./CCW
IR_1_2b_12	665255	3886556	-	Fault	152	70	156	Left Lat./CCW
IR_1_2b_12	665255	3886556	-	Fault	330	76	26	Left Lat./CCW
IR_1_2b_12	665255	3886556	-	Fault	126	83	31	Left Lat./CCW
IR_1_2b_12	665255	3886556	-	Fault	92	87	170	Left Lat./CCW
IR_1_2b_12	665255	3886556	-	Fault	301	88	170	Left Lat./CCW
IR_1_2b_12	665255	3886556	-	Fault	292	78	118	Normal
IR_1_2b_12	665255	3886556	-	Fault	220	85	108	Normal
IR_1_2b_12	665255	3886556	-	Fault	89	88	120	Normal
IR_1_2b_12	665255	3886556	-	Fault	88	62	162	Right Lat./CW
IR_1_2b_12	665255	3886556	-	Fault	110	64	24	Right Lat./CW
IR_1_2b_12	665255	3886556	-	Fault	296	72	178	Right Lat./CW
IR_1_2b_12	665255	3886556	-	Fault	115	73	15	Right Lat./CW
IR_1_2b_12	665255	3886556	-	Fault	87	73	45	Right Lat./CW
IR_1_2b_12	665255	3886556	-	Fault	98	74	10	Right Lat./CW
IR_1_2b_12	665255	3886556	-	Fault	104	78	12	Right Lat./CW
IR_1_2b_12	665255	3886556	-	Fault	92	80	8	Right Lat./CW
IR_1_2b_12	665255	3886556	-	Fault	270	80	16	Right Lat./CW
IR_1_2b_12	665255	3886556	-	Fault	97	80	162	Right Lat./CW
IR_1_2b_12	665255	3886556	-	Fault	99	81	12	Right Lat./CW
IR_1_2b_12	665255	3886556	-	Fault	166	82	145	Right Lat./CW
IR_1_2b_12	665255	3886556	-	Fault	284	82	153	Right Lat./CW
IR_1_2b_12	665255	3886556	-	Fault	282	83	7	Right Lat./CW
IR_1_2b_12	665255	3886556	-	Fault	272	83	12	Right Lat./CW
IR_1_2b_12	665255	3886556	-	Fault	88	83	26	Right Lat./CW
IR_1_2b_12	665255	3886556	-	Fault	10	85	8	Right Lat./CW
IR_1_2b_12	665255	3886556	-	Fault	265	85	8	Right Lat./CW
IR_1_2b_12	665255	3886556	-	Fault	284	87	22	Right Lat./CW
IR_1_2b_12	665255	3886556	-	Fault	96	87	163	Right Lat./CW
IR_1_2b_12	665255	3886556	-	Fault	266	88	7	Right Lat./CW
IR_1_2b_12	665255	3886556	-	Fault	87	88	150	Right Lat./CW
IR_1_2b_12	665255	3886556	-	Fault	96	88	163	Right Lat./CW
IR_1_2b_12	665255	3886556	-	Fault	283	89	135	Right Lat./CW
IR_1_2b_12	665255	3886556	-	Fault	112	79	-	Undetermined
IR_1_2b_12	665255	3886556	-	Fault	344	85	-	Undetermined
IR_1_2b_12	665255	3886556	-	Fault	330	85	-	Undetermined
IR_1_2b_12	665255	3886556	-	Fault	97	85	-	Undetermined
IR_1_2b_12	665255	3886556	-	Plain C	265	87	-	Undetermined
IR_1_2b_12	665255	3886556	-	Plain C	261	88	-	Undetermined
IR_1_2b_12	665255	3886556	-	Plain C	246	81	-	Undetermined
IR_1_2b_12	665255	3886556	-	Plain C	271	83	-	Undetermined
IR_1_2b_12	665255	3886556	-	Plain S	250	84	-	Undetermined
IR_1_2b_12	665255	3886556	-	Plain S	258	85	-	Undetermined
IR_1_2b_12	665255	3886556	-	Plain S	256	85	-	Undetermined
IR_1_2b_12	665255	3886556	-	Plain S	238	86	-	Undetermined
IR_1_2b_12	665255	3886556	-	Plain S	232	83	-	Undetermined
IR_1_2b_12	665255	3886556	-	Plain S	234	85	-	Undetermined
IR_1_2b_12	665255	3886556	-	Plain S	227	79	-	Undetermined
IR_1_2b_12	665255	3886556	-	Plain S	242	83	-	Undetermined
IR_1_2b_12	665255	3886556	-	Plain S	244	83	-	Undetermined

IR_1_2b_12	665255	3886556	-	Plain S	245	88	-	Undetermined
IR_1_2b_12	665255	3886556	-	Plain S	216	81	-	Undetermined
IR_1_2b_12	665255	3886556	-	Riedel	318	74	-	Undetermined
IR_1_2b_12	665255	3886556	-	Riedel	130	58	-	Undetermined
IR_1_2b_12	665255	3886556	-	Riedel	105	88	-	Undetermined
IR_1_2b_12	665255	3886556	-	Riedel	306	88	-	Undetermined
IR_1_2b_12	665255	3886556	-	Riedel	302	42	-	Undetermined
IR_1_2b_12	665255	3886556	-	Riedel	118	78	-	Undetermined
IR_1_2b_12	665255	3886556	-	Riedel	110	81	-	Undetermined
IR_1_2b_12	665255	3886556	-	Riedel	108	83	-	Undetermined
IR_1_3b_12	668596	3886433	-	Fault	279	72	173	Right Lat./CW
IR_1_3b_12	668596	3886433	-	Fault	71	75	16	Right Lat./CW
IR_1_3b_12	668596	3886433	-	Fault	272	75	155	Right Lat./CW
IR_1_3b_12	668596	3886433	-	Fault	84	77	163	Right Lat./CW
IR_1_3b_12	668596	3886433	-	Fault	96	78	12	Right Lat./CW
IR_1_3b_12	668596	3886433	-	Fault	298	79	72	Reverse
IR_1_3b_12	668596	3886433	-	Fault	97	82	10	Right Lat./CW
IR_1_3b_12	668596	3886433	-	Fault	94	83	100	Undetermined
IR_1_3b_12	668596	3886433	-	Fault	94	83	160	Right Lat./CW
IR_1_3b_12	668596	3886433	-	Fault	292	85	25	Right Lat./CW
IR_1_3b_12	668596	3886433	-	Fault	250	85	88	Normal
IR_1_4_12	648699	3887113	-	Fault	81	52	7	Right Lat./CW
IR_1_4_12	648699	3887113	-	Fault	113	60	12	Right Lat./CW
IR_1_4_12	648699	3887113	-	Fault	112	60	17	Right Lat./CW
IR_1_4_12	648699	3887113	-	Fault	300	64	140	Right Lat./CW
IR_1_4_12	648699	3887113	-	Fault	116	65	28	Right Lat./CW
IR_1_4_12	648699	3887113	-	Fault	277	68	93	Undetermined
IR_1_4_12	648699	3887113	-	Fault	282	68	-	Undetermined
IR_1_4_12	648699	3887113	-	Fault	122	71	29	Right Lat./CW
IR_1_4_12	648699	3887113	-	Fault	117	77	9	Right Lat./CW
IR_1_4_12	648699	3887113	-	Fault	264	81	-	Undetermined
IR_1_4_12	648699	3887113	-	Fault	273	82	-	Undetermined
IR_1_4_12	648699	3887113	-	Fault	275	85	163	Right Lat./CW
IR_1_4_12	648699	3887113	-	Fault	106	86	95	Normal
IR_1_4_12	648699	3887113	-	Fault	257	87	8	Right Lat./CW
IR_1_4_12	648699	3887113	-	Plain C	103	80	9	Right Lat./CW
IR_1_4_12	648699	3887113	-	Plain C	268	80	12	Right Lat./CW
IR_1_4_12	648699	3887113	-	Plain C	274	34	179	Undetermined
IR_1_4_12	648699	3887113	-	Plain C	264	82	-	Undetermined
IR_1_4_12	648699	3887113	-	Plain C	88	71	-	Undetermined
IR_1_4_12	648699	3887113	-	Plain C	85	66	-	Right Lat./CW
IR_1_4_12	648699	3887113	-	Plain C	85	78	-	Right Lat./CW
IR_1_4_12	648699	3887113	-	Plain C	83	81	-	Right Lat./CW
IR_1_4_12	648699	3887113	-	Plain C	264	83	-	Undetermined
IR_1_4_12	648699	3887113	-	Plain C	266	85	-	Undetermined
IR_1_4_12	648699	3887113	-	Plain C	268	83	-	Undetermined
IR_1_4_12	648699	3887113	-	Plain C	260	80	-	Undetermined
IR_1_4_12	648699	3887113	-	Plain C	261	81	-	Undetermined
IR_1_4_12	648699	3887113	-	Plain S	278	64	-	Undetermined
IR_1_4_12	648699	3887113	-	Plain S	225	80	-	Undetermined
IR_1_4_12	648699	3887113	-	Plain S	230	80	-	Undetermined
IR_1_4_12	648699	3887113	-	Plain S	60	81	-	Undetermined
IR_1_4_12	648699	3887113	-	Plain S	235	88	-	Undetermined
IR_1_4_12	648699	3887113	-	Plain S	54	60	-	Undetermined
IR_1_4_12	648699	3887113	-	Plain S	55	65	-	Undetermined
IR_1_4_12	648699	3887113	-	Plain S	48	56	-	Undetermined
IR_1_4_12	648699	3887113	-	Plain S	226	80	-	Undetermined
IR_1_4_12	648699	3887113	-	Plain S	228	81	-	Undetermined
IR_1_4_12	648699	3887113	-	Riedel	9	85	8	Left Lat./CCW

IR_1_4_12	648699	3887113	-	Riedel	129	78	10	Right Lat./CW
IR_1_4_12	648699	3887113	-	Riedel	139	83	18	Right Lat./CW
IR_1_4_12	648699	3887113	-	Riedel	124	73	18	Right Lat./CW
IR_1_4_12	648699	3887113	-	Riedel	184	77	152	Left Lat./CCW
IR_1_4_12	648699	3887113	-	Riedel	220	81	167	Left Lat./CCW
IR_1_4_13	648699	3887113	-	Plain C	277	68	179	Right Lat./CW
IR_1_5_12	648152	3887159	-	Ext.Fracture	230	75	-	Undetermined
IR_1_5_12	648152	3887159	-	Ext.Fracture	225	78	-	Undetermined
IR_1_5_12	648152	3887159	-	Ext.Fracture	230	74	-	Undetermined
IR_1_5_12	648152	3887159	-	Ext.Fracture	224	84	-	Undetermined
IR_1_5_12	648152	3887159	-	Ext.Fracture	148	84	-	Undetermined
IR_1_5_12	648152	3887159	-	Fault	80	62	167	Undetermined
IR_1_6_12	648115	3887106	-	Ext.Fracture	220	88	-	Undetermined
IR_1_6_12	648115	3887106	-	Ext.Fracture	231	88	-	Undetermined
IR_1_6_12	648115	3887106	-	Ext.Fracture	246	79	-	Undetermined
IR_1_7_12	655791	3886235	-	Calcite Vein	124	62	-	Undetermined
IR_1_7_12	655791	3886235	-	Calcite Vein	124	79	-	Undetermined
IR_1_7_12	655791	3886235	-	Calcite Vein	126	70	-	Undetermined
IR_1_7_12	655791	3886235	-	Calcite Vein	127	75	-	Undetermined
IR_1_7_12	655791	3886235	-	Calcite Vein	304	79	-	Undetermined
IR_1_7_12	655791	3886235	-	Calcite Vein	149	76	-	Undetermined
IR_1_7_12	655791	3886235	-	Calcite Vein	127	76	-	Undetermined
IR_1_7_12	655791	3886235	-	Calcite Vein	322	81	-	Undetermined
IR_1_7_12	655791	3886235	-	Calcite Vein	129	83	-	Undetermined
IR_1_7_12	655791	3886235	-	Calcite Vein	120	71	-	Undetermined
IR_1_7_12	655791	3886235	-	Calcite Vein	131	83	-	Undetermined
IR_1_7_12	655791	3886235	-	Calcite Vein	126	85	-	Undetermined
IR_1_7_12	655791	3886235	-	Calcite Vein	141	81	-	Undetermined
IR_1_7_12	655791	3886235	-	Fault	162	56	3	Left Lat./CCW
IR_1_7_12	655791	3886235	-	Fault	182	68	173	Left Lat./CCW
IR_1_7_12	655791	3886235	-	Fault	54	81	6	Left Lat./CCW
IR_1_7_12	655791	3886235	-	Fault	318	83	170	Left Lat./CCW
IR_1_7_12	655791	3886235	-	Fault	226	84	152	Left Lat./CCW
IR_1_7_12	655791	3886235	-	Fault	121	65	100	Normal
IR_1_7_12	655791	3886235	-	Fault	190	70	98	Normal
IR_1_7_12	655791	3886235	-	Fault	116	76	111	Normal
IR_1_7_12	655791	3886235	-	Fault	98	87	85	Normal
IR_1_7_12	655791	3886235	-	Fault	136	56	4	Right Lat./CW
IR_1_7_12	655791	3886235	-	Fault	311	80	20	Right Lat./CW
IR_1_7_12	655791	3886235	-	Fault	310	84	35	Right Lat./CW
IR_1_7_12	655791	3886235	-	Fault	98	87	160	Right Lat./CW
IR_1_7_12	655791	3886235	-	Fault	92	87	21	Right Lat./CW
IR_1_7_12	655791	3886235	-	Fault	272	88	21	Right Lat./CW
IR_1_7_12	655791	3886235	-	Fault	204	78	163	Undetermined
IR_1_7_12	655791	3886235	-	Fault	26	84	158	Undetermined
IR_1_7b_12	655550	3887639	-	Calcite Vein	186	70	-	Undetermined
IR_1_7b_12	655550	3887639	-	Calcite Vein	178	85	-	Undetermined
IR_1_7b_12	655550	3887639	-	Calcite Vein	176	86	-	Undetermined
IR_1_7b_12	655550	3887639	-	Calcite Vein	181	85	-	Undetermined
IR_1_7b_12	655550	3887639	-	Calcite Vein	181	77	-	Undetermined
IR_1_7b_12	655550	3887639	-	Calcite Vein	138	87	-	Undetermined
IR_1_7b_12	655550	3887639	-	Calcite Vein	141	88	-	Undetermined
IR_1_7b_12	655550	3887639	-	Calcite Vein	141	87	-	Undetermined
IR_1_7b_12	655550	3887639	-	Calcite Vein	139	83	-	Undetermined
IR_1_7b_12	655550	3887639	-	Calcite Vein	136	82	-	Undetermined
IR_1_7b_12	655550	3887639	-	Calcite Vein	137	86	-	Undetermined
IR_1_7b_12	655550	3887639	-	Fault	138	46	44	Right Lat./CW
IR_1_7b_12	655550	3887639	-	Fault	142	68	12	Right Lat./CW
IR_1_7b_12	655550	3887639	-	Fault	132	69	3	Undetermined

IR_1_7b_12	655550	3887639	-	Fault	132	69	104	Undetermined
IR_1_7b_12	655550	3887639	-	Fault	306	82	163	Undetermined
IR_1_7b_12	655550	3887639	-	Fault	133	84	61	Normal
IR_1_7b_12	655550	3887639	-	Fault	252	87	7	Right Lat./CW
IR_1_7b_12	655550	3887639	-	Fault	107	88	9	Right Lat./CW
IR_2_1_12	606401	3879123	-	Fault	210	52	160	Right Lat./CW
IR_2_1_12	606401	3879123	-	Fault	105	58	15	Right Lat./CW
IR_2_1_12	606401	3879123	-	Fault	120	88	10	Right Lat./CW
IR_2_10_12	660351	3887372	-	Ext.Fracture	262	87	-	Undetermined
IR_2_10_12	660351	3887372	-	Ext.Fracture	50	70	-	Undetermined
IR_2_10_12	660351	3887372	-	Ext.Fracture	232	83	-	Undetermined
IR_2_10_12	660351	3887372	-	Ext.Fracture	230	87	-	Undetermined
IR_2_10_12	660351	3887372	-	Ext.Fracture	235	90	-	Undetermined
IR_2_10_12	660351	3887372	-	Ext.Fracture	234	89	-	Undetermined
IR_2_10_12	660351	3887372	-	Ext.Fracture	230	89	-	Undetermined
IR_2_10_12	660351	3887372	-	Ext.Fracture	43	88	-	Undetermined
IR_2_10_12	660351	3887372	-	Ext.Fracture	49	90	-	Undetermined
IR_2_10_12	660351	3887372	-	Ext.Fracture	63	84	-	Undetermined
IR_2_10_12	660351	3887372	-	Ext.Fracture	52	90	-	Undetermined
IR_2_10_12	660351	3887372	-	Fault	128	51	76	Normal
IR_2_10_12	660351	3887372	-	Fault	68	80	-	Undetermined
IR_2_10_12	660351	3887372	-	Fault	62	88	-	Undetermined
IR_2_11_b_12	658479	3888982	-	Ext.Fracture	262	84	-	Undetermined
IR_2_11_b_12	658479	3888982	-	Ext.Fracture	228	90	-	Undetermined
IR_2_11_b_12	658479	3888982	-	Ext.Fracture	304	90	-	Undetermined
IR_2_11_b_12	658479	3888982	-	Ext.Fracture	35	90	-	Undetermined
IR_2_11_b_12	658479	3888982	-	Ext.Fracture	305	90	-	Undetermined
IR_2_11_b_12	658479	3888982	-	Ext.Fracture	157	73	-	Undetermined
IR_2_11_b_12	658479	3888982	-	Ext.Fracture	166	80	-	Undetermined
IR_2_11_b_12	658479	3888982	-	Ext.Fracture	242	78	-	Undetermined
IR_2_11_b_12	658479	3888982	-	Ext.Fracture	253	81	-	Undetermined
IR_2_11_b_12	658479	3888982	-	Ext.Fracture	254	81	-	Undetermined
IR_2_11_b_12	658479	3888982	-	Ext.Fracture	100	82	-	Undetermined
IR_2_11_b_12	658479	3888982	-	Ext.Fracture	105	85	-	Undetermined
IR_2_11_b_12	658479	3888982	-	Ext.Fracture	326	74	-	Undetermined
IR_2_11_b_12	658479	3888982	-	Ext.Fracture	88	89	-	Undetermined
IR_2_11_b_12	658479	3888982	-	Ext.Fracture	270	84	-	Undetermined
IR_2_11_b_12	658479	3888982	-	Ext.Fracture	205	90	-	Undetermined
IR_2_11_b_12	658479	3888982	-	Ext.Fracture	259	87	-	Undetermined
IR_2_11_b_12	658479	3888982	-	Fault	63	88	-	Undetermined
IR_2_11_b_12	658479	3888982	-	Fault	333	89	-	Undetermined
IR_2_11_b_12	658479	3888982	-	Fault	310	90	-	Undetermined
IR_2_14_12	660406	3887071	-	Calcite Vein	128	68	80	Normal
IR_2_14_12	660406	3887071	-	Calcite Vein	125	77	92	Normal
IR_2_14_12	660406	3887071	-	Calcite Vein	315	82	162	Right Lat./CW
IR_2_14_12	660406	3887071	-	Calcite Vein	320	84	-	Undetermined
IR_2_14_12	660406	3887071	-	Calcite Vein	304	88	-	Undetermined
IR_2_14_12	660406	3887071	-	Calcite Vein	136	76	-	Undetermined
IR_2_14_12	660406	3887071	-	Calcite Vein	128	58	-	Undetermined
IR_2_14_12	660406	3887071	-	Calcite Vein	140	70	-	Undetermined
IR_2_14_12	660406	3887071	-	Calcite Vein	135	71	-	Undetermined
IR_2_14_12	660406	3887071	-	Fault	286	35	76	Normal
IR_2_14_12	660406	3887071	-	Fault	316	38	70	Normal
IR_2_14_12	660406	3887071	-	Fault	115	52	53	Normal
IR_2_14_12	660406	3887071	-	Fault	350	54	-	Undetermined
IR_2_14_12	660406	3887071	-	Fault	340	54	-	Undetermined
IR_2_14_12	660406	3887071	-	Fault	338	58	88	Normal
IR_2_14_12	660406	3887071	-	Fault	298	60	92	Normal
IR_2_14_12	660406	3887071	-	Fault	15	60	-	Undetermined

IR_2_14_12	660406	3887071	-	Fault	112	62	87	Normal
IR_2_14_12	660406	3887071	-	Fault	271	62	-	Undetermined
IR_2_14_12	660406	3887071	-	Fault	309	68	93	Normal
IR_2_14_12	660406	3887071	-	Fault	128	69	10	Right Lat./CW
IR_2_14_12	660406	3887071	-	Fault	178	82	-	Undetermined
IR_2_16_12	659976	3887923	-	Fault	95	77	-	Undetermined
IR_2_16_12	659976	3887923	-	Fault	260	81	45	Right Lat./CW
IR_2_16_12	659976	3887923	-	Fault	260	81	45	Right Lat./CW
IR_2_16_12	659976	3887923	-	Fault	278	84	-	Undetermined
IR_2_16_12	659976	3887923	-	Fault	91	86	134	Normal
IR_2_16_12	659976	3887923	-	Fault	91	86	134	Normal
IR_2_16_12	659976	3887923	-	Fault	94	86	-	Undetermined
IR_2_16_12	659976	3887923	-	Fault	91	88	154	Right Lat./CW
IR_2_16_12	659976	3887923	-	Fault	91	88	154	Right Lat./CW
IR_2_16b_12	673806	3887016	-	Fault	140	62	130	Normal
IR_2_16b_12	673806	3887016	-	Fault	300	70	150	Right Lat./CW
IR_2_16b_12	673806	3887016	-	Fault	108	74	40	Undetermined
IR_2_16b_12	673806	3887016	-	Fault	96	75	177	Right Lat./CW
IR_2_16b_12	673806	3887016	-	Fault	115	75	80	Normal
IR_2_16b_12	673806	3887016	-	Fault	104	78	68	Reverse
IR_2_16b_12	673806	3887016	-	Fault	290	80	35	Right Lat./CW
IR_2_16b_12	673806	3887016	-	Fault	100	80	140	Right Lat./CW
IR_2_16b_12	673806	3887016	-	Fault	128	80	146	Right Lat./CW
IR_2_16b_12	673806	3887016	-	Fault	275	80	168	Right Lat./CW
IR_2_16b_12	673806	3887016	-	Fault	294	83	10	Right Lat./CW
IR_2_16b_12	673806	3887016	-	Fault	111	83	178	Right Lat./CW
IR_2_16b_12	673806	3887016	-	Fault	138	84	170	Right Lat./CW
IR_2_16b_12	673806	3887016	-	Fault	89	85	12	Right Lat./CW
IR_2_16b_12	673806	3887016	-	Fault	188	85	170	Right Lat./CW
IR_2_16b_12	673806	3887016	-	Fault	310	87	-	Undetermined
IR_2_16b_12	673806	3887016	-	Fault	106	87	-	Undetermined
IR_2_16b_12	673806	3887016	-	Fault	307	89	162	Right Lat./CW
IR_2_18_12	621715	3885650	-	Fault	285	44	162	Right Lat./CW
IR_2_18_12	621715	3885650	-	Fault	88	66	140	Right Lat./CW
IR_2_18_12	621715	3885650	-	Fault	80	67	160	Left Lat./CCW
IR_2_18_12	621715	3885650	-	Fault	98	68	170	Right Lat./CW
IR_2_18_12	621715	3885650	-	Fault	105	70	105	Reverse
IR_2_18_12	621715	3885650	-	Fault	102	72	16	Right Lat./CW
IR_2_18_12	621715	3885650	-	Fault	158	72	154	Right Lat./CW
IR_2_18_12	621715	3885650	-	Fault	195	79	149	Left Lat./CCW
IR_2_18_12	621715	3885650	-	Fault	185	80	152	Left Lat./CCW
IR_2_18_12	621715	3885650	-	Fault	3	85	147	Right Lat./CW
IR_2_18_12	621715	3885650	-	Fault	274	86	171	Right Lat./CW
IR_2_18_12	621715	3885650	-	Fault	284	86	42	Right Lat./CW
IR_2_18_12	621715	3885650	-	Fault	195	88	12	Left Lat./CCW
IR_2_18_12	621715	3885650	-	Fault	81	88	154	Right Lat./CW
IR_2_22_12	631339	3885285	-	Fault	11	68	110	Normal
IR_2_22_12	631339	3885285	-	Fault	94	68	-	Undetermined
IR_2_22_12	631339	3885285	-	Fault	64	72	12	Right Lat./CW
IR_2_22_12	631339	3885285	-	Fault	90	72	104	Normal
IR_2_22_12	631339	3885285	-	Fault	60	76	6	Right Lat./CW
IR_2_22_12	631339	3885285	-	Fault	292	78	100	Normal
IR_2_22_12	631339	3885285	-	Fault	292	78	165	Right Lat./CW
IR_2_22_12	631339	3885285	-	Fault	140	78	-	Normal
IR_2_23_12	630939	3885308	-	Fault	120	45	92	Normal
IR_2_23_12	630939	3885308	-	Fault	101	54	94	Normal
IR_2_23_12	630939	3885308	-	Fault	111	60	84	Normal
IR_2_23_12	630939	3885308	-	Fault	82	62	84	Normal
IR_2_23_12	630939	3885308	-	Fault	81	63	75	Normal

IR_2_23_12	630939	3885308	-	Fault	124	67	-	Undetermined
IR_2_23_12	630939	3885308	-	Fault	92	68	72	Undetermined
IR_2_23_12	630939	3885308	-	Fault	114	68	91	Normal
IR_2_23_12	630939	3885308	-	Fault	101	74	24	Undetermined
IR_2_23_12	630939	3885308	-	Fault	91	74	144	Undetermined
IR_2_23_12	630939	3885308	-	Fault	114	76	81	Normal
IR_2_23_12	630939	3885308	-	Fault	110	76	168	Right Lat./CW
IR_2_23_12	630939	3885308	-	Fault	113	76	-	Right Lat./CW
IR_2_23_12	630939	3885308	-	Fault	100	77	86	Normal
IR_2_23_12	630939	3885308	-	Fault	110	78	7	Right Lat./CW
IR_2_23_12	630939	3885308	-	Fault	110	78	10	Right Lat./CW
IR_2_23_12	630939	3885308	-	Fault	112	80	170	Right Lat./CW
IR_2_23_12	630939	3885308	-	Fault	77	80	-	Undetermined
IR_2_23_12	630939	3885308	-	Fault	118	81	114	Normal
IR_2_23_12	630939	3885308	-	Fault	281	84	91	Normal
IR_2_5_12	590662	3878889	-	Ext.Fracture	68	80	-	Undetermined
IR_2_5_12	590662	3878889	-	Ext.Fracture	264	83	-	Undetermined
IR_2_5_12	590662	3878889	-	Ext.Fracture	62	84	-	Undetermined
IR_2_5_12	590662	3878889	-	Ext.Fracture	250	90	-	Undetermined
IR_2_5_12	590662	3878889	-	Ext.Fracture	54	80	-	Undetermined
IR_2_5_12	590662	3878889	-	Ext.Fracture	72	80	-	Undetermined
IR_2_5b_12	592698	3877562	-	Fault	52	70	80	Reverse
IR_2_5b_12	592698	3877562	-	Fault	234	75	-	Undetermined
IR_2_5b_12	592698	3877562	-	Fault	52	78	-	Undetermined
IR_2_5b_12	592698	3877562	-	Fault	256	78	-	Undetermined
IR_2_5b_12	592698	3877562	-	Fault	50	79	-	Undetermined
IR_2_5b_12	592698	3877562	-	Fault	58	80	-	Left Lat./CCW
IR_2_5b_12	592698	3877562	-	Fault	65	82	-	Undetermined
IR_2_5b_12	592698	3877562	-	Fault	55	84	-	Undetermined
IR_2_5b_12	592698	3877562	-	Fault	250	84	-	Undetermined
IR_2_5b_12	592698	3877562	-	Fault	68	85	-	Undetermined
IR_2_5b_12	592698	3877562	-	Fault	44	86	-	Undetermined
IR_2_5b_12	592698	3877562	-	Fault	35	87	-	Undetermined
IR_2_5b_12	592698	3877562	-	Fault	67	90	-	Undetermined
IR_2_8_12	661287	3886063	-	Fault	120	64	48	Normal
IR_2_8_12	661287	3886063	-	Fault	288	68	22	Right Lat./CW
IR_2_8_12	661287	3886063	-	Fault	10	79	166	Left Lat./CCW
IR_2_8_12	661287	3886063	-	Fault	270	80	15	Right Lat./CW
IR_2_8_12	661287	3886063	-	Fault	240	80	166	Left Lat./CCW
IR_2_8_12	661287	3886063	-	Fault	94	80	174	Right Lat./CW
IR_2_8_12	661287	3886063	-	Fault	30	80	-	Undetermined
IR_2_8_12	661287	3886063	-	Fault	60	80	-	Undetermined
IR_2_8_12	661287	3886063	-	Fault	274	82	4	Right Lat./CW
IR_2_8_12	661287	3886063	-	Fault	101	84	5	Right Lat./CW
IR_2_8_12	661287	3886063	-	Fault	106	84	160	Right Lat./CW
IR_2_8_12	661287	3886063	-	Fault	32	84	165	Left Lat./CCW
IR_2_8_12	661287	3886063	-	Fault	8	84	170	Left Lat./CCW
IR_2_8_12	661287	3886063	-	Fault	128	85	40	Right Lat./CW
IR_2_8_12	661287	3886063	-	Fault	50	86	174	Left Lat./CCW
IR_2_8_12	661287	3886063	-	Fault	283	88	28	Right Lat./CW
IR_2_8_12	661287	3886063	-	Fault	60	88	-	Undetermined
IR_2_9_12	660689	3886175	-	Calcite Vein	150	80	-	Undetermined
IR_2_9_12	660689	3886175	-	Calcite Vein	151	82	-	Undetermined
IR_2_9_12	660689	3886175	-	Calcite Vein	140	80	-	Undetermined
IR_2_9_12	660689	3886175	-	Fault	12	5	-	Undetermined
IR_2_9_12	660689	3886175	-	Fault	110	38	114	Normal
IR_2_9_12	660689	3886175	-	Fault	110	38	170	Right Lat./CW
IR_2_9_12	660689	3886175	-	Fault	140	40	-	Right Lat./CW
IR_2_9_12	660689	3886175	-	Fault	98	62	150	Right Lat./CW

IR_2_9_12	660689	3886175	-	Fault	98	65	5	Right Lat./CW
IR_2_9_12	660689	3886175	-	Fault	108	76	170	Right Lat./CW
IR_2_9_12	660689	3886175	-	Fault	106	84	-	Right Lat./CW
IR_2_9_12	660689	3886175	-	Plain C	89	80	150	Right Lat./CW
IR_2_9_12	660689	3886175	-	Plain C	106	84	160	Right Lat./CW
IR_2_9_12	660689	3886175	-	Plain C	108	76	170	Right Lat./CW
IR_2_9_12	660689	3886175	-	Plain S	230	65	-	Right Lat./CW
IR_2_9_12	660689	3886175	-	Plain S	240	82	-	Right Lat./CW
IR_2_9_12	660689	3886175	-	Plain S	238	69	-	Right Lat./CW
IR3	605700	3885467	901	Fault	68	75	-	Right Lat./CW
IR3	631545	3881129	924	Fault	82	90	-	Undetermined
IR3	631359	3883808	997	Fault	317	83	-	Undetermined
IR3	631359	3883808	997	Fault	324	85	175	Undetermined
IR3	631033	3884480	1012	Fault	295	79	90	Normal
IR3	631033	3884480	1012	Fault	275	86	-	Normal
IR3	631469	3886031	1079	Fault	315	76	-	Normal
IR3	614343	3884752	1084	Fault	280	84	175	Right Lat./CW
IR3_16b	653881	3888692	1163	Ext.Fracture	124	51	-	Undetermined
IR3_16b	653881	3888692	1163	Ext.Fracture	126	75	-	Undetermined
IR3_18	653689	3887469	1207	Ext.Fracture	105	63	35	Right Lat./CW
IR3_18	653689	3887469	1207	Ext.Fracture	314	70	56	Normal
IR3_18	653689	3887469	1207	Ext.Fracture	345	84	85	Reverse
IR3_18	653689	3887469	1207	Fault	161	52	80	Normal
IR3_18	653689	3887469	1207	Fault	105	63	170	Right Lat./CW
IR3_18	653689	3887469	1207	Fault	335	67	60	Reverse
IR3_18	653689	3887469	1207	Fault	135	72	150	Right Lat./CW
IR3_18	653689	3887469	1207	Fault	297	77	50	Reverse
IR3_19	655089	3886115	1082	Fault	86	27	20	Left Lat./CCW
IR3_19	655089	3886115	1082	Fault	209	27	152	Left Lat./CCW
IR3_19	655089	3886115	1082	Fault	52	39	34	Right Lat./CW
IR3_19	655089	3886115	1082	Fault	115	43	90	Normal
IR3_19	655089	3886115	1082	Fault	50	43	138	Right Lat./CW
IR3_19	655089	3886115	1082	Fault	330	51	93	Normal
IR3_19	655089	3886115	1082	Fault	132	64	90	Normal
IR3_19	655089	3886115	1082	Fault	294	67	108	Normal
IR3_19	655089	3886115	1082	Fault	285	74	45	Right Lat./CW
IR3_19	655089	3886115	1082	Fault	153	76	27	Right Lat./CW
IR3_19	655089	3886115	1082	Fault	75	84	135	Reverse
IR3_19	655089	3886115	1082	Fault	82	88	123	Normal
IR3_22	655492	3886517	1050	Fault	138	36	103	Normal
IR3_22	655492	3886517	1050	Fault	143	52	87	Normal
IR3_22	655492	3886517	1050	Fault	168	53	84	Normal
IR3_22	655492	3886517	1050	Fault	125	55	107	Normal
IR3_22	655492	3886517	1050	Fault	349	59	65	Normal
IR3_22	655492	3886517	1050	Fault	330	65	80	Normal
IR3_22	655492	3886517	1050	Fault	331	66	60	Normal
IR3_22	655492	3886517	1050	Fault	331	66	65	Normal
IR3_22	655492	3886517	1050	Fault	331	66	90	Normal
IR3_22	655492	3886517	1050	Fault	338	71	69	Normal
IR3_22	655492	3886517	1050	Fault	325	72	74	Normal
IR3_22	655492	3886517	1050	Fault	332	73	79	Normal
IR3_22	655492	3886517	1050	Fault	100	88	80	Normal
IR3_22	655492	3886517	1050	Fault	136	88	90	Normal
IR3_22	655492	3886517	1050	Fault	135	89	90	Reverse
IR3_23	655440	3886391	1065	Fault	3	54	136	Right Lat./CW
IR3_23	655440	3886391	1065	Fault	52	69	24	Left Lat./CCW
IR3_23	655440	3886391	1065	Fault	310	70	76	Reverse
IR3_23	655440	3886391	1065	Fault	105	70	170	Right Lat./CW
IR3_23	655440	3886391	1065	Fault	45	76	57	Reverse

IR3_23	655440	3886391	1065	Fault	212	78	25	Left Lat./CCW
IR3_23	655440	3886391	1065	Fault	14	78	45	Undetermined
IR3_23	655440	3886391	1065	Fault	14	78	66	Undetermined
IR3_23	655440	3886391	1065	Fault	187	80	40	Left Lat./CCW
IR3_23	655440	3886391	1065	Fault	355	80	115	Reverse
IR3_23	655440	3886391	1065	Fault	94	81	163	Left Lat./CCW
IR3_23	655440	3886391	1065	Fault	32	84	28	Left Lat./CCW
IR3_23	655440	3886391	1065	Fault	225	86	23	Left Lat./CCW
IR3_23	655440	3886391	1065	Fault	14	88	10	Left Lat./CCW
IR3_23	655440	3886391	1065	Fault	6	90	76	Normal
IR3_23	655440	3886391	1065	Fault	6	90	177	Left Lat./CCW
IR3_24	636597	3888781	1159	Fault	310	62	90	Reverse
IR3_24	636597	3888781	1159	Fault	170	76	-	Undetermined
IR3_24	636597	3888781	1159	Fault	337	79	-	Undetermined
IR3_25	641645	3887762	1196	Fault	127	31	100	Normal
IR3_25	641645	3887762	1196	Fault	105	34	95	Normal
IR3_25	641645	3887762	1196	Fault	70	71	168	Right Lat./CW
IR3_25	641645	3887762	1196	Fault	32	77	0	Right Lat./CW
IR3_25	641645	3887762	1196	Fault	235	77	45	Right Lat./CW
IR3_25	641645	3887762	1196	Fault	95	82	82	Normal
IR3_26	649835	3882427	934	Fault	60	84	-	Undetermined
IR3_27	649594	3882665	937	Fault	267	67	-	Undetermined
IR3_27	649594	3882665	937	Fault	80	77	27	Right Lat./CW
IR3_27	649594	3882665	937	Fault	82	81	11	Undetermined
IR3_28	649166	3884929	991	Fault	332	56	158	Right Lat./CW
IR3_28	649166	3884929	991	Fault	326	60	20	Right Lat./CW
IR3_28	649166	3884929	991	Fault	135	67	0	Right Lat./CW
IR3_28	649166	3884929	991	Fault	322	72	150	Left Lat./CCW
IR3_28	649166	3884929	991	Fault	75	72	155	Left Lat./CCW
IR3_28	649166	3884929	991	Fault	160	72	164	Left Lat./CCW
IR3_28	649166	3884929	991	Fault	325	78	165	Right Lat./CW
IR3_28	649166	3884929	991	Fault	85	79	3	Right Lat./CW
IR3_28	649166	3884929	991	Fault	202	81	-	Left Lat./CCW
IR3_28	649166	3884929	991	Fault	156	84	168	Right Lat./CW
IR3_28	649166	3884929	991	Fault	116	86	170	Right Lat./CW
IR3_28	649166	3884929	991	Fault	88	90	170	Right Lat./CW
IR3_29	649007	3885127	1006	Fault	84	77	160	Right Lat./CW
IR3_29	649007	3885127	1006	Fault	56	78	8	Right Lat./CW
IR3_29	649007	3885127	1006	Fault	245	78	162	Right Lat./CW
IR3_29	649007	3885127	1006	Fault	155	81	174	Left Lat./CCW
IR3_29	649007	3885127	1006	Fault	335	84	170	Left Lat./CCW
IR3_29	649007	3885127	1006	Fault	310	88	10	Right Lat./CW
IR3_30	647672	3887096	-	Fault	287	33	73	Reverse
IR3_30	647672	3887096	-	Fault	130	67	165	Left Lat./CCW
IR3_30	647672	3887096	-	Fault	215	74	155	Right Lat./CW
IR3_30	647672	3887096	-	Fault	95	82	8	Right Lat./CW
IR3_30	647672	3887096	-	Fault	177	89	149	Left Lat./CCW
IR3_30	647672	3887096	-	Fault	20	90	5	Right Lat./CW
IR3_31	644401	3884176	963	Fault	329	71	73	Normal
IR3_31	644401	3884176	963	Fault	254	75	20	Right Lat./CW
IR3_31	644401	3884176	963	Fault	97	76	40	Right Lat./CW
IR3_31	644401	3884176	963	Fault	271	77	160	Right Lat./CW
IR3_31	644401	3884176	963	Fault	148	78	3	Left Lat./CCW
IR3_31	644401	3884176	963	Fault	303	78	25	Left Lat./CCW
IR3_31	644401	3884176	963	Fault	342	78	162	Left Lat./CCW
IR3_31	644401	3884176	963	Fault	84	79	143	Right Lat./CW
IR3_31	644401	3884176	963	Fault	310	79	158	Left Lat./CCW
IR3_31	644401	3884176	963	Fault	318	80	18	Left Lat./CCW
IR3_31	644401	3884176	963	Fault	280	80	20	Left Lat./CCW

IR3_31	644401	3884176	963	Fault	254	83	167	Right Lat./CW
IR3_31	644401	3884176	963	Fault	254	83	168	Right Lat./CW
IR3_31	644401	3884176	963	Fault	71	83	169	Left Lat./CCW
IR3_31	644401	3884176	963	Fault	303	85	35	Left Lat./CCW
IR3_31	644401	3884176	963	Fault	264	86	152	Right Lat./CW
IR3_32	644675	3884077	957	Fault	138	71	3	Left Lat./CCW
IR3_32	644675	3884077	957	Fault	93	76	15	Right Lat./CW
IR3_32	644675	3884077	957	Fault	84	79	13	Right Lat./CW
IR3_32	644675	3884077	957	Fault	89	85	11	Right Lat./CW
IR3_33	624179	3879610	940	Fault	305	55	160	Undetermined
IR3_34A	624308	3879680	933	Fault	66	67	80	Reverse
IR3_34A	624308	3879680	933	Fault	64	84	90	Reverse
IR3_34A	624308	3879680	933	Fault	48	88	78	Reverse
IR3_34B	624525	3879863	944	Fault	118	69	30	Left Lat./CCW
IR3_34C	624869	3880265	977	Fault	325	74	160	Left Lat./CCW
IR3_34C	624869	3880265	977	Fault	335	76	158	Left Lat./CCW
IR3_35	624841	3880770	1067	Fault	90	60	162	Right Lat./CW
IR3_35	624841	3880770	1067	Fault	162	73	12	Left Lat./CCW
IR3_35	624841	3880770	1067	Fault	266	79	0	Right Lat./CW
IR3_36	631413	3878212	869	Fault	181	72	-	Left Lat./CCW
IR3_36	631413	3878212	869	Fault	192	83	-	Left Lat./CCW
IR3_37	620017	3880585	1054	Fault	140	74	23	Undetermined
IR3_37	620017	3880585	1054	Fault	140	74	67	Undetermined
IR3_37	620017	3880585	1054	Fault	318	77	104	Undetermined
IR3_37	620017	3880585	1054	Fault	318	77	173	Right Lat./CW
IR3_37	620017	3880585	1054	Fault	25	90	23	Undetermined
IR3_38	613079	3880321	1152	Fault	354	81	23	Left Lat./CCW
IR3_38	613079	3880321	1152	Fault	330	83	82	Normal
IR3_38	613079	3880321	1152	Fault	144	90	78	Undetermined
IR3_39	605793	3883780	892	Fault	77	81	172	Undetermined
IR3_39	605793	3883780	892	Fault	287	84	175	Right Lat./CW
IR3_39	605793	3883780	892	Fault	80	86	0	Right Lat./CW
IR3_39	605793	3883780	892	Fault	246	86	4	Right Lat./CW
IR3_40	607622	3883206	949	Fault	87	74	0	Right Lat./CW
IR3_40	607622	3883206	949	Fault	3	80	-	Undetermined
IR3_40	607622	3883206	949	Fault	307	84	-	Undetermined
IR3_40	607622	3883206	949	Fault	14	85	-	Undetermined
IR3_40	607622	3883206	949	Fault	321	89	-	Undetermined
IR3_40	607622	3883206	949	Fault	75	90	-	Undetermined
IR3_40	607622	3883206	949	Fault	20	90	-	Undetermined
IR3_41	617979	3885113	1158	Fault	133	75	15	Right Lat./CW
IR3_41	617979	3885113	1158	Fault	304	80	0	Right Lat./CW
IR3_41	617979	3885113	1158	Fault	336	83	12	Right Lat./CW
IR3_41	617979	3885113	1158	Fault	310	88	137	Right Lat./CW
IR3_42	665249	3886923	1056	Ext.Fracture	275	80	-	Undetermined
IR3_42	665249	3886923	1056	Ext.Fracture	275	85	-	Undetermined
IR3_42	665249	3886923	1056	Ext.Fracture	276	80	-	Undetermined
IR3_42	665249	3886923	1056	Ext.Fracture	277	76	-	Undetermined
IR3_42	665249	3886923	1056	Ext.Fracture	310	72	-	Undetermined
IR3_42	665249	3886923	1056	Ext.Fracture	325	70	-	Undetermined
IR3_42	665249	3886923	1056	Fault	91	87	13	Right Lat./CW
IR3_43	664122	3886237	1062	Ext.Fracture	121	66	-	Undetermined
IR3_43	664122	3886237	1062	Ext.Fracture	131	81	-	Undetermined
IR3_43	664122	3886237	1062	Ext.Fracture	132	80	-	Undetermined
IR3_43	664122	3886237	1062	Fault	168	48	9	Left Lat./CCW
IR3_43	664122	3886237	1062	Fault	7	67	167	Left Lat./CCW
IR3_43	664122	3886237	1062	Fault	242	73	150	Right Lat./CW
IR3_43	664122	3886237	1062	Fault	97	76	145	Right Lat./CW
IR3_43	664122	3886237	1062	Fault	271	78	163	Right Lat./CW

IR3_43	664122	3886237	1062	Fault	100	79	27	Right Lat./CW
IR3_43	664122	3886237	1062	Fault	325	83	42	Left Lat./CCW
IR3_43	664122	3886237	1062	Fault	92	85	165	Right Lat./CW
IR3_43	664122	3886237	1062	Fault	195	85	169	Left Lat./CCW
IR3_43	664122	3886237	1062	Fault	94	90	13	Right Lat./CW
IR3_43	664122	3886237	1062	Fault	20	90	29	Left Lat./CCW
IR3_43	664122	3886237	1062	Fault	155	90	67	Normal
IR3_43	664122	3886237	1062	Plain S	233	76	-	Undetermined
IR3_43	664122	3886237	1062	Plain S	199	74	-	Undetermined
IR3_43	664122	3886237	1062	Plain S	263	77	-	Undetermined
IR3_43	664122	3886237	1062	Plain S	64	73	-	Undetermined
IR3_44	669401	3886730	1146	Fault	101	38	0	Right Lat./CW
IR3_44	669401	3886730	1146	Fault	13	71	-	Left Lat./CCW
IR3_44	669401	3886730	1146	Fault	40	73	-	Left Lat./CCW
IR3_44	669401	3886730	1146	Fault	46	90	20	Left Lat./CCW
IR3_45	668423	3886421	1080	Fault	103	53	86	Normal
IR3_45	668423	3886421	1080	Fault	265	72	29	Right Lat./CW
IR3_45	668423	3886421	1080	Fault	136	72	153	Right Lat./CW
IR3_45	668423	3886421	1080	Fault	84	77	27	Right Lat./CW
IR3_45	668423	3886421	1080	Fault	280	77	30	Left Lat./CCW
IR3_45	668423	3886421	1080	Fault	132	78	25	Right Lat./CW
IR3_45	668423	3886421	1080	Fault	122	79	5	Left Lat./CCW
IR3_45	668423	3886421	1080	Fault	266	86	0	Right Lat./CW
IR3_45	668423	3886421	1080	Fault	120	86	18	Right Lat./CW
IR3_45	668423	3886421	1080	Fault	109	90	50	Reverse
IR3_46	654596	3886039	1044	Fault	134	39	90	Normal
IR3_46	654596	3886039	1044	Fault	326	58	160	Left Lat./CCW
IR3_46	654596	3886039	1044	Fault	276	60	84	Normal
IR3_46	654596	3886039	1044	Fault	86	60	84	Reverse
IR3_46	654596	3886039	1044	Fault	349	65	12	Left Lat./CCW
IR3_46	654596	3886039	1044	Fault	32	65	160	Right Lat./CW
IR3_46	654596	3886039	1044	Fault	22	69	4	Right Lat./CW
IR3_46	654596	3886039	1044	Fault	29	76	174	Right Lat./CW
IR3_46	654596	3886039	1044	Fault	156	78	130	Undetermined
IR3_46	654596	3886039	1044	Fault	127	79	30	Right Lat./CW
IR3_46	654596	3886039	1044	Fault	165	79	34	Left Lat./CCW
IR3_46	654596	3886039	1044	Fault	22	83	169	Right Lat./CW
IR3_46	654596	3886039	1044	Fault	271	84	0	Left Lat./CCW
IR3_46	654596	3886039	1044	Fault	296	84	86	Reverse
IR3_46	654596	3886039	1044	Fault	17	84	170	Right Lat./CW
IR3_47	617823	3884972	1173	Fault	122	65	150	Right Lat./CW
IR3_47	617823	3884972	1173	Fault	20	75	8	Right Lat./CW
IR3_47	617823	3884972	1173	Fault	79	90	22	Right Lat./CW
IR3_47	617823	3884972	1173	Fault	79	90	28	Right Lat./CW
IR3_47	617823	3884972	1173	Fault	79	90	36	Right Lat./CW
IR3_47	617823	3884972	1173	Fault	79	90	46	Normal
IR3_48	652493	3884735	1013	Fault	290	66	5	Undetermined
IR3_48	652493	3884735	1013	Fault	160	72	-	Right Lat./CW
IR3_48	652493	3884735	1013	Fault	50	74	2	Right Lat./CW
IR3_48	652493	3884735	1013	Fault	208	76	-	Undetermined
IR3_48	652493	3884735	1013	Fault	7	79	-	Undetermined
IR3_48	652493	3884735	1013	Fault	71	80	-	Undetermined
IR3_48	652493	3884735	1013	Fault	302	82	3	Right Lat./CW
IR3_48	652493	3884735	1013	Fault	92	82	-	Undetermined
IR3_48	652493	3884735	1013	Fault	110	84	-	Undetermined
IR3_48	652493	3884735	1013	Fault	252	85	-	Undetermined
IR3_48	652493	3884735	1013	Fault	290	86	165	Undetermined
IR3_48	652493	3884735	1013	Fault	240	88	-	Undetermined
IR3_48	652493	3884735	1013	Fault	210	90	152	Undetermined

IR3_49	652494	3885366	1032	Fault	282	65	18	Left Lat./CCW
IR3_49	652494	3885366	1032	Fault	160	70	170	Right Lat./CW
IR3_49	652494	3885366	1032	Fault	226	70	173	Right Lat./CW
IR3_49	652494	3885366	1032	Fault	349	88	45	Right Lat./CW
IR3_7	600850	3884440	898	Calcite Vein	65	70	-	Undetermined
IR3_7	600850	3884440	898	Calcite Vein	84	90	-	Undetermined
IR3_7	600850	3884440	898	Calcite Vein	94	74	-	Undetermined
IR3_7	600513	3884456	898	Fault	68	64	14	Right Lat./CW
IR3_7	600850	3884440	898	Fault	74	74	10	Right Lat./CW
IR3_7	600513	3884456	898	Fault	65	74	16	Left Lat./CCW
IR3_7	600513	3884456	898	Fault	225	78	170	Left Lat./CCW
IR3_7	600513	3884456	898	Fault	66	80	10	Right Lat./CW
IR3_7	600850	3884440	898	Fault	80	81	0	Left Lat./CCW
IR3_7	600850	3884440	898	Fault	80	81	162	Left Lat./CCW
IR3_7	600850	3884440	898	Fault	52	84	0	Right Lat./CW
IR3_7	600850	3884440	898	Fault	56	84	172	Right Lat./CW
IR3_8	644860	3887119	1094	Fault	75	56	20	Right Lat./CW
IR3_8	644860	3887119	1094	Fault	118	60	165	Left Lat./CCW
IR3_8	644860	3887119	1094	Fault	122	62	164	Left Lat./CCW
IR3_8	644860	3887119	1094	Fault	110	63	165	Left Lat./CCW
IR3_8	644860	3887119	1094	Fault	95	64	18	Right Lat./CW
IR3_8	644860	3887119	1094	Fault	132	64	170	Left Lat./CCW
IR3_8	644860	3887119	1094	Fault	94	66	5	Right Lat./CW
IR3_8	644860	3887119	1094	Fault	135	68	150	Left Lat./CCW
IR3_8	644860	3887119	1094	Fault	126	68	168	Left Lat./CCW
IR3_8	644860	3887119	1094	Fault	85	70	10	Right Lat./CW
IR3_8	644860	3887119	1094	Fault	134	70	155	Right Lat./CW
IR3_8	644860	3887119	1094	Fault	115	71	165	Left Lat./CCW
IR3_8	644860	3887119	1094	Fault	117	74	163	Left Lat./CCW
IR3_8	644860	3887119	1094	Fault	150	75	155	Left Lat./CCW
IR3_8	644860	3887119	1094	Fault	127	75	165	Left Lat./CCW
IR3_8	644860	3887119	1094	Fault	120	76	174	Left Lat./CCW
IR3_8	644860	3887119	1094	Fault	86	76	176	Right Lat./CW
IR3_8	644860	3887119	1094	Fault	130	80	24	Right Lat./CW
IR3_8	644860	3887119	1094	Fault	125	80	168	Left Lat./CCW
IR3_8	644860	3887119	1094	Fault	176	80	172	Left Lat./CCW
IR3_8	644860	3887119	1094	Fault	130	80	174	Left Lat./CCW
IR3_8	644860	3887119	1094	Fault	84	85	86	Reverse
IR4_10	623827	3879346	-	Fault	68	37	62	Reverse
IR4_10	623827	3879346	-	Fault	15	55	120	Reverse
IR4_10	623827	3879346	-	Fault	60	72	24	Right Lat./CW
IR4_10	623827	3879346	-	Fault	242	74	40	Right Lat./CW
IR4_10	623827	3879346	-	Fault	228	77	80	Reverse
IR4_10	623827	3879346	-	Fault	44	78	173	Right Lat./CW
IR4_10	623827	3879346	-	Fault	244	84	10	Right Lat./CW
IR4_10b	624303	3879228	-	Fault	295	27	80	Reverse
IR4_10b	624303	3879228	-	Fault	62	62	155	Undetermined
IR4_10b	624303	3879228	-	Fault	47	66	130	Reverse
IR4_10b	624303	3879228	-	Fault	41	71	102	Reverse
IR4_10b	624303	3879228	-	Fault	44	71	-	Undetermined
IR4_10b	624303	3879228	-	Fault	41	75	143	Left Lat./CCW
IR4_10b	624303	3879228	-	Fault	45	76	82	Reverse
IR4_10b	624303	3879228	-	Fault	55	80	145	Undetermined
IR4_10b	624303	3879228	-	Fault	39	84	120	Reverse
IR4_10b	624303	3879228	-	Fault	50	86	80	Reverse
IR4_10b	624303	3879228	-	Fault	52	88	112	Reverse
IR4_9	623778	3879244	-	Fault	54	46	110	Reverse
IR4_9	623778	3879244	-	Fault	85	47	-	Left Lat./CCW
IR4_9	623778	3879244	-	Fault	50	50	120	Reverse

IR4_9	623778	3879244	-	Fault	65	50	-	Undetermined
IR4_9	623778	3879244	-	Fault	20	54	82	Reverse
IR4_9	623778	3879244	-	Fault	114	54	155	Undetermined
IR4_9	623778	3879244	-	Fault	30	58	94	Reverse
IR4_9	623778	3879244	-	Fault	82	68	45	Reverse
IR4_9	623778	3879244	-	Fault	75	70	85	Reverse
IR4_9	623778	3879244	-	Fault	76	72	64	Reverse
IR4_9	623778	3879244	-	Fault	89	74	103	Reverse
IR4_9	623778	3879244	-	Fault	10	80	92	Reverse
IR4_9	623778	3879244	-	Fault	72	83	167	Right Lat./CW
IR4_9	623778	3879244	-	Fault	205	86	20	Right Lat./CW
IR4_9	623778	3879244	-	Fault	180	86	54	Normal

Neogene Bedding Orientation data

UTM WGS84					UTM WGS84				
Lat. E°	Long. N°	Z (m)	Azimut	Dip	Lat. E°	Long. N°	Z (m)	Azim ut	Dip
600817	3884450	-	255	10	619970	3879845	1004	94	60
625270	3885841	-	200	16	647677	3886895	1004	264	65
641348	3895575	-	222	14	631756	3893569	1006	287	11
641395	3895439	-	261	24	654679	3883953	1006	115	44
641526	3894709	-	248	23	655082	3885121	1006	72	12
641660	3893336	-	277	12	610195	3883457	1007	215	6
641895	3892338	-	252	34	661236	3886363	1007	263	33
642009	3892474	-	250	28	644300	3884720	1008	45	9
655530	3891711	-	311	25	619965	3889947	1010	240	24
665255	3886556	-	48	40	644016	3884747	1010	0	0
665255	3886556	-	50	40	654866	3884339	1010	45	19
665255	3886556	-	67	40	648980	3885122	1011	264	4
665255	3886556	-	70	30	647753	3887306	1012	288	26
648699	3887113	-	70	30	655206	3885662	1013	77	90
655791	3886235	-	75	30	647738	3887135	1014	270	33
655791	3886235	-	75	80	655158	3885352	1014	93	9
655791	3886235	-	77	40	663054	3885156	1014	145	17
655791	3886235	-	81	30	631306	3892914	1015	284	10
655550	3887639	-	87	30	654789	3889672	1016	264	20
655550	3887639	-	88	40	610324	3883090	1018	296	26
606401	3879123	-	90	50	647768	3887241	1018	280	30
606401	3879123	-	93	22	652496	3884908	1018	142	14
606401	3879123	-	107	80	661398	3886240	1019	240	37
606401	3879123	-	108	71	654543	3883672	1020	129	55
606401	3879123	-	110	72	610350	3883084	1022	233	43
606401	3879123	-	114	64	610392	3883083	1022	0	0
606401	3879123	-	116	40	654749	3889607	1023	220	20
660406	3887071	-	180	20	630645	3889205	1024	277	12
621715	3885650	-	186	30	631635	3890176	1024	266	24
631339	3885285	-	195	60	617765	3886660	1028	284	17
660689	3886175	-	180	30	631006	3884886	1028	100	10
605243	3880292	869	75	24	652609	3885648	1029	168	29
605473	3879193	869	305	47	654933	3884477	1029	61	20
631413	3878212	869	272	16	624903	3880552	1030	63	40
605436	3879230	872	107	43	628058	3888804	1030	299	29
604345	3881469	874	300	11	647731	3887185	1030	270	33
600224	3883994	876	285	16	655214	3885836	1030	108	90
605471	3879402	877	123	43	648496	3887767	1031	270	27
604890	3880526	878	31	16	664149	3886272	1034	238	37
605734	3883906	878	313	10	616970	3887448	1035	214	10

605737	3881568	881	250	12	630695	3888665	1035	260	16
600779	3879076	883	85	40	613980	3879890	1036	213	16
600105	3879446	884	124	42	648927	3887179	1038	194	25
606048	3885824	884	232	10	619183	3889084	1039	255	12
600196	3883597	885	290	26	632476	3895201	1042	281	24
604696	3882590	885	48	15	665317	3886402	1042	224	14
604824	3880868	885	55	10	630780	3887673	1047	288	20
631435	3878347	886	58	8	624854	3880611	1049	65	50
604851	3880544	887	92	11	631120	3885327	1049	218	7
631437	3879683	888	55	13	617625	3886022	1053	241	23
631554	3880034	888	30	6	649057	3887191	1054	201	26
606053	3883762	892	271	4	649809	3887648	1054	267	26
606296	3885711	895	264	16	665253	3886923	1059	216	16
631367	3879302	895	330	6	648792	3893170	1060	260	24
600470	3883143	896	40	15	654640	3889487	1061	258	27
631338	3879077	896	290	7	655210	3892759	1063	292	31
600513	3884456	898	290	14	663405	3885194	1063	152	25
631656	3880355	898	55	10	631819	3887565	1066	84	42
600463	3882954	900	10	19	614147	3884839	1067	265	18
605700	3885467	901	247	16	654591	3886222	1067	219	14
631649	3880581	901	32	9	631237	3886110	1072	280	30
614428	3878276	902	94	61	655601	3886692	1072	350	24
606208	3884017	905	205	7	614401	3884904	1073	268	29
631606	3880764	907	20	26	649638	3893173	1075	276	31
624120	3879275	909	110	87	631428	3885821	1076	225	24
600958	3884408	911	210	14	649799	3887434	1076	115	37
608523	3885132	913	274	12	621569	3887983	1077	283	12
608717	3885901	913	239	23	632333	3887584	1077	50	17
624269	3879437	916	264	81	649100	3887287	1077	235	33
631553	3880914	916	45	20	648882	3894046	1078	260	30
644574	3882809	916	94	52	655722	3893048	1078	29	28
600084	3879008	917	96	30	626267	3887451	1079	305	9
631553	3880980	917	23	28	654031	3888972	1080	297	29
631406	3878501	919	275	6	654498	3889371	1080	310	27
607000	3883084	922	253	7	655690	3887491	1081	340	32
606522	3883672	923	188	12	668423	3886421	1081	230	12
631545	3881129	924	16	15	643101	3889321	1082	315	23
632724	3881925	929	63	18	654586	3886160	1084	101	20
651834	3882478	929	62	14	670436	3886655	1086	293	12
633378	3881986	931	85	12	648757	3894590	1087	250	19
624377	3879696	932	60	68	654282	3889223	1087	315	45
644550	3883595	933	91	33	653879	3889049	1088	291	15
632371	3881761	934	73	12	653965	3886240	1089	147	74
625126	3878743	935	94	43	626107	3887272	1090	304	19
599689	3879022	936	89	44	610917	3882482	1093	210	5
607007	3883036	936	139	4	655546	3894416	1093	266	18
625177	3879280	937	93	55	644860	3887119	1094	290	34
644509	3883791	937	88	28	644860	3887119	1094	298	29
632159	3881757	938	45	27	673492	3886924	1097	64	24
634395	3881341	938	75	15	648198	3895716	1099	254	14
633194	3882493	939	45	10	654189	3889075	1099	288	30
624179	3879610	940	0	0	655736	3893098	1099	267	20
631593	3881429	941	25	28	673364	3886930	1099	90	28
650393	3883526	942	73	81	642628	3888940	1101	325	28
624525	3879863	944	32	26	655449	3886985	1101	325	17
649361	3883647	944	82	74	655027	3895061	1102	256	25
607427	3883063	945	208	10	647856	3895909	1103	260	15
644459	3883287	946	86	43	648561	3895105	1106	261	15
649313	3883879	946	80	70	647505	3896480	1107	250	18

607328	3883330	947	216	2	654420	3889268	1107	305	90
649317	3883594	947	76	64	649446	3893226	1109	260	44
649324	3883799	947	81	77	670222	3886688	1110	292	25
625194	3879532	948	89	54	662222	3890266	1112	284	24
607622	3883206	949	312	8	636250	3889725	1113	258	18
615728	3890397	949	262	8	632969	3887133	1114	268	22
649325	3883713	949	84	81	670032	3886732	1114	292	25
654727	3882793	949	271	83	649404	3887413	1115	226	41
624269	3879661	950	37	35	653956	3888447	1117	300	26
649280	3884015	950	71	70	613097	3880048	1119	77	13
652112	3883339	950	33	12	642472	3888475	1119	284	14
611576	3886597	951	240	16	654691	3896052	1119	266	16
649329	3883561	952	72	68	653938	3888782	1123	290	23
654712	3883060	952	278	80	653925	3888275	1124	276	16
625121	3879670	954	77	58	650061	3887466	1126	244	28
625159	3879198	955	85	54	653851	3888546	1127	290	24
617501	3889596	956	265	12	622777	3887025	1128	285	20
625192	3879394	956	77	50	669725	3886769	1128	272	27
644342	3884082	956	55	11	660997	3892331	1130	260	19
645178	3883869	957	95	32	659915	3890669	1131	330	19
620192	3879823	958	96	88	663951	3896376	1133	265	14
625120	3879844	958	65	55	642283	3888244	1136	210	11
644702	3883953	958	114	28	659884	3890741	1136	307	38
644458	3883919	960	78	21	660870	3892315	1140	258	50
614917	3879129	961	55	22	642287	3888235	1141	284	33
648664	3885823	961	276	11	659849	3890873	1143	310	27
648593	3885860	962	275	15	659912	3890897	1144	315	33
644738	3884114	963	113	6	669421	3886752	1148	271	34
648253	3886516	963	288	30	625359	3885939	1150	280	31
652318	3883815	964	32	29	654947	3897119	1150	276	20
649279	3883958	965	75	78	659956	3890973	1150	323	38
624771	3879924	966	66	37	613079	3880321	1152	242	18
654760	3883251	966	106	74	625470	3885841	1152	242	18
625123	3878872	967	95	47	636568	3888968	1152	216	20
648517	3885993	968	275	24	660645	3892283	1152	290	48
631638	3881660	970	64	46	659970	3891041	1153	309	43
649193	3884252	970	70	55	653849	3888162	1154	296	23
611835	3886046	971	287	13	660003	3891086	1154	283	75
648349	3886373	971	275	25	636884	3888936	1155	214	14
649226	3884120	971	72	69	617979	3885113	1158	251	32
625023	3878989	973	78	64	636703	3888743	1160	239	27
644677	3884363	973	72	21	660408	3892156	1161	283	43
648775	3885762	974	0	0	638776	3889165	1162	240	52
649181	3884305	974	70	34	641844	3887986	1162	277	54
625094	3879945	975	65	59	659984	3891242	1162	300	36
644664	3884540	975	0	0	638691	3889071	1165	230	39
654755	3883302	975	115	86	638941	3889123	1165	306	26
624869	3880265	977	43	30	660238	3891952	1165	285	48
644376	3884342	977	76	9	653799	3888088	1167	296	23
652423	3884012	977	100	59	659959	3891362	1168	260	30
609969	3884157	978	226	12	639007	3889066	1171	290	34
616918	3888298	978	252	20	617823	3884972	1173	241	13
648417	3886248	979	274	25	638945	3889236	1174	244	22
648039	3886723	981	280	24	641747	3887826	1174	289	58
648896	3885524	981	265	11	622016	3885964	1175	284	43
647821	3887372	984	265	29	641617	3887925	1177	323	84
649169	3884716	984	62	18	638715	3888972	1178	242	20
652667	3884493	985	119	58	636748	3888020	1179	276	6
649171	3884475	986	86	36	625487	3885658	1180	274	13

624926	3880355	988	67	31	641705	3887793	1187	287	89
631768	3883307	988	60	31	660149	3891796	1187	279	44
654790	3883407	988	110	72	653633	3887575	1191	270	42
614021	3879469	991	81	14	654107	3897986	1191	250	20
620096	3879842	991	88	72	636651	3888177	1192	250	28
654774	3883347	992	115	84	660103	3891370	1193	270	35
647698	3886803	993	281	24	621511	3885769	1195	277	30
617031	3888190	994	282	19	660149	3891553	1195	280	35
625117	3880020	994	54	43	641571	3887857	1196	298	42
647682	3887114	996	269	27	653769	3887682	1198	280	30
649136	3884535	996	94	37	653782	3887870	1202	293	26
654622	3883802	996	104	39	653656	3887318	1205	387	32
654697	3883470	996	133	86	638345	3888905	1208	256	20
655072	3884810	996	56	16	638284	3888761	1210	261	25
631359	3883808	997	77	10	621665	3885648	1211	264	31
648921	3885345	997	279	7	653699	3887478	1214	265	53
661477	3886155	1000	275	42	638361	3888211	1266	290	40
649109	3884988	1001	94	11	637108	3887725	1276	46	33
654726	3884141	1001	120	24	637245	3887747	1277	23	43
613837	3879535	1002	315	10	637266	3887820	1292	67	53
612682	3885725	1003	224	23	632655	3882235	-	70	25
657155	3885836	-	38	29	632681	3881981	-	110	20
649828	3884935	-	73	41					

Appendix C: Manuscript submitted to GSA Bulletin the 2nd of January 2015

Spatio-temporal evolution of intraplate strike-slip faulting: the Neogene-Quaternary Kuh-e-Faghan Fault, Central Iran

**Gabriele Calzolari⁽¹⁾, Federico Rossetti^(1;*), Marta Della Seta⁽²⁾, Reza Nozaem ⁽³⁾,
Valerio Olivetti⁽⁴⁾, Maria Laura Balestrieri⁽⁵⁾, Domenico Cosentino⁽¹⁾, Claudio Faccenna⁽¹⁾,
Finlay M. Stuart⁽⁶⁾, Gianluca Vignaroli⁽¹⁾**

¹Dipartimento di Scienze, Università Roma Tre, Largo S. L. Murialdo 1, 00146 Roma, Italy

²Dipartimento di Scienze della Terra, “Sapienza” Università di Roma, Piazzale Aldo Moro 5, 00185 Rome, Italy

³Department of Geology, Imam Khomeini International University, 34149-16818 Qazvin, Iran

⁴Centre de Recherche et d’Enseignement de Géosciences de l’Environnement, Avenue Louis Philibert BP 80, 13545 Aix en Provence, France

⁵CNR-Istituto di Geoscienze e Georisorse, Via G. La Pira 4, 50121 Firenze, Italy

⁶Scottish Universities Environmental Research Centre, Scottish Enterprise Technology Park, East Kilbride G75 0QF, UK

() Corresponding Author*

Email: federico.rossetti@uniroma3.it

Tel: +390657338082

Fax: +3957338201

ABSTRACT

Central Iran provides an ideal site to study the long-term morphotectonic response to nucleation and propagation of intraplate faulting. In this study, a multidisciplinary approach that integrates structural and stratigraphic field investigations with apatite (U+Th)/He (AHe) thermochronology is used to reconstruct the spatio-temporal evolution of the Kuh-e-Faghan Fault (KFF) in northeastern Central Iran. The KFF defines a narrow, ca. 80 km long, deformation zone that consists of three main broadly left stepping, E-W trending, right-lateral fault strands which cut through the Mesozoic-Paleozoic substratum and the Neogene-Quaternary sedimentary cover. AHe thermochronology results indicate that the intra-fault blocks along the KFF experienced two major episodes of fault-related exhumation at ~18 Ma and ~4 Ma. The ~18 Ma faulting/exhumation episode is chiefly recorded by the structural and depositional architecture of the Neogene deposits along the KFF. In particular, a source-to-sink scenario can be reconstructed for this time frame, where topographic growth caused the synchronous erosion/exhumation of the pre-Neogene units and deposition of the eroded material in the surrounding fault-bounded continental depocenters. Successively, the KFF gradually entered a period of relative tectonic quiescence and, probably, of regional subsidence during which a thick pile of fine-grained onlapping sediments were deposited. This may have caused resetting of the He ages of apatite in the pre-Neogene and the basal Neogene successions. The ~4 Ma faulting episode caused the final exhumation of the fault system, resulting in the current fault zone and topographic architecture. The two fault-related exhumation episodes fit with the regional early Miocene collision-enhanced uplift/exhumation, and the late Miocene–early Pliocene widespread tectonic reorganization of the Iranian plateau. The reconstructed long-term, spatially and temporally punctuated fault system evolution in intraplate Central Iran during Neogene-Quaternary times may reflect states of far-field stress changes at the collisional boundaries. The major outcomes of this study have important implications on (i) understanding the propagation and spatio-temporal evolution of intraplate strike-slip fault systems; and (ii) the Neogene-Quaternary kinematic and tectonic evolution of Central Iran.

INTRODUCTION

The distribution of deformation in intraplate settings is a function of the spatial and temporal changes in plate boundary deformation, modulated by the non-rigid behaviour of the continental lithosphere (Molnar, 1988). In such settings the stresses and forces that produce intraplate deformation are thought to be governed by plate margin dynamics and, in particular, by the degree of tectonic coupling at the collisional interface (Ellis, 1996; Ziegler et al., 1998). As demonstrated by regional and global stress field maps, compressional horizontal stresses can be transferred from the plate margins across large distances, through continental and oceanic lithosphere (e.g. Zoback, 1992; Heidbach et al., 2001; Heidbach et al., 2008). This is best illustrated in regions affected by continental collision, where seismicity extends deep into the continental plate interiors, thus defining broad and diffuse zones of deformation (e.g. Central Iran, Turkey and Tibetan plateau; Hatzfeld and Molnar, 2010).

Seismological and geodetic studies of intraplate deformation demonstrate that strike-slip faulting is the primary process by which such horizontal movements are accommodated and stresses are transferred further away from the collision front (e.g. Molnar and Tapponnier, 1975; Nilforoushan et al., 2003; Vernant et al., 2004; Allen et al., 2011; Walpersdorf et al., 2014). Strike-slip dominated continental deformation zones typically consist of interlinked systems of fault- and shear zone-bounded blocks that partition strain to form complex regions of displacement, internal distortion and rigid block rotations on various scales (e.g. Dewey et al., 1986; Foster and Gleadow, 1992; Marshak et al., 2000; Walker and Khatib, 2006). This is mostly due to the intrinsic structural inheritance of continental crust and lithosphere, acquired through the continuous incorporation of plate margin structures by continental collision and accretion processes that operate for geologically long periods of time. Such structures, constitute major zones of mechanical anisotropy and vertical planar fabric, which, once incorporated into the plate interiors, influence the location, orientation and style of deformation during successive phases of reactivation at various spatial and temporal scale (Sutton and Watson, 1986; Salvini et al., 1997; Holdsworth et al., 2001).

The longevity of intraplate strike-slip fault systems and their intimate linkage to plate boundary dynamics makes them excellent strain markers of the intraplate deformation response to continental collision. A detailed understanding of the spatial and temporal distribution of crustal deformation accommodated along strike-slip faults is therefore central to unravelling regimes and modes through which continental tectonics operate.

The cause of crustal strain, topographic growth and exhumation along strike-slip faults is a complex feedback between near-field (<20 km) boundary conditions and far-field plate tectonic driving mechanisms (Buscher and Spotila, 2007). Moreover, several processes and conditions have

been invoked to explain topographic growth and focused exhumation along strike-slip systems and may play an important role in regional exhumation and topographic patterns: (1) the degree of obliquity of the plate motion vector with respect to the fault trace (e.g. Sanderson and Marchini, 1984; Fossen and Tikoff, 1993; Robin and Cruden, 1994; Cunningham, 2013), (2) structural irregularities such as stepovers (Aydin and Nur, 1985; Hilley and Arrowsmith, 2008; Finzi et al., 2009; Carne and Little, 2012), (3) variations in master fault dip (Dair and Cooke, 2009), (4) enhanced erosion due to the highly fractured rocks (Molnar et al., 2007; Cox et al., 2012), (5) pervasive tectonically induced fracturation and associated volume increase (5 to 10% volume increase; Braun, 1994; Schopfer and Steyrer, 2001; Le Guerroué and Cobbold, 2006; Schrank and Cruden, 2010), and (6) changes in plate motion (Fitzgerald et al., 1993; Fitzgerald et al., 1995). Furthermore, the amount of exhumation along a strike-slip fault is not always simply correlated with the degree of transpression or with the composition of the juxtaposed rocks (Spotila et al., 2007a; b). Finally, it is important to emphasize that local topography of fault systems can perturb the local stress field affecting fault orientation (Fialko et al., 2005), fault-slip direction (Cowgill et al., 2004) and fault strength (Koons et al., 2002).

This study describes the Neogene-Quaternary structural architecture, stratigraphic evolution and exhumation history of the Kuh-e-Faghan Fault (KFF) system, a major shear belt situated at the northern margin of the Lut Block in Central Iran (Fig. 1). The aim is to understand: (i) how intraplate tectonic deformation propagates and evolves in space and time; and (ii) its impact on the long-term, fault-controlled landscape evolution. Field studies are integrated with apatite (U+Th)/He (AHe) thermochronology to link structures to the distribution of topographic relief and spatial variations in exhumation rate. We document E-W oriented dextral strike-slip tectonics associated with two distinct episodes of fault-related exhumation at ~18 Ma and ~4 Ma. A conceptual model of fault initiation and propagation is then proposed that bears implications on activation and kinematic evolution of the intraplate strike-slip fault systems in Central Iran during Neogene-Quaternary times.

GEOLOGICAL BACKGROUND

The Arabia-Eurasia collision zone is one of the largest and most spectacular examples of continental convergent deformation on Earth (Hatzfeld and Molnar, 2010). Convergence may have initiated in the mid-Jurassic (Agard et al., 2005; Agard et al., 2011) and culminated with the Arabia–Eurasia continental collision through a polyphase tectonic history: (i) collision is estimated to have started at the Eocene–Oligocene boundary (e.g. Jolivet and Faccenna, 2000; Hessami et al., 2001; McQuarrie et al., 2003; Ershov et al., 2003; Vincent et al., 2005; Hafkenscheid et al., 2006; Robertson et al., 2006; Vincent et al., 2007; Boulton and Robertson, 2007; Allen and Armstrong, 2008; Morley et al., 2009; Homke et al., 2009; Homke et al., 2010; Mouthereau et al., 2012); (ii) a regional increase

in collision-related uplift, exhumation, and subsidence in adjacent basins, beginning in the early Miocene, as documented by thermochronological (Axen et al., 2001; Guest et al., 2006; Verdel et al., 2007; Okay et al., 2010; Gavillot et al., 2010; Madanipour et al., 2013; Ballato et al., 2013), stratigraphic (e.g. Hessami et al., 2001; Guest et al., 2006; Mouthereau et al., 2007; Ballato et al., 2008; Morley et al., 2009; Khadivi et al., 2009; Ballato et al., 2011) and structural (e.g. Allen et al., 2004; Mouthereau et al., 2007) evidence; and (iii) a widespread tectonic reorganization during late Miocene–early Pliocene, as attested by enhanced exhumation in the Alborz and Talesh mountains (Axen et al., 2001; Rezaeian et al., 2012; Madanipour et al., 2013), fault kinematic changes in the Kopeh Dagh (Shabanian et al., 2009a; Shabanian et al., 2009b; Shabanian et al., 2010) and in the Zagros–Makran transfer zone (Regard et al., 2005), which is thought to have resulted in the current regional kinematic configuration (Allen et al., 2004). The lag-time (15–20 Ma) between phase (i) and phase (ii), has been interpreted by Ballato et al. (2011) as two-phase collisional process. During the initial, “soft” stage of continental collision, plate convergence was absorbed along the subduction zone, while a minor fraction was accommodated by the upper-plate by contractional deformation. During the second stage it is inferred that the decrease in convergence rate by 20 Ma was associated with the “hard” collision of unstretched Arabian lithosphere, which ultimately caused widespread upper-plate deformation (Ballato et al., 2011). The evidence gathered in those studies principally comes from the orogenic belts situated at the edges of the Iranian plateau (Fig. 1; Zagros Alborz, Kopeh Dagh and Talesh). By contrast, little is known about the deformation history of the intraplate domain of Central Iran.

The Central East Iran Microcontinent (CEIM) consists of an amalgamation of continental blocks bordered by topographically prominent mountain ranges, comprising the Kopeh Dagh, Alborz and Talesh orogenic belts to the north, and the Zagros orogenic belt and Makran active subduction related complex to the north-west and south (Fig. 1). In particular, the CEIM includes the Lut, Tabas, and Yazd microblocks (Aghanabati, 2004), which are bounded by linear mountain-belts developed along major strike-slip fault zones that have peculiar stratigraphy, deformation style and pattern of recent seismicity (Berberian and King, 1981; Berberian, 2014).

The GPS displacement vectors indicate a NNE motion of the Arabian plate relative to Eurasia of ~25 mm/yr (Sella et al., 2002; McClusky et al., 2003; Vernant et al., 2004; Reilinger et al., 2006; Walpersdorf et al., 2014). Such convergence is mostly absorbed in the orogenic terrains through contractional deformation (Zagros, Alborz, Kopeh Dagh and Talesh in the north) (Fig. 1). The CEIM is moving northward at 6–13 mm/yr with respect to the stable Afghan crust at the eastern edge of the collision zone (Walpersdorf et al., 2014). Such differential motion is largely accommodated by the active strike-slip faults systems bounding the CEIM, which are organized into N-S dextral (from west

to east: the Deshir, Anar, Nayband–Gowk, and Nehbandan faults) and E–W sinistral (from north to south: Doruneh and Dasht-e Bayaz faults) shears (Fig. 1). Various studies have detailed their kinematics and total cumulative shear along the active strike-slip faults systems of Central Iran, using geologic and geomorphic displaced markers from satellite imagery (Walker and Jackson, 2004; Allen et al., 2004; Allen et al., 2011; Farbod et al., 2011). Taking into account the present-day slip rates ($\sim 2\text{--}10$ mm/yr) along the major fault systems, the onset of strike-slip tectonics is inferred to date back to ~ 5 Ma (Allen et al., 2004). This shear pattern is assumed to be accompanied by diffuse rigid block rotation and strain partitioning during ongoing Arabia-Eurasia convergence (Jackson and McKenzie, 1984; Walker et al., 2004; Walker and Jackson, 2004; Walker and Khatib, 2006; Fattahi et al., 2007; Allen et al., 2011; Farbod et al., 2011). Significant, post-Miocene counter-clockwise rotation ($25\text{--}35^\circ$) has been documented in the Lut and Tabas block, whereas no significant rotation has been detected north of the Doruneh Fault (Mattei et al., 2012).

In a recent study, Nozaem et al. (2013) documented important post-Neogene to Quaternary right-lateral strike-slip tectonics along the Kuh-e–Sarhangi Fault on north western edge of the Lut block (Fig. 1), less than 40 km south of the sub-parallel, active left-lateral Doruneh Fault (Tchalenko et al., 1973; Fattahi et al., 2007; Farbod et al., 2011). This post-Neogene faulting is proposed to have occurred due to the tectonic reactivation of the northeastward extension of the late Neoproterozoic to early Paleozoic Kashmar–Kerman Tectonic Zone (Ramezani and Tucker, 2003; Rossetti et al., 2014; Fig. 1) in response to a kinematically induced stress field scenario (Nozaem et al., 2013). Similarly, Javadi et al. (2013) documented a polyphase kinematic history for the Doruneh Fault, with a major change from right- to left-lateral during the late Miocene-early Pliocene times.

The Kuh-e-Faghan fault zone

Our study focuses on a linear mountainous ridge (~ 80 km long and ~ 15 km wide; maximum elevation of ~ 1700 m), associated with the E–W oriented Kuh-e-Faghan Fault (KFF, Figs. 1–3). This fault system truncates the northern termination of the Kuh-e–Sarhangi fault system (Nozaem et al., 2013) and is located 25 km south of the Doruneh Fault, extending eastward for ~ 80 km (Fig 2). The KFF system and the surrounding areas are seismically active (Fig. 2), with maximum recorded magnitude between 4 and 5.5 and the focal depths < 35 km (Farbod et al., 2011).

The KFF is an E–W oriented brittle deformation zone which cuts pre-Neogene units (Paleozoic-Mesozoic basement, made of carbonate and subordinate shale and arenitic deposits) and the unconformably overlying Neogene and Quaternary continental successions (Behroozi et al., 1987; Eftekhari-Nezhad et al., 1976; Ghomashi et al., 2001; Jalilian et al., 1992) (Fig. 3). Fault kinematics along the KFF are poorly described, with strike-slip (Behroozi et al., 1987; Eftekhari-Nezhad et al.,

1976; Ghomashi et al., 2001; Jalilian et al., 1992) vs. reverse (Hassami et al., 2003; Javadi et al., 2013) kinematics proposed so far.

Paleogeographic and sedimentological studies (Amini, 1997; Berberian and King, 1981) refer the Neogene deposits alongside the KFF to the Upper Red Formation of Central Iran (Berberian, 1974). The Upper Red Formation is the first continental deposit unconformably lying above the marine, late Oligocene–middle Miocene Qom Formation (Berberian, 1974; Deneshian and Ramezani Dana, 2007; Ballato et al., 2008; Hadavi et al., 2010). It consists of conglomerates, sandstones, siltstones, marls and evaporites (Amini, 1997; Ballato et al., 2008; Ballato et al., 2011; Morley et al., 2009). Due to the lack of biostratigraphical markers or radiometrically datable units, the age and duration of the Upper Red Formation are not well constrained. Based on the magnetostratigraphic study of the Eyvanekey section in southern Alborz Mountains, Ballato et al. (2008) proposed a Burdigalian to Tortonian (17.5–7.5 Ma) age.

Quaternary successions unconformably cover the Neogene units and consist of alluvial fans and terraced alluvial plain deposits. The analysis of the Quaternary landscape evolution of the KFF is still ongoing (Calzolari et al., in prep). Nonetheless, similar generations of alluvial fans and alluvial plain deposits have been recognized and dated in neighbouring regions. Walker and Fattahi (2011) reviewed the late Quaternary deposits of eastern Iran. They recognized that several generations of alluvial fans, as well as regional arrangement of river terraces and playa lake deposits could be explained by Late Pleistocene and Holocene environmental changes with aggradation phases occurring between 30 and 13 ka and between 9 and 7 ka, alternating with erosive phases, controlled by regional climatic forcing. Similar generations of alluvial fans have been recognized in the neighbouring regions and infrared stimulated luminescence age of <10 ka (end of the Last Glacial Maximum) was obtained for the deposition of the Shesh–Taraz fan along the Doruneh fault (Fattahi et al., 2007).

Neogene Stratigraphy

The Upper Red Formation of the study area is a ~4 km thick fining-upward succession of continental deposits, which include three main unconformity bounded stratigraphic units, hereafter referred as sedimentary Cycle-1, Cycle-2, and Cycle-3, respectively (Fig. 3). The schematic generalised vertical sections, together with the corresponding stick-logs, for the northern and southern area of the KFF are reported in Figure 5, where the estimated thickness variations have been measured along the relative geological cross-sections (Fig. 3).

Cycle-1 consists of breccias that distally evolve into crudely stratified conglomerates (hereafter referred as Ng-C), which lie above a major angular unconformity (Fig. 5a) onto pre-Neogene rocks.

The majority of the conglomerates and breccias are clast-supported; however, transition into matrix supported conglomerates seldom occurs in the upper part of the cycle. The matrix (up to 25%) is usually made of dark red to pale grey mudstone and siltstone. It is worth noting that clasts making up the bulk of the basal deposits have been directly sourced from the proximal pre-Neogene substratum. The clasts vary from boulder to cobble size. Here we interpret these breccias (Ng-B) as talus deposits sourced by the local linear mountain ridge whereas the Ng-C conglomerates are referred to alluvial fan deposits. In places the basal deposits include up to 1 m of boulder deposits made of breccias and/or conglomerates, indicating reworking of the older part of Cycle-1 deposits. Transition to the upper part of Cycle-1 varies from gradual to sharply on angular unconformity (Fig. 5a). Where basal breccias are absent the upper part of Cycle-1 unconformably overlies the basement units with deposits consisting of clast-supported, crudely- to well-stratified polymictic conglomerates, with relatively rounded and sorted clasts. In places, imbricated clasts, arranged in 0.5 to 3.5 m-thick lenticular and, at times, laterally discontinuous beds point to fluvial channel deposits. Remarkably, according to differences in lithofacies from the upper part of the Cycle-1, a distinction can be made between the western and eastern areas. Along the western area, the conglomerates generally exhibit less rounded and more chaotically organized clasts, with matrix rich horizons showing convolute sedimentary structures. By contrast, along the eastern sector, the conglomerate deposits are typically interbedded with subordinate, fining upwards, 10 to 50 cm thick sandstones packages. Concave upwards erosional surfaces and lenticular beds geometries are common. These differences in the Cycle-1 lithofacies could be referred to the presence of more unstable sedimentary basin linked to uplifting local source areas in the western part with respect to the eastern region of the study area. Cycle-1 shows large lateral thicknesses variations. In particular, the basal talus breccias occur only along the western part of the study area (Fig. 3). The thickness varies strongly across-strike of the KFF from south to north, reaching up to 450 m and 100 m, respectively (Fig. 4). The overlying alluvial fan conglomerates of Ng-C are thickest (~500 m) along the geological cross-section A-B (Fig. 3), but, more commonly, does not exceed 300 m in thickness (Fig. 4). Cycle-1 is interpreted as a high-energy deposit. The poorly sorted, texturally immature and chaotic nature of the basal breccias, coupled with the clast lithology all suggest very proximal deposition likely by block fall and in proximal fans and/or as talus cones, on steep slopes. The laterally continuous nature of the upper part of Cycle-1 deposits also suggests that deposition occurred within an alluvial fan complex in the west area and a broad, well-fed alluvial plain to the east.

Cycle-2 consists of decimetre-thick bedded, well-sorted, mineralogically and texturally immature medium to coarse silty red sandstone (hereafter referred as Ng-SSi). Cycle-2 red sandstones usually show planar to cross lamination, and unconformably cover the Ng-C deposits (Fig. 5b). In

places, the Ng-SSi deposits are characterized by cross-trough bedding alternating with subordinate horizons of coarse gravelly sandstones. Straight crested symmetric, lunate and linguoid ripples are all common feature of the Cycle-2 deposits, together with locally bioturbated horizons and surfaces exhibiting mud cracks and casts. These two types of facies represent the channel/bank and overbank deposits, respectively. We here interpret those deposits as related to a fluvio/palustrine environment possibly proximal to a wide, well-fed alluvial plain capable to be supplied by relatively well-sourced material. The proximity of the source area was unable to produce mineralogically and texturally mature sediments. Cycle-2 is absent in the westernmost part of the KFF and generally increase in thickness eastward, where it reaches its maximum (575 m) along the geological cross-sections G-H and I-J (Figs. 3 and 5). Progressive angular unconformities affecting those continental deposits are very common, especially in the lower part of Cycle-2 (Fig. 5b).

Cycle-3 deposits form two distinct units: Ng-GM and Ng-MS (Fig. 3). Unit Ng-GM shows a strong angular unconformity at the base (Fig. 5d), and consists of a thick marly succession punctuated by gypsum layers. These latter are up to a few 10s cm thick bedded, marls and silty-mudstones, interbedded with centimetre-thick secondary gypsum horizons. Some tens of centimetre-thick fine sandstone beds are also present, with infrequent planar to cross laminated horizons. Desiccation cracks and mud casts are also common (Fig. 5b). The gypsum horizons are typically secondary, showing a clear displacive character of the gypsum crystals, which also occur along bedding surfaces and fractures. In places, this secondary origin for the gypsum layers is responsible for the deformation and disruption of the original layering of the marly deposit. The basal and upper part of the Ng-GM unit are characterized by meter-thick red marls and silts, relatively free of gypsum, interbedded with pale yellow gypsiferous silty marls.

The subsequent Ng-MS unit conformably overlies Ng-GM deposits. It consists of a few 10s cm of pale red to beige, massively bedded marls and silty-mudstone, with millimetre scale layering. These are interbedded with subordinate 0.5 to 2.5 m-thick cross-bedded, at times laterally discontinuous, light brown, medium to coarse sandstones. Bedding surfaces exhibiting small-scale straight crested asymmetric ripples are rare but not uncommon. The Ng-GM unit is inferred to be deposited under different climate conditions, ranging from dry episodes, characterized by evaporation dominated events (secondary gypsum grew within sediments), to wetter climate condition, showed by suspension dominated deposits (massive and layered marls and silty-mudstones) or deposits sedimented in an environment dominated by a relatively high energy tractional and unidirectional turbulent flow (rippled silty-marls and fine sands). Such sedimentary characteristics are representative of playa mud flats and playa lake environments (Reading, 2009). The marls and silty-mudstones of the Ng-MS unit, mainly characterized by millimetre-scale layering and some rare

rippled surfaces, are indicative of deposition in wet period from a low energy shallow lacustrine environment, where deposition occurred primarily by suspension settling and secondarily by laminar and turbulent flow. The subordinate meters-thick cross-bedded sandstone have been deposited by more turbulent and energetic flow and represent deposition during periods of increased sediment supply from riverine input.

Overall, Cycle-3 deposits mostly crops out in the northern areas of the KFF. The basal unit of Cycle-3 (Ng GM) is absent in the western part of the KFF, and reaches its maximum thickness (~450 m; Figs. 3 and 4) in the central sector of the study area and then thins out eastward. In contrast, the Ng MS unit extends throughout the northern KFF area, reaching a maximum thickness of ~1230 m (see cross section IJ in Fig. 3).

Structural architecture

The basement units exhibit a steeply-dipping ENE-WSW oriented planar fabric, similar to the neighbouring Kuh-e-Sarhangi Fault system (Nozaem et al., 2013). The Neogene deposits show bedding attitudes dipping away from, and striking sub-parallel to the axis of the topographic divide, arranged to form a broad eastward plunging antiformal geometry. Moreover, the bedding dip angle of the Neogene deposits generally decreases away from the boundary fault system (Fig. 3).

The structural architecture of the KFF system consists of three, broadly left stepping E-W striking fault strands, hereafter referred as the western (WFS) and central (CFS) fault strands that abut against a major fault NW-SE to E-W striking eastern fault segment (EFS) (Fig 3). The fault strands have along-strike lengths of 30 to 40 km and their associated fault damage zones bound E-W elongated ridges. A number of 501 striated fault surfaces (over a total number of 1040 structural data) occurring in the basement, the Neogene and Quaternary deposits were measured in the field. Fault kinematics was obtained based on classical criteria for brittle shear zones, such as fault offset, growth fibres, and Riedel shears (Petit, 1987; Doblas, 1998). Fault population analysis was performed through the software Daisy 3 (Salvini, 2004; <http://host.uniroma3.it/progetti/fralab>). The cumulative fault data set shows high-to sub-vertical dips, with a maximum frequency distribution at 85° and a mean dip value of 75°. The maximum frequency distribution of fault strikes shows a maximum at N94°, with subordinate N131° and N47°. The frequency distribution of the pitch angle of the measured slickenlines attests for dominant strike-slip kinematics with maxima at 12° and 162° and subordinate dip-slip population (84°). In particular, the analysis shows that ~72% of the slickenline pitches are sub-horizontal (0° to 45° and 135° to 180°) and less than 28% exhibit sub-vertical (45° to 135°) pitches. The mean pitch values is 2° that further attests for the dominant strike-slip tectonics in the study area (see inset in Figure 3).

In the following, a systematic description of the fault system architecture and kinematics along the main fault strands is provided.

Western fault strand

The WFS runs W-E for more than 35 km on the southern side of the KFF (Fig 3), with distinct along-strike fault zone architecture when moving eastward from the western fault tip. The western fault tip is defined by a broad (wavelength of ~5 km), E-W striking, south-verging antiformal fold that affects the basal Ng-C deposits with a monocline geometry. The fold axial trace maps out ~ 20 km and separates gently dipping ($< 20^\circ$) strata to the north from steeply dipping ($> 40^\circ$) strata to the south, with an eastward periclinal geometry (Fig. 3). The fault planes rarely cuts through Ng-C strata and therefore the fault is considered as blind (Fig. 3). Moving eastward along the WFS trace, the southern limb of the monocline becomes increasingly steeper to overturned and is dissected by numerous subvertical fault strands (see the geological cross-section A-B in Figure 3). These fault strands define a ~50 m thick fault damage zone, made of verticalized, E-W striking fractured rock panels along which the abrupt contact between the basal Neogene conglomerates (Ng-C) and the gypsiferous marls (Ng-GM) occur (Fig. 6a). Shearing is dominantly localised along major E-W striking right-lateral slip zones, associated with synthetic, minor NW-SE ones (stereoplot is Fig. 6a).

Further to the east, the WFS bends NE to form a major restraining bend seen to affect the Neogene deposits, with positive flower structures in cross-section and a contractional strike-slip duplex (Woodcock and Fischer, 1986) in map view (see Fig. 3 and geological cross sections E-F and E2-F2 in Fig. 3). The duplex bounding faults are developed within the Neogene deposits; however faults are seen to affect also the Quaternary alluvial deposits (see below). The contractional jog is associated with development of a tight NE-SW trending syncline, mapping out subparallel to the main fault trace and affecting the Ng-C and the unconformable Ng-SSi deposits. The fold profile shows a moderately north dipping southeastern flank with a steep to overturned northwestern flank, with a periclinal doubly plunging geometry (Fig. 3). The northwestern fold limb is dissected by major, NE striking sub-vertical fault strands that cause the tectonic repetitions among the Neogene units. The duplex-bounding faults are subvertical, with major fault slip localization occurring along the northwestern boundary fault zone. This fault zone consists of ~300 m thick damage zone, defined by subvertical panels of cataclastic fault rocks and cohesive fault breccias (Fig. 6b). Dextral kinematics is attested by drag folding of the Neogene strata along the principal displacement zone, which documents for the dominant right-lateral shear component of the contractional strike-slip duplex (Figs. 6c-d). Measured fault surfaces strike NE-SW; offset bedding truncations, Riedel shears and

calcite slickenfibers, systematically document either right-lateral oblique strike-slip or reverse kinematics (Fig. 6e).

Central fault strand

The CFS runs W-E for about 30 km on the northern side of the KFF, defining a sharp break in slope between the topographically elevated basement rock units and the Neogene-Quaternary sedimentary covers (Fig. 3). In the central part of the CFS, basement-cover relations are well preserved, with fault zone localization occurring within the basement units and only marginally within the Neogene deposits (Ng-C and Ng-GM) units (see the geological cross sections A-B and C-D in Fig. 3). In the field, they generally appear as broad (up to 100 m wide) deformation zones, associated with verticalized rock panels affected by diffuse brittle deformation (Fig. 7a). The shear deformation is principally accommodated within the weaker basement shale and silt beds, while the stronger sandstone and siltstones remain partially coherent to define fault lithons (Figs. 7a-b). The slip zones are typically delocalized, defined by meter to tens of meter thick bands of cataclastic material. As in the WFS, well-developed fault surfaces with striations and kinematic indicators are rare but not uncommon, and localized slip zones and fault gouges are extremely rare. Brittle deformation in the Ng-C deposits is characterized by a dominant set of sub-vertical E-W striking cataclastic zones, generally with less of 1 m of thickness. Striated fault surfaces provide sub-horizontal pitch values and the fault kinematics is systematically right-lateral. Subsidiary, steeply-dipping NW-SE dextral and NNE-SSW left-lateral faults are also reported (see the stereoplot in Fig. 7c).

Continuing to the east, the CFS bends southward and branches out into four main NW-SE oriented subvertical fault segments, that in map view are arranged to form a 10 km wide, trailing extensional imbricate fan (Woodcock and Fischer, 1986), also referred as to “horsetail-type” transtensive termination (Granier, 1985) (Fig. 3). The dominant strike-slip motion along the CFS passes into a lozenge-shaped extensional/transtensional kinematics at its tip, consistent with dextral offset, that are filled up by the Ng-GM deposits (Fig. 3). Striated fault surfaces either show dip-slip normal or oblique-to-strike-slip dextral kinematics, attesting for the dominant transtensional regime of faulting. Within the Ng-GM deposits, faulting is accommodated by diffuse zones of deformation, hundreds of meters wide, characterized by evenly spaced (meters apart) sets of NW-SE striking faults that accommodate both oblique-slip and normal dip-slip displacements. It is worth nothing that many of these mesoscale faults show vertically decreasing offsets and some of them vertically die out in the sediment, clearly indicating syn-depositional faulting (Fig. 7b).

Eastern fault strand

The EFS is a ~ 40 km long, sub-vertical fault zone, made of the coalescence of several synthetic faults to form a major curvilinear slip zone and prominent range front, striking from NW-SE to E-W at its eastward termination (Fig. 3). The fault zone shows a decametre-to-hectometre thick damage zone that comprises numerous mesoscale fault segments cutting through the pre-Neogene basement units that are tectonically juxtaposed with the Ng-GM successions. In particular, the NW segment abruptly cuts an E-W striking Neogene basin boundary fault strand. It continues eastward bending to E-W direction and cutting through a relatively plain area, showing a prominent linear fault scarp in the Neogene deposits that can be traced continuously eastward for more than 20 km in the Quaternary alluvial plain (Fig. 8a). The fault zone bending to the E-W direction corresponds to a widening of the fault damage zone, reaching thickness in excess of 300 m and prominent up-to-tens of meter thick fault cores. The fault cores consists of ultracataclastic bands and fault gouges, separated by brecciated fault rocks and sheared lithons (Fig. 8b). Major fault surfaces are typically sub-vertical, NW-SE and E-W striking and exhibit sub-horizontals slickenlines (pitch: 5-15°; see stereoplot in Fig. 8b). Typically, most of the striated fault surfaces are decorated by hematite coatings. Fault kinematics as deduced by synthetic Riedel shear planes, together with calcite slickenfibers, grain grooves and lunate fractures systematically point to dominant right-lateral slip (Figs. 8c-d). Significantly, decameter-scale, S-C fabrics are observed along coherent tracts of the principal displacement zone of the EFS and continue over significant distances (> 300 m), both along the basement-Neogene contacts and within the Neogene deposits (Figs. 9a-b). Within these deformation zones, S surfaces are defined by dissolution seams and strike NW-SE, the C-surfaces strike roughly E-W to ENE-SSW. Lineations are provided by slickenlines on the C-surfaces that systematically are subhorizontal. The S-C fabrics are associated with NW-SE striking, steeply dipping extensional fractures and calcite- and gypsum-bearing vein sets. Overall, the geometric relationships among the different structural elements are compatible with right-lateral shearing (Fig. 9c). Finally, Meter-thick coesive and foliated cataclasites are seldom observed to form the fault rocks along the slip zones developed within the Neogene deposits.

Quaternary faulting

The Quaternary successions along the KFF consist of a wide array of alluvial fan and fluvial deposits, made of conglomerates, gravels and sands exhibiting various degree of consolidation. These deposits lie upon a regional erosional surface (pediment) cut through the strongly tilted Neogene units (Fig. 6b). Evidence of Quaternary faulting (and fracturing) have been documented along the WFS and the EFS (see Fig. 3 for sites location), where faulting is dominated by right-lateral strike-slip fault zones.

Along the contractional bending that terminates the WFS to the east, right-lateral and oblique-slip faults cut through the Quaternary terraced deposits, juxtaposing and squeezing together lenses of Quaternary and Neogene sediments (Figs. 10a-b). Such faults show transpressive right-lateral kinematics, compatible with what found to affect the Neogene deposits (Fig. 10c).

Along the EFS, Quaternary faulting is documented both along the principal displacement zone and along subsidiary, synthetic fault strands (Fig. 3). Along the prominent E-W striking fault scarp that defines the geomorphic expression of the EFS (Fig. 8a), Quaternary deposits are extensively affected by a set of sub-vertical fracture arrays. Further to the east, along the NW-SE fault systems that make up the transtensional leading embriate fan of a major fault right-lateral segment to the north of the EFS, extensional and right-lateral oblique-slip faults involve the Ng-GM deposits and the Quaternary alluvial covers (Fig. 3). Evidence of Quaternary faulting is documented along an E-W striking, minor fault strand. In this area, E-W oriented sub-vertical faults cut through the gypsiferous Neogene units and into the Quaternary alluvial deposits, displaying calcite slickenlines and small-scale drag fold compatible with right-lateral kinematics (Fig. 10d and e).

AHe thermochronology

The low closure temperature for the apatite (U+Th)/He system (65–70°C for typical rates of cooling and grain sizes; Farley, 2000) makes it particularly useful for assessing age of the late-stage deformation/exhumation history affecting the uppermost portions of the crust, where brittle deformation and faulting predominates.

Samples from the basement units ($n = 6$) and basal Neogene deposits (Ng-C and Ng-SSi units; $n = 11$) were collected for AHe thermochronology along an approximate constant elevation transect parallel to the KFF trace (mean altitude of 1070 m; Fig. 11). The samples are from the arenitic portions of the Paleozoic and Mesozoic deposits and the Neogene basal sandy intercalations of Cycle-1 and -2. The quantity and quality of apatite grains is highly variable. In most of the samples, apatite grains appear as rounded with frosted surfaces, making the identification of inclusion-free grains difficult. Consequently, eight samples were excluded from the analysis due to their poor apatite quality (Fig. 11).

The analytical protocol adopted in this study follows Foeken et al. (2006; 2007). Refer to Appendix for methods and analytical procedure. Single grain ages corrected for α -ejection (Farley et al., 1996) generally show a good within-sample reproducibility (Table 1). Mean ages and standard deviation are plotted in Figure 11. Three samples show single grain ages that does not overlap within two standard deviations with the other ages of the same sample. Because these three grains have low U and Th content, we consider them as outliers and they were not included in the mean age

calculation. All samples have mean and single grain AHe ages that are younger than the stratigraphic age, indicating that all were reset. The ages indicate a Miocene to Pliocene cooling/exhumation history. Mean ages range from 2.9 ± 1.5 Ma to 20 ± 2.6 Ma, and define two mean age populations, clustering at ~ 18 and ~ 4 Ma (Table 1).

The spatial distribution of the AHe ages shows two broad areas where cooling ages are clustered into old and young age groups, respectively: (i) the western area, comprising the topographically prominent fault bounded basement high to the west of the EFS; and (ii) the eastern area, located alongside of the EFS (Fig. 11). The AHe age distribution in the western area shows that the basement bedrocks experienced a similar exhumation/cooling history during and since the early Miocene, ~ 18 Ma, with the exception of sample IR-10, which exhibits a much younger cooling age of ~ 3 Ma. The AHe ages from the eastern area are systematically younger, clustering at ~ 4 Ma. This pattern is not uniform, as sample IR-17, from the pre-Neogene basement, shows an older age of ~ 8 Ma. The distribution of AHe ages indicates a pattern that may relate to differential exhumation/cooling history along-strike of the KFF.

DISCUSSION

The multidisciplinary dataset presented in this study offers significant spatial and temporal constraints on the geological history and evolution of the KFF system at the northern edge of the Lut Block, Central Iran (Fig. 1). In addition, by linking structures, stratigraphy and thermochronology to the long-term response to crustal deformation in intraplate settings the results may elucidate the way strike-slip faulting nucleates and propagates.

Structural synthesis

The geological investigation shows that the KFF consists of a broad, E-W striking deformation zone made of a complex array of fault strands. Three main, left stepping, right-lateral fault segments are recognised to cut through the Paleozoic and Mesozoic basement units and the Neogene-Quaternary sedimentary covers (Fig. 3). These fault zones are tens of kilometres long and cut at high angle the NE-SW striking planar fabrics of the basement bedrock (Fig. 3), ruling out a major contribution of tectonic reactivation during the KFF development. As such, the cumulative fault population analysis may provide insights into the stress regimes and strain conditions during the KFF development (e.g, Storti et al., 2006). The right-lateral fault population (261 of 501 data) provides a mean strike cluster at $N91^\circ$. This is interpreted as the strike of the principal displacement zone (PDZ) of the KFF. The normal faults and extensional veins strike data (111 data) cluster at $N135^\circ$. These angular relationships suggest fault zone development in response to a (local) regional direction of the

maximum principal stress ($R\sigma_1$) trending NW-SE, at an angle of $\sim 44^\circ$ from the PDZ. This implies simple shear dominated strike-slip deformation (simple shear wrenching in Fossen et al., 1994) during the KFF development, in agreement with the mean pitch angle (2°) of the fault slickenlines as obtained from the cumulative fault data set (see Fig. 3). Within this scenario, the along-strike spatial variation of the fault population orientation, kinematics and strain regimes (restraining and releasing areas) reflect the different ways by which the overall E-W right lateral shear is accommodated, distributed and partitioned along the principal and minor fault strands of the KFF system (Fig. 3).

Fault zone architecture and structural characteristics markedly vary along-strike. There is an eastward increase in shear localization within the main fault zones, from distributed deformation characterized by cataclastic fault rocks in the west (the WFS and CFS) to localized and mature fault zones characterized by ultracataclastic fault gouges (distributed cataclastic flow) and S-C fabrics in the east (the EFS). It is known that porous rocks such those that make up the basal deposits of the faulted Neogene strata along the KFF, display a transition from dilatant, brittle behaviour to shear-enhanced compaction and macroscopically ductile behaviour with increasing effective pressure at constant temperature (Rutter and Hadizadeh, 1991; Scholz, 2002; Paterson et al., 2005; Wong and Baud, 2012). This is documented along the KFF by eastward variation of deformation mechanisms from pure brittle fracturing to coupled cataclastic flow and dissolution creep during S-C fabric development. This is also in agreement with occurrence of hematite-coated fault surfaces systematically observed on the EFS (Fig. 8c and d), which attests to focused fluid flow during fault zone localisation, a process that cannot occur at shallow (< 3 km) crustal depths (Caine et al., 1996; Rowland and Sibson, 2004; Sheldon et al., 2006). Such lines of evidence suggest shear deformation occurred under different confining pressure conditions moving eastward. Differential lithostatic loading between the western and the eastern areas is supported by the stratigraphic and thermochronological data (see below), which shows an overall eastward increase in the Neogene sediment thickness (up to ~ 3.8 km) and fault-related exhumation post-dating Neogene sedimentation, respectively.

Faulting is intimately associated with regional bulging (antiformal folding) of the Neogene deposits (Fig. 3), providing further constraints on the KFF growth and evolution. In particular, the along-strike space-time overprinting relationships between fault-parallel folding along the KFF can be reconstructed (at various scales) from field observations. It is inferred that early folding was caused by the dilatant behaviour during initial fracturing due to fault nucleation from the basement. Folding was then amplified by fault zone propagation (fault-related folding; both vertically and along-strike) in the Neogene deposits. With increasing shearing, deformation zones mature into discrete through-going fault zones, which localize deformation, preventing further fold amplification. This overall

antiformal geometry is better preserved in the west (cross sections A-B and C-F in Fig. 3), while it dies out eastward and is abruptly interrupted by the EFS (Fig. 3).

Major strike-slip faults such as the KFF typically accommodate large displacement via an array of evolving strands. Estimation of the fault offset along the KFF is hampered by the lack of homologous markers cut by the major fault strands. Nevertheless, first-order estimates from the single fault strands can be obtained from empirically-derived scaling law for faults, relating fault displacement (D) to fault length (L), fault damage zone (DT) and fault core (CT) thickness (e.g. Fossen, 2010) respectively. Based on the field observation, the D-L diagram provides displacement values ranging from 10^2 to 10^4 m. These estimates are in the range of those obtained from the DT-D and CT-D diagrams. A further indication of the magnitude of the apparent horizontal offset along the fault strands that make up the KFF can be derived from the basement outcrop pattern across the NW-SE striking trace of the EFS (Fig. 3). The basement block to the north of the EFS is in fact inferred to have been displaced south-eastward from its original position. In this scenario, a horizontal displacement of ~ 10 km can be proposed, which fits well with the above estimates. Based on these estimates, it is therefore plausible to assume that the cumulative displacement accumulated along the right-lateral KFF deformation zone should have been in the order of tens of kilometres.

Neogene stratigraphic architecture: linking faulting to sedimentation

The Neogene deposits associated with the KFF consist of a fining-upward succession, up to 3.8 km-thick, which is arranged in three main sedimentary cycles. The field observations document a progressive up-section decline in syn-depositional tilting, recorded by the gradual disappearance of progressive angular unconformities, coupled with a gradual waning of synsedimentary faulting from Cycle-1 to the base of Cycle-3 (Figs 5a-c and 7d). The presence of syn-sedimentary faulting, together with the overall syn-depositional architecture of the Neogene deposits indicate that their deposition and tilting were controlled by localized uplift along KFF system suggesting fault-related topographic growth during the fault system propagation. In such a scenario, the texturally immature and proximally sourced breccias and conglomerates of Cycle-1, are the stratigraphic marker of the growing linear topography associated with the KFF development. Furthermore, the Neogene deposits show variation in facies distribution and thicknesses along-strike of the KFF. In particular: (i) the lower portion of Cycle-1, consisting of talus breccias (unit Ng-B), is only present in the western areas (WFS and CFS) with greatest preserved thicknesses documented along the central WFS (Fig. 3). This indicates that the fault-related topographic high, from which the breccia deposits were sourced, was initially confined to the western region. The greatest thickness of talus breccia deposits along the WFS (Figs. 3 and 5) indicates that the southern side of the KFF experienced greater sediment supply

influx and/or greater accommodation space; and (ii) the upper unit of Cycle-3 deposits are the thickest (constituting more than half of the total Neogene stratigraphic succession) and the most laterally continuous. Their thickness, lateral stratigraphic continuity, and lack of synsedimentary deformation, indicate that it was deposited during a period of tectonic quiescence and most probably of regional subsidence.

Lastly, the KFF Neogene stratigraphic succession and the along-strike changes in sedimentary facies, depositional architectures and thicknesses reflect a history of sedimentary basins strongly influenced by tectonics and modulated by regional and local environmental changes. The eastward increase in the thickness of the Neogene deposits may reflect a migrating depocenter, controlled by the eastward propagation and evolution of the KFF during the Neogene.

A two stage exhumation history

The AHe thermochronological data set defines two mean age populations, clustering at ~18 and ~4 Ma. The early Miocene exhumation episode is recorded by the basement samples IR5, IR8 and IR15, that are located along the southwestern and central zones of the KFF. The early Pliocene exhumation episode is chiefly recorded from the Neogene deposits along the EFS (Fig. 11).

This early Miocene episode is interpreted as the beginning of faulting, topographic growth and exhumation along the KFF. A source-to-sink scenario is inferred for this time lapse, when the fault-related topographic growth caused the synchronous erosion/exhumation of the topographically prominent basement units and deposition of the eroded material in the surrounding lowland depocenter. This is supported by (i) the proximal nature of the basal Ng-C conglomerates; (ii) the presence of progressive angular unconformities in the basal portion of the Neogene sedimentary successions (Cycle-1 and -2); and (iii) the bedding steepness that gradually decreases away from the boundary fault of the fault systems and up section.

The fact that Neogene sediments from the EFS show AHe ages younger than their source rocks indicate that they have been thermally reset. Indeed, the reconstructed Neogene stratigraphy indicates that the succession is up to 3.8 km thick (Fig. 4), well above the thickness needed to reset the AHe system at the base of the succession in a normal continental geothermal setting (25-30 °C/km; Chapman, 1986). It is therefore inferred that with the exception of the western and central area of the KFF zone (i.e., samples IR-5, IR-8 and IR-15 in Fig. 11), the thickness of these Neogene deposits was sufficient to reset the (U+Th)/He system of the detrital apatite in both the pre-Neogene and the basal Neogene successions. In these areas, a renewed fault activity and fault-related exhumation occurred at ~4Ma. This exhumation episode is further documented by the northward and southward post-depositional tilting of the Neogene units, particularly the Ng-GM deposits. This event

was characterized by widespread erosion that preferentially targeted the lithologically weaker Cycle-3 marls. In contrast to the first event, there is no stratigraphic record documenting the topographic growth and general unroofing along the KFF. In fact, a major erosional unconformity marks the contact between Neogene and Quaternary deposits. Sample IR-18 exhibits an average age that lies between the two mean age clusters. This may reflect partial resetting. Finally, the occurrence of the second exhumation episode along the KFF allows constrains the topmost Neogene successions must be more than 4 Ma. This is compatible with a stratigraphic position equivalent to that of the Upper Red Formation.

It emerges that the KFF experienced a punctuated history of fault-related exhumation events. This first fault-related exhumation event started at ~18 Ma and progressively waned to a period of relative tectonic quiescence and generalised subsidence during deposition of Cycle-3, some time before ~4 Ma. This time lapse probably corresponded to the time when syn-sedimentary faulting and tilting ended (mainly during the deposition of the Cycle-3 Ng-GM deposits). In the absence of any age constraint on the Neogene stratigraphy, the exhumation rate associated to the first exhumation episode can not be estimated.

The second exhumation event started in early Pliocene (~4Ma) and is likely responsible for the present structural architecture of the KFF. For each sample that records the early Pliocene event, AHe ages were converted to exhumation rates using a typical continental geothermal gradient of 25°C/km (e.g. Chapman, 1986), an long-term averaged annual surface temperature of 16°C <http://en.climate-data.org/location/5127/> and a closure temperature of 70°C. Accordingly, the depth of the base of the apatite partial retention zone prior to the onset of denudation must be ~2.1 km. Assuming that the closure isotherms are roughly parallel to local mean elevation and taken into consideration that samples were collected from approximately the same mean elevation at each location, exhumation rates were not adjusted for local sample elevation. The calculated exhumation rates vary between 0.4 and 0.7 km/Ma, with a mean exhumation rate of 0.5 km/Ma. Not having a constrain on the regional mean surface elevation during the early Pliocene, a reliable rock uplift rate cannot be estimated.

Exhumation rates along regional strike-slip fault systems have been shown to vary greatly both between and within fault systems. For example, along the San Andreas Fault system, exhumation rates span from 0.03 to 10 km/Ma, with mean values of 0.4 km/Ma (Spotila et al., 1998; Spotila et al., 2001; Spotila et al., 2007b; Buscher and Spotila, 2007; Spotila et al., 2007a; Niemi et al., 2013). Furthermore, Spotila et al. (2007b) show that the exhumation rate variations along the San Andreas Fault do not simply correlate with the degree of transpression (plate obliquity), precipitation or rock erodibility. Mean exhumation rates seem to be somewhat higher in the Alaskan Range fault system,

in the order of ~ 1 km/Ma (Fitzgerald et al., 1995), possibly affected by highly erosive glacial processes (Headley et al., 2013). Therefore, the calculated long-term exhumation rates for the KFF system in intraplate Central Iran are comparable with those found along major plate boundaries associated strikes-slip systems.

The exhumation rates are comparable with those obtained for the Alborz (0.2-0.7 km/Ma; Axen et al. (2001) Ballato et al. (2013), and the Zagros (~ 0.2 -0.6 km/Ma; Mouthereau (2011), for the same time frame. The fact that regional exhumation along major orogenic belts and focused exhumation located along intraplate strike-slip fault systems exhibit comparable rates suggests similar denudation rates despite the tectonic setting or the scale of the exhuming area. This seems to suggest that the rate of denudation/exhumation is likely mainly climate-controlled, but its location and scale is strongly controlled by tectonic processes. This inference is also supported by the ages of the Quaternary faulted alluvial deposits already dated in the surroundings, which are coherent with the climate-driven late Quaternary aggradation phases generally recorded in the region (Regard et al., 2006; Fattahi et al., 2007; Walker and Fattahi, 2011; Foroutan et al., 2014).

The long-term evolution: fault nucleation, propagation, and growth

Deformation in intraplate settings is generally not confined to narrow linear belts, but it is often distributed along broad zones of diffuse deformation (e.g. Molnar and Tapponnier, 1975; McKenzie and Jackson, 1983; Storti et al., 2003). Analogue modeling studies have shown that strike-slip fault systems nucleate and evolve from distributed to localized, through-going fault strands (for review Dooley and Schreurs, 2012). On the assumption that the topographic evolution and stratigraphic response was structurally controlled during the documented two-stage history of fault zone development, a five-step model is proposed for the long-term evolution of the KFF (Fig. 12).

(i) ***Fault system nucleation.*** The fault nucleation stage is attested by the initial topographic growth and basement exhumation, in a scenario of diffuse deformation at ~ 18 Ma (Fig. 12a). Topographic growth is inferred to have been achieved by a combination of: (a) local transpressive regimes (e.g. Sanderson and Marchini, 1984; Fossen and Tikoff, 1993; Robin and Cruden, 1994; Cunningham, 2013), (b) structural irregularities such as stepovers (Aydin and Nur, 1985; Hilley and Arrowsmith, 2008; Finzi et al., 2009; Carne and Little, 2012), (c) local variations in master fault dip (Dair and Cooke, 2009), (d) pervasive, tectonically-induced fracturing and associated volume increase (5 to 10%; Braun, 1994; Schopfer and Steyrer, 2001; Le Guerroué and Cobbold, 2006; Schrank and Cruden, 2010). The net result of these processes operating together and over different spatial and temporal scales is the growth of a topographically prominent bulge along the evolving fault zone (Fig. 12a). In the absence of well-developed drainage networks the eroded material is

mainly mobilized by gravity-driven processes and deposited into the adjacent basins as thick packages of proximally-sourced breccias at the base of the Neogene Cycle-1 (Ng-B and -C).

(ii) ***Fault localization and propagation.*** Faulting is likely initially accommodated by a network of distributed en-echelon Riedel shears that successively merged by sideways propagation or linkage to form major, through-going master faults (Fig. 12b). In this context, due to the strain hardening and velocity-strengthening properties of poorly consolidated syn-tectonic sediments (e.g. Scholz, 2002), fault propagation is inhibited within the newly deposited material. This has the effect of favouring faulting along areas free of unconsolidated sediments, causing faulting activity to migrate inwards, gradually localizing along sub-vertical fault zones at the basement-sediment interface (Le Guerroué and Cobbold, 2006; Fig. 12b). The positive feedback between topographic growth, erosion, sedimentation and inward fault migration is the primary driver for the progressive narrowing of the fault system and of the associated topographic growth. As a result, syn-sedimentary faulting accompanies the topographic growth and the progressive tilting of the deposits. The progressively more developed drainage network produced increasingly mature sediments, transitioning into the fluvial Ng-C conglomerates. With continuous deformation, the drainage network develops further, creating larger catchments capable of producing yet more texturally mature sediments. Such conditions produce proximal alluvial fans deposits consisting of gravelly sandstones, intermediate alluvial plains consisting of clinostratified and cross-bedded channel fill and bar sandstones deposits, which distally evolve into fluvio-palustrine facies (Neogene Cycle-2 deposits). Distribution of the Cycle-2 deposits indicates increasing thicknesses towards the NE, suggesting preferred sediment influx/rooting towards this region (Fig. 12b).

(iii) ***Fault termination and tectonic quiescence.*** Development of trailing extensional imbricate fan terminations at the eastern fault tips (Woodcock and Fischer, 1986; Figs. 3 and 12c) attests to strike-slip shear dissipation at fault zone terminations. The extensional/transtensional faulting and the associated tectonically-controlled subsiding depocenters (cf. Wu et al., 2009) occurs at the same time as deposition of the basal part of the Neogene Cycle-3 (Ng-GM deposits). Their distribution and the syn-tectonic character of its deposition allow us to define the distribution and geometries of the subsiding areas and basin boundary faults (Fig. 12c). Tectonic activity progressively wanes during the deposition of unit Ng-GM, as attested by the gradual up-section disappearance of syn-sedimentary faulting and tilting. Successively, the Ng-MS deposits cover the entire KFF area. Their thickness, lateral stratigraphic continuity and lack of syn-sedimentary deformation indicate that they are deposited during a period of tectonic quiescence and, most probably, of regional subsidence (Fig. 12d).

(iv) ***Renewed Faulting***. Deformation and faulting activity resumes at ~4Ma, reactivating most of the pre-existing faults strands and creating new ones that propagates further eastward (Fig. 12e). This renewed fault activity is considered to be responsible for the current fault zone architecture, developed in a regime of simple shear dominated strike-slip faulting. It affected an along-strike heterogeneous upper crustal section, as caused by the anisotropic distribution of the Neogene deposits. To the east, where higher confining pressure is provided by the thick Neogene sediments (up to 3.8 km), combined cataclastic flow and dissolution creep allow mature fault zones to develop. To the west, the reduced confining pressure means the fault zone was more delocalized and characterized by dilatant brittle behaviour of the Neogene deposits. This led to development of broad zones of pervasively fractured rock, associated with volume increase accommodated by vertical bulging (WFS and CFS). The renewed topography growth along the KFF is accompanied by widespread erosion and unroofing (Fig. 12e). In the western area, topographic growth is also achieved by the left-stepping geometry between the right-lateral WFS and the CFS. The fact that no syn-tectonic deposits are preserved in the proximity (tens of kilometres) of the KFF during this second event suggests that it was accompanied by an important erosional phase -testified by a regional pediment cutting the tilted Neogene deposits- during which the eroded material could get efficiently transported away from the KFF area. According to the available literature, in the Late Quaternary and Holocene new, likely climate-driven aggradation phases took place as testified by the different generations of alluvial fans and fluvial terraces widely recognized in the region (Regard et al., 2006; Fattahi et al., 2007; Walker and Fattahi, 2011; Foroutan et al., 2014). Evidence of right-lateral transpressional shear affecting these Quaternary alluvial deposits along the KFF system (Fig. 10) suggests that the transpressional regime renewed and is probably still active along the KFF. Finally, the eastward propagation of the KFF system, with a progressive localization of strain, was likely responsible for the present topography of the KFF deformation zone.

Regional implications

Our study documents Neogene to Quaternary right-lateral kinematics along the KFF, at the northern edge of the Lut block, in the intraplate domain of Central Iran (Fig. 1). This new evidence, together with analogous results from the Kuh-e-Sarhangi Fault (Nozaem et al., 2013) to the southwest, and the pre-Pliocene slip history as reconstructed from the Doruneh Fault (Farbod et al., 2011; Javadi et al., 2013) to the north, outline the regional significance of the right-lateral strike-slip intraplate deformation zones along the northern edge of the Lut Block in the framework of the Neogene-Quaternary kinematic evolution of Central Iran (Fig. 1). The AHe thermochronology results indicate that the intra-fault blocks along the KFF experienced two major episodes of fault-related exhumation,

during the early Miocene (at ~18 Ma) and during the early Pliocene (at ~4 Ma), respectively. These exhumation episodes fit with the major stages of formation of the Iranian plateau.

The early Miocene tectonic/exhumation event recognized along the KFF is in good agreement with the regional thermochronological results, as obtained from the Zagros, Alborz and Talesh areas (Ballato et al., 2013; Madanipour et al., 2013). It also correlates well with the late-stage, early Miocene exhumation of the Kashmar-Kerman Tectonic Zone (Fig. 1), which is interpreted as the transition from extension to compression in the region (Verdel et al., 2007). Within this context, the reconstructed source-to-sink scenario along the KFF places onset of deposition of Neogene continental successions of the Upper Red Formation in Central Iran at the early Miocene. This age is compatible with the Burdigalian-Messinian age of the Upper Red Formation (Ballato et al., 2008), but contrasts with the recently proposed Burdigalian-Serravallian age for the “e” member of the Qom Formation (Hadavi et al., 2010), which instead implies a possible post-Serravallian onset of the continental deposition of the Upper Red Formation. This suggests a diachronic distribution of the Neogene continental deposits and the control operated by regional tectonics on the Neogene sedimentary facies distribution and stratigraphy in Central Iran.

The early Pliocene event is coeval with a regional tectonic reorganization, as inferred from the recognized acceleration in uplift rates in the Alborz and Talesh mountains and by fault kinematic changes in the Kopeh Dagh and along the Zagros-Makran Transfer zone (Axen et al., 2001; Regard et al., 2005; Shabanian et al., 2009a; Hollingsworth et al., 2010; Rezaeian et al., 2012; Madanipour et al., 2013). It is worth noting that this age is also in agreement with previous inference on the onset of the intraplate strike-slip tectonics in the region (Allen et al., 2004). Finally, the Miocene-Pliocene boundary also corresponds to the time lapse when the Zagros collisional zone became overthickened to sustain further shortening (Allen et al., 2004; Austermann and Iaffaldano, 2013). Despite the ultimate cause of the Pliocene regional tectonic re-organization across the Iranian Plateau is still uncertain, our AHe age data constitute the first direct documentation of such Pliocene event in Central Iran. Assuming that the faulting started at ~4 Ma and continued at a constant rate, estimates of the slip rates based on the estimated horizontal apparent displacement along the KFF (EFS) are in the range of ~2-2.5 mm/yr. The calculated slip rate is comparable with those obtained for the E-W oriented strike-slip Doruneh Fault ranging from 1.3-2.5 mm/yr (Fattahi et al., 2007; Farbod et al., 2011; Walpersdorf et al., 2014) and Dasht-e-Bayaz fault ranging from 1-2.5 mm/yr (Berberian and Yeats, 1999; Walker et al., 2004).

The major implication of the results of this study is that a reappraisal of the Neogene-Quaternary space-time kinematic evolution and fault distribution within Central Iran is needed. In particular, evidence of Neogene-Quaternary NW-SE to E-W right-lateral strike-slip kinematics acting

at rates compatible with the regional average values along the northern edge of the Lut Block to the south of the Doruneh Fault is not compatible with the current kinematic configuration proposed for Central Iran. This is commonly framed into a scenario of dynamic rupture achieved through N-S dextral and E-W sinistral slip zones, associated with rigid block rotations and strain partitioning (Allen et al., 2004; Walker and Jackson, 2004; Allen et al., 2011; Mattei et al., 2012; Walpersdorf et al., 2014). In particular, modeling the GPS with a block rotation model suggests that the rotations have been going on at a similar rate ($1 \pm 0.4^\circ/\text{Ma}$) over the last 12 Ma (Walpersdorf et al., 2014). This steady-state scenario contrasts with the Neogene-Quaternary kinematic configuration recently derived for the northern boundary of the Lut Block, where punctuated events of fault zone (re)activation and kinematic shift have documented in space and time (Javadi et al., 2013; Noazem et al., 2013; this study).

It is thus inferred that intraplate response to regional convergence is a function of the tectonic coupling/uncoupling at the collisional boundaries, which ultimately modulates the localized *vs.* distributed style of deformation. We tentatively propose the Neogene-Quaternary deformation in the Iranian plateau has been primarily controlled by the spatial and temporal variations in the degree of coupling along the Arabia-Eurasia collision interface, in the frame of a constant N-S directed convergence velocity scenario (McQuarrie and van Hinsbergen, 2013). Indeed, the along-strike variation from continent-continent convergence in the Zagros to ocean-continent convergence in the Makran and, hence, for a fully to a partially coupled collisional boundary (Fig. 1), might have imposed a northeastward escape component to the intraplate domain with polycyclic reactivation of the Kashmar-Kerman Tectonic Zone along the Kuh-e-Saranghi, Kuh-e-Faghan and Doruneh fault strands (Verdel et al., 2007; Nozaem et al., 2013; Javadi et al., 2013).

Implications for topographic growth along intraplate strike-slip faults

Integration of the multidisciplinary data set presented in this study ultimately results in a long-term, spatially and temporally punctuated fault system evolution. Based on the regional scenario and synchronicity with the regional deformation events leading to the growth of the Iranian Plateau, the reason for the nonlinear temporal evolution of intraplate faulting is partially imputable to changes in the regional (far field) stress regime through time. Tectonic stresses and forces are generated at the plate margins and are transferred to the intraplate domains, where they interact with pre-existing structures and local (near-field) kinematically-induced stress regimes. Several other processes operate in the near-field at the scale of the developing fault system, such as the spatial changes in the degree of fault development and maturity and structural complexity during fault development. The spatial-temporal changes in those interactions and feedbacks regulate the way plate boundary stresses are

transferred to the intraplate domains and may ultimately be responsible for the punctuated development of intraplate deformation and associated topographic growth. In particular, the study recognizes that due to the strain hardening and velocity-strengthening properties of poorly consolidated syn-tectonic sediments, fault propagation is inhibited within the newly deposited material. This has the effect of favoring faulting along areas free of unconsolidated sediments, causing faulting activity to migrate inwards, gradually localizing along sub-vertical fault zones at the “basement-sediment” interface (basin-bounding faults). The positive feedback between topographic growth, erosion, sedimentation and inward fault migration is the primary driver for the progressive fault zone localization, narrowing of the fault system and of its topographic growth.

CONCLUSIONS

The main results of this study can be summarized as follows:

The KFF consists of a major E-W striking, 80 km long right-lateral strike-slip brittle deformation zone, made up of three broadly left stepping, E-W striking, right-lateral, strike-slip fault strands, which cut through the Neogene sedimentary cover and the unconformably overlying Quaternary deposits;

The structural investigation reveals the KFF is characterized by simple shear dominated right-lateral strike-slip deformation. The along-strike spatial variation of the fault population orientation, kinematics and strain regimes (restraining and releasing areas) reflect the different ways by which the overall E-W right lateral shear is accommodated, distributed and partitioned along the principal and minor fault strands of the KFF system.

AHe thermochronology indicates the KFF system propagation was punctuated in time and space, and associated with two major episodes of fault-related exhumation, at ~18 Ma (Early Miocene) and ~4 Ma (Early Pliocene).

Collectively the stratigraphic, structural and thermochronological datasets shows that the KFF nucleated in the west and propagated eastward in two punctuated events.

The first faulting/exhumation episode is chiefly recorded by the structural and depositional architecture of the Neogene deposits along the KFF, where a source-to-sink scenario can be reconstructed for this time frame, when topographic growth caused the synchronous erosion/exhumation of the pre-Neogene units and deposition of the eroded material in the surrounding fault-bounded continental depocenters.

Successively, the KFF gradually entered a period of relative tectonic quiescence and, probably, regional subsidence during which a thick pile of fine-grained onlapping sediments were

deposited, and caused the resetting of the (U+Th)/He system of the detrital apatite grains hosted both within the pre-Neogene and the basal Neogene successions. The second faulting episode at ~4 Ma, recorded by the AHe ages and by the further tilting of the Neogene deposits, caused the final fault zone exhumation of the fault system, resulting in the current fault zone and topographic architecture.

The two fault-related exhumation events are nearly coincident with (1) the well documented acceleration of collision-related uplift in the early Miocene along the Arabia-Eurasia collision zone, and (2) the inferred tectonic reorganization of central Iran and the beginning of strike slip tectonics in central-eastern Iran.

Results from this study suggest that (i) the intraplate deformation zones are particularly sensitive to major tectonic changes occurring at the plate boundaries (far-field effects), and, as such, they can be regarded as a gage for plate-tectonics induced state of stress changes at the plate boundaries; (ii) intraplate strike-slip fault systems propagation and evolution is accompanied by substantial topographic growth, exhumation erosion and production of syn-tectonic deposits, whose distribution, geometry and facies characteristics are strongly influenced by the spatio-temporal propagation history and structural evolution of the fault system (near field effects).

ACKNOWLEDGMENTS

Special thanks go to M.R. Mazinini for assistance during field work. Manager and staff of Khaney-e-Moallem of Kashmar are warmly thanked for their kind hospitality. We also thank Ali Rastpour and Hassan Faraji for driving to the field and logistic support. F. Salvini is thanked for his advice during fault population analysis. This project has been funded by TOPOMOD Marie Curie ITN project (Grant agreement 264517).

REFERENCES

- Agard, P., Omrani, J., Jolivet, L., and Mouthereau, F., 2005, Convergence history across zagros (Iran): Constraints from collisional and earlier deformation: *International Journal of Earth Sciences*, v. 94, no. 3, p. 401-419, doi: 10.1007/s00531-005-0481-4.
- Agard, P., Omrani, J., Jolivet, L., Whitechurch, H., Vrielynck, B., Spakman, W., Monié, P., Meyer, B., and Wortel, R., 2011, Zagros orogeny: A subduction-dominated process: *Geological Magazine*, v. 148, no. 5-6, p. 692-725, doi: 10.1017/s001675681100046x.
- Aghanabati, A., 2004, *Geology of Iran*, Geological Survey of Iran.
- Allen, M., Jackson, J., and Walker, R., 2004, Late Cenozoic reorganization of the Arabia-Eurasia collision and the comparison of short-term and long-term deformation rates: *Tectonics*, v. 23, no. 2, doi: 10.1029/2003tc001530.

- Allen, M. B., and Armstrong, H. A., 2008, Arabia–Eurasia collision and the forcing of mid-Cenozoic global cooling: *Palaeogeography, Palaeoclimatology, Palaeoecology*, v. 265, no. 1, p. 52-58.
- Allen, M. B., Kheirkhah, M., Emami, M. H., and Jones, S. J., 2011, Right-lateral shear across Iran and kinematic change in the Arabia-Eurasia collision zone: *Geophysical Journal International*, v. 184, no. 2, p. 555-574, doi: 10.1111/j.1365-246X.2010.04874.x.
- Amini, A., 1997, Provenance and depositional environment of the Upper Red Formation, central zone Iran [Ph.D. thesis]: The University of Manchester.
- Austermann, J., and Iaffaldano, G., 2013, The role of the Zagros orogeny in slowing down Arabia-Eurasia convergence since ~5 ma: *Tectonics*, v. 32, no. 3, p. 351-363, doi: 10.1002/tect.20027.
- Axen, G. J., Lam, P. S., Grove, M., Stockli, D. F., and Hassanzadeh, J., 2001, Exhumation of the West-Central Alborz mountains, Iran, Caspian subsidence, and collision-related tectonics: *Geology*, v. 29, no. 6, p. 559, doi: 10.1130/0091-7613(2001).
- Aydin, A., Nur, A. 1985, The types and role of stepovers in strike-slip tectonics, *in*: Biddle K. T., Christie-Blick N. eds., *Strike-Slip Deformation, Basin Formation, and Sedimentation: The Society of Economic Paleontologists and Mineralogists, Special Publication*, v. 37 , pp. 35–45.
- Ballato, P., Nowaczyk, N. R., Landgraf, A., Strecker, M. R., Friedrich, A., and Tabatabaei, S. H., 2008, Tectonic control on sedimentary facies pattern and sediment accumulation rates in the Miocene foreland basin of the southern Alborz mountains, northern Iran: *Tectonics*, v. 27, no. 6, doi: 10.1029/2008tc002278.
- Ballato, P., Uba, C. E., Landgraf, A., Strecker, M. R., Sudo, M., Stockli, D. F., Friedrich, A., and Tabatabaei, S. H., 2011, Arabia-Eurasia continental collision: Insights from late Tertiary foreland-basin evolution in the Alborz mountains, northern Iran: *Geological Society of America Bulletin*, v. 123, p. 106-131, doi: 10.1130/b30091.1.
- Ballato, P., Stockli, D. F., Ghassemi, M. R., Landgraf, A., Strecker, M. R., Hassanzadeh, J., Friedrich, A., and Tabatabaei, S. H., 2013, Accommodation of transpressional strain in the Arabia-Eurasia collision zone: New constraints from (U-Th)/He thermochronology in the Alborz mountains, north Iran: *Tectonics*, v. 32, no. 1, p. 1-18, doi: 10.1029/2012tc003159.
- Behrooz, A., Sahbaei, M., Etemadi, N., Zedeh, A. A., Ghomashi, A., and Moghtader, M., 1987, Feyz Abad: Geological Survey of Iran, scale 1:100000.
- Berberian, M., 1974, A brief geological description of North-Central Iran: *Materials for the Study of the Seismotectonics of Iran; North-Central Iran: Geol. Survey of Iran Report*, v. 29, p. 127-138.
- Berberian, M., and King, G., 1981, Towards a paleogeography and tectonic evolution of Iran: *Canadian journal of earth sciences*, v. 18, no. 2, p. 210-265.

- Berberian, M., and Yeats, R. S., 1999, Patterns of historical earthquake rupture in the Iranian Plateau: *Bulletin of the Seismological Society of America*, v. 89, no. 1, p. 1.
- Berberian, M., 2014, Earthquakes and coseismic surface faulting on the Iranian Plateau, Elsevier Science.
- Boulton, S. J., and Robertson, A. H., 2007, The Miocene of the hatay area, S Turkey: Transition from the Arabian passive margin to an underfilled foreland basin related to closure of the southern Neotethys Ocean: *Sedimentary Geology*, v. 198, no. 1, p. 93-124.
- Braun, J., 1994, Three-dimensional numerical simulations of crustal-scale wrenching using a non-linear failure criterion: *Journal of Structural Geology*, v. 16, no. 8, p. 1173-1186.
- Buscher, J. T., and Spotila, J. A., 2007, Near-field response to transpression along the southern san andreas fault, based on exhumation of the northern San Gabriel mountains, southern California: *Tectonics*, v. 26, no. 5.
- Caine, J. S., Evans, J. P., and Forster, C. B., 1996, Fault zone architecture and permeability structure: *Geology*, v. 24, no. 11, p. 1025-1028, doi: 10.1130/0091-7613(1996)024<1025:fzaaps>2.3.co;2.
- Carne, R., and Little, T., 2012, Geometry and scale of fault segmentation and deformational bulging along an active oblique-slip fault (Wairarapa Fault, New Zealand): *Geological Society of America Bulletin*, v. 124, no. 7-8, p. 1365-1381.
- Chapman, D., 1986, Thermal gradients in the continental crust: Geological Society, London, Special Publications, v. 24, no. 1, p. 63-70.
- Cowgill, E., Yin, A., Arrowsmith, J. R., Feng, W. X., and Shuanhong, Z., 2004, The Akato Tagh bend along the Altyn Tagh Fault, northwest Tibet 1: Smoothing by vertical-axis rotation and the effect of topographic stresses on bend-flanking faults: *Geological Society of America Bulletin*, v. 116, no. 11-12, p. 1423-1442.
- Cox, S. C., Stirling, M. W., Herman, F., Gerstenberger, M., and Ristau, J., 2012, Potentially active faults in the rapidly eroding landscape adjacent to the Alpine Fault, central southern Alps, New Zealand: *Tectonics*, v. 31, doi: 10.1029/2011tc003038.
- Cunningham, D., 2013, Mountain building processes in intracontinental oblique deformation belts: Lessons from the Gobi corridor, Central Asia: *Journal of Structural Geology*, v. 46, p. 255-282, doi: 10.1016/j.jsg.2012.08.010.
- Dair, L., and Cooke, M. L., 2009, San Andreas fault geometry through the San Gorgonio Pass, California: *Geology*, v. 37, no. 2, p. 119-122, doi: 10.1130/g25101a.1.

- Daneshian, J., and Dana, L. R., 2007, Early Miocene benthic foraminifera and biostratigraphy of the Qom formation, Deh Namak, Central Iran: *Journal of Asian Earth Sciences*, v. 29, no. 5, p. 844-858.
- Dewey, J., Hempton, M., Kidd, W., Saroglu, F. t., and Şengör, A., 1986, Shortening of continental lithosphere: The neotectonics of Eastern Anatolia—a young collision zone: Geological Society, London, Special Publications, v. 19, no. 1, p. 1-36.
- Doblas, M., 1998, Slickenside kinematic indicators: *Tectonophysics*, v. 295, no. 1, p. 187-197.
- Dooley, T. P., and Schreurs, G., 2012, Analogue modelling of intraplate strike-slip tectonics: A review and new experimental results: *Tectonophysics*, v. 574, p. 1-71, doi: 10.1016/j.tecto.2012.05.030.
- Eftekhari-Nezhad, J., Aghanabati, A., Hamzeshpour, B., and Baroyant, V., 1976, Kashmar: Geological Survey of Iran, scale 1:250000.
- Ellis, S., 1996, Forces driving continental collision: Reconciling indentation and mantle subduction tectonics: *Geology*, v. 24, no. 8, p. 699-702.
- Ershov, A. V., Brunet, M.-F., Nikishin, A. M., Bolotov, S. N., Nazarevich, B. P., and Korotaev, M. V., 2003, Northern Caucasus basin: Thermal history and synthesis of subsidence models: *Sedimentary Geology*, v. 156, no. 1, p. 95-118.
- Farbod, Y., Bellier, O., Shabanian, E., and Abbassi, M. R., 2011, Geomorphic and structural variations along the Doruneh Fault System (Central Iran): *Tectonics*, v. 30, doi: 10.1029/2011tc002889.
- Farley, K., Wolf, R., and Silver, L., 1996, The effects of long alpha-stopping distances on (U-Th)/He ages: *Geochimica et Cosmochimica Acta*, v. 60, no. 21, p. 4223-4229.
- Farley, K., 2000, Helium diffusion from apatite: General behavior as illustrated by durango fluorapatite: *Journal of Geophysical Research: Solid Earth* (1978–2012), v. 105, no. B2, p. 2903-2914.
- Fattahi, M., Walker, R. T., Khatib, M. M., Dolati, A., and Bahroudi, A., 2007, Slip-rate estimate and past earthquakes on the doruneh fault, Eastern Iran: *Geophysical Journal International*, v. 168, no. 2, p. 691-709, doi: 10.1111/j.1365-246X.2006.03248.x.
- Fialko, Y., Rivera, L., and Kanamori, H., 2005, Estimate of differential stress in the upper crust from variations in topography and strike along the Aar Andreas fault: *Geophysical Journal International*, v. 160, no. 2, p. 527-532.
- Finzi, Y., Hearn, E. H., Ben-Zion, Y., and Lyakhovsky, V., 2009, Structural properties and deformation patterns of evolving strike-slip faults: Numerical simulations incorporating damage rheology: *Pure and Applied Geophysics*, v. 166, no. 10-11, p. 1537-1573.

- Fitzgerald, P. G., Stump, E., and Redfield, T. F., 1993, Late cenozoic uplift of denali and its relation to relative plate motion and fault morphology: *Science*, v. 259, no. 5094, p. 497-499, doi: 10.1126/science.259.5094.497.
- Fitzgerald, P. G., Sorkhabi, R. B., Redfield, T. F., and Stump, E., 1995, Uplift and denudation of the Central Alaska ange - a case-study in the use of apatite fission-track thermochronology to determine absolute uplift parameters: *Journal of Geophysical Research-Solid Earth*, v. 100, no. B10, p. 20175-20191, doi: 10.1029/95jb02150.
- Foeken, J., Stuart, F. M., Dobson, K. J., Persano, C., and Vilbert, D., 2006, A diode laser system for heating minerals for (U+Th)/He chronometry: *Geochemistry, Geophysics, Geosystems*, v. 7, no. 4.
- Foeken, J., Persano, C., Stuart, F.M., and Ter Voorde, M., 2007. Role of topography in isotherm perturbation: Apatite (U - Th)/He and fission track results from the Malta tunnel, Tauern Window, Austria *Tectonics* v. 26 doi: 10.1029/2006TC002049
- Foroutan, M., Meyer, B., Sébrier, M., Nazari, H., Murray, A., Le Dortz, K., Shokri, M., Arnold, M., Aumaître, G., and Bourlès, D., 2014, Late Pleistocene-Holocene right slip rate and paleoseismology of the Nayband fault, western margin of the Lut Block, Iran: *Journal of Geophysical Research: Solid Earth*, v. 119, no. 4, p. 3517-3560.
- Fossen, H., 2010, *Structural geology*, Cambridge University Press.
- Fossen, H., and Tikoff, B., 1993, The deformation matrix for simultaneous simple shearing, pure shearing and volume change, and its application to transpression-transtension tectonics: *Journal of Structural Geology*, v. 15, no. 3, p. 413-422.
- Fossen, H., Tikoff, B., and Teyssier, C., 1994, Strain modeling of transpressional and transtensional deformation: *Norsk Geologisk Tidsskrift*, v. 74, no. 3, p. 134-145.
- Foster, D. A., and Gleadow, A. J., 1992, Reactivated tectonic boundaries and implications for the reconstruction of southeastern australia and Northern Victoria Land, Antarctica: *Geology*, v. 20, no. 3, p. 267-270.
- Gavillot, Y., Axen, G. J., Stockli, D. F., Horton, B. K., and Fakhari, M. D., 2010, Timing of thrust activity in the High Zagros fold-thrust belt, Iran, from (U+Th)/He thermochronometry: *Tectonics*, v. 29, no. 4.
- Ghomashi, A., Masoomi, R., Hosseiny, S. Z., Taheri, J., Shamanian, G., Kaveh, N. S., Baheremand, M., and Razavi, M. A., 2001, *Kashmar: Geological Survey of Iran*, scale 1:100000.
- Granier, T., 1985, Origin, damping, and pattern of development of faults in granite: *Tectonics*, v. 4, no. 7, p. 721-737.

- Guest, B., Stockli, D. F., Grove, M., Axen, G. J., Lam, P. S., and Hassanzadeh, J., 2006, Thermal histories from the central Alborz Mountains, northern Iran: implications for the spatial and temporal distribution of deformation in northern Iran: *Geological Society of America Bulletin*, v. 118, no. 11-12, p. 1507-1521.
- Hadavi, F., Moghaddam, M. N., and Mousazadeh, H., 2010, Burdigalian–serravalian calcareous nannoplanktons from Qom Formation, north-center Iran: *Arabian Journal of Geosciences*, v. 3, no. 2, p. 133-139.
- Hafkenscheid, E., Wortel, M., and Spakman, W., 2006, Subduction history of the Tethyan region derived from seismic tomography and tectonic reconstructions: *Journal of Geophysical Research: Solid Earth* (1978–2012), v. 111, no. B8.
- Hassami, K., Jamali, F., and Tabassi, H., 2003, Major active faults of Iran: International institute of earthquake engineering and seismology of Iran Press.
- Hatzfeld, D., and Molnar, P., 2010, Comparisons of the kinematics and deep structures of the Zagros and Himalaya and of the Iranian and Tibetan plateaus and geodynamic implications: *Reviews of Geophysics*, v. 48, no. 2.
- Headley, R. M., Enkelmann, E., and Hallet, B., 2013, Examination of the interplay between glacial processes and exhumation in the Saint Elias Mountains, Alaska: *Geosphere*, v. 9, no. 2, p. 229-241, doi: 10.1130/ges00810.1.
- Heidbach, O., Tingay, M., Barth, A., Reinecker, J., Kurfeß, D., and Müller, B., 2001, World stress map: *Naturwissenschaften*, v. 88, p. 357-371.
- Heidbach, O., Tingay, M., Barth, A., Reinecker, J., Kurfeß, D., and Müller, B., 2008, The world stress map database release 2008, doi: 10.1594/gfz: WSM. Rel2008.
- Hessami, K., Ko, H. A., Talbot, C. J., Tabasi, H., and Shabanian, E., 2001, Progressive unconformities within an evolving foreland fold–thrust belt, Zagros Mountains: *Journal of the Geological Society*, v. 158, no. 6, p. 969-981.
- Hilley, G. E., and Arrowsmith, J. R., 2008, Geomorphic response to uplift along the Dragon's Back pressure ridge, Carrizo Plain, California: *Geology*, v. 36, no. 5, p. 367-370, doi: 10.1130/g24517a.1.
- Holdsworth, R., Handa, M., Miller, J., and Buick, I., 2001, Continental reactivation and reworking: An introduction: *Geological Society, London, Special Publications*, v. 184, no. 1, p. 1-12.
- Hollingsworth, J., Fattahi, M., Walker, R., Talebian, M., Bahroudi, A., Bolourchi, M. J., Jackson, J., and Copley, A., 2010, Oroclinal bending, distributed thrust and strike-slip faulting, and the accommodation of Arabia–Eurasia convergence in NE Iran since the Oligocene: *Geophysical Journal International*, p. no-no, doi: 10.1111/j.1365-246X.2010.04591.x.

- Homke, S., Vergés, J., Serra-Kiel, J., Bernaola, G., Sharp, I., Garcés, M., Montero-Verdú, I., Karpuz, R., and Goodarzi, M. H., 2009, Late Cretaceous–Paleocene formation of the proto–Zagros foreland basin, Lurestan Province, SW Iran: *Geological Society of America Bulletin*, v. 121, no. 7-8, p. 963-978.
- Homke, S., Vergés, J., Van Der Beek, P., Fernández, M., Saura, E., Barbero, L., Badics, B., and Labrin, E., 2010, Insights in the exhumation history of the NW Zagros from bedrock and detrital apatite fission-track analysis: evidence for a long-lived orogeny: *Basin Research*, v. 22, no. 5, p. 659-680, doi: 10.1111/j.1365-2117.2009.00431.x.
- Jackson, J., and McKenzie, D., 1984, Active tectonics of the Alpine—Himalayan Belt between western Turkey and Pakistan: *Geophysical Journal International*, v. 77, no. 1, p. 185-264.
- Jalilian, M., Etemadi, N., Zadeh, A. A., Manouchehri, M., Pour, M. J. V., Tehrani, N. A., Behrouzi, A., Kholghi, M. H., and Naini, M. A., 1992, Torbat-e-Heydarieh: Geological Survey of Iran, scale 1:250000.
- Javadi, H. R., Ghassemi, M. R., Shahpasandzadeh, M., Guest, B., Ashtiani, M. E., Yassaghi, A. L. I., and Kouhpeyma, M., 2013, History of faulting on the Doruneh Fault System: implications for the kinematic changes of the Central Iranian Microplate: *Geological Magazine*, v. 150, no. 04, p. 651-672, doi: 10.1017/s0016756812000751.
- Jolivet, L., and Faccenna, C., 2000, Mediterranean extension and the Africa-Eurasia collision: *Tectonics*, v. 19, no. 6, p. 1095-1106.
- Khadivi, S., Mouthereau, F., Larrasoana, J. C., Vergés, J., Lacombe, O., Khademi, E., Beamud, E., Melinte-Dobrinescu, M., and Suc, J. P., 2009, Magnetostratigraphy of synorogenic Miocene foreland sediments in the Fars arc of the Zagros Folded Belt (SW Iran): *Basin Research*, doi: 10.1111/j.1365-2117.2009.00446.x.
- Koons, P., Zeitler, P., Chamberlain, C., Craw, D., and Meltzer, A., 2002, Mechanical links between erosion and metamorphism in Nanga Parbat, Pakistan Himalaya: *American Journal of Science*, v. 302, no. 9, p. 749-773.
- Le Guerroué, E., and Cobbold, P. R., 2006, Influence of erosion and sedimentation on strike-slip fault systems: Insights from analogue models: *Journal of Structural Geology*, v. 28, no. 3, p. 421-430, doi: 10.1016/j.jsg.2005.11.007.
- Madanipour, S., Ehlers, T. A., Yassaghi, A., Rezaeian, M., Enkelmann, E., and Bahroudi, A., 2013, Synchronous deformation on orogenic plateau margins: Insights from the Arabia–Eurasia collision: *Tectonophysics*, v. 608, p. 440-451, doi: 10.1016/j.tecto.2013.09.003.
- Marshak, S., Karlstrom, K., and Timmons, J. M., 2000, Inversion of Proterozoic extensional faults: An explanation for the pattern of Laramide and Ancestral Rockies intracratonic deformation,

- United States: *Geology*, v. 28, no. 8, p. 735-738, doi: 10.1130/0091-7613(2000)28<735:iopefa>2.0.co;2.
- Mattei, M., Cifelli, F., Muttoni, G., Zanchi, A., Berra, F., Mossavvari, F., and Eshraghi, S. A., 2012, Neogene block rotation in central Iran: Evidence from paleomagnetic data: *Geological Society of America Bulletin*, v. 124, no. 5-6, p. 943-956.
- McClusky, S., Reilinger, R., Mahmoud, S., Sari, D. B., and Tealeb, A., 2003, GPS constraints on Africa (Nubia) and Arabia plate motions: *Geophysical Journal International*, v. 155, no. 1, p. 126-138.
- McKenzie, D., and Jackson, J., 1983, The relationship between strain rates, crustal thickening, palaeomagnetism, finite strain and fault movements within a deforming zone: *Earth and Planetary Science Letters*, v. 65, no. 1, p. 182-202.
- McQuarrie, N., Stock, J., Verdel, C., and Wernicke, B., 2003, Cenozoic evolution of Neotethys and implications for the causes of plate motions: *Geophysical research letters*, v. 30, no. 20.
- McQuarrie, N., and van Hinsbergen, D. J., 2013, Retrodeforming the Arabia-Eurasia collision zone: Age of collision versus magnitude of continental subduction: *Geology*, v. 41, no. 3, p. 315-318.
- Molnar, P., 1988, Continental tectonics in the aftermath of plate tectonics: *nature*, v. 335, no. 6186, p. 131-137.
- Molnar, P., and Tapponnier, P., 1975, Cenozoic tectonics of Asia: Effects of a continental collision: *Science*, v. 189, no. 4201, p. 419-426.
- Molnar, P., Anderson, R. S., and Anderson, S. P., 2007, Tectonics, fracturing of rock, and erosion: *Journal of Geophysical Research-Earth Surface*, v. 112, no. F3, doi: 10.1029/2005jf000433.
- Morley, C. K., Kongwung, B., Julapour, A. A., Abdolghafourian, M., Hajian, M., Waples, D., Warren, J., Otterdoom, H., Srisuriyon, K., and Kazemi, H., 2009, Structural development of a major late cenozoic basin and transpressional belt in Central Iran: The central basin in the Qom-Saveh area: *Geosphere*, v. 5, no. 4, p. 325-362, doi: 10.1130/ges00223.1.
- Mouthereau, F., 2011, Timing of uplift in the Zagros belt/Iranian plateau and accommodation of late Cenozoic Arabia–Eurasia convergence: *Geological Magazine*, v. 148, no. 5-6, p. 726-738, doi: 10.1017/s0016756811000306.
- Mouthereau, F., Tensi, J., Bellahsen, N., Lacombe, O., De Boisgrollier, T., and Kargar, S., 2007, Tertiary sequence of deformation in a thin-skinned/thick-skinned collision belt: The Zagros Folded Belt (Fars, Iran): *Tectonics*, v. 26, no. 5, doi: 10.1029/2007tc002098.
- Mouthereau, F., Lacombe, O., and Vergés, J., 2012, Building the Zagros collisional orogen: timing, strain distribution and the dynamics of Arabia/Eurasia plate convergence: *Tectonophysics*, v. 532-535, p. 27-60, doi: 10.1016/j.tecto.2012.01.022.

- Niemi, N. A., Buscher, J. T., Spotila, J. A., House, M. A., and Kelley, S. A., 2013, Insights from low-temperature thermochronometry into transpressional deformation and crustal exhumation along the San Andreas fault in the western Transverse Ranges, California: *Tectonics*, v. 32, no. 6, p. 1602-1622, doi: 10.1002/2013tc003377.
- Nilforoushan, F., Masson, F., Vernant, P., Vigny, C., Martinod, J., Abbassi, M., Nankali, H., Hatzfeld, D., Bayer, R., Tavakoli, F., Ashtiani, A., Doerflinger, E., Daignières, M., Collard, P., and Chéry, J., 2003, GPS network monitors the Arabia-Eurasia collision deformation in Iran: *Journal of Geodesy*, v. 77, no. 7-8, p. 411-422, doi: 10.1007/s00190-003-0326-5.
- Nozaem, R., Mohajjel, M., Rossetti, F., Della Seta, M., Vignaroli, G., Yassaghi, A., Salvini, F., and Eliassi, M., 2013, Post-Neogene right-lateral strike-slip tectonics at the north-western edge of the Lut Block (Kuh-e-Sarhangi Fault), Central Iran: *Tectonophysics*.
- Okay, A. I., Zattin, M., and Cavazza, W., 2010, Apatite fission-track data for the Miocene Arabia-Eurasia collision: *Geology*, v. 38, no. 1, p. 35-38, doi: 10.1130/g30234.1.
- Paterson, M. S., Wong, T.-f., Paterson, M. S., Geologist, A., and Géologue, A., 2005, *Experimental rock deformation: The brittle field*, Springer.
- Petit, J., 1987, Criteria for the sense of movement on fault surfaces in brittle rocks: *Journal of Structural Geology*, v. 9, no. 5, p. 597-608.
- Ramezani, J., and Tucker, R. D., 2003, The Saghand region, central Iran: U-Pb geochronology, petrogenesis and implications for Gondwana tectonics: *American Journal of Science*, v. 303, no. 7, p. 622-665.
- Reading, H. G., 2009, *Sedimentary environments: Processes, facies and stratigraphy*, Wiley.
- Regard, V., Bellier, O., Thomas, J. C., Bourlès, D., Bonnet, S., Abbassi, M. R., Braucher, R., Mercier, J., Shabanian, E., Soleymani, S., and Fegghi, K., 2005, Cumulative right-lateral fault slip rate across the Zagros—Makran transfer zone: role of the Minab—Zendan fault system in accommodating Arabia—Eurasia convergence in southeast Iran: *Geophysical Journal International*, v. 162, no. 1, p. 177-203, doi: 10.1111/j.1365-246X.2005.02558.x.
- Regard, V., Bellier, O., Braucher, R., Gasse, F., Bourlès, D., Mercier, J., Thomas, J. C., Abbassi, M. R., Shabanian, E., and Soleymani, S., 2006, ¹⁰Be dating of alluvial deposits from Southeastern Iran (the Hormoz Strait area): *Palaeogeography, Palaeoclimatology, Palaeoecology*, v. 242, no. 1-2, p. 36-53, doi: <http://dx.doi.org/10.1016/j.palaeo.2006.05.012>.
- Reilinger, R., McClusky, S., Vernant, P., Lawrence, S., Ergintav, S., Cakmak, R., Ozener, H., Kadirov, F., Guliev, I., and Stepanyan, R., 2006, GPS constraints on continental deformation in the Africa-Arabia-Eurasia continental collision zone and implications for the dynamics of plate interactions: *Journal of Geophysical Research: Solid Earth* (1978–2012), v. 111, no. B5.

- Rezaeian, M., Carter, A., Hovius, N., and Allen, M. B., 2012, Cenozoic exhumation history of the Alborz Mountains, Iran: New constraints from low-temperature chronometry: *Tectonics*, v. 31, no. 2, p. n/a-n/a, doi: 10.1029/2011tc002974.
- Robertson, A. H., Ustaömer, T., Parlak, O., Ünlügenç, U. C., Taşlı, K., and Inan, N., 2006, The Berit transect of the Tauride thrust belt, S Turkey: Late Cretaceous–Early Cenozoic accretionary/collisional processes related to closure of the Southern Neotethys: *Journal of Asian Earth Sciences*, v. 27, no. 1, p. 108-145.
- Robin, P. Y. F., and Cruden, A. R., 1994, Strain and vorticity patterns in ideally ductile transpression zones: *Journal of Structural Geology*, v. 16, no. 4, p. 447-466, doi: 10.1016/0191-8141(94)90090-6.
- Rossetti, F., Nozaem, R., Lucci, F., Vignaroli, G., Gerdes, A., Nasrabadi, M., and Theye, T., 2014, Tectonic setting and geochronology of the Cadomian (Ediacaran-Cambrian) magmatism in Central Iran, Kuh-e-Sarhangi region (NW Lut Block): *Journal of Asian Earth Sciences*, no. 0, doi: <http://dx.doi.org/10.1016/j.jseaes.2014.07.034>.
- Rowland, J., and Sibson, R., 2004, Structural controls on hydrothermal flow in a segmented rift system, Taupo Volcanic Zone, New Zealand: *Geofluids*, v. 4, no. 4, p. 259-283.
- Rutter, E., and Hadizadeh, J., 1991, On the influence of porosity on the low-temperature brittle—Ductile transition in siliciclastic rocks: *Journal of Structural Geology*, v. 13, no. 5, p. 609-614.
- Salvini, F., Brancolini, G., Busetti, M., Storti, F., Mazzarini, F., and Coren, F., 1997, Cenozoic geodynamics of the Ross Sea region, Antarctica: Crustal extension, intraplate strike-slip faulting, and tectonic inheritance: *Journal of Geophysical Research: Solid Earth* (1978–2012), v. 102, no. B11, p. 24669-24696.
- Salvini, F., 2004, Daisy 3 the structural data integrated system analyzer., p. Available at Software University of Roma Tre, Roma: <http://host.uniroma3.it/progetti/fralab>.
- Sanderson, D. J., and Marchini, W., 1984, Transpression: *Journal of Structural Geology*, v. 6, no. 5, p. 449-458.
- Scholz, C. H., 2002, *The mechanics of earthquakes and faulting*, Cambridge university press.
- Schopfer, M. P., and Steyrer, H. P., 2001, Experimental modeling of strike-slip faults and the self-similar behavior: *MEMOIRS-GEOLOGICAL SOCIETY OF AMERICA*, p. 21-28.
- Schrank, C. E., and Cruden, A. R., 2010, Compaction control of topography and fault network structure along strike-slip faults in sedimentary basins: *Journal of Structural Geology*, v. 32, no. 2, p. 184-191.
- Sella, G. F., Dixon, T. H., and Mao, A., 2002, Revel: A model for recent plate velocities from space geodesy: *J. geophys. Res.*, v. 107, no. 10.1029, p. 209-226.

- Shabanian, E., Bellier, O., Siame, L., Arnaud, N., Abbassi, M. R., and Cochemé, J.-J., 2009a, New tectonic configuration in NE Iran: Active strike-slip faulting between the Kopeh Dagh and Binalud mountains: *Tectonics*, v. 28, no. 5, doi: 10.1029/2008tc002444.
- Shabanian, E., Siame, L., Bellier, O., Benedetti, L., and Abbassi, M. R., 2009b, Quaternary slip rates along the northeastern boundary of the Arabia-Eurasia collision zone (Kopeh Dagh Mountains, Northeast Iran): *Geophysical Journal International*, v. 178, no. 2, p. 1055-1077, doi: 10.1111/j.1365-246X.2009.04183.x.
- Shabanian, E., Bellier, O., Abbassi, M. R., Siame, L., and Farbod, Y., 2010, Plio-quaternary stress states in NE Iran: Kopeh Dagh and Allah Dagh-Binalud mountain ranges: *Tectonophysics*, v. 480, no. 1-4, p. 280-304, doi: 10.1016/j.tecto.2009.10.022.
- Sheldon, H., Barnicoat, A., and Ord, A., 2006, Numerical modelling of faulting and fluid flow in porous rocks: an approach based on critical state soil mechanics: *Journal of Structural Geology*, v. 28, no. 8, p. 1468-1482.
- Spotila, J. A., Farley, K. A., and Sieh, K., 1998, Uplift and erosion of the San Bernardino Mountains associated with transpression along the San Andreas fault, California, as constrained by radiogenic helium thermochronometry: *Tectonics*, v. 17, no. 3, p. 360-378, doi: 10.1029/98tc00378.
- Spotila, J. A., Farley, K. A., Yule, J. D., and Reiners, P. W., 2001, Near-field transpressive deformation along the San Andreas fault zone in southern California, based on exhumation constrained by (U-Th)/He dating: *Journal of Geophysical Research: Solid Earth*, v. 106, no. B12, p. 30909-30922, doi: 10.1029/2001jb000348.
- Spotila, J. A., House, M. A., Niemi, N. A., Brady, R. C., Oskin, M., and Buscher, J. T., 2007a, Patterns of bedrock uplift along the San Andreas fault and implications for mechanisms of transpression: *Geological Society of America Special Papers*, v. 434, p. 15-33, doi: 10.1130/2007.2434(02).
- Spotila, J. A., Niemi, N., Brady, R., House, M., Buscher, J., and Oskin, M., 2007b, Long-term continental deformation associated with transpressive plate motion: The San Andreas fault: *Geology*, v. 35, no. 11, p. 967-970, doi: 10.1130/g23816a.1.
- Storti, F., Holdsworth, R. E., and Salvini, F., 2003, Intraplate strike-slip deformation belts: *Geological Society, London, Special Publications*, v. 210, no. 1, p. 1-14.
- Storti, F., Rossetti, F., Läufer, A. L., and Salvini, F., 2006, Consistent kinematic architecture in the damage zones of intraplate strike-slip fault systems in North Victoria Land, Antarctica and implications for fault zone evolution: *Journal of Structural Geology*, v. 28, no. 1, p. 50-63, doi: 10.1016/j.jsg.2005.09.004.

- Sutton, J., and Watson, J. V., 1986, Architecture of the continental lithosphere: *Philosophical Transactions of the Royal Society of London. Series A, Mathematical and Physical Sciences*, v. 317, no. 1539, p. 5-12.
- Tchalenko, J., Berberian, M., and Behzadi, H., 1973, Geomorphic and seismic evidence for recent activity on the Doruneh Fault, Iran: *Tectonophysics*, v. 19, no. 4, p. 333-341.
- Verdel, C., Wernicke, B. P., Ramezani, J., Hassanzadeh, J., Renne, P. R., and Spell, T. L., 2007, Geology and thermochronology of Tertiary Cordilleran-style metamorphic core complexes in the Saghand region of central Iran: *Geological Society of America Bulletin*, v. 119, no. 7-8, p. 961-977, doi: 10.1130/b26102.1.
- Vernant, P., Nilforoushan, F., Hatzfeld, D., Abbassi, M. R., Vigny, C., Masson, F., Nankali, H., Martinod, J., Ashtiani, A., Bayer, R., Tavakoli, F., and Chéry, J., 2004, Present-day crustal deformation and plate kinematics in the Middle East constrained by GPS measurements in Iran and northern Oman: *Geophysical Journal International*, v. 157, no. 1, p. 381-398, doi: 10.1111/j.1365-246X.2004.02222.x.
- Vincent, S. J., Morton, A. C., Carter, A., Gibbs, S., and Barabadze, T. G., 2007, Oligocene uplift of the Western Greater Caucasus: an effect of initial Arabia–Eurasia collision: *Terra Nova*, v. 19, no. 2, p. 160-166.
- Vincent, S. J., Allen, M. B., Ismail-Zadeh, A. D., Flecker, R., Foland, K. A., and Simmons, M. D., 2005, Insights from the Talysh of Azerbaijan into the Paleogene evolution of the South Caspian region: *Geological Society of America Bulletin*, v. 117, no. 11-12, p. 1513-1533, doi: 10.1130/b25690.1.
- Walker, R., and Jackson, J., 2004, Active tectonics and late Cenozoic strain distribution in central and eastern Iran: *Tectonics*, v. 23, no. 5, doi: Artn Tc5010 Doi 10.1029/2003tc001529.
- Walker, R., Jackson, J., and Baker, C., 2004, Active faulting and seismicity of the Dasht-e-Bayaz region, Eastern Iran: *Geophysical Journal International*, v. 157, no. 1, p. 265-282, doi: 10.1111/j.1365-2966.2004.02179.x.
- Walker, R. T., and Fattahi, M., 2011, A framework of Holocene and Late Pleistocene environmental change in eastern Iran inferred from the dating of periods of alluvial fan abandonment, river terracing, and lake deposition: *Quaternary Science Reviews*, v. 30, no. 9, p. 1256-1271.
- Walker, R. T., and Khatib, M. M., 2006, Active faulting in the birjand region of ne iran: *Tectonics*, v. 25, no. 4, doi: 10.1029/2005tc001871.
- Walpersdorf, A., Manighetti, I., Mousavi, Z., Tavakoli, F., Vergnolle, M., Jadidi, A., Hatzfeld, D., Aghamohammadi, A., Bigot, A., and Djamour, Y., 2014, Present-day kinematics and fault slip

rates in eastern Iran, derived from 11 years of GPS data: *Journal of Geophysical Research: Solid Earth*, v. 119, no. 2, p. 1359-1383.

Wong, T.-f., and Baud, P., 2012, The brittle-ductile transition in porous rock: A review: *Journal of Structural Geology*, v. 44, p. 25-53.

Woodcock, N. H., and Fischer, M., 1986, Strike-slip duplexes: *Journal of Structural Geology*, v. 8, no. 7, p. 725-735.

Ziegler, P. A., Van Wees, J.-D., and Cloetingh, S., 1998, Mechanical controls on collision-related compressional intraplate deformation: *Tectonophysics*, v. 300, no. 1, p. 103-129.

Zoback, M. L., 1992, First-and second-order patterns of stress in the lithosphere: The world stress map project: *Journal of Geophysical Research: Solid Earth* (1978–2012), v. 97, no. B8, p. 11703-11728.

FIGURES

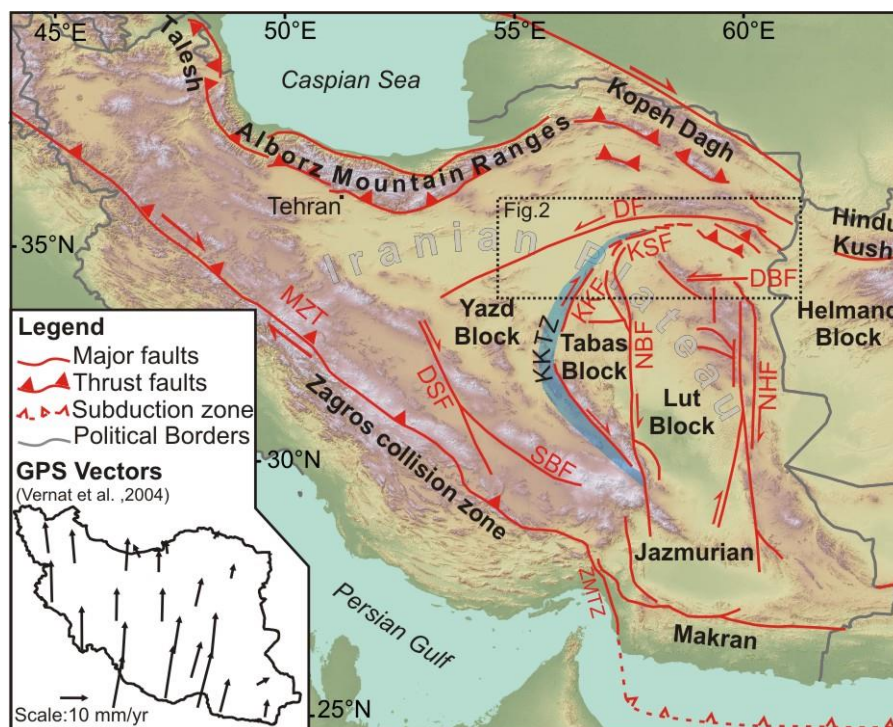


Figure 1

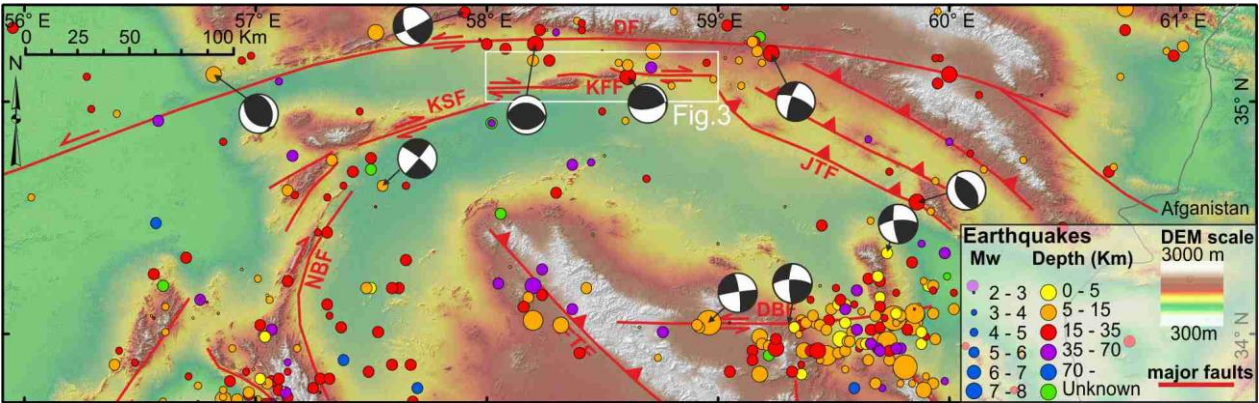


Figure 2

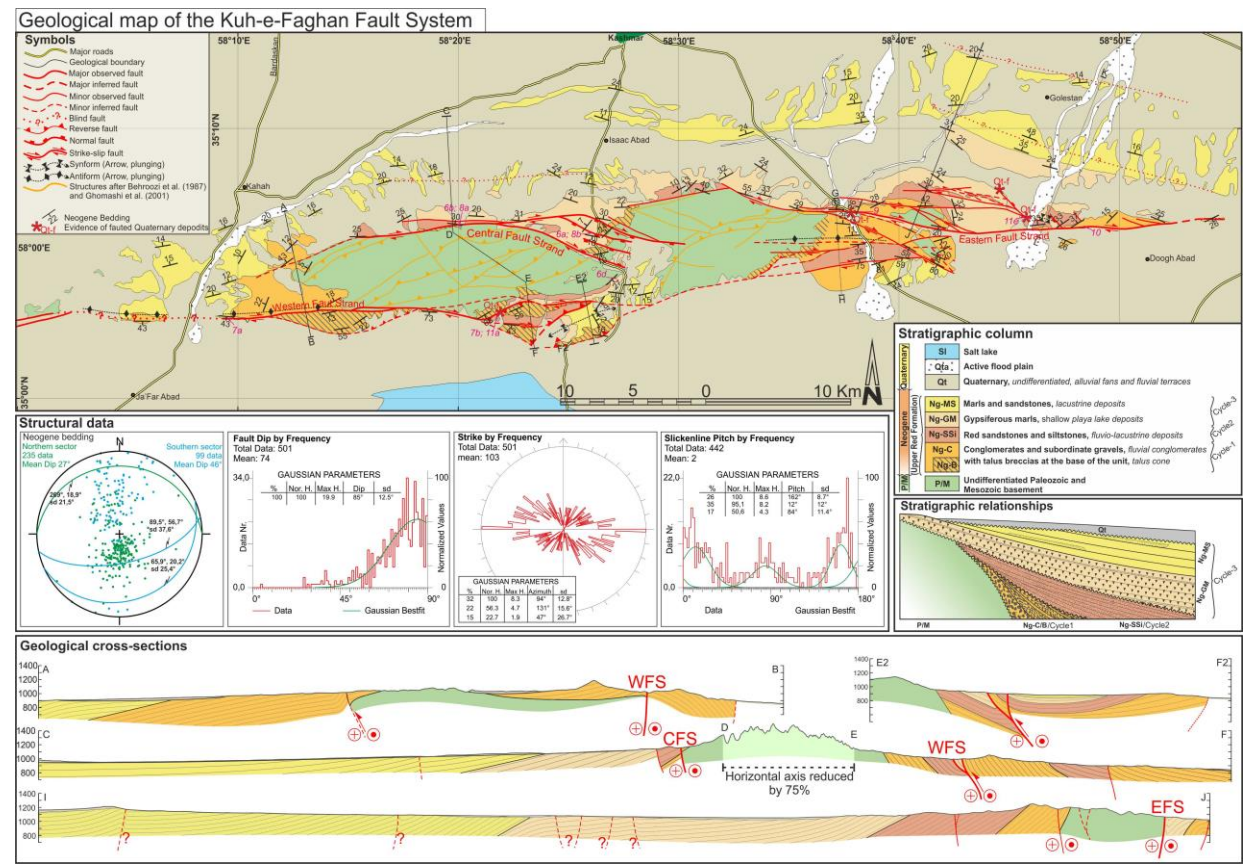


Figure 3

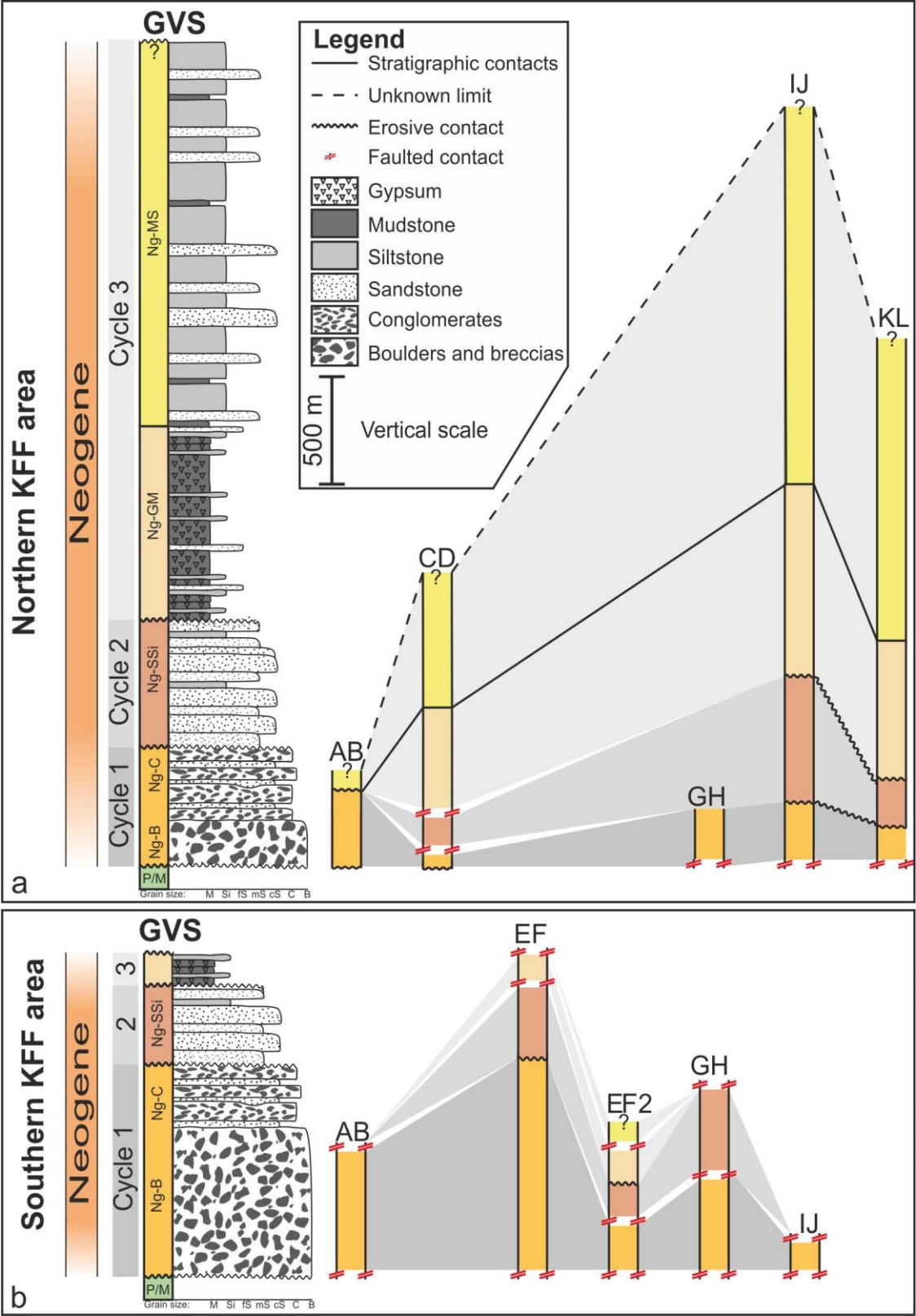


Figure 4

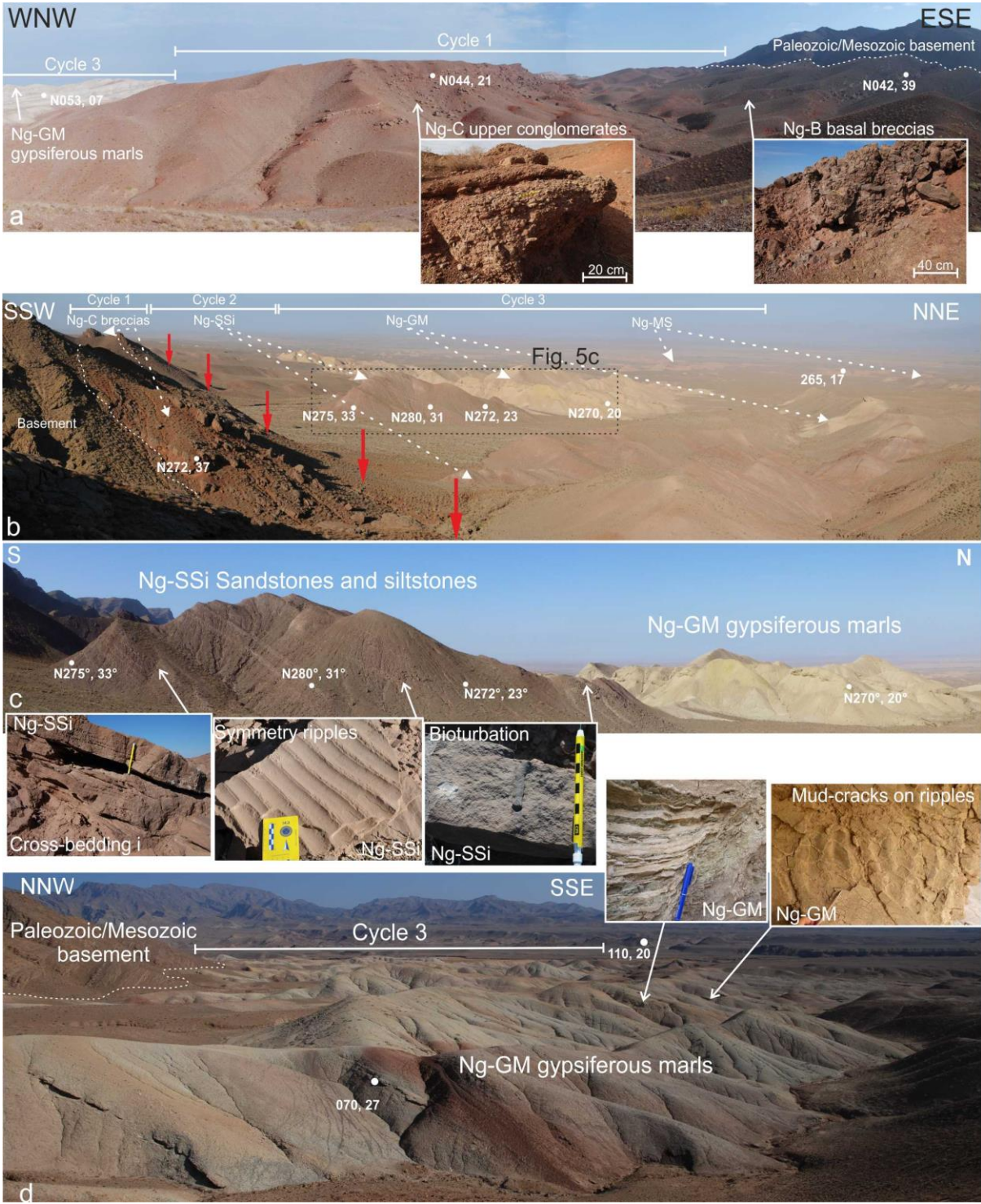


Figure 5

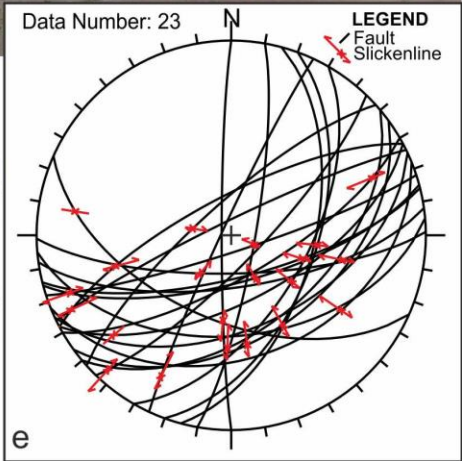
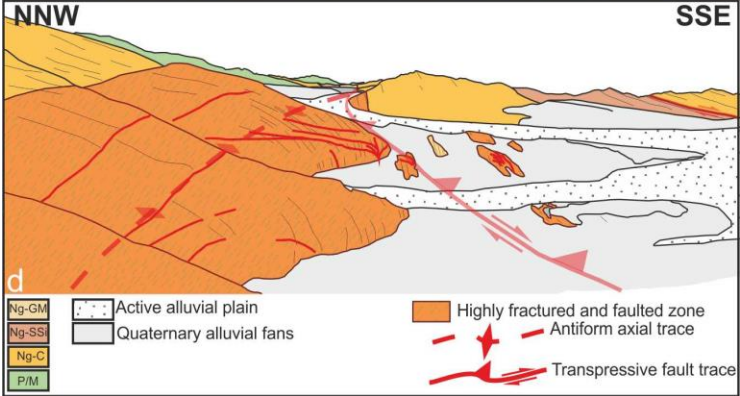
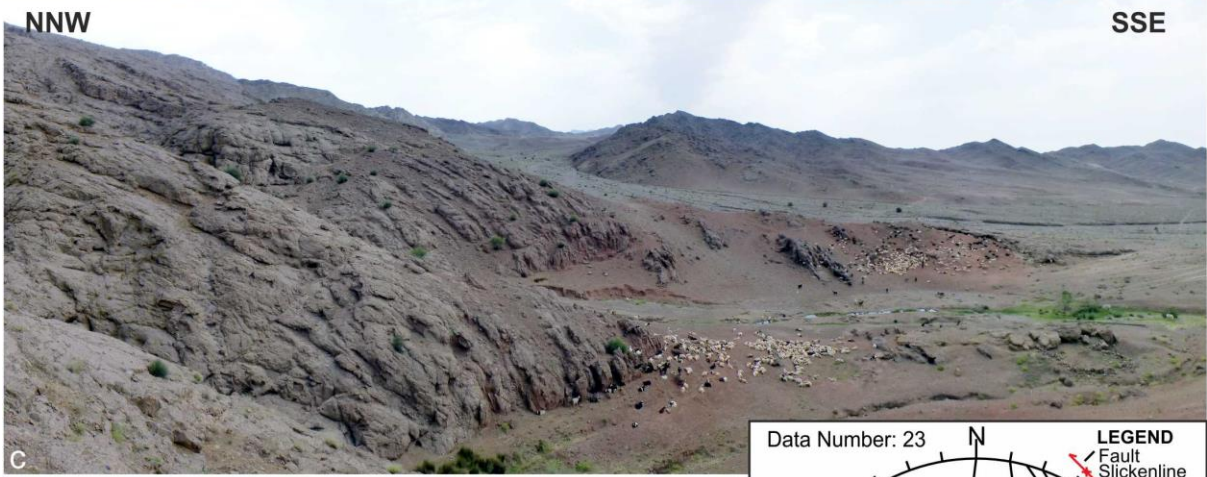
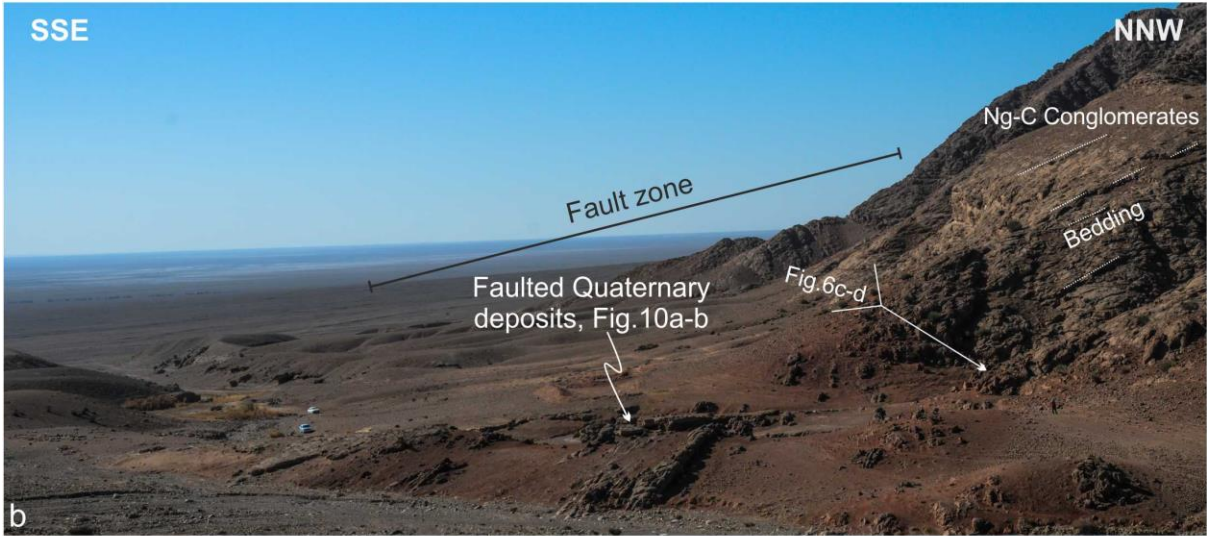


Figure 6

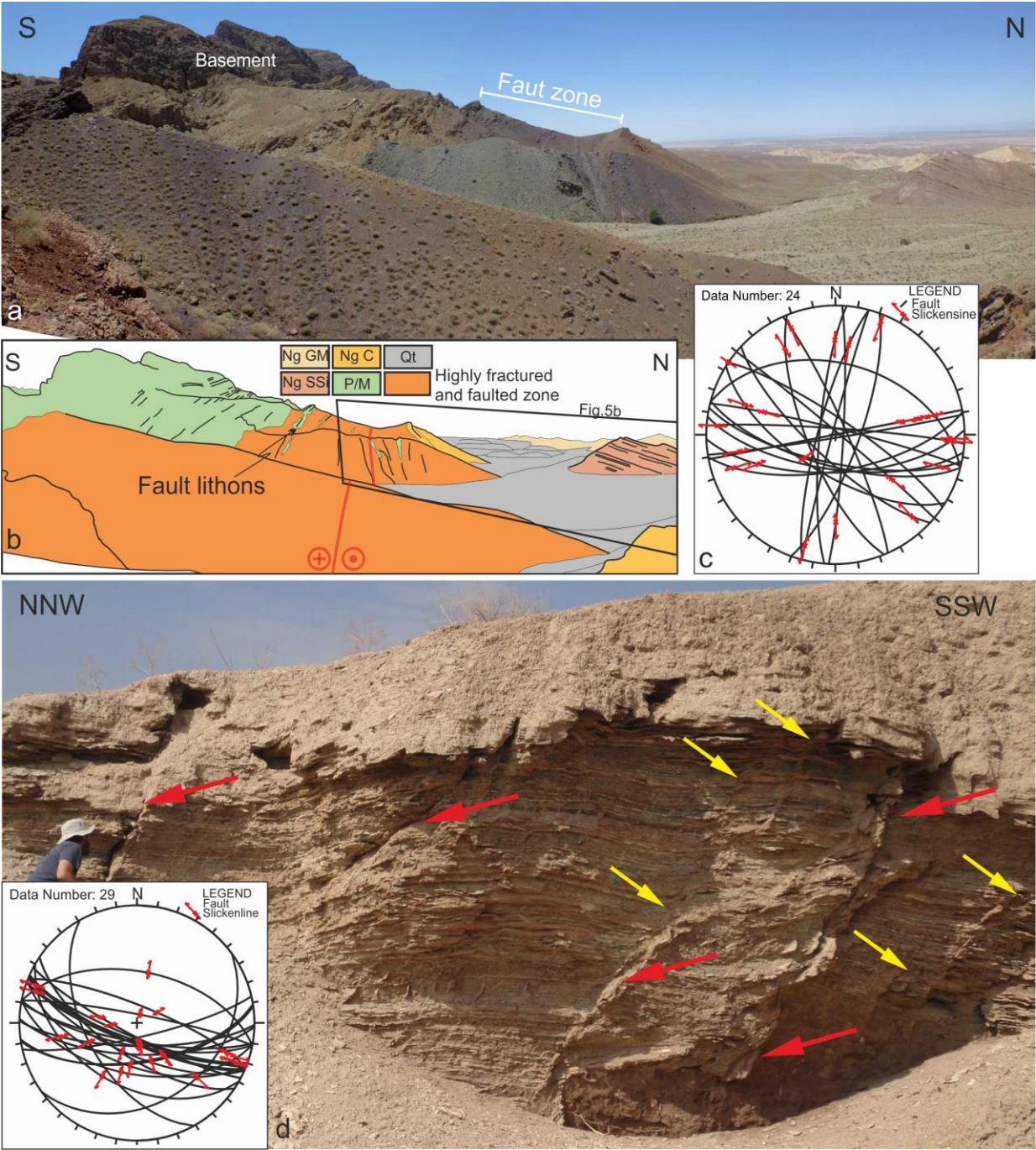


Figure 7

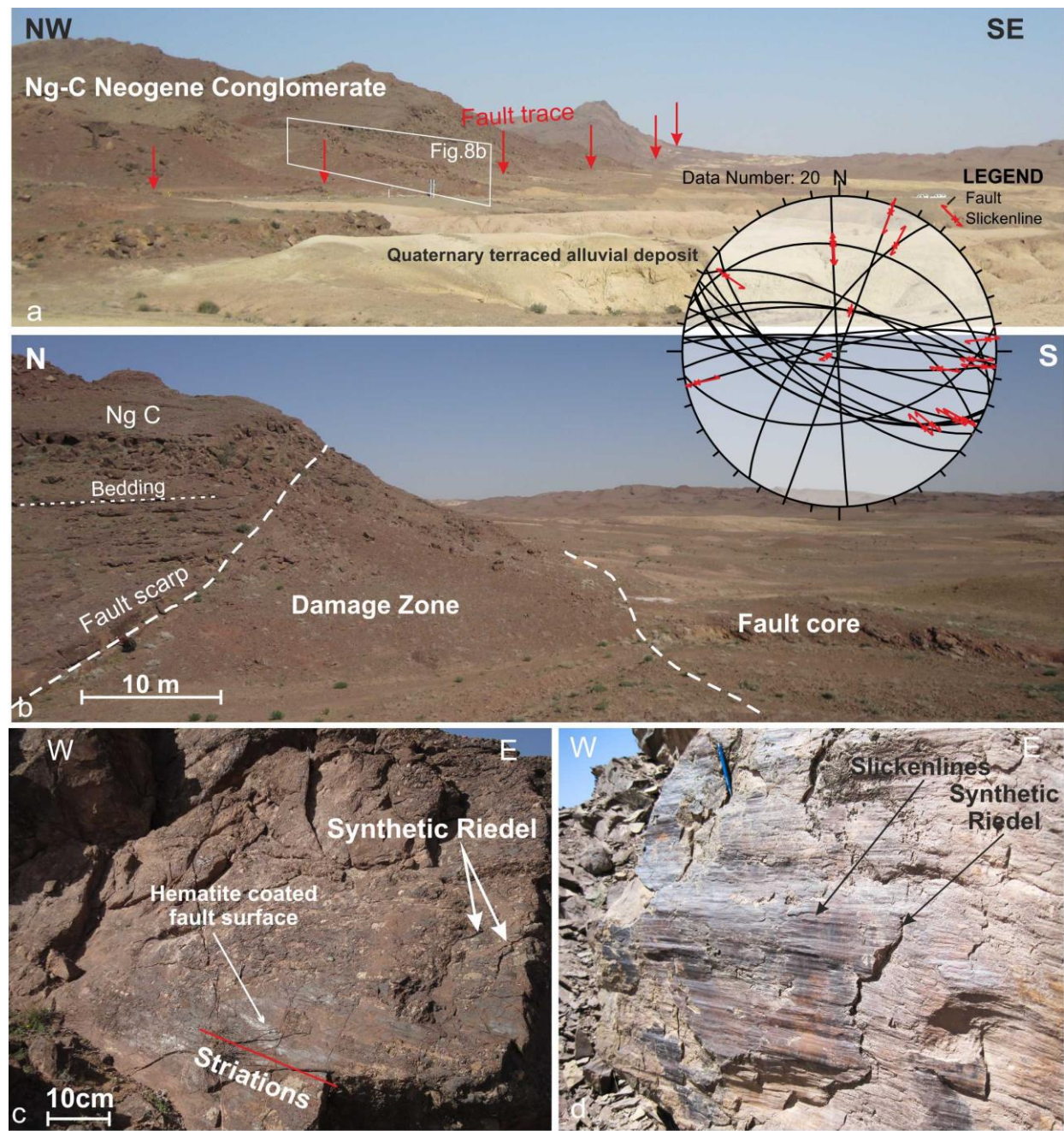


Figure 8

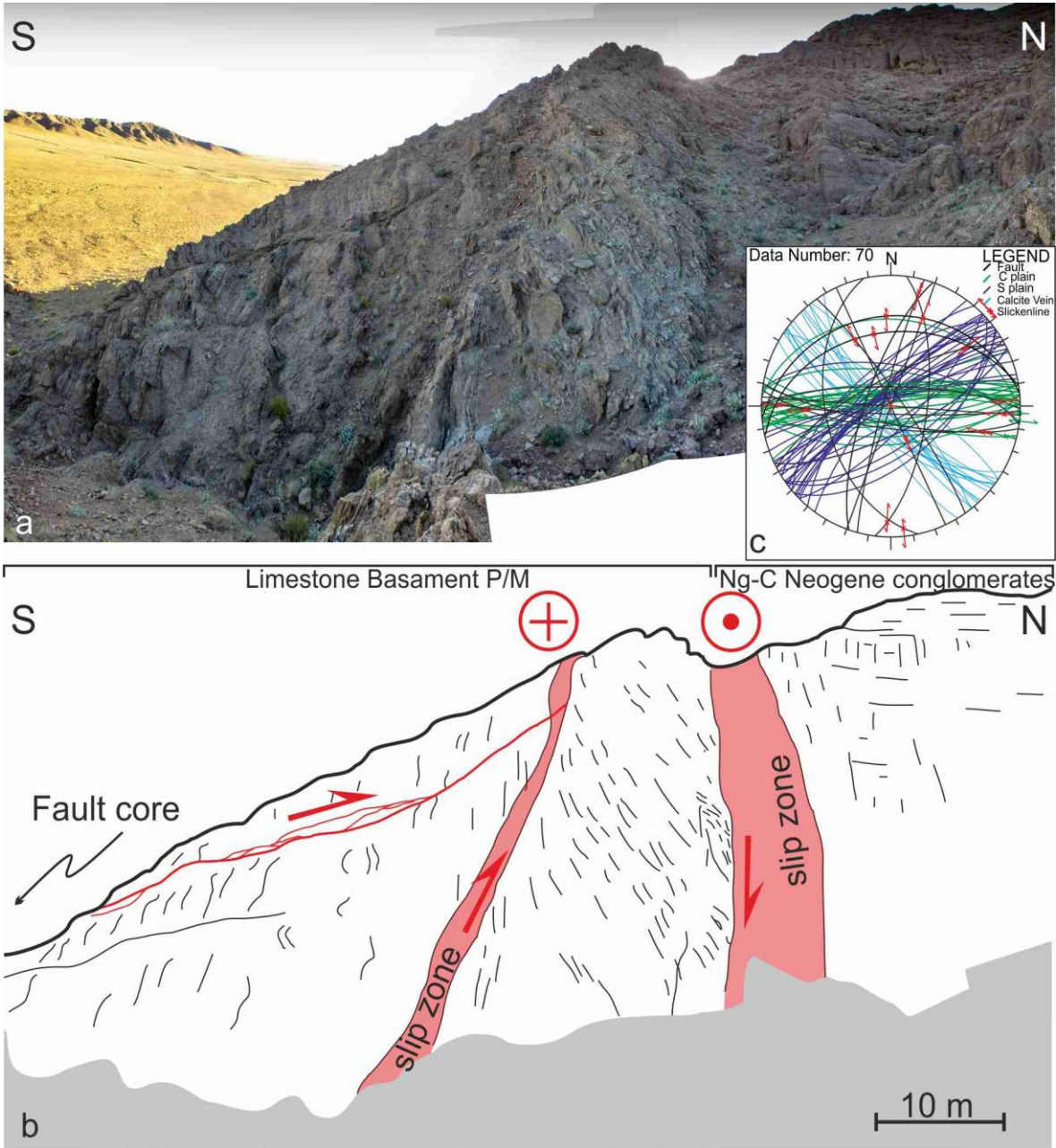


Figure 9

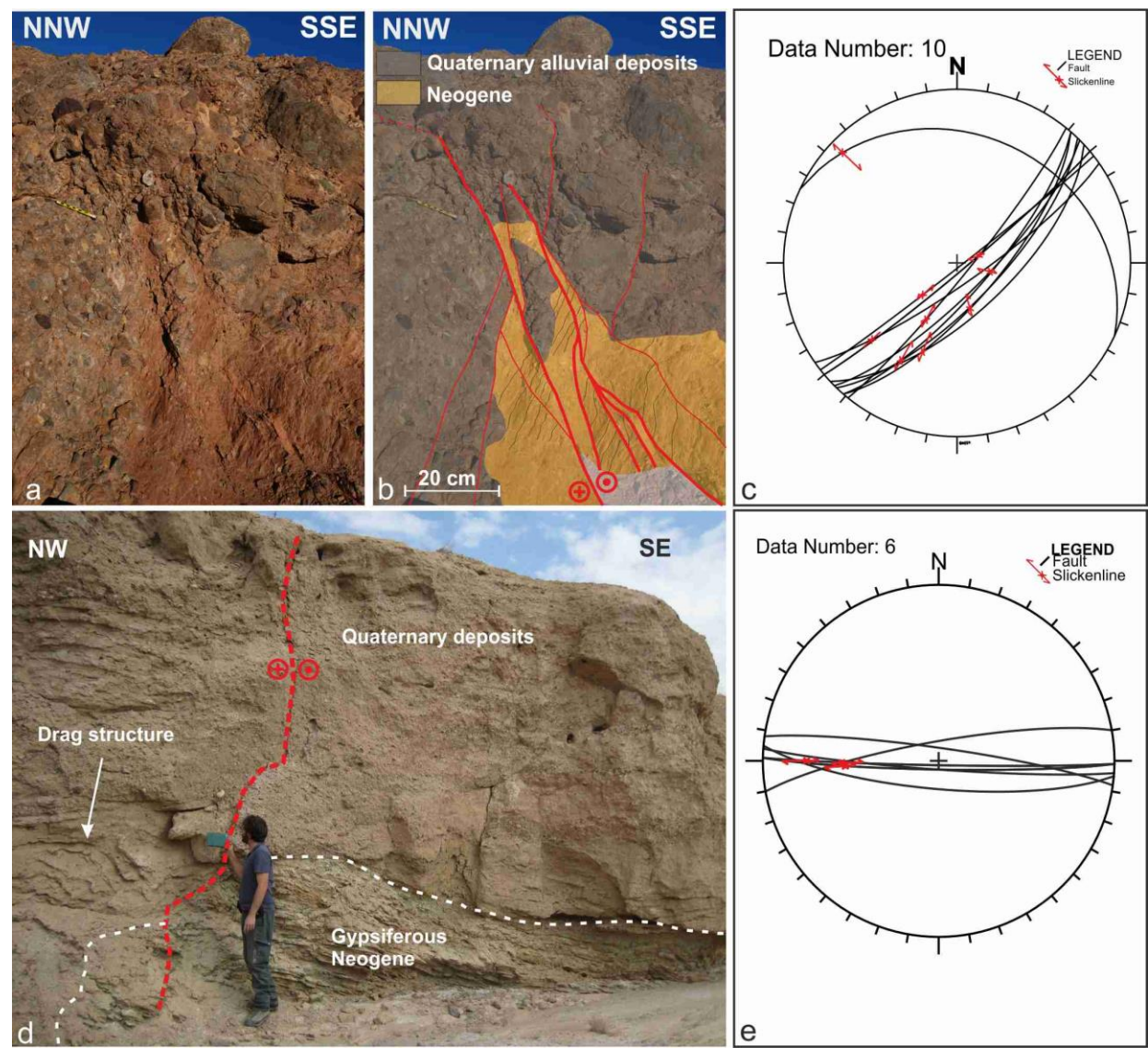


Figure 10

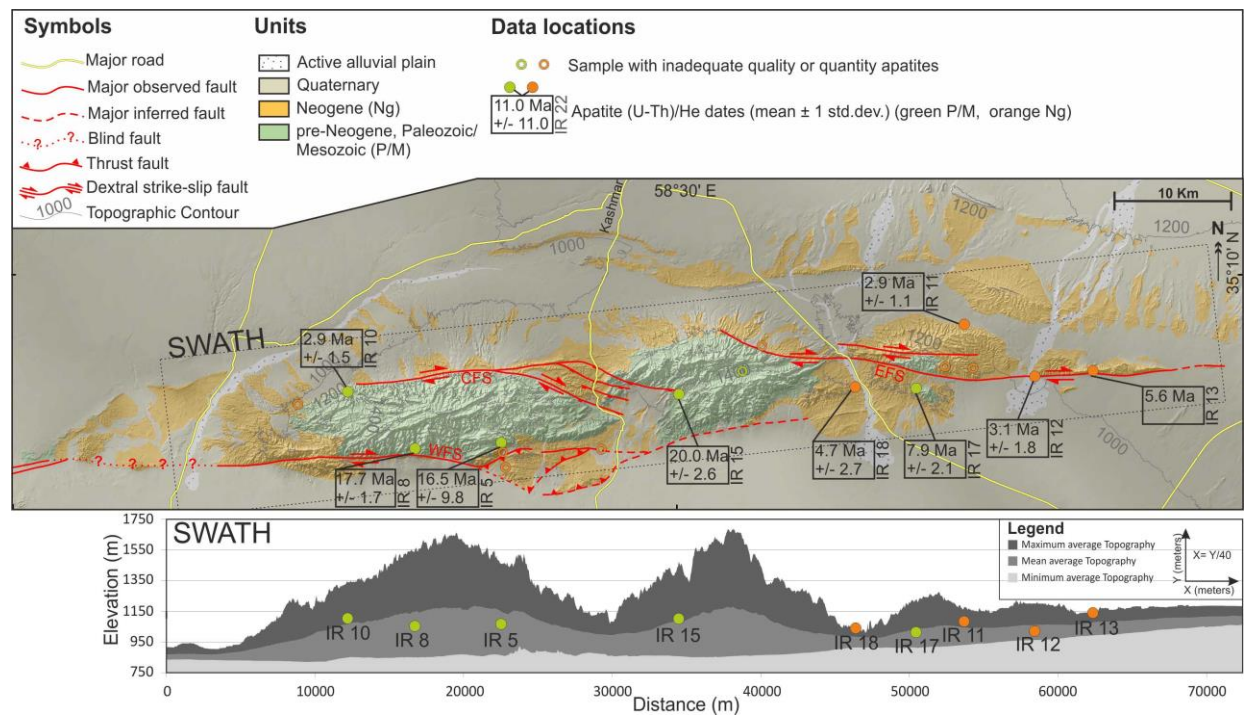


Figure 11

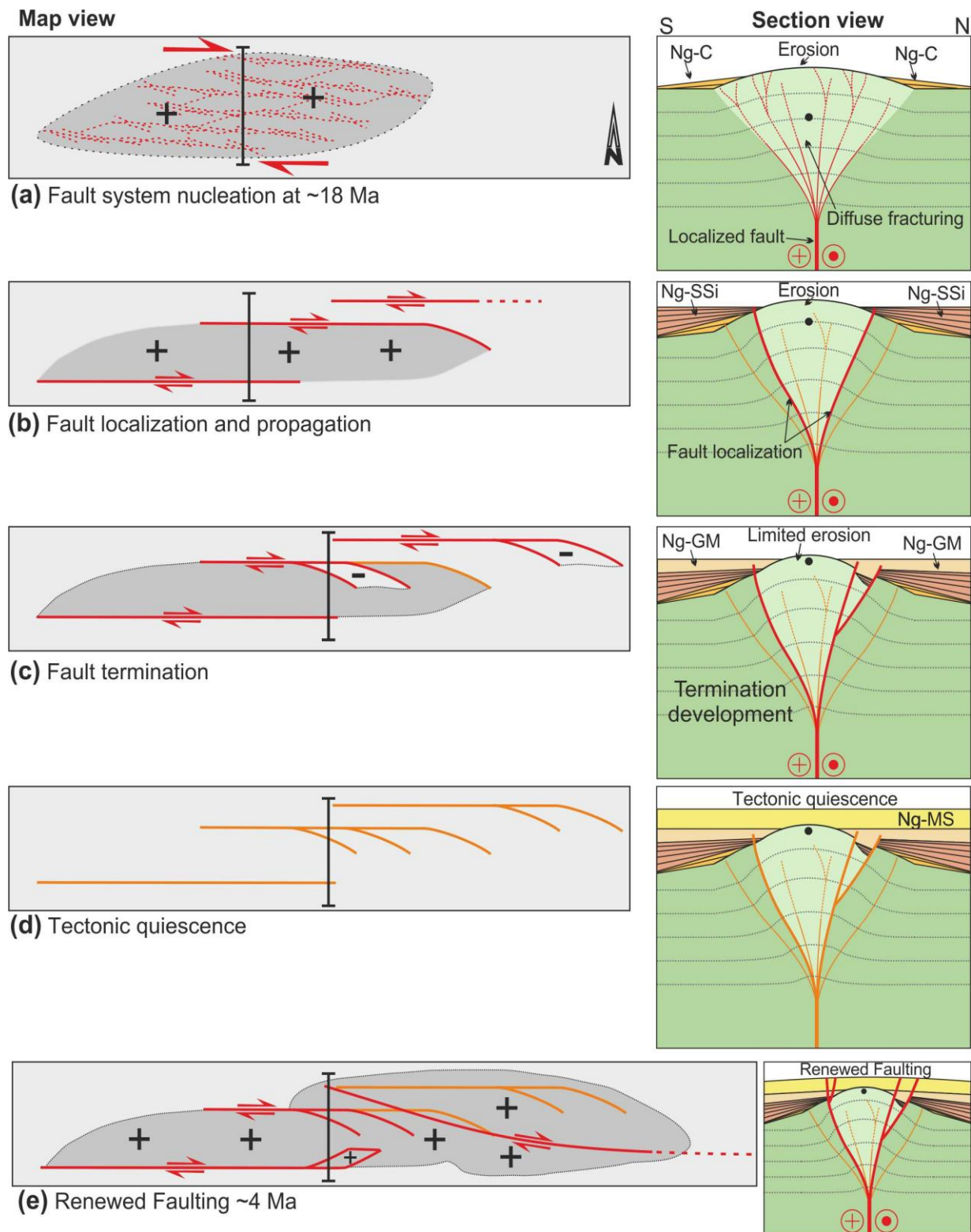


Figure 12

FIGURE CAPTIONS

Figure 1. Simplified tectonic map of Iran, showing the main collisional and intraplate strike-slip fault domains accommodating the Arabia-Eurasia convergence (modified after Berberian and

King, 1981). The dashed rectangle indicates the study area. DBF: Dasht-e-Bayaz Fault; DF: Doruneh Fault; DSF: Dehshir fault; KKF Kalmard-Kuhbanan Fault, KSF: Kuh-e-Sarhangi Fault; MZT: Main Zagros Trust; NBF: Nayband Fault; NHF: Nehbandan fault; SBF: Shahr-e-Babak Fault; ZMTZ: Zagros-Makran Transfer Zone. The inset shows GPS velocities vectors in Iran relative to stable Eurasia (Vernant et al., 2004).

Figure 2. Simplified tectonic map of northern Central Iran, showing the historical and instrumental seismicity of the area. Focal mechanisms are taken from the Harvard catalog (<http://www.globalcmt.org/CMTsearch.html>). Epicentres are from the ISC EHB Bulletin (International Seismic Centre, Thatcham, United Kingdom, 2009, <http://www.isc.ac.uk>) and earthquake catalogue at Iranian Institute of Earthquake Engineering and Seismology; <http://www.iiess.ac.ir>. The white rectangle indicates the location of the study area and the extent of the map in Figure 3.

Figure 3. Structural map of the study area and interpretative geological cross-section (solid lines) across the structure of the Kuh-e-Faghan Fault. The inset shows the cumulative structural data set showing the bedding attitude (projected as pole to plane on a Schmidt net, lower hemisphere projection), in the Neogene deposits and the Cumulative polymodal Gaussian statistics (with errors quoted at 1σ (sd) level) as obtained from the collected fault population. Results are shown as rose diagram for strikes, and frequency distribution histograms for dip and slickenline pitch values (Data processing through the software DAISY3 (Salvini, 2004; <http://host.uniroma3.it/progetti/fralab/>).

Figure 4. Generalized vertical stratigraphic section of the Neogene deposits for the northern (a) and southern (b) sector of the study area. The series of stick-logs report the unit thicknesses measured along the relative geological cross-sections shown in Figure 3. Scale and legend in (a) apply to both figures.

Figure 5. (a) Panoramic view of Cycle-1 deposits onlapping onto the Paleozoic and Mesozoic basement. Note the angular contact between the basal breccias (Ng-B) and the upper Ng-C fluvial conglomerates. Insert showing deposits characteristics. Cycle-3 onlaps directly onto cycle-1. (b) Panoramic view showing the three sedimentary cycles and their stratigraphic relations. The fault trace of the CFS is marked by red arrows. (c) Progressive angular unconformities within Cycle-2. The inserts show the range of sedimentary structure, observed within Cycle-2 attesting for its fluvio-palustrine depositional environment. (d) panoramic view showing Cycle-3 onlapping directly onto

the Paleozoic and Mesozoic basement units. Bedding strike and dip measurement are marked by white dots. The inserts shows the range of sedimentary structure observed within the basal unit of Cycle-3 attesting for its lacustrine/playa lake depositional environment. White dotted line shows the contact between Neogene sediments and basement units. See Figure 3 for location.

Figure 6. Structures along the WFS. (a) Panoramic view (looking eastward), showing the core of the antiformal structure defined by the structural arrangement of the Neogene conglomerates (Ng-C). Note steepening of the southward limb approaching the WFS trace. The fault zone is defined by verticalized panels of cataclastic conglomerates (Ng-C) in tectonic contact with the gypsiferous marls (Ng-GM). The stereoplot (Schmidt net, lower hemisphere projection) details the collected fault data set. (b) The eastward termination of the WFS. Panoramic view (looking westward), showing the sub-vertical, ~400 meter thick damage zone associated with the NE bending of the WFS, which abruptly interrupts the monoclinial attitude of the Ng-C deposits. The fault zone involves the Quaternary alluvial and terraced deposits. (c) Hectometer-scale drag folding along a major dextral transpressive fault strand and interpretative line drawing (d) affecting the Ng-C deposits when approaching the trace of the WFS. The fold is E/SE-plunging with an axial trace at an angle to the fault trace. (e) Stereoplot (Schmidt net, lower hemisphere projection) showing the collected fault data. Fault slip is dominated by dextral and reverse kinematics along NE-SW striking, steeply dipping fault strands. See Figure 3 for location of the field pictures.

Figure 7. Structures along the WFS. (a) The basement-Neogene fault contact along the western tip of the CFS (looking westward). (b) Interpretative line drawing of Figure 8a, showing the fault zone architecture and fault zone localisation along the verticalized weaker basement shale units. (c) The stereoplot details the collected fault data set (Schmidt net, lower hemisphere projection). (d)-(e) Mesoscale NW-SE striking fault systems in the Ng-GM deposits along the eastward termination of the WFS. Note the syn-sedimentary character of faulting: the faults (red arrow) die out upwards into the sediments (yellow arrow), which are progressively sealed. The stereoplot (Schmidt net, lower hemisphere projection) details the collected fault data set. WNW-ESE right-lateral and oblique (transtensional)- and normal-slip faults are observed. See Figure 3 for location of field pictures.

Figure 8. Panoramic view (looking northeastward) of the prominent break in slope that defines the trace of the EFS, bounding Neogene (Ng-C) and Quaternary deposits. (b) Structural architecture of the fault zone across the EFS, exhibiting pluridecameter-thick, sub-vertical damage zone and fault core. The stereoplot shows the collected fault data set (Schmidt net, lower hemisphere

projection). Faulting is dominated by WNW-ESE striking right-lateral faults associated to minor antithetic NNE-SSW striking left-lateral ones (c)-(d) Examples of polished, E-W striking, hematite-coated fault surfaces, exhibiting prominent sub-horizontal striations. The kinematic indicators as provided by synthetic Riedel shears, lunate fractures and abrasion steps attest for right-lateral kinematics. See Figure 3 for location of field pictures.

Figure 9. Field example of S-C fabric development along the main trace of the EFS. (a) Outcrop-scale and schematic line drawing (b) showing S-C tectonites developed along the main trace of the EFS bounding the basement-Neogene (Ng-C) contact (See Figure 3 for location of field picture). Note the occurrence of meter-thick, E-W striking sub-vertical ultracataclastic right-lateral slip zones that bound the main fault rock types. (c) Stereoplot (Schmidt net, lower hemisphere projection) showing the angular relationships between the S-C fabrics, the vein array and the main strike-slip fault surfaces, compatible with overall right-lateral shear.

Figure 10. Quaternary faulting. (a) Outcrop picture and line drawing (b) showing fault strands cutting through the Neogene (Ng-C) and the overlying Quaternary alluvial deposits shown in Figure 6b. (c) Stereoplot showing the collected fault data (Schmidt net, lower hemisphere projection) set in the locality of Figure 10a. The faults strike NE-SW and show dextral and reverse kinematics. Steeply-dipping NE-SW right-lateral and reverse faults cutting through and involving Neogene and Quaternary deposits. (d) E-W striking right-lateral fault cutting through alluvial Quaternary deposits overlying Ng-Gm deposits. (e) Stereoplot showing the collected fault data (Schmidt net, lower hemisphere projection) set in the locality of Figure 10d. See Figure 3 for location of field pictures.

Figure 11. Structural map of the Kuh-e-Faghan Fault on shaded Topographic Elevation Model, showing location of the samples used for AHe thermochronology, together with mean age results from each sample indicated (see Table 1). Distribution of AHe sample elevations and ages projected to an alongs-strike topographic SWATH profile (40 times vertical exaggeration) along the KFF.

Figure 12. Conceptual spatio-temporal model for the long-term evolution of the Kuh-e-Faghan right-lateral fault system (see text for further details). Key to the figure: dark grey areas with plus (+), uplift; light grey areas with minus (-), subsidence; red, active fault; orange inactive fault. For lithological symbols refer to Figure 3.

Appendix D: Manuscript to be submitted to Tectonics**DECIPHERING TECTONIC VS CLIMATIC FINGERPRINT IN THE QUATERNARY GEOMORPHIC SIGNAL OF THE NORTH-WESTERN EDGE OF THE LUT BLOCK (CENTRAL IRAN)**

Gabriele Calzolari⁽¹⁾, Marta Della Seta^{(2)*}, Federico Rossetti⁽¹⁾, Reza Noazem⁽³⁾, Gianluca Vignaroli⁽¹⁾, Domenico Cosentino⁽¹⁾, Claudio Faccenna⁽¹⁾

¹Dipartimento di Scienze, Università Roma Tre, Largo S. L. Murialdo 1, 00146 Roma, Italy

²Dipartimento di Scienze della Terra, "Sapienza" Università di Roma, Piazzale Aldo Moro 5, 00185 Rome, Italy

³Department of Geology, Imam Khomeini International University, 34149-16818 Qazvin, Iran

ABSTRACT

Intraplate Central Iran provides ideal sites to study the topographic and geomorphic response to the nucleation and propagation of faulting, due to the development and preservation of spectacular tectonic landforms. Recent works documented Neogene to Quaternary right-lateral strike-slip tectonics along two major fault systems in the north-western edge of Lut Block. Nevertheless, the Quaternary faulting, its space-time relationships and the landscape evolution in response to climatic and tectonic forcing are still not detailed in this area. This work provides constraints on: (i) topographic inheritance of the long term (Myr) punctuated history of fault nucleation, propagation and exhumation along the north-western edge of Lut Block; (ii) Late Quaternary climatically-controlled aggradation phases, responsible for three generations of alluvial landforms at ~53, ~25 and ~6 ka; (iii) tectonic control on pediment formation and alluvial fan architecture; (iv) minimum Holocene age of Quaternary right-lateral strike-slip faulting; (v) age of alluvial landforms then used as geomorphic markers of Late Quaternary to Holocene fault-related uplift.

Spatial and temporal constraints on the Quaternary activity of the right-lateral strike-slip deformation zone at the northern edge of the Lut Block impose consideration of a new kinematic model for active faulting in Central Iran. Crustal thickening and micro-block lateral extrusion during ongoing Arabia-Eurasia collision may provide a feasible scenario in alternative to rigid block rotation.

INTRODUCTION

Crustal deformation in tectonically active regions produces topographic perturbations on the Earth's surface at multiple spatial scale, through isostatic/dynamic-, fold- or fault-related uplift/subsidence. Geomorphic processes tend to counterbalance the growth of topographic perturbations, over time scales that depend on the wavelength of the morpho-structures as well as on climate changing over space and time (Burbank, 1992; Burbank et al., 1996; Whipple and Tucker, 1999; Whipple, 2001; Montgomery et al., 2001; Mitchell and Montgomery, 2006). Roe et al. (2006) defined climate, erosion and tectonics as a "triumvirate" that control rock and surface uplift in mountainous terrains. Furthermore, the scientific literature on this topic outlined clearly that they also interact through mutual feedback relationships (Morisawa and Hack, 1985; England and Molnar, 1990; Whipple and Tucker, 1999; Willet et al., 2006; Wegmann and Pazzaglia, 2009).

Over decadal time scales the rate of crustal deformation can be directly monitored through geodetic techniques, both satellite-based such as D-InSAR (i.e. Massonnet et al., 1993) and GPS (i.e. Serpelloni et al., 2013) and ground-based such as TLS (i.e. Wilkinson et al., 2010). The record of longer-timescale deformation is instead encoded in geological and/or geomorphic signatures that, however, encompass the time/space superimposition of climatic and tectonic inputs (Bull, 1991, 2009; Merritts et al., 1994; Bridgland and Westaway, 2008).

The geomorphic signature of crustal deformation can be best decrypted over the kyr time scale, at which erosion/deposition rates, drainage network geometry, longitudinal river elevation profiles, and topography all reflect the interaction between surface uplift rate and the dynamics of Earth surface processes. Drainage network provides the most rapid response to topographic perturbations (Jackson et al., 1996; Whipple, 2004; Castelltort et al., 2012; Royden and Perron, 2013; Willett et al., 2014) and their deposits record information about climate (Bull 1977; Ritter et al. 1995; Frostick and Reid 1989; Harvey 2003). Feedback in river dynamics occur since changes in base level can

be driven not only by tectonics (rock uplift) and climate (eustasy) but also by drainage re-organization (i.e. Whipple, 2004; Castelltort et al., 2012; Fubelli et al., 2014). Moreover, fault-offset along rivers have been widely used to quantify localized deformation (Allen, 1965; Replumaz et al., 2001; Hubert-Ferrari et al., 2002; Walker and Jackson, 2002) as well as statistical progressive rotation of streams crossing fault zones have been used to infer fault kinematics (Belisario et al., 1999).

Due to the increasing availability of remotely sensed data, considerable focus is set on the processing of high-resolution DEMs to extract topographic and morphometric information about landforms (Tarboton et al., 1991; Whittaker et al., 2008). For the estimation of morpho-evolution rates in response to tectonics and climate geomorphic markers are widely used (Rockwell et al., 1984; Molnar et al., 1994; Di Bucci et al., 2003; Schiattarella et al., 2006; Della Seta et al., 2008; Troiani and Della Seta, 2008, 2011; Pérez-Peña et al., 2009; Gioia et al., 2014; Giano et al., 2014). They are represented by areal and/or linear landforms that display: i) a known initial, undeformed geometry; ii) a known age; iii) high preservation potential with respect to the time scale of the tectonic processes being studied (Burbank and Anderson, 2012). By examining the plano-altimetric configuration of geomorphic markers, qualitative and/or quantitative tools for isolating the topographic effects ascribable to active tectonics have been developed (Keller and Pinter, 2001; Troiani and Della Seta, 2008; Pedrera et al., 2009) also through the geostatistical analysis (Johansson, 1999; Troiani and Della Seta, 2011; Gioia et al., 2014).

For a correct use of geomorphic markers, it is very important the contribution of both detailed geomorphological surveys and advanced geochronological methods (i.e. cosmogenic and OSL dating) able to provide even more significant constraints for the analysis of the morpho-evolution rates and their variability over different paleoclimatic frames. In addition to methods based on the estimation of erosion/deformation rates from geomorphic markers (Pérez-Peña et al., 2009; Gioia et al., 2014), the geomorphic response to tectonic perturbations can be quantified through river incision rates (Stock and Montgomery, 1999; Whipple and Tucker, 1999; Lavé and Avouac, 2001; Brocard et al., 2003; Burbank et al., 1996; Pederson et al., 2006; Whittaker et al., 2007; Finnegan et al., 2014) or through near-surface erosion rates obtained by cosmogenic nuclides techniques (Brown et al., 1995; Cyr et al., 2010).

Intraplate Central Iran provides ideal sites to study the topographic and geomorphic response to the nucleation and propagation of faulting due to the development and preservation of spectacular tectonic landforms. Recent works documented Neogene to Quaternary right-lateral strike-slip tectonics along the NE-SW Kuh-e-Sarhangi Fault (Nozaem et al., 2013) and the E-W Kuh-e-Faghan Fault (Calzolari et al., submitted) on the north-western edge of Lut Block (Fig. 1). Although evidence of Quaternary faulting was documented, age of Quaternary faulting, its space-time relationships and the associated landscape evolution are not detailed. Characterization of these aspects may provide a clue for understanding feedback relationships among tectonics, surface processes and climate within an active intraplate deformation zone.

Focusing on the Kuh-e-Faghan Fault system, this paper aims at: (i) defining the topographic and geomorphic signature of Quaternary faulting along the north-western edge of the Lut Block; (ii) constraining the temporal fault activity along the Kuh-e-Sarhangi Fault and the E-W Kuh-e-Faghan Fault systems; and (iii) discussing the tectonic vs. climatic fingerprints in the Quaternary landscape evolution. To accomplish these aims we perform: (i) topographic analysis to outline the surface evidence of ongoing crustal deformation; (ii) field structural and geomorphological surveys, integrated with aerial photo interpretation, to define the different generations of Quaternary landforms and sediments and to reconstruct their depositional architecture; (iii) OSL dating of Quaternary deposits to correlate them with regionally constrained ones, to use the associated landforms as suitable geomorphic markers and to provide a minimum age constraint to Quaternary faulting; and (iv) morphometric analyses on geomorphic markers to unravel the tectonic fingerprint in Quaternary landscape evolution.

GEOLOGICAL BACKGROUND

The Arabia-Eurasia convergence, which culminated with the continental collision at the Eocene–Oligocene boundary (e.g. Jolivet and Faccenna, 2000; Allen et al., 2004; Agard et al., 2011; Mouthereau et al., 2012), is responsible for the spectacular Cenozoic crustal deformation in Iran (Hatzfeld and Molnar, 2010). The convergence is still ongoing as testified by the GPS velocity vectors (Fig. 1) indicating a NNE motion of the Arabian plate relative to Eurasia of ~25 mm/yr (Sella et al.,

2002; McClusky et al., 2003; Nilforoushan et al., 2003; Vernant et al., 2004; Reilinger et al., 2006; Walpersdorf et al., 2014). Such convergence is mostly accommodated through contractional deformation affecting the Zagros, Alborz, Kopeh Dagh and Talesh regions (Allen et al., 2004; Hatzfeld and Molnar, 2010; Jackson et al., 1995; Talebian and Jackson, 2002, 2004; Walker and Jackson, 2004) (Fig. 1). These mountain ranges bound the Central East Iran Microcontinent (CEIM), which consists of a mosaic of continental blocks (Yazd, Tabas and Lut in Fig. 1) (Aghanabati, 2004), which are bounded by linear mountain-belts developed along major strike-slip fault zones that have peculiar stratigraphy, deformation style, and pattern of recent seismicity (Berberian and King, 1981; Berberian, 2014). Active strike-slip fault systems bounding the CEIM accommodate its differential motion that according to recently published GPS data is moving northward at 6–13 mm/yr with respect to the stable Afghan crust at the eastern edge of the collision zone (Walpersdorf et al., 2014; Fig. 1a). These fault systems are organized into N-S dextral (from west to east: the Deshir, Anar, Nayband–Gowk, and Nehbandan faults) and E–W sinistral (from north to south: Doruneh and Dasht-e Bayaz faults) shears (Fig. 1a) and the kinematics and total cumulative shear along the active strike-slip fault systems have been detailed, using both geological and geomorphic displaced markers from satellite imagery (Walker and Jackson, 2004; Allen et al., 2004; Allen et al., 2011; Farbod et al., 2011). Taking into account the present-day slip rates (~2–10 mm/yr) along the major fault systems, the onset of strike-slip tectonics is inferred to date back to ~5 Ma (Allen et al., 2004). Destructive earthquakes occurred in Central Iran in recent years and last century (e.g. Tabas in 1979, $M_s=7.7$; Dasht-e Bayaz in 1979, $M_w=7.1$; Bam 2003, $M_w=6.5$), testifying for the high seismicity and active tectonics along these fault strands (Hessami et al., 2003).

The Tabas and Yazd blocks are separated by a nearly 600 km long, arcuate and structurally complex fault-bounded belt known as the Kashmar–Kerman Tectonic Zone, where remarkable exposures of the deeper sections (upper Neoproterozoic to lower Paleozoic in age) of the central Iran basement occur (Ramezani and Tucker, 2003; Rossetti et al., 2014). In a recent study, Nozaem et al. (2013) proposed post-Neogene to Quaternary tectonic reactivation of the Kashmar–Kerman Tectonic Zone along the Kuh-e-Sarhangi Fault (KSF) as a major right-lateral strike-slip fault. Furthermore, right-lateral strike-slip faulting was recently documented also for the Kuh-e-Faghan Fault system (KFF) to the east of the KSF (Calzolari et al., submitted; Figs. 1 and 2). The KSF and KFF are located ~40 km south of the sub-parallel, active left-lateral Doruneh Fault (Tchalenko et al., 1973; Fattahi et al., 2007; Farbod et al., 2011; Figs. 1 and 2). Javadi et al. (2013) documented a polyphase kinematic history for the Doruneh Fault, with a major change from right- to left-lateral during the late Miocene-early Pliocene times. The seismicity of the KSF-KFF area (Fig. 1b) is poorly known, although already discussed by Berberian (1976, 1977), who generally describes the KSF as a Quaternary fault. Some earthquake epicenters have been localized in the KSF area, with maximum recorded magnitude between 4 and 5 and focal depths less than 30 km. The only focal mechanism solution available is located ~40 km southward, where right-lateral strike-slip kinematics sub-parallel to the strike of KSF has been reported (Farbod et al., 2011). As for the seismicity of the KFF area, several historical earthquake epicenters are located along the KFF, with maximum recorded magnitude between 6 and 7 and maximum focal depths between 35 and 70 km.

Neogene to Quaternary tectonic and geomorphological setting

The KSF-KFF deformation zone defines a segmented linear, ~150 km long, topographic relief, with elevations up to ~1800 m that elevates from the Quaternary alluvial deposits of the Kavir-e-Namak (southern) and Kavir-e-Kaj (northern) plains. The overall fault zone architecture is dominated by distributed and partitioned right-lateral strike-slip tectonics that operated along a main SW-NE to E-W striking displacement zone (Nozaem et al., 2013; Calzolari et al., submitted; Figs. 1 and 2). The axial zone of the KSF-KFF deformation zone is made up of Neoproterozoic and Paleozoic–Mesozoic basement units (Eftekhar-Nezhad et al., 1977; Ruttner et al., 1970; Sahandi et al., 2010; Nozaem et al., 2013; Rossetti et al., 2014) in fault contact with the Neogene and Quaternary deposits of the Kavir plains (Fig. 2).

The field evidence documents that the main fault slip occurred in pre-Quaternary times, with major fault damage zones developed within the Neogene units. Two major episodes of fault-related exhumation, in Early Miocene (~18 Ma) and Early Pliocene (~4 Ma) were evidenced by apatite U-Th/He thermochronology along the KFF that, along with stratigraphic and structural data indicated the KFF system nucleated in the west and propagated eastward (Calzolari et al., submitted). A

source-to-sink scenario was reconstructed for the first faulting/exhumation episode and is chiefly recorded by the structural and depositional architecture of the Neogene deposits widely outcropping along the KFF. The second faulting episode at ~4 Ma, caused the final fault zone exhumation and the current fault zone architecture. Nonetheless, significant fault activity occurred during the Quaternary, with overall fault-fracture pattern coherent with right-lateral wrenching (Nozaem et al., 2013; Calzolari et al., submitted; Fig. 2).

The KSF-KFF deformation zone is surrounded by bajadas made of different generations of Quaternary alluvial fans and alluvial plain deposits. These deposits lie upon a regional erosional surface (paleo-pediment) cutting through the strongly tilted Neogene units (Fig. 2). The Quaternary morpho-evolution is in fact likely dominated by the erosion/deposition dynamics of the drainage network developed on these fault-controlled ridges. In such a climatic environment, alluvial fan and alluvial plain development is generally spectacular due to: (i) lack of vegetation cover favoring channel shifting; (ii) occasional thunderstorms capable of revitalizing the streams allowing them to evacuate large volumes of sediments; (iii) availability of large quantities of debris produced by weathering processes (Bull, 1977; Cooke et al., 1993; Harvey, 1997). Although in the present KFF desert environment the entire drainage network is ephemeral, its dynamics developed over a climate-changing time span and was controlled by changes in local base levels, likely controlled by tectonics and drainage re-arrangement.

Similar alluvial fans have been interpreted as having developed during Quaternary cold periods as described by Beaumont (1972) for the southern piedmont of the Alborz Mountains, and Dufaure et al. (1978) for the Zendan fault area in southeast Iran. Recently, Walker and Fattahi (2011) reviewed the late Quaternary deposits of eastern Iran. The authors recognized that several generations of telescopic alluvial fans, as well as regional arrangement of river terraces and lake deposits could be explained by Late Pleistocene and Holocene environmental changes with aggradation phases occurring between ~30 and 13 ka and between ~9 and 7 ka, alternating with erosive phases, all controlled by regional climatic forcing. As for the erosive phases, in-situ produced cosmogenic ^{10}Be provided surface abandonment ages for different Quaternary alluvial surfaces in the Hormoz Strait area at 5.6 ± 0.6 ka (offset of the mid-Holocene humid period), 8.4 ± 1.0 , 12.8 ± 1.0 ka (onset of the dry Younger Dryas cold and dry episode), 20.1 ± 1.5 (end of the Last Glacial Maximum), and 44.0 ± 3.4 ka (Regard et al., 2006). Similar generations of alluvial fans have been recognized in the neighbor regions (Foroutan et al., 2014) and IRSL (infrared stimulated luminescence) age of <10 ka was obtained for the deposition of the Shesh–Taraz fan along the Doruneh fault (Fattahi et al., 2007).

TOPOGRAPHY OF THE KFF

The KFF deformation zone defines an E-W oriented, up to 17 km wide, linear ridge reaching a maximum elevation of ~1700 m and thinning out to the east. The KFF associated ridge can be subdivided into two main topographic domains (Fig. 3a). The ~42 km long western domain prominently elevates above the southern Kavir-e-Namak salt plain, with the axial region characterized by rugged and steep terrains (slope angle $>15^\circ$; Fig. 3b) and high local relief (>100 m; Fig. 3c). Peripheral areas are characterized by less elevated and gentler dipping terrains (slope angle $\sim 2\text{--}5^\circ$) with lower local relief (<50 m) (Fig. 3c) mostly corresponding to the bajadas of Quaternary alluvial fans. The boundaries between axial and peripheral areas of such domain are marked by sharp breaks in slope in correspondence of the fan apexes (Fig. 3b), which are located close to the main fault strands, hereafter referred as the western (WFS), the central (CFS) and eastern (EFS), respectively (Figs. 2 and 3a).

The linear topography of the western domain is internally interrupted by a low relief area, which dissects the ridge from north to south in a jagged fashion. This low relief area matches the lozenge-shaped transtensional basin developed by the four main fault segments of the SE-ward bending termination of the CFS, filled by Neogene deposits (Fig. 2). The ~23 km long eastern domain is bounded to the south by the EFS and shows an overall eastward narrowing and decreasing in elevation and relief (Fig. 3). It is dissected by a southward draining active alluvial plain, which separates two sub-domains characterized by different topographic characters. To the west a broadly E-W elongated oval relief, ~10 km long and 3.5 km wide, shows discontinuous E-W oriented narrow ridges and associated valleys. To the east, a very narrow ~10 km long, E-W oriented linear ridge, marks the termination of the KFF. The whole KFF ridge shows a prominent, roughly E-W oriented

divide that separates a broader and gentler northward draining slope from a narrower and steeper southward draining slope (Fig. 3d).

The local-scale topographic filtering (see Appendix for methods adopted) quantifies the wavelength of the above described topographic domains, which mirror the eastward increase in shear localization within the main fault zones (Fig. 4). The western topographic domain starts to get picked up with the 10-km filter, while the eastern topographic domain has a 2-km wavelength.

The above evidence are confirmed by the topographic data of the longitudinal swath profile (SWP5 in Fig. 5). This swath profile outlines very well the above described, fault-bounded longitudinal topographic domains. The western one shows higher maximum topography, relief and a quite constant base level (minimum topography). The eastern topographic domain is characterized by an overall eastward decrease in the maximum topography and relief, likely due to the eastward lowering ratio between surface- and rock uplift in response to the higher erodibility of the Neogene sediments outcropping to the east, with respect to the basement units outcropping to the west. Furthermore, an eastward increase of minimum topography of the range was observed, that corresponds to a progressively higher (i.e. transient) base level of erosion (roughly corresponding to the paleo-pediment unconformably cutting the Neogene units).

The four across-strike oriented swath profiles outline the local topographic signal of the KFF and Doruneh Fault, marked by sharp breaks in local relief (Fig. 5). Furthermore, they show that in the western part of the KFF the northern base level of the ridge is a well-developed flattish alluvial plain up to 170 m higher than the southern alluvial plain (Fig. 5). These plains are bordered by slightly-dipping alluvial fan systems which connect them to the slopes of both the Doruneh fault-related ridge and the KFF western topographic domain. Such alluvial plains progressively disappear eastward, where the more elevated paleo-pediment sculpted in the Neogene units (Fig. 2) is partly covered by a southward dipping bajada of alluvial fans, likely fed only by the Doruneh fault-related ridge.

GEOMORPHIC SIGNATURE OF THE KFF

Evidence of drainage network evolution

Although in the present KFF desert environment the entire drainage network is ephemeral, its dynamics developed over a climate-changing time span. Moreover, in a landscape far from the sea and dominated by the growth of fault-related linear ridges, separated by intermontane basins, drainage system re-arrangement was most likely controlled by local base levels (Jackson et al., 1996; Bennett et al., 2006), given by the two northern- and southern large plains, bounding the ridge, with a maximum difference in elevation of ~170 m in the west and progressively waning eastward. Presently, the northern plain is drained by two major competing rivers, that in their middle reaches cut into the ridge. This configuration is likely due to stream piracy operated by the rivers draining the southern Kavir-e-Namak alluvial-to-salt lake plain (Fig. 6). These two rivers mark the lateral boundaries of the western topographic domain of the KFF ridge and their upper reaches are westward- and eastward-flowing respectively, with a very low-relief divide, clearly closer to the eastern boundary. The latter evidence suggests that the westward-flowing river exerted the most effective headward erosion and progressively captured the streams flowing on the northern slope of the KFF ridge, as testified by their progressive westward curvature close to the confluence with the main river. This evidence is in agreement with the progressive eastward decrease of elevation difference between the northern- and southern plain, which conceivably gave higher stream power to the westward-flowing river. The latter consequently created a very large (~300 km²) alluvial fan in the Kavir-e-Namak plain (Fig. 6), likely after the breakthrough of a topographic threshold along the WFS, separating the northern plain from the southern one. This breakthrough could have caused the capture of the river originally draining westward, along the border of the KFF ridge (Fig. 6). The southern plain is drained by westward flowing rivers that are likely to have progressively captured the streams from the southern slope of the KFF ridge. Both the plains are presently connected to the same local base level in the Kavir-e-Namak salt lake plain.

Quaternary landforms and deposits

The KFF drainage network originated three generations of Quaternary landforms and deposits, that we recognized and mapped by integrating geomorphological field survey with DEM terrain analysis and aerial photo interpretation (Fig. 7). They consist of alluvial fans and alluvial plains made

of a wide array of conglomerates, gravels and sands, exhibiting various degree of consolidation. The clasts making up the deposits principally consist of yellow, grey and black fossiliferous limestone, dolomite, sandstone and shale, belonging to the basement units indicating that the deposits have been sourced from the basement and Neogene units. Principally in the terraced alluvial plain deposits, subordinate amounts of quartz pebbles and volcanoclastic sediments are also present. Since this lithologies are exotic in the KFF area, they have been most probably sourced from the Doruneh Fault area and transported to the KFF by the southward draining alluvial systems.

Three major geomorphological zones were recognized in the KFF area, based on the landforms and deposits type associations. *Zone 1* is located on northern slope of the KFF western topographic domain (Fig. 7). *Zone 2* is located to the south of the KFF western topographic domain (Fig. 7). *Zone 3* develops across the EFS (Fig. 7).

In *Zone 1* three generations of alluvial fans have been identified (Qt1N, Qt2N and Qt3N, Fig. 7b₁). They can be distinguished through their degree of surface re-incision (Fig. 7a₂) and their relative top and bottom surface elevation which systematically decreases from Qt1N to Qt3N (e.g. cross-section t-t', Fig. 7b₂). In particular, the Qt1N alluvial fan deposits are generally poorly preserved and their fan geometry is often fragmented. They are always found lying above the regional erosional surface cut through the strongly tilted Neogene units (Fig. 8a-b) and the top surface exhibit extremely incised and rugged topography (Fig. 7a₂). The geometries of Qt2N alluvial fan deposits are better preserved and exhibit relatively less incised top surfaces. They are found entrenched in Qt1N, and often into the regional erosional surface (Fig. 8b), with their bottom and top surface generally located at lower elevation than the Qt1N's. The Qt3N alluvial fan deposits geometries are the most well preserved and exhibit very little top surface incision. They are relatively deeply entrenched into both Qt1N and Qt2N fans and they lie further below the regional erosional surface (Fig. 8b). Collectively the three fan generations display geometric relations and characteristics typical of telescopically arranged fan system. Nevertheless, in the distal portion they make up a wide bajada which generally drains northward into alluvial plains, that are currently drained by the two above mentioned competing ephemeral river systems flowing to the west-southwest and east-southeast, respectively.

In *Zone 2* three other generations of alluvial fans are documented (Qt1S, Qt2S and Qt3S, Fig. 7b₁). They make up a wide bajada, which generally drains southward into the Kaver-e-Namak alluvial-to-salt lake plain. Qt1S and Qt2S deposits are restricted to proximal regions of the bajada, close to the southern mountain front. They represent remnants of alluvial fan apexes, which are now suspended tens of meters above the present rivers draining the plain. Qt3S alluvial fans make up most of the southern bajada and extend from the mountain front to the southern plain. Collectively the three fan generations of *Zone 2* exhibit a stacked architecture (Fig. 7a₃).

Zone 3 is characterized by three generations of terraced alluvial plain deposits, which extend throughout the zone. These alluvial plain deposits were sourced both from the KFF topographically prominent linear ridge and the Doruneh fault area (to the north) as attested by the presence of mixed clast population of KFF basement rocks and volcanoclastic, quartz rich from the Doruneh fault area. An example of the three generations of fluvial terraces comes from the central southward draining river (Fig. 7b₄), where the terraces (T1, T2, T3) are hanging at different elevation above the active river bed (Fig. 9). The oldest terrace (T1), lies directly onto the paleo-pediment sculpted in the Neogene bedrock, while T2 and T3 are mainly entrenched within both the T1 deposits and paleo-pediment surface (Fig. 8h). The alluvial terraces T1, T2, and T3, lie at 18, 5 and 3 m, respectively, above the active river bed. Furthermore, to the northwest the T2 and Qt2N deposits seem to be interfingered and their top surfaces to be morphologically correlated, plausibly indicating their synchronous generation (Fig. 9a).

The regional erosive angular unconformity on which lie the Quaternary deposits, that is sculpted in the Neogene strongly tilted deposits, extends throughout the area and is identifiable both to the north (Fig. 8a-c) and south (Fig. 8d) of the KFF mountainous ridge. The unconformity surface is represented by a paleo-pediment that can be traced tens of kilometers both along and away from the KFF, especially to the north of the KFF ridge (Fig. 8a-b). Such paleo-pediment surface strikes sub-parallel to and dips away from the KFF prominent linear topography and exhibits slope angles <7° which generally tend to decrease away from the KFF structure.

As for the sedimentological characters of the Quaternary deposits two main types are recognized in the three zones: (i) alluvial fan deposits, found in *Zone 1* and *Zone 2* and (ii) alluvial plain deposits principally found in *Zone 3*. The alluvial fans generally exhibit variable characteristics from

the apex to the distal part. Chaotic, clast-supported, highly angular, proximal breccia and conglomerate deposits characterize the apex area (the first 200 to 300 m) with maximum particle size of 35 cm (Fig. 8e). The central part of the fan system is characterized by relatively more texturally mature and rounded, matrix-supported conglomerates arranged into 30 to 100 cm thick beds exhibiting normal grading and infrequent cross-stratification in the upper part of the beds. In this area the clast size is up to 15 cm (Fig. 8f). The distal portion of the fan deposits is characterized by cross-stratified and at times clino-stratified gravelly sands, exhibiting normal grading and infrequent concave upwards erosional surfaces. The deposits can contain clasts with maximum particle size of 5 cm (Fig. 8g). The alluvial plain deposits principally consist of sandy large-scale lenticular beds, exhibiting some cross-stratification and concave upward erosional surfaces with gravelly horizons (Fig. 8h).

QUATERNARY FAULTING AND OSL DATING

Quaternary faulting from the study area has been previously reported Nozaem et al., (2013) and Calzolari et al., (submitted). A cumulative number of 216 fault surfaces (51 with striated surfaces) are recovered from the Quaternary deposits.

Fault population analysis was performed through the software Daisy 3 (Salvini, 2004; <http://host.uniroma3.it/progetti/fralab>); results are shown at the bottom of Figure 2. The KSF shows the maximum frequency distribution of fault strikes at N61°, with a subordinate population at N30°. Faults show high-to sub-vertical dips, with a maximum frequency distribution at 85° and a mean dip value of 80°. The frequency distribution of the pitch angle of the measured slickenlines attests for dominant strike-slip kinematics with mean pitch value of 7°. A minor dip slip component of slip is documented in the slickenlines, coherent with the transpressional regime of shearing along the KSF (Nozaem et al. (2013)). The KFF shows fault strikes distribution with a maximum at N87 and high-to sub-vertical dips, with a mean dip value of 82°. Despite the few measured slickenline pitch angles (11 data), a dominant strike- to oblique-slip kinematics (pitch angle < 45°) is documented.

The OSL dating method for Quaternary geochronology was adopted in order to (i) correlate the mapped Quaternary deposits to the ones already dated in the region; (ii) to use these landforms as suitable geomorphic markers; and (iii) to provide a minimum age constraint to the Quaternary faulting along the north-western edge of the Lut Block. Samples were collected from key stratigraphic horizons and from the Quaternary faulted deposits along the KSF-KFF deformation zone (see Fig. 2 for location). We concentrated the sampling on faulted alluvial and fluvial deposits, possibly including deposits from all the three recognized generations (Fig. 10). The quartz grains used for OSL dating originally come from the pre-Neogene bedrock. For each site, we sampled at a depth > 1m below the top depositional surface or below eventual cut-and-fill structures within the deposit, in order to avoid the risk of rejuvenated ages. The OSL data were acquired at the LABER OSL Lab, Waterville, Ohio (USA). Details on the analytical methods and protocols are provided in the Appendix.

In the Khakestary village site along the KSF, the Quaternary alluvium, which unconformably overlays the Mesozoic and Paleozoic basement rocks, is cut by sub vertical faults and associated fractures (Nozaem et al., 2013). Surface expression of the fault traces can be continuously followed on the ground (Fig. 10a). Faults are steeply dipping, striking from N20° to E–W (stereonet insert in Fig. 10a). When possible, interpretation of the kinematic indicators and stratigraphic offsets point to dominant right-lateral strike-slip with a minor reverse kinematics. Sample IR07 (Fig. 10b and c) was collected from a quite cemented sand layer of the older of two terraced alluvial fans, with alternating sand and gravel layers (Fig. 10c). The top surface of the deposit lies at ~900 m a.s.l. and the age provided by OSL dating is 56.82 ± 4.1 ka (Tab. 1).

Close to the north-eastern tip of the KSF at the Kal-e-Sorkh village (Fig. 10d), a number of faults and fractures were observed to cut Quaternary alluvial fan deposits (Nozaem et al., 2013). The fault traces cut through the cross bedding in the alluvium allowing estimation of the offset amount in the order of few centimeters. The main fault population strikes ENE. When preserved, a right-lateral strike-slip kinematics has been observed (Fig. 10e and f). Notably, several faults and fractures reach the surface, cutting the recent colluvium. Sample IR06 was collected from a terraced alluvial fan, with alternating sand and gravel layers. We sampled a medium sand level characterized by cross-stratification. The top surface of the deposit lies at ~850 m a.s.l. and the age provided by OSL dating is 25.54 ± 1.43 ka (Tab. 1).

Two samples (IR10 and IR11) were collected from terraced and faulted alluvial deposits outcropping in the area between the KFF and the KSF (Fig. 11a). Sample IR10 is from a silty-sandy terraced alluvial deposit affected by a fracture pattern coherent with the KFF deformation trend. The top surface of the deposit lies at ~875 m a.s.l (stereoplot insert in Fig. 11a and Fig.11b). Sample IR11 is from a quite cemented silty-sandy terraced alluvial deposit with gravelly beds. The top surface of the deposit lies at ~858 m a.s.l. and the deposit shows a SW-NE fracture pattern coherent with the KSF system and by a younger E-W fracture pattern coherent with the KFF (stereoplot insert in Fig. 11a and Fig.11c). OSL age obtained for the deposit affected by SW-NE and superimposed E-W fracture patterns (IR10) is 52.59 ± 4.04 ka, while the age of the deposit affected by the lonely E-W fracture pattern (IR11) is 5.28 ± 0.53 ka (Tab. 1).

Finally, 4 samples were collected from the KFF area (IR01, IR02, IR16 and IR17). Sample IR01 is from a mostly sandy alluvial deposit, with gravelly lenses. The top surface of the deposit lies at ~980 m a.s.l. and corresponds to the highest (T1) of the three fluvial terraces of *Zone 3* (Figs. 9b). Sample IR02 is from a sandy layer of an alluvial deposit entrenched in the previous one. The top surface of the deposit lies at ~965 m a.s.l. and corresponds to the lowest (T3) of the above mentioned fluvial terraces (Figs. 7b₄). Both the samples were collected along the prominent E-W striking fault scarp that defines the geomorphic expression of the EFS, where T1 and T3 alluvial terraces are extensively affected by a set of sub-vertical fracture array (Fig. 12a and b). The obtained ages for these deposits are 50.49 ± 3.34 ka and 8.06 ± 0.60 ka, respectively (Tab. 1). Sample IR16 is from a sandy-gravelly alluvial deposit from the terraced alluvial plain of the easternmost river dissecting the KFF ridge (Fig 12c). The top of the deposit is 5 m above the present river bed and lies at ~1040 m a.s.l. and provided an OSL age of 5.16 ± 0.41 ka (Tab. 1). The deposit is affected by E-W oriented sub-vertical faults cutting through the gypsiferous Neogene units and into the Quaternary alluvial deposits. Calcite slickenlines and small-scale drag fold are coherent with right-lateral kinematics (stereoplot insert in Fig. 12c).

Finally, sample IR17 is from a silty-to sandy matrix supported terraced alluvial fan deposit with gravelly lenses and belongs to the Qt2N alluvial fan generation in *Zone 1*, close to the CFS of the KFF (Fig. 7b₂ and 12d). The top surface of the deposit lies at ~1050 m a.s.l. and obtained OSL age is 25.86 ± 6.50 ka (Tab. 1).

To summarize, the OSL dating results shown in Table 1 provided ages of the Quaternary deposits surrounding the KSF-KFF deformation zone ranging between Late Pleistocene and Holocene. River fill terraces T1 and T3 are 50.49 ± 3.34 and 8.06 ± 0.6 ka respectively and alluvial fan Qt2N is 25.86 ± 6.5 ka. Furthermore, field evidence also indicate that Qt2N and T2 are coeval and correlated, as attested by their documented interfingering outcrop geometry. Therefore it is inferred the correlation between the three generation of alluvial fans and the three orders of alluvial terraced deposits. Collectively, three age clusters for deposition can be identified at ~6, ~25 and ~53 ka. These ages are coherent with the OSL and IRSL ages obtained regionally for the Quaternary alluvial deposits in eastern Iran (Walker and Fattahi, 2011, and references therein), and with the ^{10}Be surface abandonment ages obtained by Regard et al. (2006).

Furthermore, the OSL ages constrain the active faulting along the KSF and KFF intraplate deformation zones. In particular, in the KFF area three generations of Quaternary deposits with ages clustering at ~6 ka and one at ~53 ka are cut by major and minor faults with documented right lateral strike-slip kinematics and orientations compatible with the overall KFF system. The age of faulting obtained for the two sites along the KSF (~25 ka for IR06 and ~56 ka for IR07) is in agreement with that already hypothesized by Nozaem et alii (2013). Finally, it is worth to note that the top surface elevation of the same generation of landforms systematically increases eastwards. This is particularly significant for the youngest generation of alluvial plain deposits, whose elevation ranges from 869 m a.s.l. in the westernmost KFF area to 1038 m a.s.l. in the easternmost (Tab.1).

STATISTICAL ALLUVIAL FAN SLOPE ANGLE ANALYSIS

The above results document the topographic signal of the KFF and its Quaternary geomorphic response. OSL ages evidenced that the KFF is affected by active right-lateral strike-slip faulting, but also that the Quaternary erosion/aggradation phases, associated to the morpho-evolution of the ridge, are coherent with the regionally recognized ones. However, what it is not clear is if sin and/or post sedimentary fault-related uplift, already documented during the Neogene (Calzolari et al., submitted), also occurred during the Quaternary.

Geomorphic processes on alluvial fans and pediments are considered as proxies for base-level changes and tectonic activity along faulted mountain front (Bull, 2009). In particular, in tectonically active regions the arrangement of alluvial fan generations along a mountain front is the result of the competition among uplift rate, channel downcutting rate, and pediment aggradation/degradation rate. Typically, stacked generations of alluvial fans develop with dominant aggradation where uplift is the main base-level changing process. On the other hand, telescopic alluvial fans develop if the apex of fan deposition shifts down where stream-channel downcutting is the dominant geomorphic process (Bull, 2007).

According to the alluvial fan architecture observed in geomorphological *Zone 1* (telescopic alluvial fans) and *Zone 2* (stacked alluvial fans) it seems that the northern front of the KFF ridge could have experienced more important stream-channel downcutting than the southern one. This is in agreement with the drainage network evolution, and in particular with the evidence that rivers draining the northern plain are considerably entrenched due to headward erosion that likely propagated to the streams draining the northern slope. On the other hand, *Zone 2* corresponds to the steepest limb (dip angle $>40^\circ$) of the broad, E-W striking, asymmetric and south-verging antiformal fold, closer to the localized active deformation zone of the WFS and thus likely experiencing uplift-driven base-level changes (Fig. 2). Since the alluvial fan sets in the two geomorphological zones developed synchronously, the climate cannot be invoked as factor controlling channel downcutting vs uplift rates, most likely influenced by drainage network re-arrangement. Nonetheless, even in the case of drainage re-arrangement as main base-level changing process, the eventual ongoing fault-related uplift can be univocally testified by progressive tilting of alluvial fan surfaces (Bull, 1977; Giano, 2011).

In order to assess if any fault-related uplift tilted the Quaternary deposits in the KFF system, ideally it is necessary to reconstruct the original bottom and top surfaces of the deposits, which means using them as geomorphic markers. This is not an easy task since in most cases such surfaces are not exposed and/or have been incised and reshaped by erosion. Nevertheless, geomorphological *Zone 1* with its telescopically arranged alluvial fan deposits provides the best area to assess if the tilting continued during the Quaternary times. In this area, three generation of alluvial fans entrenched into each other are documented.

We performed a statistical alluvial fan slope angle analysis focused on two areas of *Zone 1* where the fan systems are approximately oriented N-S. Those two areas are marked on Fig. 7 as “west” and “east” respectively. The analysis used a purposely-developed routine to extract, from the DEM of the area, the elevation data points of the top surface remnants of single alluvial fans, excluding the areas of the fan which had been re-incised by stream channels (see Appendix for methodological details and complete numerical results).

Fig. 13 shows the results of fan slope angle analysis for the three alluvial fan generation within “west” and “east” areas (Fig. 7b). The plot shows the mean slope angle of the different alluvial fan generations, located at their average elevation, along four sectors (A, B, C, and D in Fig. 7b) for the two selected areas. The northing range of fault segments position is also indicated. The analysis clearly shows that there are differences in slope angle and elevation both between different fan generations (within the same sector) and between the two selected areas.

It might be argued that the different alluvial fans top surface angles reflect the deposits grain size changes between the three fan generations and/or the special changes in grain size and consequently in slope angle from fan apex to the distal portions of each fan. Nevertheless, the three generations of alluvial fan deposits exhibit similar maximum particle size for comparable distances from the mountain front (Fig. 8e-g). Furthermore, comparing the obtained alluvial fan slope angle with those found on other alluvial fans in semi-arid settings (e.g. Blissenbach, 1954) it is very clear that our data consistently exceed the expected slope angles (Fig. 14). Moreover, the observed maximum particle size of the KFF alluvial fans (~35 cm at the apex, 15 cm in the central part, 5 cm in the distal part) seem to be much smaller than the expected one. This indicates that the Quaternary alluvial fans top surfaces slope do not represent the original depositional slope, demonstrating therefore, that post depositional tilting has occurred.

To summarize the results of fan slope angle analysis (Fig. 13), it is possible to appreciate some general trends: i) fan tilting is greater towards the faults and seems to decrease proportionally away from it; ii) tilting is generally greater in Qt1 fans and progressively decreases in Qt2 and Qt3; iii) tilting and elevation of the three alluvial fan generations is greater in the “east” area; iv) in the “west” area

the three fan generations show generally decreasing slopes from Qt1w to Qt3w, their profiles seem to be disturbed in correspondence of an inferred fault at the end of Sector B (Fig. 7b) and generally merge at the end of sector C; v) by contrast in the “east” area Qt1e and Qt2e show approximately parallel slope profiles though located at different elevations, Qt3e is less tilted and its profile crosses Qt1w and Qt2w at the end of Sector C; vi) in both the “west” and “east” area Qt3 in Sector D seems to be less tilted but at a higher elevation than the other two alluvial fan generations.

The fact that the tilting generally decreases away from the principal faults indicates that the driver of such tilting are the fault themselves. The slope profile geometries of the Quaternary fans in area “west” indicate that tilting occurred at least since the time of deposition of Qt1w fans. On the other hand, the slope profile geometries of the Quaternary fans in area “east” indicate that tilting occurred after the deposition of Qt2e onwards.

DISCUSSION

The dataset presented in this study provides significant spatial and temporal constraints on the Quaternary activity of the KSF and KFF systems at the northern edge of the Lut Block, Central Iran. In particular, the OSL dataset indicates fault activity post ~50 ka through Holocene times, attesting for active tectonics under the control operated by right-lateral wrenching. It is worth noting that the right-lateral strike-slip tectonics was accommodated along NE-SW and E-W striking fault systems that interfere in space and time. In particular, a link can be found between the topographic signal, the punctuated exhumation history and style of deformation in the eastward propagating KFF system. The progressive eastward topographic growth of the KFF deformation zone is confirmed by the eastward increase of minimum topography of the range, that corresponds to a progressively higher (i.e. transient) relict base level of erosion, roughly corresponding to the paleo-pediment surface (Fig. 8c-d). In particular, a first 10-km wavelength signal, corresponding to the ~42 km long western topographic domain, is likely the topographic fingerprint of the first diffuse-to-localized deformation event (~18 Ma). The overall eastward narrowing, decreasing in elevation and relief and ~23 km long eastern topographic domain, can be instead identified as the remnant of the topographic signal of the second (~4 Ma) exhumation event. The fact that no syn-tectonic deposits are preserved in the proximity (tens of kilometers) of the KFF during the second exhumation event at ~4 Ma suggests that it was accompanied by an important Plio-Pleistocene erosional phase, testified by the regional paleo-pediment cutting the tilted Neogene deposits.

Deciphering climatic vs tectonic fingerprint in the Quaternary geomorphic signal

The fault-related topographic arrangement of the KSF-KFF deformation zone strongly conditioned the Quaternary drainage network evolution in the area in response to base-level changes. Beyond the topographic control on drainage network development, river dynamics responded to both climatic and active tectonic forcing, that influenced the Quaternary erosion/deposition dynamics around the linear ridges.

Field surveys outlined three generation of alluvial fans (Qt1 to Qt3) and river fill terraces (T1 to T3) which have been correlated and chronologically constrained to three clusters of ~53, ~25 and ~6 ka, respectively. These ages are consistent with OSL and IRSL ages obtained regionally for the Quaternary alluvial fan deposits in eastern Iran (Walker and Fattahi, 2011; and references therein), and with the ¹⁰Be surface abandonment ages obtained by Regard et al. (2006), univocally indicating that alluvial deposition dynamics in the KSF and KFF area is the result of Late Quaternary and Holocene, climate-driven aggradation phases that affected the entire Iranian Plateau. The lack of Quaternary deposits older than ~53 ka suggests also that the erosive phase responsible for the paleo-pediment formation likely continued until the Late Pleistocene. Of course, such a long pedimentation phase cannot be ascribed only to climatic forcing, since climate changes are worldwide documented over the entire Pleistocene. Therefore Quaternary tectonics must be taken into account as additional forcing on geomorphic processes.

The first tectonic fingerprint in the area is given by the architecture of the three alluvial fan generations developed around the KFF ridge. In fact, the telescopic arrangement of alluvial fans on the northern piedmont of the KFF ridge and the stacked arrangement on the southern one can be related to: i) the asymmetric growth of the ridge according to the position of the fault strands along which fault localization occurred; ii) the re-arrangement of the drainage network in response to and with the effect of local base-levels changes. But the most important Quaternary tectonic fingerprint

was deciphered through the quantitative alluvial fan slope analysis performed in geomorphological Zone1 (Fig.13). In fact the documented tilting of the alluvial fan deposits cannot have been caused by other processes than fault-related topographic growth of the KFF during the Late Quaternary to Holocene.

From the results of this analysis the total surface uplift and the surface uplift rate, in correspondence of the main faults, can be tentatively calculated. The observed difference in elevation between the fan profiles of the three generations (Fig. 13) is potentially due to a combination of tectonic uplift, erosion/deposition dynamics and thus possibly to differently dominated base-level changes. Nevertheless, a conservative estimation of the tectonic uplift rate can be performed by taking into account only the fraction of elevation difference due to tilting quantified by slope angle difference between Qt1 and Qt3 for the sector closer to the major faults. Thus we just measured this component of elevation difference in correspondence of the mean N-S projected fault location (elevation differences is marked by dw and de in Fig. 13). The obtained dw and de values are 44 and 49 m respectively. However, from the fan profiles geometries it is clear that in “west” area a progressive tilting of Qt1, Qt2, and Qt3 occurred since the deposition of Qt1N, whereas in “east” area it occurred since the deposition of Qt2N (parallel to Qt1N). Therefore, the uplift rate in correspondence with the fault is 0.9 and 2.6 mm/yr for the “west” and “east” areas, respectively. It is worth to note that these considerably different uplift rates are not to be considered as representative neither over the long-time scale nor over the entire fault-related ridge, but it is likely that the single fault strands of the KFF evolved through punctuated, diachronous and likely in some cases coseismic events.

Finally, the eastward propagation of the KFF system up to present is testified also by: i) the eastward increase of top surface elevation of the same generation of alluvial landforms and particularly for the youngest generation of terraced alluvial plain deposits (~6 ka), whose elevation ranges from 869 m a.s.l. in the westernmost KFF area to 1038 m a.s.l. in the easternmost; ii) the documented Late Pleistocene (KSF and KFF) to Holocene (KFF) right-lateral strike-slip faulting. This evidence together with the strong seismicity of the area indisputably implies that KSF and KFF are major active fault systems in the northern edge of the Lut Block.

Implications for the active fault architecture in Central Iran

The results presented in this study document that a major active right-lateral strike-slip deformation belt bound the north-western edge of the Lut Block, along a cumulative length of ~200 km from NE-SW to E-W. This active strike-slip shear belt is localised along the north-eastward termination of the Kashmar-Kerman tectonic zone (Fig. 1), suggesting polyphase re-activation of structurally inherited discontinuities during Neogene-Quaternary times.

Similarly to major intraplate active strike-slip fault zones (e.g., North Anatolian Fault, San Andreas Fault), the reconstructed fault pattern documents geometrical segmentation of the KSF-KFF fault zone, with potential impact on the slip distribution and surface rupture propagation (e.g. Schwartz and Coppersmith, 1984; Barka and Kadinsky-Cade, 1988; Wesnousky, 1988; Scholz, 1990; Lettis et al., 2002; Langridge et al., 2002; Wesnousky, 2006).

Despite no direct evidence is provided on the actual slip rates along the KSF-KFF fault zone, a kinematic connection with the sub-parallel, left-lateral Doruneh Fault (Figs. 1 and 2) is indicated by the concurrent Quaternary activity of both faults (Tchalenko et al., 1973; Fattahi et al., 2007; Farbod et al., 2011; Javadi et al., 2013). As already suggested by Noazem et al. (2013), this concurrent kinematic activity results in the NE lateral extrusion of the Yazd block along the strike-slip faults systems (NF, KKF, KSF KFF faults in Fig. 1) that reactivated the Kashmar-Kerman tectonic zone as a major right-lateral shear boundary and along the left-lateral Doruneh Fault, respectively. The lateral escape of the Yazd and Tabas Block towards the Lut Block along the Nayband Fault (Fig. 1) has been also suggested by the results of the analogue modelling of Bonini et al. (2003).

The lateral extrusion scenario is at odds with the current kinematic configuration proposed for Central Iran, commonly framed into a scenario of dynamic rupture achieved through N-S dextral and E-W sinistral slip zones, associated with rigid block rotations and strain partitioning (e.g. Allen et al., 2004; Walker and Jackson, 2004; Mattei et al., 2012; Walpersdorf et al., 2014). In particular, modeling GPS data with a block rotation model suggests that the rotations have been going on at a similar rate ($1 \pm 0.4^\circ/\text{Ma}$) over the last 12 Ma (Walpersdorf et al., 2014). However, the rigid block rotation model contrasts with the Neogene-Quaternary kinematic configuration recently recognized for the northern boundary of the Lut Block, where punctuated events of fault zone (re)activation and

space-time kinematic shifts have been documented for the Neogene-Quaternary time lapse (Farbod et al., 2011; Javadi et al., 2013; Nozaem et al., 2013; Calzolari et al., submitted; this study). Furthermore the timing for the initiation of this rigid block rotation scenario, proposed by Walpersdorf et al., (2014), is in disagreement with the estimated ~5 to ~7 Ma onset of strike-slip tectonics in south Central Iran (Allen et al., 2004; Allen et al., 2011; Walker and Jackson, 2004)

In our view, a kinematic model dominated by crustal thickening and lateral extrusion of the Yazd Block in Central Iran during the Arabia-Eurasia collision better fits the new kinematics findings and temporal evolution of deformation along the northern margin of the Lut Block. The dynamic scenario to accomplish for this new hypothesis resides in the idea that a gradual decrease in the capacity to accommodate convergence along the Zagros collisional zone since the Pliocene (Allen et al., 2004; Austermann and Iaffaldano, 2013) resulted in an overall advancing convergent plate margin with a further increase in the intraplate residual convergence. In Central Iran, this new kinematic configuration led to northward convergence velocities that decreased away from the Zagros-Makran Transfer Zone. This later kinematic configuration remained unchanged since then. Evidence provided by the GPS data, showing northward convergence vectors that generally decreased (to the northwest and east) away from the Zagros-Makran Transfer Zone (e.g. Vernant et al., 2004; Walpersdorf et al., 2014; Fig. 1) confirms this reconstruction.

CONCLUSIONS

The main results of this study can be summarized as follows:

1. Significant spatial and temporal constraints are provided on the Quaternary activity of the KSF-KFF deformation zone at the northern edge of the Lut Block (Central Iran), with right-lateral strike-slip tectonics accommodated along NE-SW and E-W striking fault systems that interfere in space and time.
2. The present topographic signal of the KFF-related ridge is likely inherited from a Neogene punctuated history of fault nucleation, propagation, and exhumation and reflects the style of deformation within the fault system.
3. The fault-related topographic arrangement of the KSF-KFF deformation zone passively influenced the Quaternary drainage network evolution, but the Quaternary erosion/deposition dynamics around the linear ridges responded also to climatic and active tectonic forcing.
4. In particular, geomorphological analysis and OSL dating outline the presence of three generations of Quaternary alluvial fans and river fill terraces associated to the dismantling of the KSF/KFF ridge. Their ages, clustered at ~53, ~25, and ~6 ka, univocally demonstrate that they have been primarily controlled by Late Pleistocene and Holocene climate-driven aggradation phases, previously recognized throughout the Iranian Plateau by other studies.
5. The tectonic fingerprint was detected in the Plio-Pleistocene long erosional phase and in the alluvial fan architecture documented along the KSF and KFF, indicating that they have been strongly influenced by the fault activity and by the consequent drainage network re-arrangement.
6. Moreover, the statistical alluvial fan slope angle analysis indicates that the KFF is still producing fault-related topographic growth. This growth is recorded by fan surfaces that are over-steepened with respect to slope angles predictable through maximum particle size of the deposits. Furthermore, a progressive increase of tilting with alluvial fan age and proximity to fault zones was recorded.
7. A new kinematic model for the Quaternary and active faulting in Central Iran is necessary. Crustal thickening and lateral extrusion of the Yazd Block during progress of the Arabia-Eurasia collision may provide an alternative feasible scenario.

APPENDIX: Methods and analytical protocols

Topographic analysis

A 10m-cell size DEM of the study area was produced using data from topographic vector maps from the National Cartographic Center of Iran. Topographic contours, independent elevation points, and river networks data were interpolated using the ANUDEM algorithm 5.3 (Hutchinson et al., 2011). In order to describe quantitatively the topography of the KFF we first produced the slope angle, aspect and local relief (Scotti et al., 2013; and references therein) maps. Then we performed a topographic analysis (D'Agostino and McKenzie, 1999; Molin et al., 2004; Wegmann et al., 2007; Molin et al., 2012) of the KFF ridge by means of: i) filtered topography at the local scale (using Focal Statistics Tool of ArcGIS 10.1 for calculating the average elevation in 1, 2.5, 5, 10 and 20 km radius circle areas), to assess the spatial distribution of topographic signals of the KFF at different wavelengths, according to different styles of faulting; ii) 5 swath profiles (Mitchell and Montgomery, 2006; Telbisz et al., 2013; Hergarten et al., 2014) to outline the ridge-scale topography through across- and along-ridge distribution of minimum (base level), mean and maximum (crest envelope) elevations and, implicitly, of local relief as proxy of uplift-driven river incision.

OSL dating

Sample preparation

For each sample pure quartz was extracted for De measurements. In OSL lab, the sample was treated firstly with 10% HCl and 30% H₂O₂ to remove organic materials and carbonates, respectively. After grain size separation, the fraction of 90-125 μ m was relatively abundant. As a result, this fraction was chosen for equivalent dose (De) determination. The grains were treated with HF acid (40%) for about 40 min, followed by 10% HCl acid to remove fluoride precipitates.

Measurement techniques

Quartz OSL measurements were performed using an automated Risø TL/OSL-20 reader. Stimulation was carried out by a blue LED ($\lambda=470\pm20$ nm) stimulation source for 40 s at 130 °C. Irradiation was carried out using a ⁹⁰Sr/⁹⁰Y beta source built into the reader. The OSL signal was detected by a 9235QA photomultiplier tube through a U-340 filter with 7.5 mm thickness.

Equivalent dose (De) measurement and age calculation

For De determination, SAR protocol was adopted. The preheat temperature is chosen to be 240 °C for 10 s and cut-heat is 180 °C for 10 s. The final De is the average of Des of all aliquots, and the error of the final De is the standard error of the De distribution. For each sample, 20 aliquots were measured for De determination.

The Quartz OSL was fast component dominated. Recycling ratios were between 0.90-1.1. Recuperation is negligible. The cosmic ray dose rate was estimated for each sample as a function of depth, altitude and geomagnetic latitude. The concentration of U, Th and K was measured by ICP-MS. The elemental concentrations were then converted into annual dose rate, taking into account of the water content effect. The final OSL age is then: De/dose-rate.

Statistical alluvial fan slope angle analysis

The routine encompasses the following steps: i) clipping the DEM to the extent of a previously mapped single fan; ii) creating a curvature map of the fan from the clipped DEM; iii) extracting from the curvature map the areas with positive and low curvature values, likely corresponding to the remnants of the fan top surface; iv) transforming these areas into a point cloud containing elevation data. To capture the downstream changes in gradient angle along the fans, this angle has been measured along the N-S direction by plotting a linear regressions through the extracted elevation point-cloud data, at 2-km intervals, for sectors A, B, C, D indicated in Fig. 7b. An example of the extracted alluvial fan top surface elevation data, the resulting linear regressions and the obtained fan parameters, for a single alluvial fan are presented in Fig. A1. A total of 71 alluvial fans were analyzed using this method in areas “west” and “east” of Zone 1. Below are listed the complete numerical results:

Table 2: Northern Quaternary alluvial fans slope angle analysis

Sector A	Sector B	Sector C	Sector D
----------	----------	----------	----------

	m^* (m)	slope (°)	C_{endA+} (m)	m^* (m)	slope (°)	C_{endB+} (m)	m^* (m)	slope (°)	C_{endC+} (m)	m^* (m)	slope (°)	C_{endD+} (m)
"WEST"												
Qt1_1	0.0677	3.87	1050									
Qt1_2	0.0909	5.19	1087									
Qt1_3	0.0787	4.50	1119									
Qt1_4	0.0891	5.09	1117									
Qt1_5	0.1024	5.85	1141									
Qt1_6	0.0823	4.71	1124	0.0373	2.14	1041						
Qt1_7				0.0412	2.36	1048	0.0341	1.95	977			
mean	0.0852	4.87	1106	0.04	2.25	1045	0.03	1.95	977			
sd	0.0118	0.67	33	0.0028	0.16	5						
Qt2_1	0.0572	3.27	1040	0.0490	2.80	937						
Qt2_2	0.0470	2.69	1050	0.0449	2.57	966						
Qt2_3				0.0288	1.65	1009						
Qt2_4	0.1099	6.27	1069	0.0301	1.73	1006						
Qt2_5	0.0572	3.28	1110	0.0433	2.48	1030						
Qt2_6	0.0482	2.76	1113	0.0345	1.97	1042	0.0244	1.40	991			
Qt2_7				0.0330	1.89	960						
Qt2_8				0.0602	3.45	1011	0.0306	1.75	952	0.0181	1.03	886
Qt2_9							0.0321	1.84	963	0.0226	1.30	922
Qt2_10				0.0367	2.10	1042	0.0310	1.77	980	0.0304	1.74	911
Qt2_11				0.0368	2.11	1046	0.0336	1.92	985			
Qt2_12							0.0254	1.45	983			
Qt2_13				0.0322	1.85	1052	0.0314	1.80	982			
Qt2_14							0.0262	1.50	988	0.0264	1.51	938
Qt2_15				0.0040	0.23	1040	0.0309	1.77	978			
Qt2_16							0.0365	2.09	980			
Qt2_17							0.0251	1.44	989	0.0226	1.30	943
Qt2_18							0.0362	2.07	982			
mean	0.0639	3.65	1076	0.0361	2.07	1012	0.0303	1.73	979	0.0240	1.38	920
sd	0.0261	1.49	34	0.0136	0.78	38	0.0042	0.24	11	0.0046	0.27	23
Qt3_1	0.0680	3.89	1024	0.0437	2.50	937						
Qt3_2	0.0469	2.69	1040	0.0659	3.77	908						
Qt3_3				0.0347	1.99	972	0.0299	1.71	911			
Qt3_4	0.0519	2.97	1047	0.0425	2.43	967						
Qt3_5	0.0583	3.34	1087	0.0403	2.31	999	0.0255	1.46	948			
Qt3_6	0.0599	3.43	1101	0.0324	1.85	1027						
Qt3_7				0.0377	2.16	1031	0.0287	1.64	969	0.0251	1.44	919
Qt3_8							0.0226	1.29	968	0.0265	1.52	913
Qt3_9							0.0246	1.41	973	0.0214	1.22	929
Qt3_10							0.0247	1.42	983	0.0245	1.41	928
Qt3_11							0.0209	1.20	988	0.0191	1.09	949
Qt3_12										0.0175	1.00	952
Qt3_13							0.0177	1.01	989	0.0181	1.03	952
Qt3_14				0.0299	1.71	1041	0.0259	1.49	980			
Qt3_15							0.0232	1.33	990	0.0245	1.41	940
Qt3_16							0.0133	0.76	990	0.0185	1.06	951
Qt3_17							0.0199	1.14	990	0.0161	0.92	958
Qt3_18	0.0412	2.36	1103	0.0350	2.01	1033	0.0222	1.27	986	0.0145	0.83	959
Qt3_19							0.0145	0.83	987	0.0156	0.90	957
mean	0.0544	3.11	1067	0.0402	2.30	991	0.0224	1.28	975	0.0201	1.15	942
sd	0.0078	0.55	34	0.0113	0.61	47	0.0048	0.28	22	0.0041	0.24	16
"EAST"												
Qt1_1				0.0899	5.14	1189						

Qt1_2				0.0513	2.94	1069			
Qt1_3				0.0763	4.36	1048			
Qt1_4				0.0407	2.33	1077			
Qt1_5				0.0573	3.28	1071			
Qt1_6	0.0888	5.07	1196	0.0742	4.24	1041			
Qt1_7				0.0518	2.96	1050			
Qt1_8				0.0787	4.50	1027			
mean	0.0893	5.10	1193	0.0614	3.52	1055			
sd	0.0008	0.04	5	0.0149	0.85	18			
Qt2_1	0.0845	4.83	1185	0.0593	3.39	1065			
Qt2_2				0.0460	2.64	1065	0.0313	1.80	998
Qt2_3				0.0543	3.11	1080	0.0396	2.27	999
Qt2_4				0.0680	3.89	1036			
Qt2_5	0.0727	4.16	1166						
Qt2_6	0.1071	6.12	1174						
Qt2_7				0.0684	3.91	1047			
Qt2_8				0.0543	3.11	1056			
mean	0.0881	2.62	1175	0.0584	1.14	1058	0.0355	0.33	999
sd	0.0175	1.00	10	0.0087	0.50	15	0.0058	0.33	1
Qt3_1				0.0424	2.43	1067	0.0318	1.82	1003
Qt3_2				0.0582	3.33	1057			
Qt3_3				0.0351	2.01	1078			
Qt3_4				0.0292	1.67	1071	0.0283	1.62	1011
Qt3_5				0.0465	2.66	1072			
Qt3_6				0.0505	2.89	1074	0.0316	1.81	1007
Qt3_7				0.0351	2.01	1087	0.0397	2.27	1007
Qt3_8				0.0337	1.93	1084	0.0362	2.07	1011
Qt3_9				0.0467	2.68	1082	0.0352	2.02	1006
Qt3_10	0.0535	3.06	1176	0.0514	2.94	1067	0.0261	1.49	1008
Qt3_11				0.0296	1.70	1059	0.0219	1.26	1016
mean	0.0535	3.06	1176	0.0417	0.54	1073	0.0313	0.27	1009
sd				0.0097	0.56	10	0.0058	0.33	4

* m is the elevation/N-S distance ratio, from which the angle is calculated

+ C_{endA} is the elevation at the northern end of each sector

Aknowledgments

Special thanks go to M.R. Mazinini for assistance during field work. Manager and staff of Khaneye-Moallem of Kashmar are warmly thanked for their kind hospitality. We also thank Ali Rastpour and Hassan Faraji for driving to the field and logistic support. This project has been funded by TOPOMOD Marie Curie ITN project (Grant agreement 264517).

REFERENCES

- Aghanabati, A., 2004, Geology of Iran, Geological Survey of Iran, Tehran.
- Agard, P., Omrani, J., Jolivet, L., Whitechurch, H., Vrielynck, B., Spakman, W., Monié, P., Meyer, B., and Wortel, R. (2011), Zagros orogeny: A subduction-dominated process, *Geol. Mag.*, 148 (5-6), 692-725, doi:10.1017/s001675681100046x.
- Allen, C. R. (1965), Transcurrent faults in continental areas, *Phil. Trans. R. Soc. Lond. Ser. A* 258, 82-89, doi:10.1098/rsta.1965.0023
- Allen, M., Jackson, J., and Walker, R. (2004), Late Cenozoic reorganization of the Arabia-Eurasia collision and the comparison of short-term and long-term deformation rates, *Tectonics*, 23, TC2008, doi:10.1029/2003TC001530

- Allen, M. B., Kheirkhah, M., Emami, M. H., and Jones, S. J. (2011), Right-lateral shear across Iran and kinematic change in the Arabia-Eurasia collision zone, *Geophys. J. Int.*, 184 (2), 555-574, doi:10.1111/j.1365-246X.2010.04874.x.
- Austermann, J., and Iaffaldano, G. (2013), The role of the Zagros orogeny in slowing down Arabia-Eurasia convergence since ~5 Ma, *Tectonics*, 32 (3), 351-363. doi:10.1002/tect.20027
- Barka, A., and Kadinsky-Cade, K. (1988), Strike-slip fault geometry in Turkey and its influence on earthquake activity, *Tectonics*, 7 (3), 663-684, doi:10.1029/TC007i003p00663
- Beaumont, P. (1972), Alluvial fans along the foothills of the Elburz Mountains, Iran, *Paleogeogr. Paleoclimatol. Paleoecol.*, 12, 251-273, doi:10.1016/0031-0182(72)90022-3
- Belisario, F., Del Monte, M., Fredi, P., Funiciello, R., Lupia Palmieri, E., and Salvini, F. (1999), Azimuthal analysis of stream orientations to define regional tectonic lines, *Z. Geomorphol., Suppl.Bd.* 118, 41-63.
- Bennett, E.R., Youngson, J.H., Jackson, J.A., Norris, R.J., Raisbeck, G.M., and Yiou, F. (2006), Combining geomorphic observations with in-situ cosmogenic isotope measurements to study anticline growth and fault propagation in Central Otago, New Zealand, *N. Z. J. Geol. Geophys.*, 49, 217-231, doi:10.1080/00288306.2006.9515161
- Berberian, M. (1976), Seismotectonic map of Iran (1:2,500,000), Geological Survey of Iran Press.
- Berberian, M. (1977), Historical seismicity map of Iran (1:5000,000), Geological Survey of Iran Press.
- Berberian, M., and King, G. (1981), Towards a paleogeography and tectonic evolution of Iran, *Can. J. Earth Sci.*, 18 (2), 210-265, doi: 10.1139/e81-019
- Berberian, M., 2014, Earthquakes and coseismic surface faulting on the Iranian Plateau, Elsevier Science, Amsterdam, The Netherlands.
- Blissenbach, E. (1954), Geology of alluvial fans in semiarid regions, *Geol. Soc. Am. Bull.*, 65 (2), 175-190, doi:10.1130/0016-7606(1954)65[175:GOAFIS]2.0.CO;2
- Blythe, A.E., Burbank, D.W., Farley, K.A., and Fielding, E.J. (2000), Structural and topographic evolution of the central Transverse Ranges, California, from apatite fission-track, (U-Th)/He and digital elevation model analyses, *Basin Res.*, 12, 97-114, doi:10.1046/j.1365-2117.2000.00116.x.
- Bonini, M., Corti, G., Sokoutis, D., Vannucci, G., Gasperini, P., Cloetingh, S., 2003. Insights from scaled analogue modelling into the seismotectonics of the Iranian region. *Tectonophysics* 376, 137-149.
- Brandon, M.T., (1996), Probability density plots for fission-track grain age distributions, *Radiat. Meas.*, 26, 663-676, doi: 10.1016/S1350-4487(97)82880-6.
- Bridgland, D., and Westaway, R. (2008), Climatically controlled river terrace staircases: A world wide Quaternary phenomenon, *Geomorphology*, 98, 285-315, doi:10.1016/j.geomorph.2006.12.032
- Barka, A., and Kadinsky-Cade, K., 1988, Strike-slip fault geometry in Turkey and its influence on earthquake activity: *Tectonics*, v. 7, no. 3, p. 663-684.
- Brocard, G. Y., Van Der Beek, P. A., Bourlès, D. L., Siame, L. L., and Mugnier, J. L., (2003), Long-term fluvial incision rates and postglacial river relaxation time in the French Western Alps from ^{10}Be dating of alluvial terraces with assessment of inheritance, soil development and wind ablation effects, *Earth Planet. Sci. Lett.*, 209(1), 197-214, doi:10.1016/S0012-821X(03)00031-1
- Brown, E.T., Stallard, R.F., Larsen, M.C., Raisbeck, G.M., and Yiou, F. (2005), Denudation rates determined from the accumulation of in situ-produced ^{10}Be in the Luquillo experimental forest, Puerto Rico, *Earth Planet. Sci. Lett.*, 129(1-4), 193-202, doi:10.1016/0012-821X(94)00249-X
- Bull, W.B. (1977), The alluvial-fan environment, *Prog. Phys. Geogr.*, 1, 222-270.

- Bull, W.B. (1991), *Geomorphic responses to climate changes*, Oxford University Press, Oxford, UK.
- Bull, W.B. (2007), *Tectonic geomorphology of mountains: a new approach to paleoseismology*, Blackwell Publishing, Oxford, UK.
- Bull, W.B. (2009), *Tectonically Active Landscapes*, John Wiley & sons, Ltd., Chichester, West Sussex, UK.
- Burbank, D.W. (1992), Characteristic size of relief, *Nature*, 359 (6395), 483-484, doi:10.1038/359483a0
- Burbank, D. W., Leland, J., Fielding, E., Anderson, R. S., Brozovic, N., Reid, M. R., and Duncan, C. (1996). Bedrock incision, rock uplift and threshold hillslopes in the northwestern Himalayas, *Nature*, 379 (6565), 505-510, doi:10.1038/379505a0
- Burbank, D.W., and Anderson, R.S. (2012), *Tectonic Geomorphology*, John Wiley & Sons, Ltd, Chichester, West Sussex, UK
- Calzolari, G., Rossetti, F., Della Seta, M., Nozaem, R., Olivetti, V., Balestrieri, M.L., Cosentino, D., Faccenna, C., Stuart, F.M., Vignaroli, G. (2015), Spatio-temporal evolution of intraplate strike-slip faulting: the Neogene-Quaternary Kuh-e-Faghan fault, Central Iran, *Geol. Soc. Am. Bull.*, under review
- Castelltort, S., Goren, L., Willett, S.D., Champagnac, J.D., Herman, F., and Braun, J. (2012), River drainage patterns in the New Zealand Alps primarily controlled by plate tectonic strain, *Nat. Geosci.*, 5, 744–748, doi:10.1038/NGEO1582
- Cockburn, H.A.P., Brown, R.W., Summerfield, M.A., and Seidl, M. A. (2000). Quantifying passive margin denudation and landscape development using a combined fission-track thermochronology and cosmogenic isotope analysis approach, *Earth Planet. Sci. Lett.*, 179 (3-4), 429-435, doi:10.1016/S0012-821X(00)00144-8
- Cooke, R., Warren, A., and Goudie, A. (1993), *Desert geomorphology*, University College of London Press, London, UK.
- Cyr, A.J., Granger, D.E., Olivetti, V., Molin, P. (2010), Quantifying rock uplift rates using channel steepness and cosmogenic nuclide-determined erosion rates: Examples from northern and southern Italy, *Lithosphere*, 2 (3), 188-198, doi:10.1130/L96.1
- D'Agostino, N., and McKenzie, D. (1999), Convective support of long-wavelength topography in the Apennines (Italy), *Terra Nova*, 11, 228-233, doi: 10.1046/j.1365-3121.1999.00252.x
- Della Seta, M., Del Monte, M., Fredi, P., and Lupia Palmieri, E. (2004), Quantitative morphotectonic analysis as a tool for detecting deformation patterns in soft-rock terrains: a case study from the southern Marche, Italy, *Geomorphologie*, 4, 267-284, doi:10.3406/morfo.2004.1224
- Della Seta, M., Del Monte, M., Fredi, P., Miccadei, E., Nesci, O., Pambianchi, G., Piacentini, T., and Troiani, F. (2008), Morphotectonic evolution of the Adriatic piedmont of the Apennines: An advancement in the knowledge of the Marche-Abruzzo border area, *Geomorphology*, 102 (1), 119-129, doi:10.1016/j.geomorph.2007.06.018
- Di Bucci, D., Mazzoli, S., Nesci, O., Savelli, D., Tramontana, M., De Donatis, M., and Borraccini, F. (2003), Active deformation in the frontal part of the Northern Apennines: insights from the lower Metauro River basin area (northern Marche, Italy) and adjacent Adriatic off-shore, *J. Geodyn.*, 36, 213-238, doi:10.1016/S0264-3707(03)00048-6
- Dufaure, J.J., Thibault, C., Kadjar, M.H., Mercier, J.L. (1978), La zone de failles du Zendan (Iran du Sud-Est): I-Gùèomorphologie et Stratigraphie du Quaternaire. paper presented at Réunion Annuelle des Sciences de la Terre (6th RAST). Soc. Geol. de France, Orsay, France.
- Eftekhari-Nezhad, J., Aghanabati, A., Hamzehpour, B., and Baroyant, V. (1976), *Kashmar: Geological Survey of Iran*, scale 1:250,000.
- England, P., and Molnar, P. (1990), Surface uplift, uplift of rocks, and exhumation of rocks, *Geology*, 18, 1173-1177, doi:10.1130/0091-7613(1990)018<1173:SUUORA>2.3.CO;2

- Farbod, Y., Bellier, O., Shabanian, E., and Abbassi, M. R. (2011), Geomorphic and structural variations along the Doruneh Fault System (Central Iran), *Tectonics*, 30, TC6014, doi:10.1029/2011TC002889.
- Farley, K. (2000), Helium diffusion from apatite: General behavior as illustrated by durango fluorapatite, *J. Geophys. Res.*(1978–2012), 105, B2, 2903-2914, doi:10.1029/1999JB900348
- Fattahi, M., Walker, R. T., Khatib, M. M., Dolati, A., and Bahroudi, A. (2007), Slip-rate estimate and past earthquakes on the Doruneh fault, Eastern Iran, *Geophys. J. Int.*, 168 (2), p. 691-709, doi: 10.1111/j.1365-246X.2006.03248.x.
- Finnegan, N. J., Schumer, R., and Finnegan, S. (2014), A signature of transience in bedrock river incision rates over timescales of 10^4 - 10^7 years, *Nature*, 505(7483), 391-394, doi:10.1038/nature12913
- Foroutan, M., Meyer, B., Sébrier, M., Nazari, H., Murray, A., Le Dortz, K., Shokri, M., Arnold, M., Aumaître, G., and Bourlès, D. (2014), Late Pleistocene-Holocene right slip rate and paleoseismology of the Nayband fault, western margin of the Lut Block, Iran, *J. Geophys. Res. Solid Earth*, 119, 3517–3560, doi:10.1002/2013JB010746.
- Frostick, L.E., and Reid, I. (1989), Climatic versus tectonic controls of fan sequences: lessons from the Dead Sea, Israel. *J. Geol. Soc.*, 146, 527-538, doi:10.1144/gsjgs.146.3.0527
- Fubelli, G., Della Seta, M., Amato, G. (2014), Drainage system adjustment in response to the opening of the Rieti intermontane basin (Central Italy): geostatistical reconstruction of the PaleoFarfa River alluvial plain, *Rend. Lincei.-Sci. Fis. Nat.*, 25 (2) Suppl., 167-176. doi:10.1007/s12210-014-0322-0
- Giano, S. (2011), Quaternary alluvial fan systems of the Agri intermontane basin (southern Italy): tectonic and climatic controls, *Geol. Carpath.*, 62 (1), 65-76, doi: 10.2478/v10096-011-0006-y
- Giano, S.I., Gioia, D., and Schiattarella, M. (2014), Morphotectonic evolution of connected intermontane basins from the southern Apennines, Italy: the legacy of the pre-existing structurally controlled landscape, *Rend. Lincei.-Sci. Fis. Nat.*, 25 (2) Suppl., 241-252, doi: 10.1007/s12210-014-0325-x
- Gioia, D., Gallicchio, S., Moretti, M., and Schiattarella, M. (2014), Landscape response to tectonic and climatic forcing in the foredeep of the southern Apennines, Italy: Insights from Quaternary stratigraphy, quantitative geomorphic analysis, and denudation rate proxies, *Earth Surf. Process. Landf.*, 39 (6), 814-835, doi:10.1002/esp.3544
- Harrison, T.M., and Zeitler, P.K., (2005), Fundamentals of Noble Gas Thermochronometry, *Rev. Mineral. Geochem.*, 58, 123-149, doi:10.2138/rmg.2005.58.5
- Harvey, A. M., 1997, The role of alluvial fans in arid zone fluvial systems, in *Arid Zone Geomorphology; Process, Form and Change in Drylands*, edited by D.S.G. Thomas, p. 231-259, Wiley, Chichester, UK
- Harvey, A.M. 2003: The response of dry-region alluvial fans to late Quaternary climatic change, in *Desertification in the Third Millenium*, edited by A.S. Alsharhan, W.W. Wood, A.S. Goudie, A. Fowler, and E.M. Abdellatie, pp. 83-98, Balkema, Rotterdam, The Netherlands, doi:10.1201/NOE9058095718.ch9
- Hatzfeld, D., and Molnar, P. (2010), Comparisons of the kinematics and deep structures of the Zagros and Himalaya and of the Iranian and Tibetan plateaus and geodynamic implications, *Rev. Geophys.*, 48, RG2005, doi:10.1029/2009RG000304
- Hergarten, S., Robl, J., and Stüwe, K. (2014), Extracting topographic swath profiles across curved geomorphic features, *Earth Surf. Dynam.*, 2, 97-104, doi:10.5194/esurf-2-97-2014
- Hessami, K., Jamali, F., Tabassi, H., 2003. Major active faults of Iran, International Institute of Earthquake Engineering and Eeismology of Iran Press, Tehran.

- Hubert-Ferrari, A., Armijo, R., King, G., Meyer, B. and Barka, A. (2002), Morphology, displacement, and slip rates along the North Anatolian Fault, Turkey, *J. Geophys. Res.*, 107, 2235, doi:10.1029/2001JB000393
- Hutchinson, M.F., Xu, T. and Stein, J.A. (2011), Recent Progress in the ANUDEM Elevation Gridding Procedure, in *Geomorphometry 2011*, edited by T. Hengel, I.S. Evans, J.P. Wilson and M. Gould, pp. 19–22. Redlands, California, USA. See: <http://geomorphometry.org/HutchinsonXu2011>.
- Jackson, D. D., Shen, Z.-k., Potter, D., Ge, X.-B. and Sung, L.-Y (1997), Southern California deformation. *Science*, 277, 1621–1622, doi:10.1126/science.277.5332.1621
- Jackson, J., Haines, A., and Holt, A. (1995), The accommodation of the Arabia–Eurasia plate convergence in Iran, *J. Geophys. Res.*, 100(B8), 15205–15219, doi:10.1029/95JB0129
- Jackson, J., Norris R., and Youngson J. (1996), The structural evolution of active fault and fold systems in central Otago, New Zealand: Evidence revealed by drainage patterns, *J. Struct. Geol.*, 18, 217–234, doi:10.1016/S0191-8141(96)80046-0
- Javadi, H. R., Ghassemi, M. R., Shahpasandzadeh, M., Guest, B., Ashtiani, M. E., Yassaghi, A. L. I., and Kouhpeyma, M., 2013, History of faulting on the Doruneh Fault System: implications for the kinematic changes of the Central Iranian Microplate, *Geol. Mag.*, 150 (4), p. 651–672, doi:10.1017/s0016756812000751, doi:10.1017/S0016756812000751
- Johansson, M. (1999), Analysis of digital elevation data for palaeosurfaces in south-western Sweden, *Geomorphology*, 26, 279–295, doi:10.1016/S0169-555X(98)00068-3
- Jolivet, L., and Faccenna, C. (2000), Mediterranean extension and the Africa-Eurasia collision, *Tectonics*, 19 (6), 1095–1106. doi:10.1029/2000TC900018
- Keller, E.A., and Pinter, N. (2001), *Active Tectonics: Earthquakes, Uplift, and Landscape* (2nd Edition), Prentice Hall, Upper Saddle River, NJ
- Langridge, R.M., Stenner, H.D., Fumal, T.E., Christofferson, S.A., Rockwell, T.K., Hartleb, R.D., Bachhuber, J., and Barka, A.A. (2002), Geometry, slip distribution, and kinetics of surface rupture on the Sakarya fault segment during the 17 August 1999 Izmit, Turkey, Earthquake, *Bull. Seismol. Soc. Amer.*, 92 (1), 107–125, doi:10.1785/0120000804
- Lavé, J., and Avouac, J. P. (2001), Fluvial incision and tectonic uplift across the Himalayas of central Nepal, *J. Geophys. Res.* (1978–2012), 106(B11), 26561–26591, doi:10.1029/2001JB000359
- Lettis, W., Bachhuber, J., Witter, R., Brankman, C., Randolph, C.E., Barka, A., Page, W.D., and Kaya, A. (2002), Influence of releasing stepovers on surface fault rupture and fault segmentation: examples from the 17 August 1999 Izmit earthquake on the North Anatolian Fault, Turkey, *Bull. Seismol. Soc. Amer.*, 92 (1), 19–42, doi:10.1785/0120000808
- Massonnet, D., Rossi, M., Carmona, C., Adragna, F., Peltzer, G., Feigl, K., and Rabaute, T. (1993), The displacement field of the Landers earthquake mapped by radar interferometry, *Nature*, 364, 138–142, doi:10.1038/364138a0
- Mattei, M., Cifelli, F., Muttoni, G., Zanchi, A., Berra, F., Mossavvari, F., and Eshraghi, S. A. (2012), Neogene block rotation in central Iran: Evidence from paleomagnetic data, *Geol. Soc. Am. Bull.*, 124 (5–6), 943–956, doi: 10.1130/B30479.1
- McClusky, S., Reilinger, R., Mahmoud, S., Sari, D. B., and Tealeb, A. (2003), GPS constraints on Africa (Nubia) and Arabia plate motions, *Geophys. J. Int.*, 155: 126–138, doi:10.1046/j.1365-246X.2003.02023.x
- Merritts, D.J., Vincent, K.R., and Wohl, E.E. (1994), Long river profiles, tectonism, and eustasy: a guide to interpreting fluvial terraces, *J. Geophys. Res.*, 99, 14,031–14,050, doi:10.1029/94JB00857
- Mitchell, S.G., and Montgomery, D.R. (2006). Influence of a glacial buzzsaw on the height and morphology of the Washington Cascade Range, Washington State, USA. *Quat. Res.*, 65 (1), 96–107, doi:10.1016/j.yqres.2005.08.018

- Molin, P., Pazzaglia, F. J., and Dramis, F. (2004), Geomorphic expression of active tectonics in a rapidly-deforming forearc, Sila Massif, Calabria, Southern Italy, *Am. J. Sci.*, 304 (7), 559-589, doi:10.2475/ajs.304.7.559
- Molin, P., Fubelli, G., Nocentini, M., Sperini, S., Ignat, P., Grecu, F., and Dramis, F. (2012), Interaction of mantle dynamics, crustal tectonics, and surface processes in the topography of the Romanian Carpathians: A geomorphological approach, *Glob. Planet. Change*, 90, 58-72, doi:10.1016/j.gloplacha.2011.05.005
- Molnar, P. (2001), Climate change, flooding in arid environments and erosion rates, *Geology*, 29 (12), 1071-1074, doi:10.1130/0091-7613(2001)029<1071:CCFIAE>2.0.CO;2
- Molnar, P., Brown, E.T., Burchfiel, B.c., Deng, Q., Feng, X., Li, J., Raisbeck, C.M., Shi, J., Wu, Z., Yiou, F., and You, H. (1994), Quaternary climate change and the formation of river terraces across growing anticlines on the north flank of the Tien Shan, China: *J. Geol.*, 102, 583-602, doi:10.1086/629700
- Montgomery, D. R., Balco, G., and Willett, S. D. (2001), Climate, tectonics, and the morphology of the Andes, *Geology*, 29, 579–582, doi:10.1130/0091-7613(2001)029<0579:CTATMO>2.0.CO;2
- Morisawa, M., and Hack, J.T. (Eds) (1985), *Tectonic Geomorphology*, Allen and Unwin, Boston, USA.
- Mouthereau, F., Lacombe, O., and Vergés, J. (2012), Building the Zagros collisional orogen: timing, strain distribution and the dynamics of Arabia/Eurasia plate convergence, *Tectonophysics*, 532-535, 27-60, doi: 10.1016/j.tecto.2012.01.022.
- Nilforoushan, F., Masson, F., Vernant, P., Vigny, C., Martinod, J., Abbassi, M., Nankali, H., Hatzfeld, D., Bayer, R., Tavakoli, F., Ashtiani, A., Doerflinger, E., Daignières, M., Collard, P., and Chéry, J. (2003), GPS network monitors the Arabia-Eurasia collision deformation in Iran, *J. Geodesy*, 77 (7-8), 411-422, doi: 10.1007/s00190-003-0326-5.
- Nozaem, R., Mohajjel, M., Rossetti, F., Della Seta, M., Vignaroli, G., Yassaghi, A., Salvini, F., and Eliassi, M. (2013), Post-Neogene right-lateral strike-slip tectonics at the north-western edge of the Lut Block (Kuh-e-Sarhangi Fault), Central Iran, *Tectonophysics*, 589, 220-233, doi:10.1016/j.tecto.2013.01.001
- Olivetti, V., Cyr, A.J., Molin, P., Faccenna, C., and Granger, D.E. (2012), Uplift history of the Sila Massif, southern Italy, deciphered from cosmogenic ¹⁰Be erosion rates and river longitudinal profile analysis, *Tectonics*, 31 (3), TC3007, doi:10.1029/2011TC003037
- Pederson, J.L., Anders, M.D., Rittenhour, T.M., Sharp, W.D., Gosse, J.C., and Karlstrom, K.E. (2006), Using fill terraces to understand incision rates and evolution of the Colorado River in eastern Grand Canyon, Arizona, *J. Geophys. Res.*, 111, F02003, doi:10.1029/2004JF000201.
- Pedraza, A., Pérez-Peña, J. V., Jesús Galindo-Zaldívar, J., Azañón, J. M., and Azor, A. (2009), Testing the sensitivity of geomorphic indices in areas of low-rate active folding (eastern Betic Cordillera, Spain). *Geomorphology*, doi:10.1016/j.geomorph.2008.09.026
- Pérez-Peña, J. V., Azañón, J. M., Azor, A., Delgado, J., and González-Lodeiro, F. (2009), Spatial analysis of stream power using GIS: SLk anomaly maps, *Earth Surf. Process. Landf.*, 34, 16-25, doi:10.1002/esp.1684
- Ramezani, J., and Tucker, R. D. (2003), The Saghand region, central Iran: U-Pb geochronology, petrogenesis and implications for Gondwana tectonics, *Am. J. Sci.*, 303 (7), 622-665, doi:10.2475/ajs.303.7.622
- Regard, V., Bellier, O., Braucher, R., Gasse, F., Bourlès, D., Mercier, J., Thomas, J. C., Abbassi, M. R., Shabanian, E., and Soleymani, S. (2006), ¹⁰Be dating of alluvial deposits from Southeastern Iran (the Hormoz Strait area), *Paleogeogr. Paleoclimatol. Paleoecol.*, 242 (1-2), 36-53, doi:http://dx.doi.org/10.1016/j.palaeo.2006.05.012.
- Reilinger, R., McClusky, S., Vernant, P., Lawrence, S., Ergintav, S., Cakmak, R., Ozener, H., Kadirov, F., Guliev, I., Stepanyan, R., Nadariya, M., Hahubia, G., Mahmoud, S., Sakr, K.,

- ArRajehi, A., Paradissis, D., Al-Aydrus, A., Prilepin, M., Guseva, T., Evren, E., Dmitrotsa, A., Filikov, S. V., Gomez, F., Al-Ghazzi, R., and Karam, G. (2006), GPS constraints on continental deformation in the Africa-Arabia-Eurasia continental collision zone and implications for the dynamics of plate interactions, *J. Geophys. Res.* (1978–2012), 111, B05411, doi:10.1029/2005JB004051
- Replumaz, A., Lacassin, R., Tapponnier, P. and Leloup, P. H. (2001), Large river offsets and Plio-Quaternary dextral slip rate on the Red River fault (Yunnan, China), *J. Geophys. Res.*, 106, 819–836, doi:10.1029/2000JB900135
- Ritter J.B., Miller J.R., Enzel Y., and Wells S.G. (1995), Reconciling the roles of tectonism and climate in Quaternary alluvial fan evolution, *Geology*, 23, 245–248, doi:10.1130/0091-7613(1995)023<0245:RTROTA>2.3.CO;2
- Rockwell, T.K., Keller, K.A., Clark, M.N., and Johnson, D.L. (1984), Chronology and rates of faulting of Ventura River terraces, California, *Geol. Soc. Am. Bull.*, 95, 1466–1474, doi:10.1130/0016-7606(1984)95<1466:CAROFO>2.0.CO;2
- Roe, G.H., Stolar, D.B., and Willett, S.D. (2006), Response of a steady-state critical wedge orogen to changes in climate and tectonic forcing, in *Tectonics, Climate, and Landscape Evolution*, *Geol. Soc. Am., Spec. Paper*, 398, Penrose Conference Series, edited by S.D. Willett, N. Hovius, M.T. Brandon, and D.M. Fisher, pp. 227–239, Boulder, Colorado, USA, doi: 10.1130/2005.2398(13).
- Royden, L., and Perron J. T. (2013), Solutions of the stream power equation and application to the evolution of river longitudinal profiles, *J. Geophys. Res. Earth Surf.*, 118, 497–518, doi:10.1002/jgrf.20031.
- Rossetti, F., Nozaem, R., Lucci, F., Vignaroli, G., Gerdes, A., Nasrabadi, M., and Theye, T. (2014), Tectonic setting and geochronology of the Cadomian (Ediacaran-Cambrian) magmatism in Central Iran, Kuh-e-Sarhangi region (NW Lut Block), *J. Asian Earth Sci.*, Available online 30 July 2014, doi:10.1016/j.jseaes.2014.07.034
- Ruttner, A., Nabavi, M.H., and Alavi, M. (1970), Geological map of Ozbak Kuh Mountain (1/100,000). Geological Survey of Iran, Tehran.
- Sahandi, M.R., Ghassemi, M.R., Ekhtiarabadi, Y., 2010. Geological map of Ghasemabad (1:100,000). Geological Survey of Iran, Tehran.
- Salvini, F., 2004, Daisy 3 the structural data integrated system analyzer., p. Available at Software University of Roma Tre, Roma: <http://host.uniroma3.it/progetti/fralab>.
- Schiattarella, M., Di Leo, P., Beneduce, P., Giano, S.I., and Martino, C. (2006), Tectonically driven exhumation of a young orogen: an example from southern Apennines, Italy, in *Tectonics, climate, and landscape evolution*, *Geol. Soc. Am., Spec. Paper*, 398, Penrose Conference Series, edited by S.D. Willett, N. Hovius, M.T. Brandon, and D. Fisher, pp. 371–385, Boulder, Colorado, USA, doi:10.1130/2006.2398(23)
- Scholz, C.H. (1990), *The Mechanics of Earthquakes and Faulting*, Cambridge University Press, Cambridge, UK.
- Schwartz, D. P., and Coppersmith, K. J. (1984), Fault behavior and characteristic earthquakes: Examples from the Wasatch and San Andreas Fault Zones, *J. Geophys. Res.*, 89, B7, 5681–5698, doi:10.1029/JB089iB07p05681
- Scotti, V.N., Molin, P., Faccenna, C., Soligo, M., and Casas-Sainz, A. (2013), The influence of surface and tectonic processes on landscape evolution of the Iberian Chain (Spain): Quantitative geomorphological analysis and geochronology, *Geomorphology*, 206, 37–57, doi:10.1016/j.geomorph.2013.09.017
- Sella, G. F., Dixon, T. H., and Mao, A. (2002), REVEL: A model for recent plate velocities from space geodesy, *J. Geophys. Res.*, 107(B4), doi:10.1029/2000JB000033
- Serpelloni, E., Faccenna, C., Spada, G., Dong, D., and Williams, S.P. (2013), Vertical GPS ground motion rates in the Euro-Mediterranean region: new evidence of velocity gradients at different

- spatial scales along the Nubia–Eurasia plate boundary, *J. Geophys. Res.*, 118 (11), 6003–6024, doi:10.1002/2013JB010102
- Silva, P.G., Harvey, A.M., Zazo, C., and Goy, J.L., (1992), Geomorphology, depositional style and morphometric relationships of Quaternary alluvial fans in the Guadalentin Depression (Murcia, Southeast Spain), *Z. Geomorphol.*, 36, 325–341.
- Stock, J. D., and Montgomery, D. R. (1999), Geologic constraints on bedrock river incision using the stream power law, *J. Geophys. Res.* (1978–2012), 104(B3), 4983–4993, doi:10.1029/98JB02139
- Talebian, M., Jackson, J. (2002), Offset on the main recent fault of NW Iran and implications for the late Cenozoic tectonics of the Arabia–Eurasia collision zone, *Geophys. J. Int.*, 150, 422–439. doi:10.1046/j.1365-246X.2002.01711.x
- Talebian, M., Jackson, J. (2004), A reappraisal of earthquake focal mechanisms and active shortening in the Zagros mountains of Iran, *Geophys. J. Int.*, 156, 506–526. doi:10.1111/j.1365-246X.2004.02092.x
- Tarboton, D.G., Bras, R.L., and Rodriguez-Iturbe, I. (1991), On the extraction of channel networks from digital elevation data, *Hydrol. Process.*, 5, 81–100, doi: 10.1002/hyp.3360050107
- Tchalenko, J., Berberian, M., and Behzadi, H. (1973), Geomorphic and seismic evidence for recent activity on the Doruneh Fault, Iran, *Tectonophysics*, 19 (4), 333–341, doi:10.1016/0040-1951(73)90027-9
- Telbisz, T., Kovács, G., Székely, B., and Szabó, J. (2013), Topographic swath profile analysis: a generalization and sensitivity evaluation of a digital terrain analysis tool: *Z. Geomorphol.*, 57 (4), 485–513, DOI: 10.1127/0372-8854/2013/0110
- Troiani, F., and Della Seta, M. (2008), The Use of the Stream Length-Gradient Index in morphotectonic analysis of small catchments: a case study from central Italy, *Geomorphology*, 102, 159–168, doi:10.1016/j.geomorph.2007.06.020
- Troiani, F., and Della Seta, M. (2011), Geomorphological response of fluvial and coastal terraces to Quaternary tectonics and climate as revealed by geostatistical topographic analysis, *Earth Surf. Process. Landf.*, 36(9), 1193–1208, doi:10.1002/esp.2145
- Vernant, P., Nilforoushan, F., Hatzfeld, D., Abbassi, M. R., Vigny, C., Masson, F., Nankali, H., Martinod, J., Ashtiani, A., Bayer, R., Tavakoli, F., and Chéry, J. (2004), Present-day crustal deformation and plate kinematics in the Middle East constrained by GPS measurements in Iran and northern Oman, *Geophys. J. Int.*, 157 (1), 381–398, doi: 10.1111/j.1365-246X.2004.02222.x.
- Walker, R., and Jackson, J. (2002), Offset and evolution of the Gowk fault, S.E. Iran: a major intra-continental strike-slip system, *J. Struct. Geol.*, 24 (11), 1677–1698, doi:10.1016/S0191-8141(01)00170-5
- Walker, R., and Jackson, J. (2004), Active tectonics and late Cenozoic strain distribution in central and eastern Iran, *Tectonics*, 23, TC5010, doi:10.1029/2003TC001529
- Walker, R. T., and Khatib, M. M. (2006), Active faulting in the Birjand region of NE Iran, *Tectonics*, 25, TC4016, doi:10.1029/2005TC001871
- Walker, R. T., and Fattahi, M. (2011), A framework of Holocene and Late Pleistocene environmental change in eastern Iran inferred from the dating of periods of alluvial fan abandonment, river terracing, and lake deposition, *Quat. Sci. Rev.*, 30 (9), 1256–1271, doi:10.1016/j.quascirev.2011.03.004
- Walpersdorf, A., Manighetti, I., Mousavi, Z., Tavakoli, F., Vergnolle, M., Jadidi, A., Hatzfeld, D., Aghamohammadi, A., Bigot, A., Djamour, Y., Nankali, H., and Sedighi, M. (2014), Present-day kinematics and fault slip rates in eastern Iran, derived from 11 years of GPS data, *J. Geophys. Res. Solid Earth*, 119, 1359–1383, doi:10.1002/2013JB010620

- Wegmann, K.W., and Pazzaglia, F.J. (2009), Late Quaternary fluvial terraces of the Romagna and Marche Apennines, Italy: Climatic, lithologic, and tectonic controls on terrace genesis in an active orogen, *Quaternary Science Reviews*, 28 (1-2), 137-165, doi:10.1016/j.quascirev.2008.10.006
- Wegmann, K. W., Zurek, B. D., Regalla, C. A., Bilardello, D., Wollenberg, J. L., Kopczynski, S. E., Ziemann, J. M., Haight, S. L., Apgar, J. D., and Zhao, C. (2007), Position of the Snake River watershed divide as an indicator of geodynamic processes in the greater Yellowstone region, western North America, *Geosphere*, 3 (4), 272-281, doi:10.1130/GES00083.1
- Wesnousky, S.G. (1988), Seismological and structural evolution of strike-slip faults, *Nature*, 335, 340-342, doi:10.1038/335340a0
- Wesnousky, S.G. (2006), Predicting the endpoints of earthquake ruptures, *Nature*, 444, 358-360, doi:10.1038/nature05275
- Whipple, K.X., and Tucker, G.E. (1999), Dynamics of the stream power incision model: implications for the height limits of mountain ranges, landscape response timescales and research needs, *J. Geophys. Res.* (1978-2012), 104, 17661-17674, doi:10.1029/1999JB900120
- Whipple, K. X. (2001), Fluvial landscape response time: How plausible is steady-state denudation?, *Am. J. Sci.*, 301, 313-325, doi:10.2475/ajs.301.4-5.313
- Whipple, K. X. (2004), Bedrock rivers and the geomorphology of active orogens, *Annu. Rev. Earth Planet. Sci.*, 32, 151-185, doi: 10.1146/annurev.earth.32.101802.120356.
- Whittaker, A. C., Cowie, P. A., Attal, M., Tucker, G. E., and Roberts, G. P. (2007), Bedrock channel adjustment to tectonic forcing: Implications for predicting river incision rates, *Geology*, 35(2), 103-106, doi:10.1130/G23106A.1
- Whittaker, A.C, Attal, M., Cowie, P.A., Tucker, G.E., and Roberts, G. (2008), Decoding temporal and spatial patterns of fault uplift using transient river long profiles, *Geomorphology*, 100, 506-526, doi:10.1016/j.geomorph.2008.01.018
- Wilkinson, M., McCaffrey, K.J.W., Roberts, G.P., Cowie, P.A., Phillips, R.J., Michetti, A., Vittori, E., Guerrieri, L., Blumetti, A.M., Bubeck, A., Yates, A., and Sileo, G. (2010), Partitioned postseismic deformation associated with the 2009 Mw 6.3 L'Aquila earthquake surface rupture measured using a terrestrial laser scanner, *Geophys. Res. Lett.*, 37, L10309, doi:10.1029/2010GL043099
- Willett, S.D., Hovius, N., Brandon, M.T., and Fisher, D.M., 2006, Introduction, in *Tectonics, climate, and landscape evolution*, *Geol. Soc. Am., Spec. Paper*, 398, Penrose Conference Series, edited by S.D. Willett, N. Hovius, M.T. Brandon, and D. Fisher, pp. vii-xi, Boulder, Colorado, USA, doi: 10.1130/2006.2398(00).
- Willett, S.D., McCoy, S.W., Perron, J.T., Goren, L., Chen, C.Y. (2014), Dynamic reorganization of river basins, *Science*, 343, 1248765, doi:10.1126/science.1248765

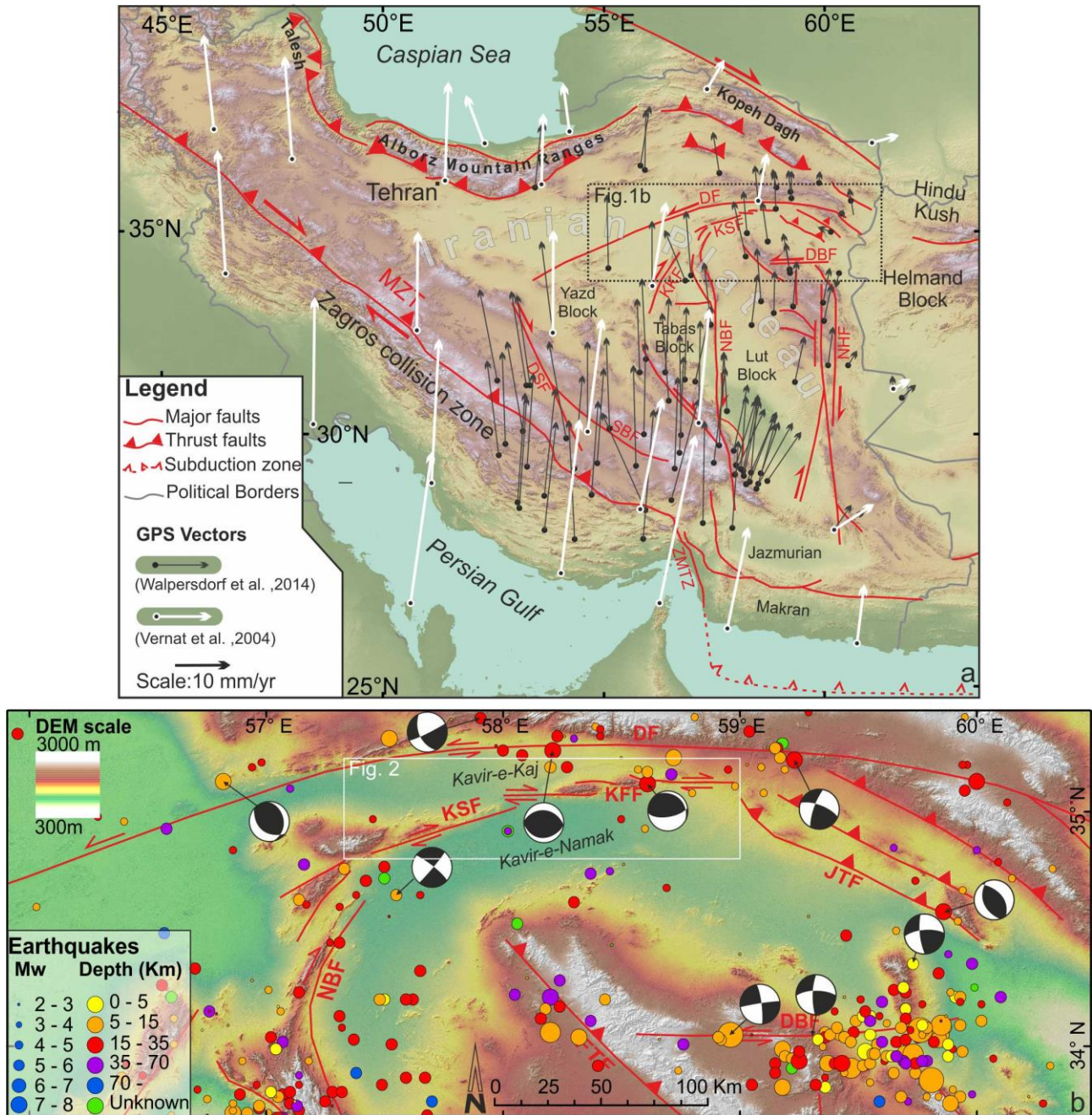


Figure 1: (a) Simplified tectonic map of Iran, showing the main collisional and intraplate strike-slip fault domains accommodating the Arabia-Eurasia convergence (modified after Berberian and King, 1981). DSF: Dehshir fault; KKF Kalmard-Kuhbanan Fault, KSF: Kuh-e-Sarhangi Fault; MZT: Main Zagros Thrust; NBF: Nayband Fault; NHF: Nehbandan fault; SBF: Shahr-e-Babak Fault; ZMTZ: Zagros-Makran Transfer Zone.; GPS velocities vectors in Iran relative to stable Eurasia are shown with different colors according to Vernant et al. (2004) and Walpersdorf et al. (2014); (b) Simplified tectonic map of northern Central Iran, showing the historical and instrumental seismicity of the area. Focal mechanisms are taken from the Harvard catalog (<http://www.globalcmt.org/CMTsearch.html>). Epicenters are from the ISC EHB Bulletin (International Seismic Centre, Thatcham, United Kingdom, 2009, <http://www.isc.ac.uk>) and earthquake catalogue at Iranian Institute of Earthquake Engineering and Seismology (<http://www.iiees.ac.ir>). The white square indicates the location of the study area and the extent of map Fig. 2.

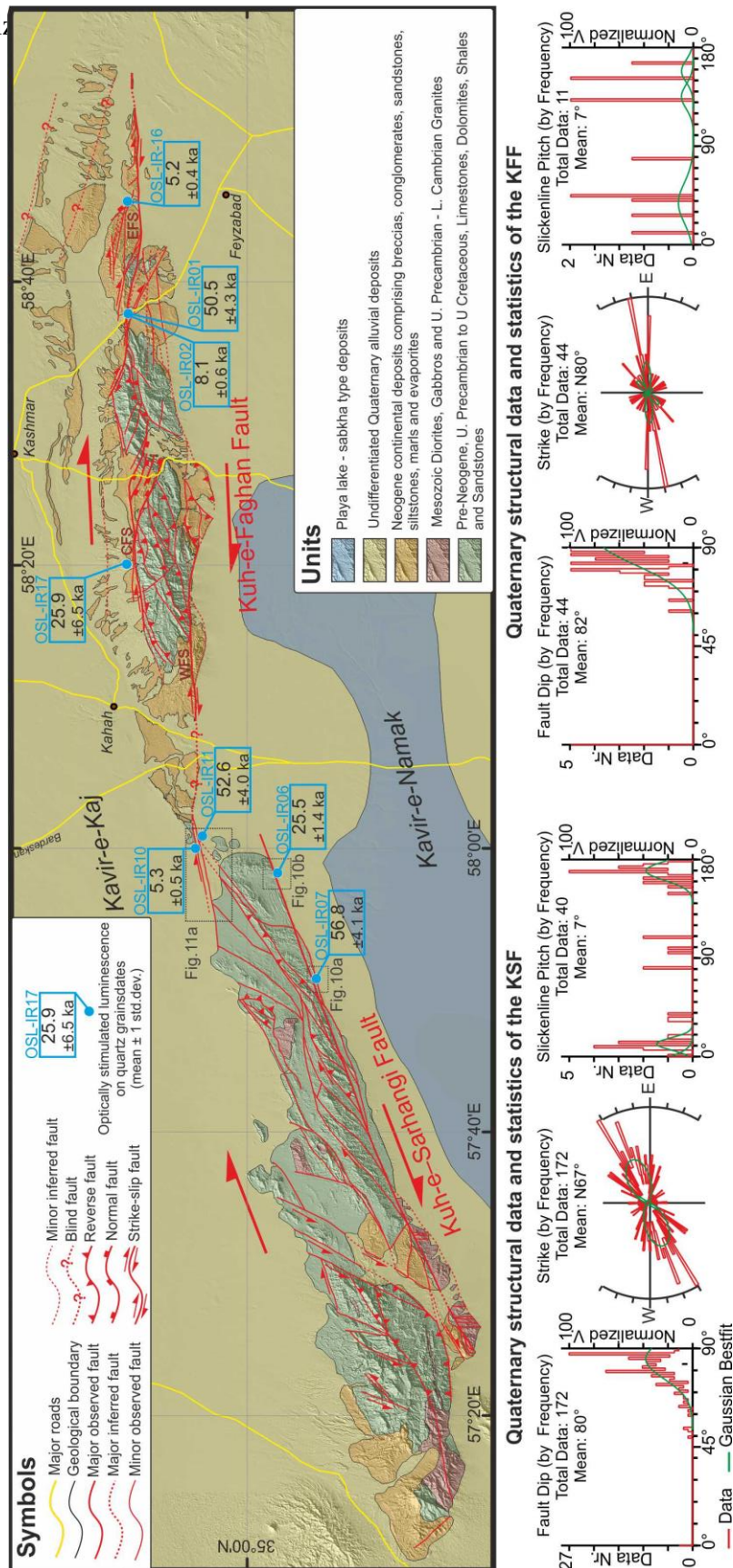


Figure 2: Geological sketch of the KSF and KFF systems along the north-western edge of the Lut block. Two geological cross-section of the KFF are also shown.

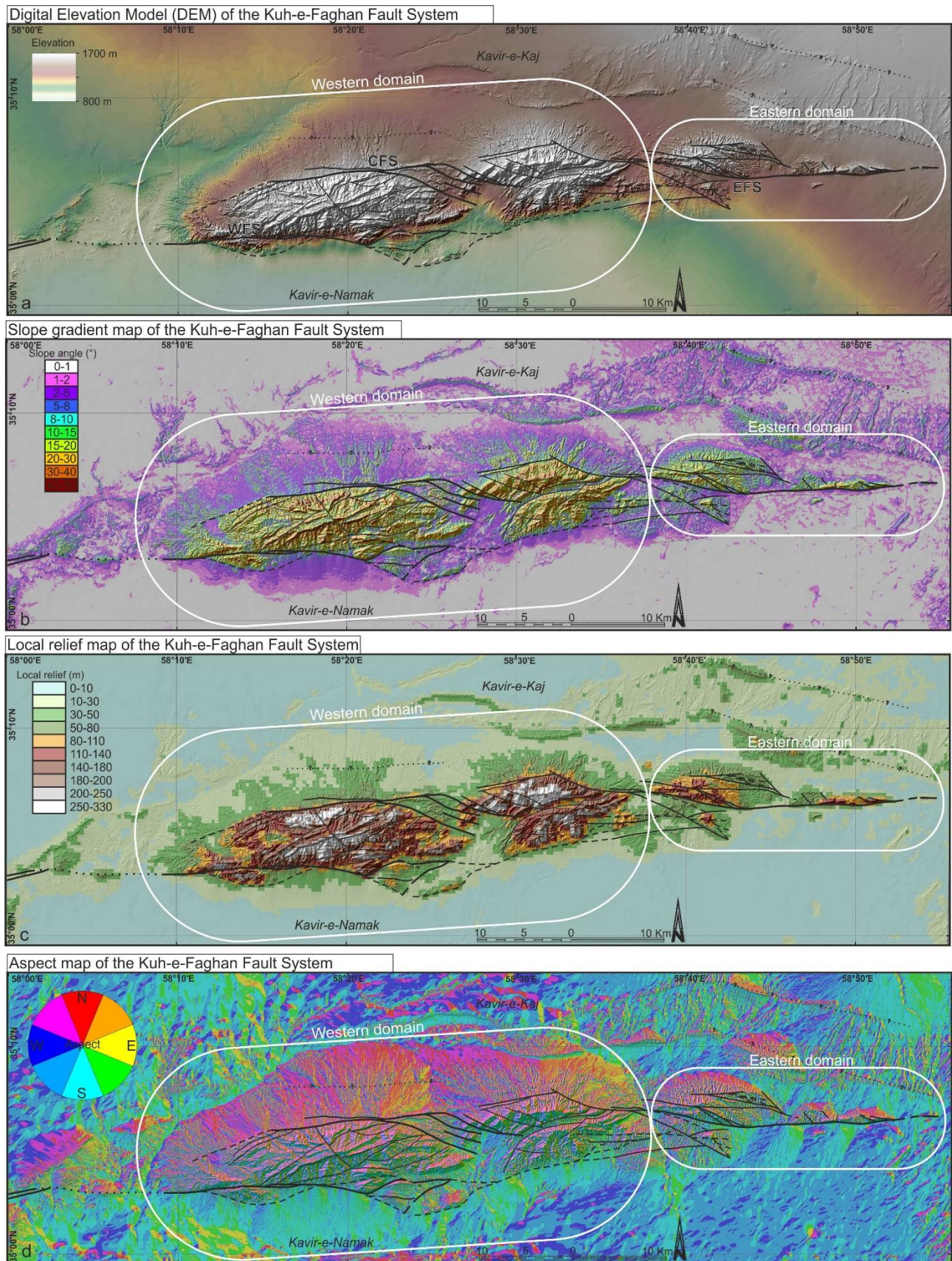


Figure 3: Maps of the study area extracted from a 10x10 m digital elevation model, with faults marked in black. (a) Topography by DEM. (b) Slope gradient map. Note the steep slope gradients along the boundary faults. (c) Local relief map. (d) Aspect map.

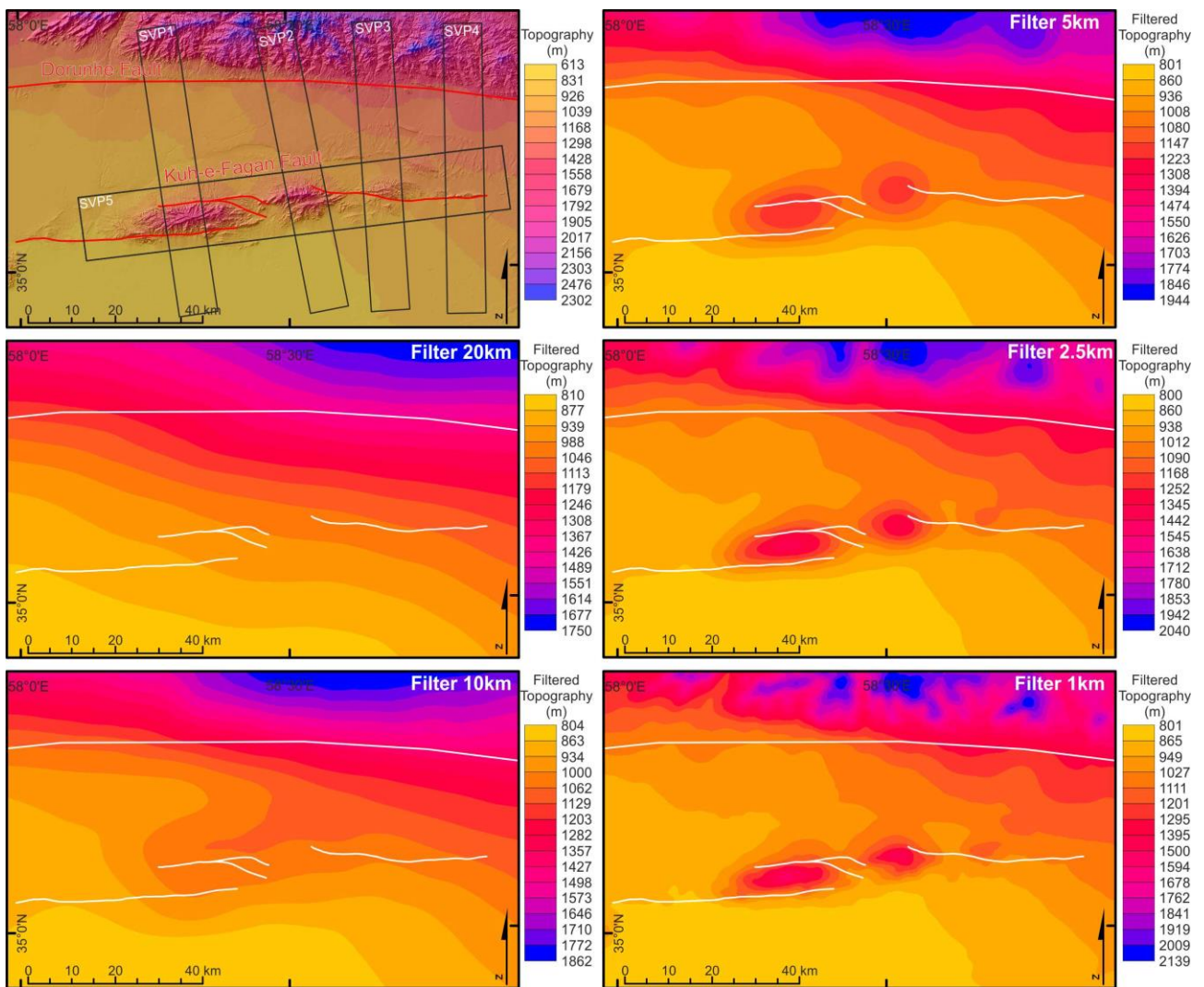


Figure 4: Filtered topography analysis performed on a 10x10 m (cell size) digital elevation model. Progressively smaller (from 20 to 1 km) radial filter was implemented.

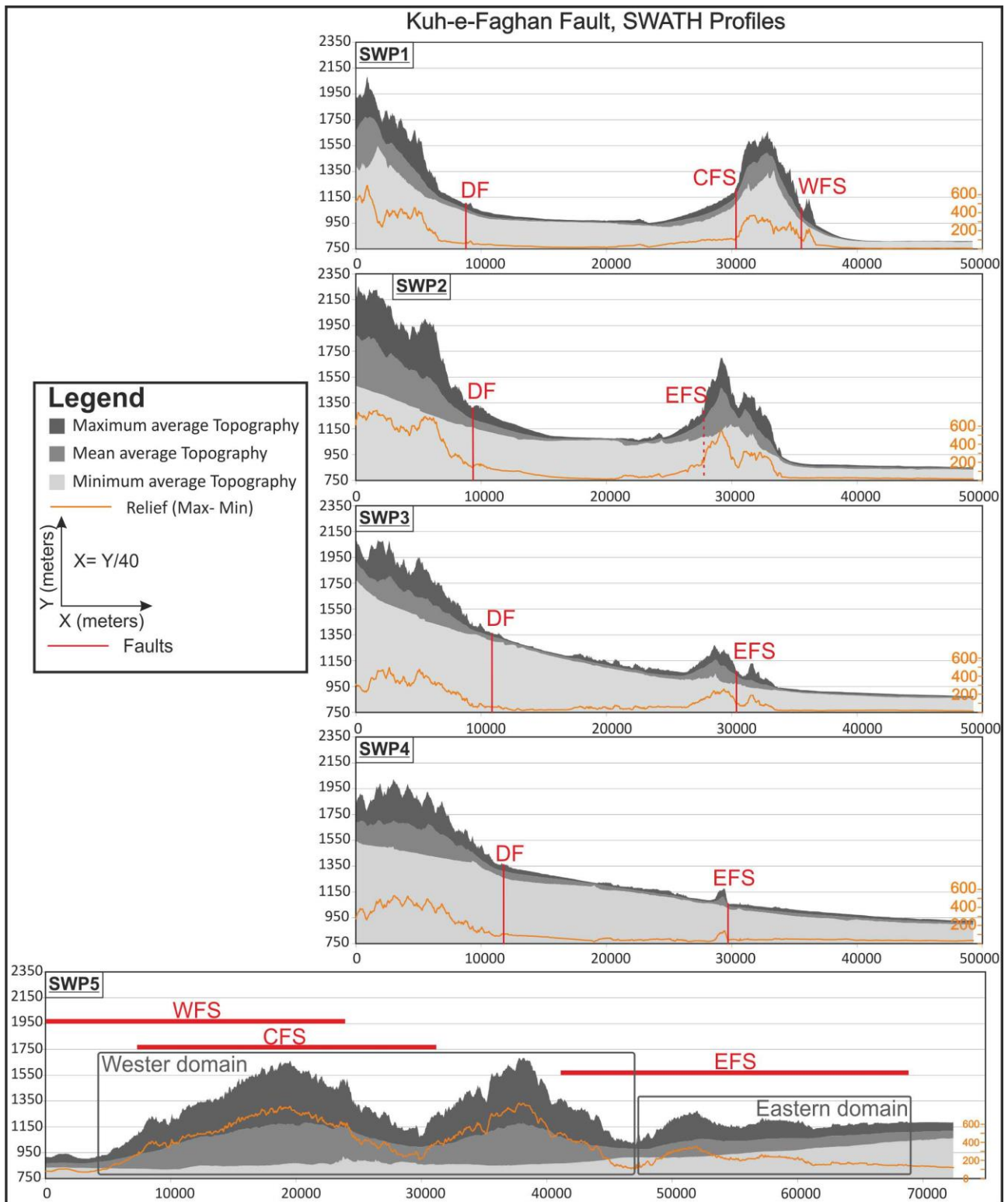


Figure 5: Swath profiles (40 times vertical exaggeration) across strike of the KFF (SWP1 to SWP4) and along strike of the KFF (SWP5) extracted from a 10x10 m digital elevation model. Locations of the swath is shown in Fig. 4.

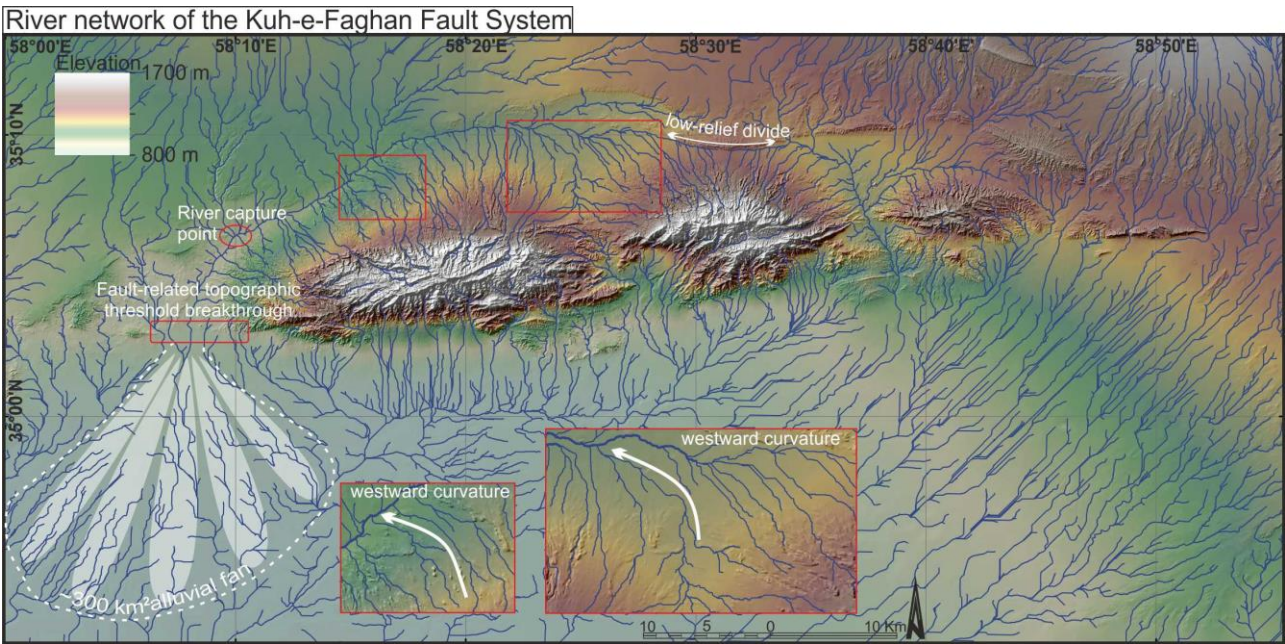
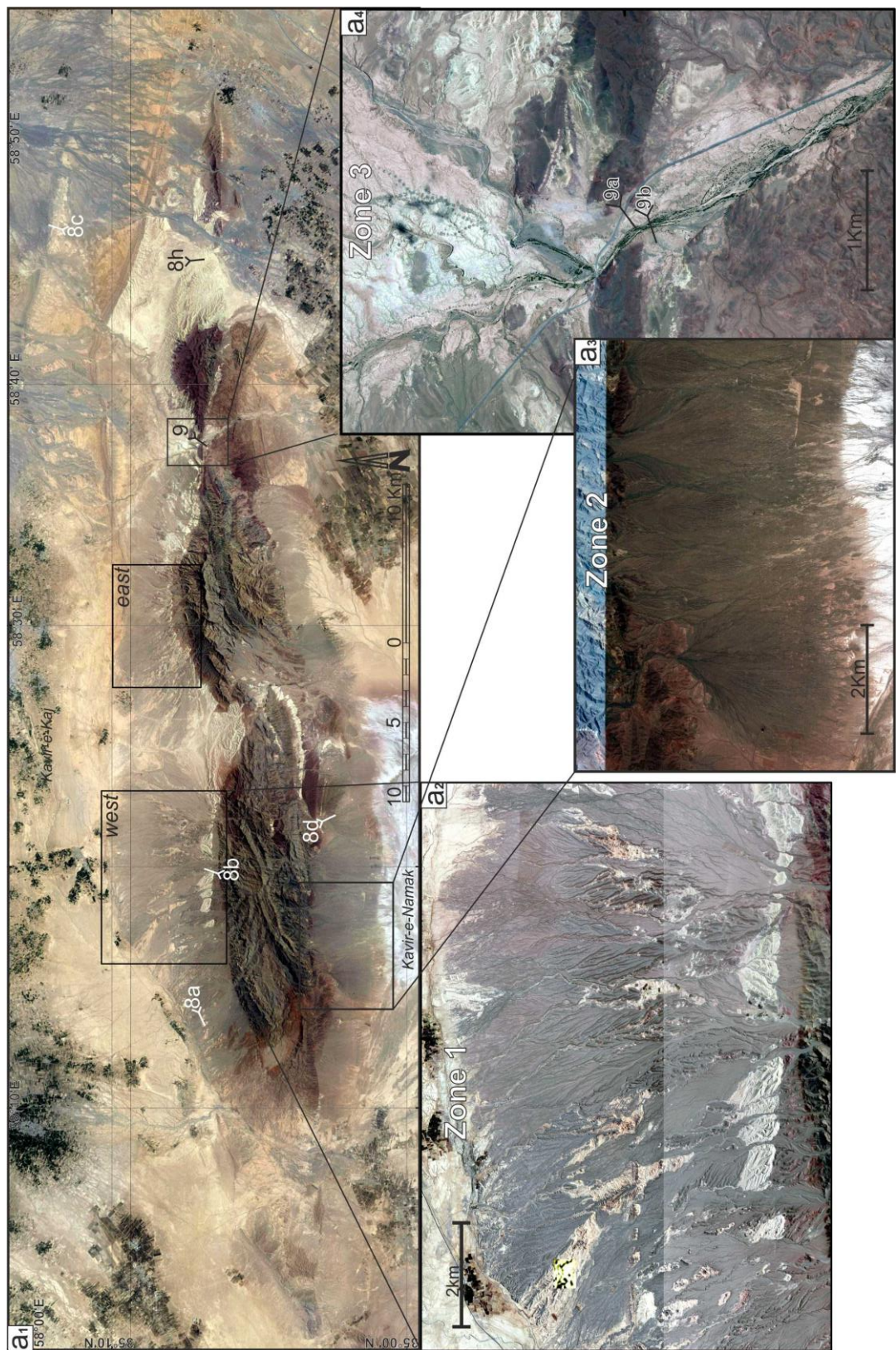


Figure 6: River network on DEM of the KFF area. Geomorphic evidence of drainage evolution are outlined. River capture point



stacked quaternary alluvial fan deposits (Zone 2); (a₄) Blow-up detailing the different generations of Quaternary terraced alluvial plain deposits (Zone 3). See Fig. 7b for details on the distribution of the different Quaternary alluvial deposits.

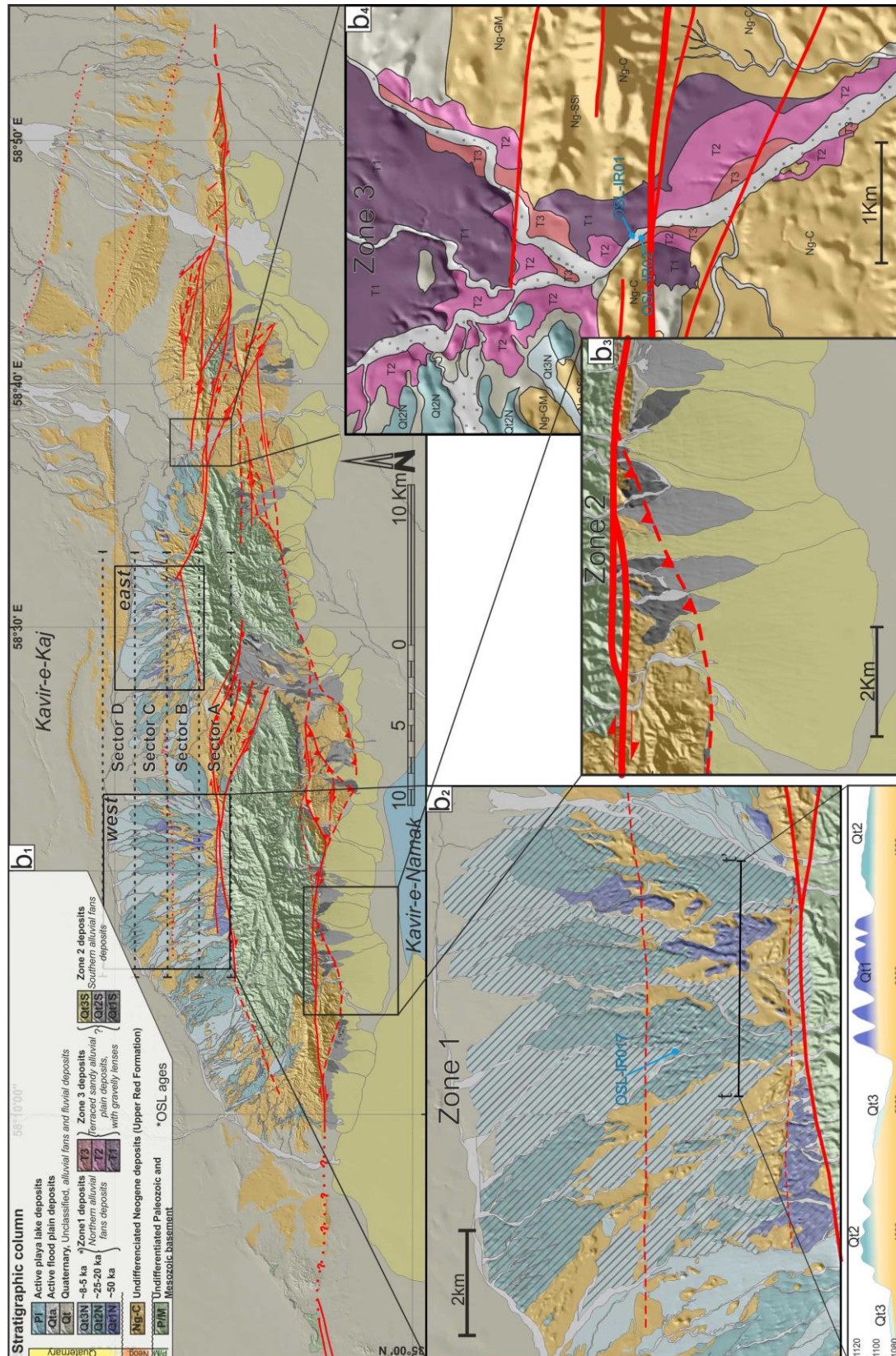


Figure 7b: . (b₁) Map of the KFF area showing the distribution of Quaternary alluvial deposits. The squares marked “west” and “east” indicate the areas where morphometric alluvial fan slope angle analysis was performed. The black dotted lines represent the boundaries of sectors in which

morphometric analysis and statistics where performed (see text). (b₂) Blow-up of the north-western Quaternary alluvial fan deposits (Zone 1) with topographic section t-t' across Qt1N, Qt2N and Qt3N deposits. Black hatched areas mark the alluvial fans used for the morphometric analysis. (b₃) Blow-up detailing the distribution of the southern stacked quaternary alluvial fan deposits (Zone 2). (b₄) Blow-up detailing the distribution of the different generations of Quaternary terraced alluvial plain deposits (Zone 3).

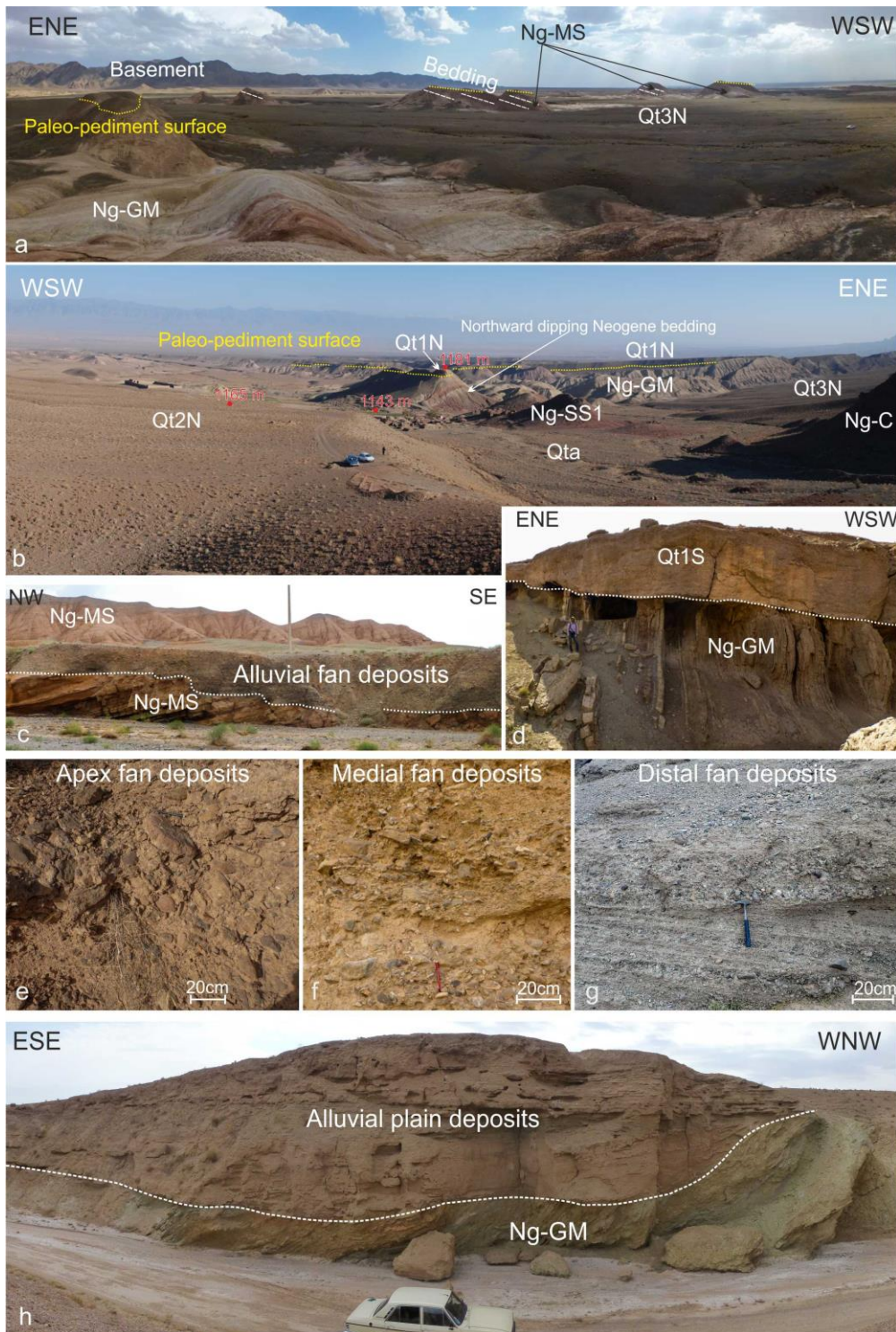


Figure 8: Outcrop examples of the Quaternary alluvial fan and alluvial plain deposits. Panoramic views of the alluvial fan deposits and their stratigraphic relations with the Neogene deposits in the

geomorphological Zone 1 (see Fig. 7a and text), viewed from the northern alluvial plain towards the fault system (a) and from the fault system (the CFS) towards the alluvial plain (b). (c) Example of the Neogene-Quaternary erosional unconformity (pediment) tens of kilometers north of the fault system. (d) Example of the Neogene-Quaternary erosional unconformity (pediment) to the south of the KFF. Example of Quaternary fan deposits characteristics from the fan apex zone (e) to the fan medial (f) and distal zone (g). (h) Outcrop example of the alluvial plain deposits in the geomorphological Zone 3. See Fig. 7a for locations.

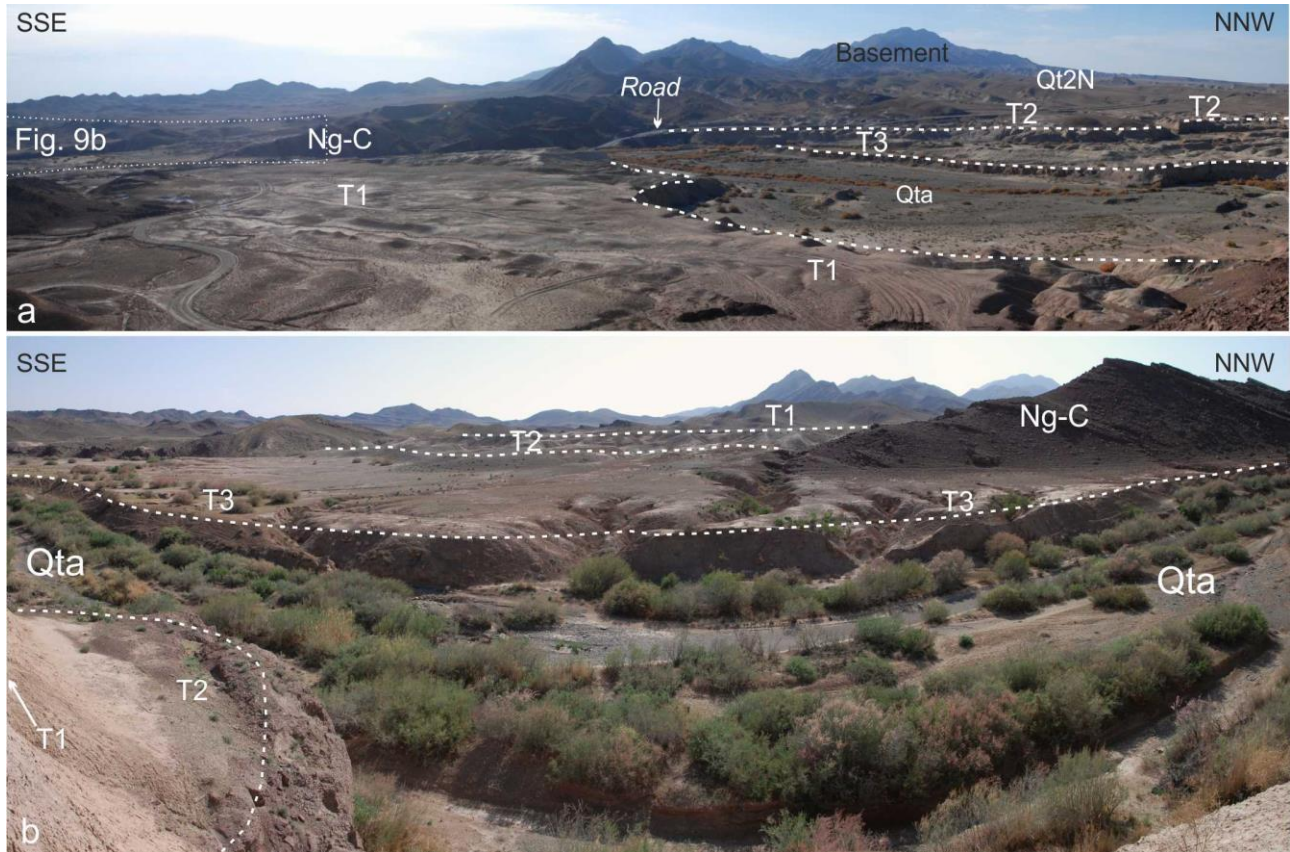


Figure 9: Panoramic view of the Quaternary fluvial terraces and their correlation with the northern alluvial fan deposits (a). (b) Detail of the altimetric relationship between the three generations of fluvial terraces. See Fig. 7a for location

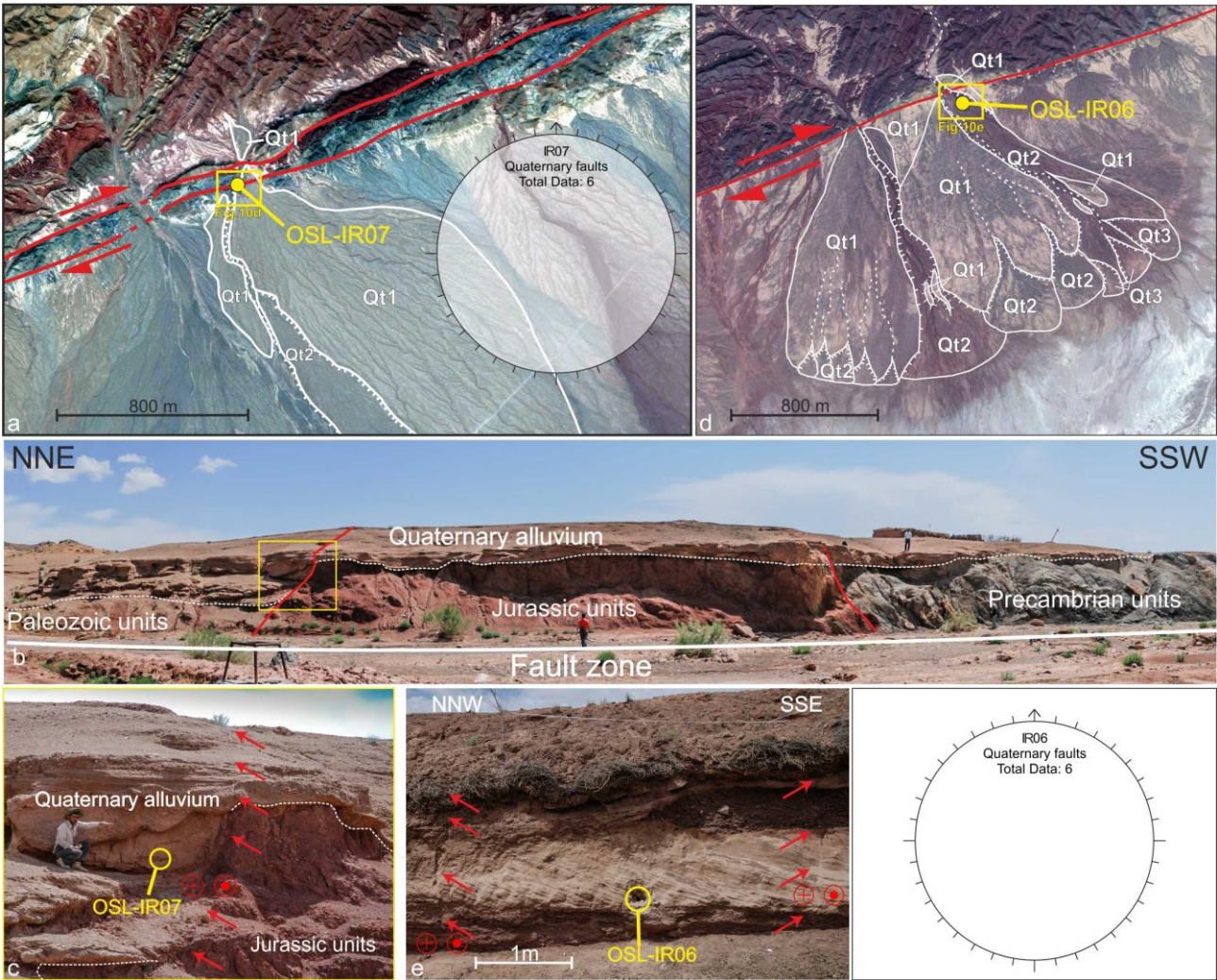


Figure 10:

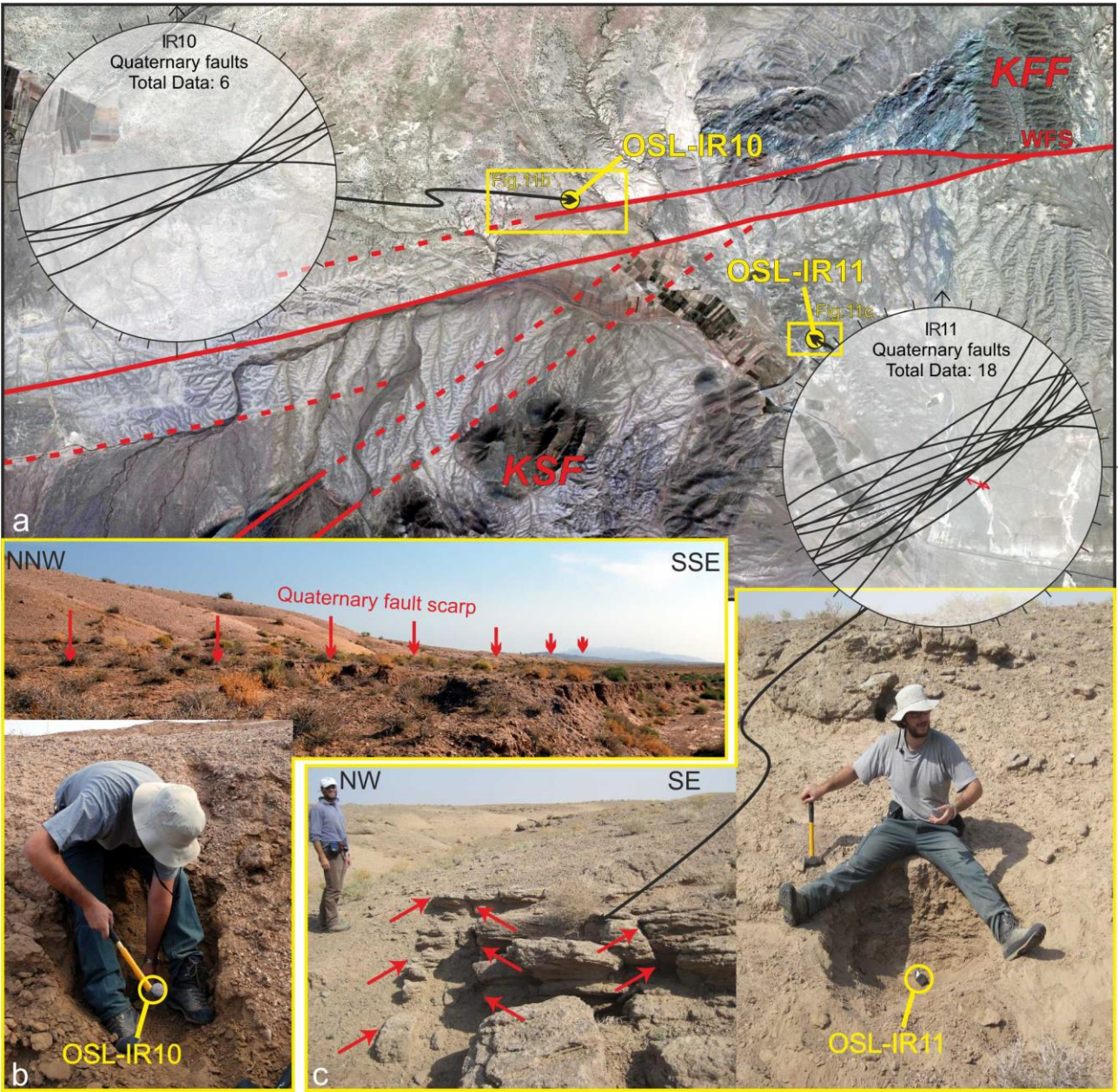


Figure 11:

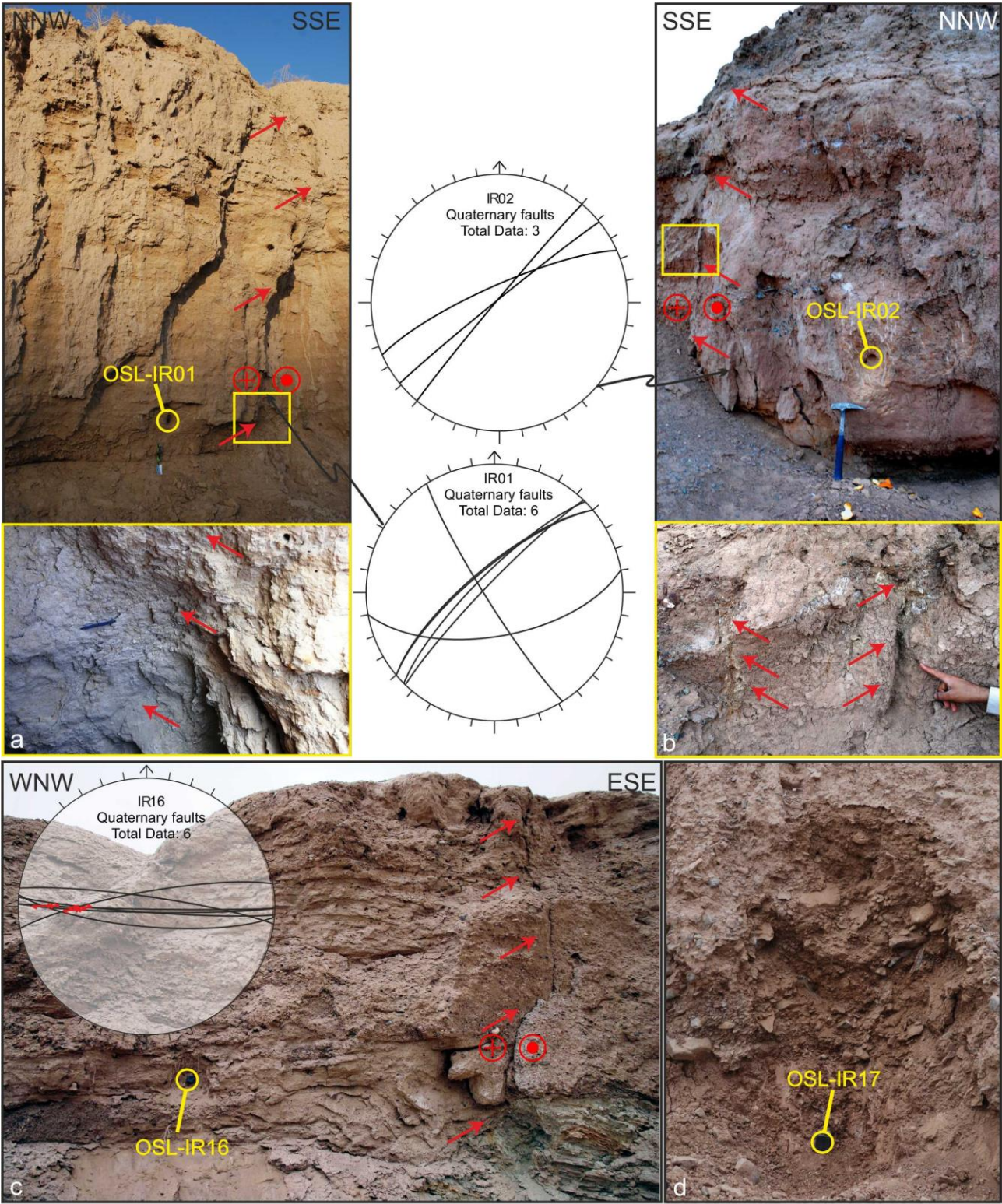


Figure 12:

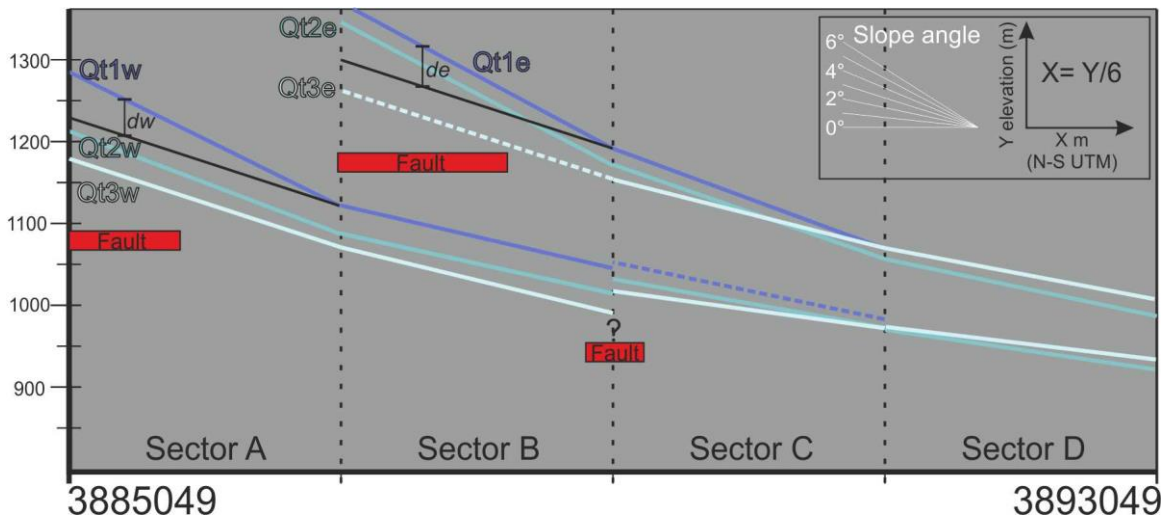


Figure 13: Results of the northern Quaternary alluvial fan slope angle analysis for areas “west” and “east” (Fig. 7). The diagram shows the mean alluvial fan slope angle and elevation for the four sectors (A, B, C and D in Fig. 7). The projected fault location extent is shown in red. *dw* and *de* marks the conservative estimate of the Qt1N surface fault-related uplift for the two areas

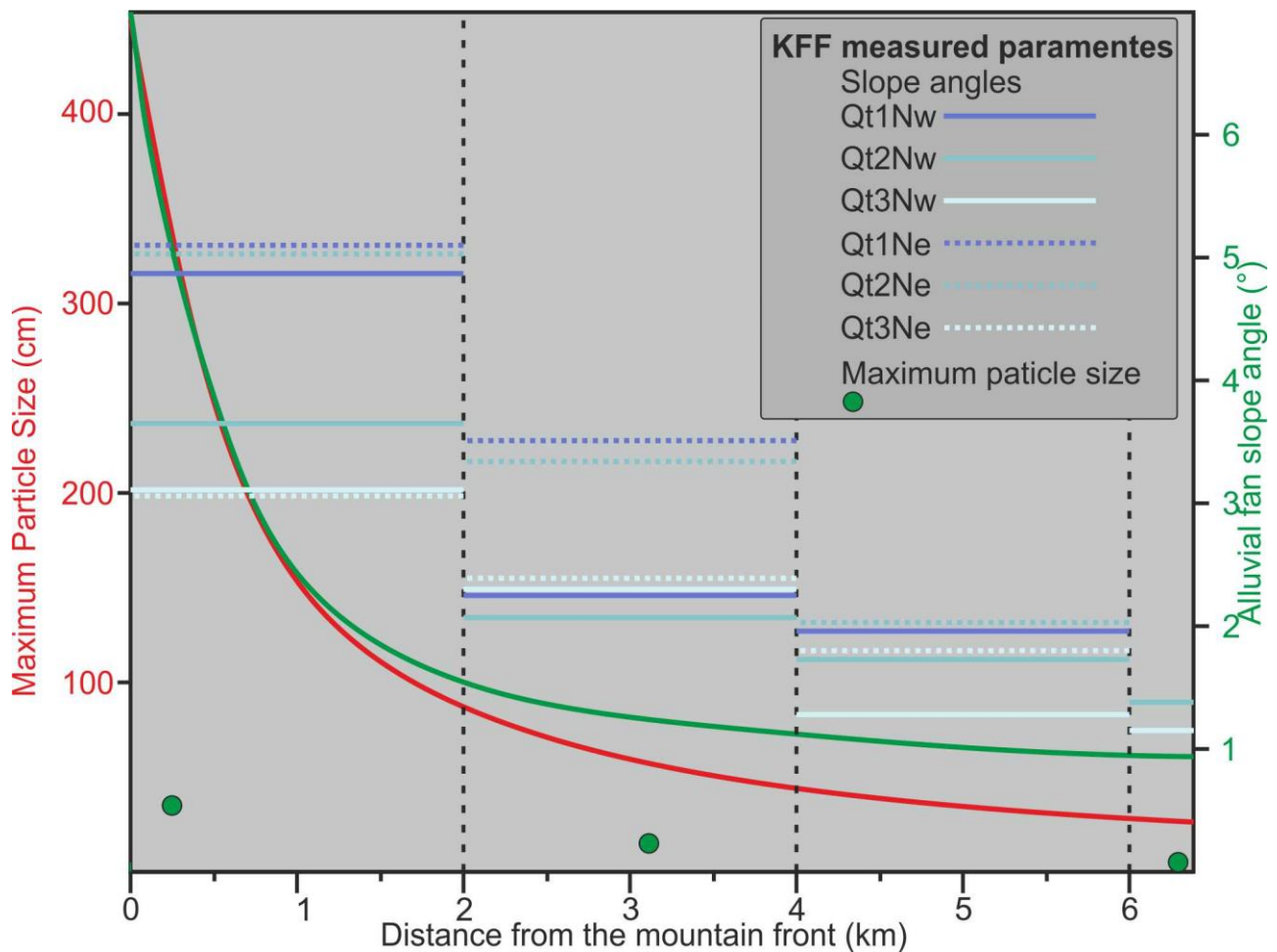


Figure 14: Comparison between the obtained mean slope angle and maximum particle size results of the KFF alluvial fans and the mean fan surface slope angle (green), observed along the radial profile on

alluvial fans in semi-arid settings (curve after Blissenbach, 1954). The corresponding mean of maximum particle size values (red) is also reported for the same alluvial fans in semi-arid settings (curve after Blissenbach, 1954).

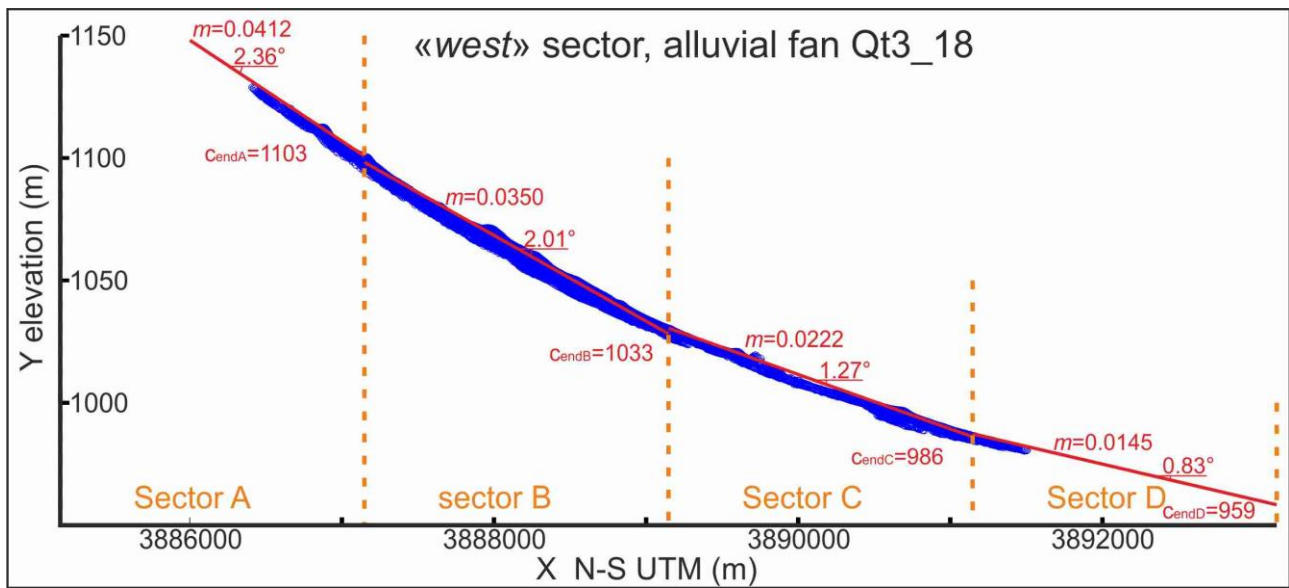


Figure A1: Example of extracted alluvial fan data plotted on a N-S transect and the calculated slope for each sector. m = slope gradient, CendX=fan elevation at the northern end of sector x